Tampere University

KIRSI VIRKKI

Photoinduced Charge Transfer Processes at Organic-Semiconductor Interfaces

Tampere University Dissertations 67

Tampere University Dissertations 67

KIRSI VIRKKI

Photoinduced Charge Transfer Processes at Organic-Semiconductor Interfaces

ACADEMIC DISSERTATION
To be presented, with the permission of
the Faculty Council of the Faculty of Engineering and Natural Sciences
of Tampere University,
for public discussion in the auditorium Pieni Sali 1
of the Festia building, Korkeakoulunkatu 8, Tampere,
on 24 May 2019, at 12 o'clock.

ACADEMIC DISSERTATION
Tampere University, Faculty of Engineering and Natural Sciences
Finland

Responsible supervisor and Custos	Professor Nikolai Tkachenko Tampere University Finland	
Pre-examiners	Professor Francis D'Souza University of North Texas USA	Research Associate Tatu Kumpulainen University of Geneva Switzerland
Opponent	Associate Professor Maria Abrahamsson Chalmers University of Technology Sweden	

The originality of this thesis has been checked using the Turnitin OriginalityCheck service.

Cover design: Roihu Inc.

ISBN 978-952-03-1101-8 (print)
ISBN 978-952-03-1102-5 (pdf)
ISSN 2489-9860 (print)
ISSN 2490-0028 (pdf)
http://urn.fi/URN:ISBN:978-952-03-1102-5

PunaMusta Oy – Yliopistopaino
Tampere 2019

Preface

This work was carried out at the Chemistry and Advanced Materials (CAM) research group at the Faculty of Engineering and Natural Sciences, at Tampere University (previously Laboratory of Chemistry and Bioengineering, Tampere University of Technology) during 2012-2019. Academy of Finland (grant no. 263486), TUT Graduate school, and Vilho, Yrjö and Kalle Väisälä Foundation are gratefully acknowledged for funding.

It has been a privilege to work in the pleasant atmosphere of the CAM group. First of all, I would like to thank my supervisor, prof. Nikolai Tkachenko for the guidance and support throughout the years, and for the patience and encouragement at the moments when the research did not proceed as expected. I am deeply grateful to prof. Helge Lemmetyinen for the opportunity to work at the Laboratory of Chemistry, starting from the summer internship almost exactly ten years ago.

All research is teamwork. I wish to express my warmest thanks to all the co-authors in the publications: the group of prof. Tomás Torres for their synthetic work as well as prof. Viacheslav Golovanov for the computational efforts. Prof. Francis D'Souza and Dr. Tatu Kumpulainen are acknowledged for their valuable comments in the pre-examination process. My dearest thanks go to all my colleagues at the CAM group. Dr. Venla Manninen, Dr. Essi Sariola-Leikas, Dr. Tero-Petri Ruoko, Mr. Arto Hiltunen and Ms. Hannele Hongell, thank you for the invaluable conversations in the office and at the lunch table throughout the years. Dr. Kati Stranius and Dr. Hanna Hakola, thank you for the peer support that has carried us all through the bright days as well as the difficult times.

Luckily, life is not all about work. I would like to thank all my friends for the precious moments in handicraft, boardgames, and outdoor activities. Special thanks to the FSK team for the unforgettable escape room experiences. Fanni and Markku, thank you for your friendship and for everything you have done for us as a family.

I would like to thank my family for all the support you have given me. Haluan kiittää vanhempiani siitä, että olette aina tukeneet minua päätöksissäni. Suurkiitos myös kaikesta siitä, mitä olette koko perheemme eteen tehneet. Isovanhempien syli on lapsille äärimmäisen turvallinen paikka. My beautiful daughters, Laura and Kielo, I am thankful for your energy and sincereness that wipes away all the work-related issues whenever I play with you. Finally, I wish to express my deepest gratitude to my husband Matti. You believed in me even when I didn't. Thank you for being on my side.

Tampere, 6.5.2019

Kirsi Virkki

Abstract

The growing energy demand of the mankind has lead to the extensive use of fossil fuels. The burning of oil, coal and natural gas has increased the global temperature and atmospheric carbon dioxide percentage to a dangerously high level. Therefore, carbon-neutral energy sources such as solar cells are needed.

In order to design more effective solar cells, a deep understanding of the primary photochemical processes in the cells is needed. Ultrafast time-resolved spectroscopy, especially transient absorption methods, are a very useful tool for investigating the reaction kinetics in order to optimize the solar cell performance.

In this thesis, kinetics of the photoinduced processes at the interface of an organic monomolecular layer and a semiconductor are studied. Such structures may be used as the active material e.g. in dye-sensitized solar cells. Two different types of organic–semiconductor hybrids were prepared: fullerenes (C_{60}) immobilized on colloidal semiconductor quantum dots (QDs), and zinc phthalocyanine (ZnPc) derivatives on nanostructured titanium dioxide (TiO_2) and zinc oxide (ZnO) surfaces. The driving force of photocurrent generation in these systems is a photonic excitation leading to an electron transfer reaction across the organic–semiconductor interface. The observed electron transfer rates vary from a few picoseconds in ZnPc monolayers on TiO_2 to ca. 100 ps in QD–fullerene systems.

Phthalocyanine derivatives are very attractive sensitizing dyes for solar cell applications because of their excellent stability and strong absorption in the red part of the spectrum. A drawback with these compounds is their tendency towards aggregation. It reduces the solar cell efficiencies due to intra-aggregate losses. There are two common methods for aggregation-reduction: the use of molecular co-adsorbates and substitution of the phthalocyanine core with bulky side groups. Both mechanisms were observed to lower the degree of aggregation in the ZnPc samples. The substitution method proved to be more efficient in terms of the lifetime of the charge-separated state.

To more realistically mimic a solar cell, a hole-transporting material (HTM) was used. Its effect on the primary photoinduced reactions in the phthalocyanine–semiconductor samples was studied. With the chosen HTM, spiro-MeOTAD, the charge separation was observed to occur first at the phthalocyanine–HTM interface, followed by electron injection into the semiconductor material.

Complete solar cell samples were prepared in order to link the ultrafast spectroscopy results to actual solar cell performance. A correlation between the degree of aggregation and the produced photocurrent was confirmed. The less aggregated samples produce a higher photocurrent per number of absorbed photons. This study indentifies bottlenecks in modern hybrid organic–semiconductor solar cell design and suggests solutions for improving the solar cell performance.

Tiivistelmä

Ihmiskunnan energiankulutus kasvaa jatkuvasti, ja tähän saakka energiaa on tuotettu lähinnä fossiilisilla polttoaineilla. Öljyn, hiilen ja maakaasun poltto on nostanut sekä ilmakehän hiilidioksidipitoisuuden että maapallon lämpötilan vaarallisen korkeiksi. Siksi tarvitaan hiilineutraaleja energiantuotantomuotoja, kuten aurinkokennoja.

Syvällinen ymmärrys aurinkokennoissa tapahtuvista valoindusoiduista kemiallisista reaktioista on tärkeää suunniteltaessa uusia, tehokkaampia aurinkokennoja. Ultranopea aikaerotteinen absorptiospektroskopia tarjoaa oivan välineen aurinkokennojen reaktiokinetiikan tutkimukseen kennojen hyötysuhteen optimoimiseksi.

Tässä työssä tutkittiin valon aikaansaamia prosesseja orgaanisten yhdisteiden ja puolijohteiden rajapinnoilla. Tällaisia rakenteita voidaan käyttää esimerkiksi väriaineherkistetyissä aurinkokennoissa. Työssä tutkittiin kahta orgaanisen aineen ja puolijohteen hybridirakennetta: fullereeneja kvanttipisteiden pinnalla, ja ftalosyaniineja nanorakenteisen titaanidioksidin ja sinkkioksidin pinnalla. Kaikissa näytteissä havaittiin valon aikaansaamia elektroninsiirtoreaktioita, jotka johtavat sähkövirran syntymiseen aurinkokennonäytteissä. Reaktioiden nopeus vaihteli muutamasta pikosekunnista (ftalosyaniini titaanidioksidin pinnalla) noin 100 ps:iin (fullereenit kvanttipisteiden pinnalla).

Ftalosyaniinijohdannaiset ovat aurinkokennokäyttöön hyvin soveltuvia väriaineita. Niillä on voimakas absorptio esityisesti punaisessa osassa spektriä, ja ne ovat hyvin stabiileja. Haittapuolena on niiden aggregoitumistaipumus. Aggregoituminen pienentää aurinkokennojen hyötysuhteita aggregaattien sisäisten häviöiden takia. Aggregoitumisen vähentämiseen on yleisesti käytössä kaksi menetelmää: seosaineet ja tilaa vievien sivuryhmien substituutio ftalosyaniinirakenteeseen. Kumpikin menetelmä vähensi aggregoitumista ftalosyaniinikerroksissa, mutta substituutiomekanismi oli tehokkaampi, kun tarkastellaan varausten erottumisen elinaikaa.

Rakenteeseen lisättiin aukonkuljetusmateriaalia (spiro-MeOTAD) oikean aurinkokennon toiminnan simuloimiseksi. Aukonkuljetusmateriaalin vaikutusta valoindusoitujen reaktioiden kinetiikkaan tutkittiin. Havaittiin, että varausten erottuminen tapahtuu ensin orgaanisen aineen ja aukonkuljetusmateriaalin rajapinnassa, minkä jälkeen ftalosyaniini luovuttaa elektronin puolijohteeseen.

Aikaerotteisten spektroskopiamittausten tulokset haluttiin myös linkittää todellisiin aurinkokennojen hyötysuhteisiin. Ftalosyaniinien aggregoitumisen ja aurinkokennojen tuottaman valovirran välillä havaittiin selkeä korrelaatio. Vähemmän aggregoituneet näytteet tuottavat suuremman sähkövirran absorboituneiden fotonien lukumäärää kohti. Työn tulokset auttoivat tunnistamaan modernien hybridiaurinkokennojen suunnittelussa esiintyviä pullonkauloja. Tulosten perusteella voidaan esittää keinoja kennojen hyötysuhteiden parantamiseksi.

Contents

Abbreviations and Symbols

A	Acceptor
AM1.5	Air mass 1.5
APCE	Absorbed photon to current efficiency
CB	Conduction band
CDCA	Chenodeoxycholic acid
CL	Compact layer
CR	Charge recombination
CT	Charge transfer
D	Donor
DOS	Density of states
EnT	Energy transfer
ET	Electron transfer
FTO	Fluorinated tin oxide
DSSC	Dye-sensitized solar cell
FF	Fill factor
FWHM	Full width of half maximum
HOMO	Highest occupied molecular orbital
HTM	Hole-transporting material
IPCE	Incident photon to current efficiency
IV	Current – voltage
LUMO	Lowest unoccupied molecular orbital
NIR	Near infrared
NP	Nanoparticle
OA	Oleic acid
OPA	Optical parametric amplifier
Pc	Phthalocyanine
PCAS	Photocurrent action spectrum
QD	Quantum dot
SAM	Self-assembled monolayer
SEM	Scanning electron microscope
SC	Semiconductor

Spiro-MeOTAD, spiro	2,2',7,7'-tetrakis(*N*,*N*-di-*p*-methoxyphenylamino)-9,9'-spirobifluorene
ssDSSC	Solid-state dye-sensitized solar cell
TA	Transient absorption
TCSPC	Time-correlated single photon counting
TOPO	Trioctylphosphine oxide
VB	Valence band
ZnOr	Zinc oxide nanorod
ZnPc	Zinc phthalocyanine

A, *Abs.*	Absorbance
ΔA	Change in absorbance
c	Concentration
I	Intensity
J	Current density
J_{max}	Current density at maximum power point
J_{sc}	Short circuit current density
λ	Wavelength
λ_{ex}	Excitation wavelength
η	Power conversion efficiency
P	Power
P_{in}	Input power
P_{max}	Maximum power
τ	Lifetime
V	Voltage
V_{max}	Voltage at maximum power point
V_{oc}	Open circuit voltage

List of Publications

I Kirsi Virkki, Sinem Demir, Helge Lemmetyinen, and Nikolai V. Tkachenko. Photoinduced Electron Transfer in CdSe/ZnS Quantum Dot–Fullerene Hybrids, *Journal of Physical Chemistry C*, vol. 119, no. 31, pp. 17561–17572, Jul. 2015.

II Kirsi Virkki, Essi Tervola, Mine Ince, Tomás Torres, and Nikolai V. Tkachenko. Comparison of Electron Injection and Recombination on TiO_2 Nanoparticles and ZnO Nanorods Photosensitized by Phthalocyanine, *Royal Society Open Science*, vol. 5, no. 7, p. 180323, Jul. 2018.

III Kirsi Virkki, Hanna Hakola, Maxence Urbani, Lara Tejerina, Mine Ince, M. Victoria Martínez-Díaz, Tomás Torres, Viktoria Golovanova, Viacheslav Golovanov, and Nikolai V. Tkachenko. Photoinduced Electron Injection from Zinc Phthalocyanines into Zinc Oxide Nanorods: Aggregation Effects, *Journal of Physical Chemistry C*, vol. 121, no. 17, pp. 9594–9605, Apr. 2017.

IV Kirsi Virkki, Essi Tervola, Maria Medel, Tomás Torres, and Nikolai V. Tkachenko. Effect of Co-Adsorbate and Hole Transporting Layer on the Photoinduced Charge Separation at the TiO_2–Phthalocyanine Interface, *ACS Omega*, vol. 3, no. 5, pp. 4947–4958, May 2018.

Author's Contribution

I K. Virkki planned the experiments, carried out the TA measurements, and conducted the exponential data fittings for all data. S. Demir conducted the titration series. N.V. Tkachenko developed the maximum entropy method for the time-resolved emission data fitting as well as the Poisson fitting model for TA results. The manuscript was drafted by K. Virkki, with contributions from all of the authors.

II K. Virkki planned and conducted the experiments. E. Tervola and K. Virkki prepared the samples for TA spectroscopy. M. Ince and T. Torres synthesized the compound. N.V. Tkachenko performed the data fitting and drafted the manuscript, with contributions from all of the authors.

III K. Virkki planned the experiments and conducted the TA measurements. H. Hakola prepared the samples. The used compounds were synthesized by M. Urbani, M. Ince, M.V. Martínez-Díaz, and T. Torres. V. Golovanova and V. Golovanov performed the molecular modelling. N.V. Tkachenko fitted the transient absorption data. The manuscript was drafted by K. Virkki, with contributions from all of the authors.

IV K. Virkki planned the experiments, conducted the TA measurements, built the IPCE measurement system and measured the IPCE spectra for the solar cell samples. E. Tervola prepared the solar cell samples and measured the IV characteristics. M. Medel and T. Torres synthesized the used compound. N.V. Tkachenko fitted the transient absorption data and drafted the manuscript, with contributions from all of the authors.

1 Introduction

The world energy supply was over 160 PWh in 2016, more than 80% of which was produced with fossil fuels (oil, coal, and natural gas).[1] The extensive use of fossil fuels has, however, increased the atmospheric carbon dioxide levels to more than 400 ppm, compared to 280 ppm in the pre-industrial times.[2] The increase in the CO_2 concentration in the atmosphere has lead to global warming of about 1 °C since the beginning of industrialization. The Intergovernmental Panel on Climate Change (IPCC) stated in their recent report that if the climate change can be stopped at 1.5 °C, the consequences will be much less harmful than at 2 °C. The risks on biodiversity and ecosystems, food and water supplies, and human health and security are estimated lower at a 1.5 °C warming than 2 °C.[3] The global warming can only be stopped by radically reducing the carbon dioxide emissions produced by the mankind. Thus, we need alternatives to the conventional energy sources.

The Sun is the ultimate source of clean, renewable, carbon-neutral energy. The potentially available solar energy has been estimated to be between 440 and 14000 PWh annually, well exceeding the total energy consumption even with the constantly increasing energy demand. Development of cost-efficient photovoltaic devices with mass production methods is perhaps the most convenient way to fulfill the energy needs in the future.

In addition to the conventional silicon solar cells, novel solar cell types are constantly being developed. All-organic solar cells are very cost-effective because they can be produced with e.g. printing and roll-to-roll techniques. As a drawback, the power conversion efficiencies of organic solar cells are lower than for silicon solar cells. Hybrid organic–semiconductor solar cells are a promising alternative to the organic solar cells, combining the advantages of both material types. Dye-sensitized solar cells (DSSCs) were first reported by Grätzel and O'Regan in 1991.[4] They consist of an interconnected network of TiO_2 nanoparticles sensitized with an organic dye. This photoanode is sandwiched between a conducting glass sheet and a top electrode, using a liquid electrolyte or a solid hole-transporting material (HTM). With solid hole-transporting materials, some of the typical downsides of liquid-electrolyte DSSCs can be overcome: the electrolyte does not corrode the photoactive materials, and there is no possibility for leakage. The best DSSC-type solar cells reach power conversion efficiencies more than 10%.[5] Using a solid hole-transporting material and co-sensitization by two different kinds of dyes, Kakiage *et al.* reported a DSSC with over 14% power conversion efficiency.[6]

When designing new materials for solar cells, their properties need to be comprehensively characterized. Knowledge on the reaction kinetics of the primary photoinduced reactions in a solar cell is essential when optimizing the cell structure and composition. Ultrafast time-resolved spectroscopy techniques are a versatile tool for studying reaction kinetics in the picosecond–millisecond time scales. This work utilizes ultrafast transient absorption

(TA) spectroscopy (the so-called pump probe method) in determining the reaction kinetics in the primary reactions involved in photocurrent generation in solar cell samples.

1.1 Research Objectives and Questions

The goal of this work is to understand the chemical reactions at an interface between an organic compound and a semiconductor substrate that are induced by photonic excitation. The reaction kinetics are studied using ultrafast transient absorption spectroscopy, and the effect of changes in the organic compound on the kinetics are studied in a series of zinc phthalocyanines (ZnPcs). Being known for their tendency towards molecular aggregation, ZnPcs lose some of their potential in photovoltaic devices. There are a few methods to reduce the aggregation. This work investigates two methods for aggregation reduction, and compares the effectiveness of these methods in enhancing the photoinduced electron transfer from the phthalocyanine into the semiconductor electrode. The thesis aims to answer the following questions:

- What kinds of photoinduced reactions occur in different organic–semiconductor systems? How do the reaction kinetics change in different semiconductor materials?
- How can the aggregation be reduced, and how do the electron transfer kinetics change in aggregated *vs.* non-aggregated ZnPc–semiconductor systems?
- How does adding a HTM effect on the ZnPc layer morphology, degree of aggregation, and the electron transfer kinetics?
- How do ZnPcs perform in solid-state dye-sensitized solar cells? Does the reduction in aggregation induce an increase in photocurrent generation?

Papers **I** and **II** study the photoinduced reactions in three different organic–semiconductor systems: quantum dot–fullerene hybrids, phthalocyanines on zinc oxide nanorods and phthalocyanines on titanium dioxide nanoparticles. The systems differ in composition, physical state as well as the direction of the electron transfer. The binding of the organic compound onto the semiconductor surface remains the same for all three systems: the organic molecules are bound to the semiconductor with carboxylic acids.

Papers **III** and **IV** investigate the phthalocyanine aggregation on zinc oxide and titanium dioxide surfaces. Two methods for aggregation reduction are studied: co-adsorbates and bulky substituents on the phthalocyanine core. At the spotlight in these publications was to find an explanation *why* the aggregation reduces the power conversion efficiencies in solar cell samples.

The addition of a HTM in the model samples was also studied in Papers **III** and **IV**. The HTM is a vital component in an actual solar cell, and therefore it is essential to know how it interacts with the dye-sensitized semiconductor layer.

Finally, full solid-state dye-sensitized solar cells were built in Paper **IV**. The solar cell performance was studied for a phthalocyanine derivative known for its aggregation tendency. Reduction of the aggregation was expected to have an effect on the solar cell performance of the sample: a less aggregated sample expectedly induces a larger photocurrent.

1.2 Outline

The core content of this thesis are ultrafast time-resolved absorption spectroscopy studies for different organic–semiconductor hybrids. Understanding the primary photoinduced reactions e.g. in a solar cell is crucial when designing new solar cell materials. Structurally, the thesis is divided in five chapters.

Chapter 1 provides the motivation for this work. The research questions that the thesis aims to answer are also formulated in this chapter.

Chapter 2 introduces the reader to the background behind this work: properties of the used photoactive materials (both organic and semiconductor materials), binding of organic compounds onto the semiconductor surface, the typical processes at an organic–semiconductor interface, and solar cell architectures.

Chapter 3 describes the experiments carried out for this thesis. The different thin film preparation methods used to fabricate the samples are depicted. Also the sample characterization methods are introduced, with main focus on the ultrafast transient absorption spectroscopy. Furthermore, the data fitting models used to analyze the time-resolved data are briefly described.

Chapter 4 summarizes the most important results that were published in Papers **I**–**IV**. The two aggregation-reducing mechanisms and their effect on the electron transfer kinetics are compared. The small energy distribution model that was used in publication **III** is used for all ZnPc samples to simplify the TA spectrum interpretation and to obtain more convergent results. Finally, performance of the ZnPcs in solid-state dye-sensitized solar cells was studied.

Chapter 5 finishes the thesis. The most important results are summarized in this chapter. To conclude the thesis, the future prospects of this research in the field of photovoltaics are discussed.

2 Background

2.1 Photoactive materials

2.1.1 Semiconductors

In regard to their electric conductivity, all materials can be divided in three categories: metals, semiconductors and insulators. What distinguishes these different groups from each other is the size of the band gap between the valence band (VB) and the conduction band (CB). In metals, the band gap is essentially nonexistent, whereas in semiconductors and insulators it is finite. What differentiates semiconductors from insulators is the size of the band gap: semiconductors can be thermally excited to have some electrons in the conduction bands, whereas insulators need an external energy source to be excited.

There are a few four-valent elements that are intrinsically semiconducting, such as silicon and germanium. The conductivity of these materials can be increased by *doping* the material, that is, adding five-valent or three-valent atoms into the crystal structure (*n*-type doping and *p*-type doping, respectively). Most semiconductors are, however, compounds. Common compound semiconductors include CdSe, GaAs, InAs, ZnS, as well as many metal oxides such as ZnO, TiO_2 and Cu_2O. Most compound semiconductors are either *p*- or *n*-type semiconductors in their pristine form, but they can also be doped to give the desired composition and electron or hole mobility.

Quantum dots

Quantum dots (QDs), or semiconductor nanoparticles (NPs), are a class of semiconductor materials with some very unique properties brought about by their small size.

Quantum dots can be produced from a variety of materials, including III-V and II-VI semiconductors (GaAs, InAs, InP, CdSe, CdS, CdTe, ZnS),[7–9] heavy-metal-free alloys (e.g. ClSeS and $CuInS_2$),[10,11] and perovskites.[12–14]

Typically, quantum dots are 2-10 nm in diameter. The small size gives rise to quantum confinement, leading to a larger band gap compared to bulk materials. QDs are often synthesized from materials with a rather small bulk band gap (< 1.7 eV), so that the quantum confinement renders the QD band gap in the visible wavelength range. The band gap, and therefore, the color of the quantum dots is directly tunable by varying the QD size. Figure 2.1 presents the absorption and emission spectra for a series of cadmium selenide QDs. The QD diameters range from ca. 3 to 5.5 nm.

Quantum dots can be synthesized with a few different methods: molecular beam epitaxy (MBE), plasma synthesis and colloidal synthesis. MBE produces single quantum dots on a solid semiconductor substrate. Epitaxial QDs can especially be used in optoelectronic

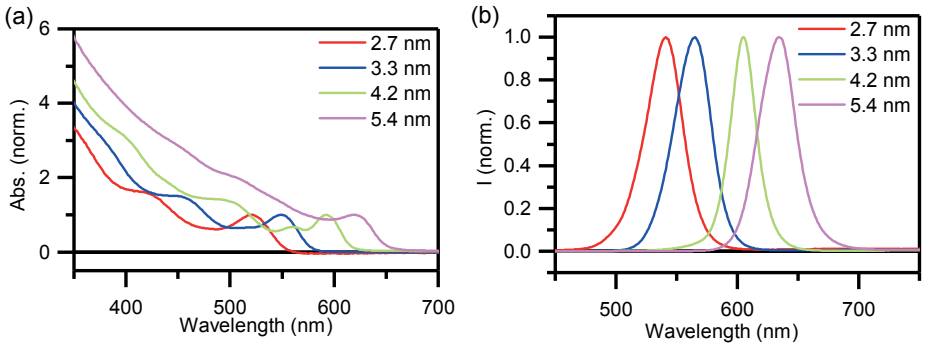

Figure 2.1: (a) Absorption and (b) emission spectra of a series of semiconductor quantum dots. The absorption and emission band positions shift to the red with the increasing quantum dot diameter.

and microwave applications, such as lasers and transistors.[15] Nonthermal plasmas can be used as a gas-phase QD fabrication method. Especially covalently bonded QDs (e.g. elemental QDs) are often fabricated with the plasma synthesis.[16,17] Liquid-phase, colloidal synthetic methods are probably the most common ways to manufacture QDs.[18–20] Colloidal synthesis resembles conventional chemical synthesis. The precursor materials are combined in an organic solution and heated, which arises a nucleation mechanism followed by nanocrystal growth. The chemical syntheses have been fine-tuned to produce highly monodisperse QD ensembles. The QDs used in this thesis were prepared with a chemical synthesis and stored as a powder for delivery and storage. For enhanced emission intensities, the QD surface can be covered with a larger band gap material. This inorganic shell passivates the surface defects in the QD, leading to a decreased number of electron traps in the QD surface and therefore increasing the fluorescence efficiency.

Intrinsically, semiconductor QDs are not soluble. They can, however, be modified to be soluble in either water or organic solvents by covering the surface with suitable organic molecules, capping agents. The capping should bear a suitable functional group for binding to the QD surface, e.g. thiol, carboxylic acid or phosphine oxide. The capping molecules coordinate onto the QD surface atoms, and the bond strength depends on the functional group. The functionality of the tail section of the capping molecule then determines the solubility of the capped QDs: carboxylic ends enable water-solubility, whereas long hydrocarbon tails make the QDs soluble in nonpolar organic solvents.

In this thesis, semiconductor core-shell QDs (CdSe/ZnS core/shell) were used. The role of the QDs is different from any other semiconductor material used in the thesis: in addition to serving as the semiconductor surface for binding organic molecules, the QDs themselves act as the photoactive material. The QDs are excited with visible light, giving rise to an electron transfer reaction from the QD into the organic electron acceptor.

2.1.2 Organic compounds

Fullerenes

Fullerenes are one of the several allotropic forms of carbon. The most commonly known allotropes, diamond, graphite, and graphene, consist of a continuous network of carbon

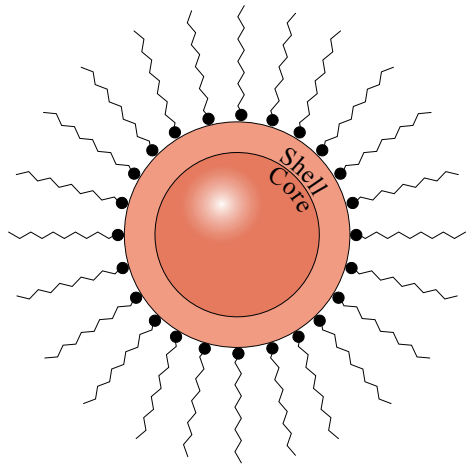

Figure 2.2: A schematic presentation of a core-shell quantum dot capped with a hydrophobic organic compound.

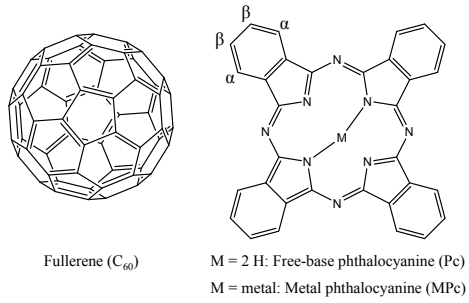

Figure 2.3: Structures of fullerene and phthtalocyanine.

atoms. On the contrary, fullerenes can be thought of individual molecules consisting merely of carbon atoms. Fullerenes can take various shapes from spherical and ellipsoidal structures to carbon nanotubes.[21] The most commonly known fullerene, buckminsterfullerene (C_{60}), consists of pentagonally and hexagonally ordered carbon atoms (Figure 2.3). The chemical and physical properties of C_{60} are quite unique. It has very high electron affinity (up to 6 electrons), and an exceptionally low reorganization energy in electron transfer reactions. Moreover, the fullerene anion C_{60}^{-} has a very distinct absorption band in the near-IR, making analysis of the electron transfer kinetics involving this species reliable and reproducible.[22,23] Fullerenes are insoluble in their pristine form, but they can be chemically modified to be soluble in suitable organic solvents. In this thesis, the only fullerene referred to is C_{60} and its derivatives.

Phthalocyanines

Phthalocyanines (Pcs) belong to the vast class of macrocyclic tetrapyrrole compounds. Unlike porphyrins and chlorophylls that are structurally very close to Pcs, phthalocyanines are not found in nature. Phthalocyanines were first discovered in the beginning of the 20^{th} century, and ever since their discovery, they have largely been used as industrial pigments.[24] Their high molar absorption coefficients, chemical modifiability, and superior

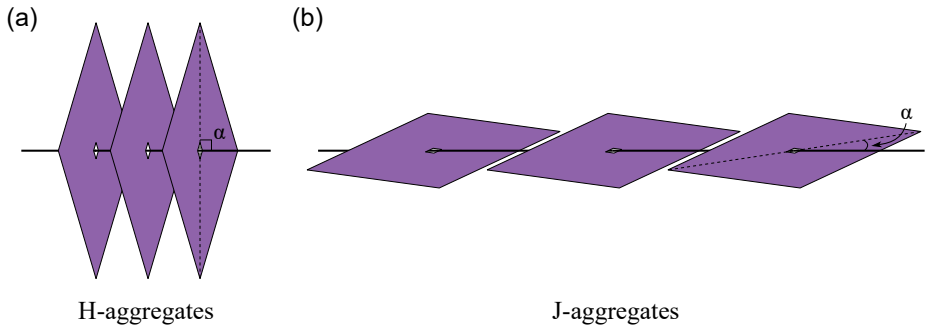

Figure 2.4: Schematic presentation of (a) H-type and (b) J-type aggregates. In H-aggregates, the phthalocyanine macrocycles are perpendicularly oriented towards the aggregate axis, whereas in J-aggregates the angle between the mean axis of the molecule and the axis of the aggregate approaches zero.

thermal and chemical stability make them likewise attractive for various applications such as catalysis, photodynamic therapy, optical filters, and photovoltaics.[25–27] Structure of the unsubstituted phthalocyanine is presented in Figure 2.3. The central cavity can coordinate a metal atom, yielding a metal phthalocyanine (MPc). Various metals have been used in different phthalocyanines, inducing changes in the chemical and optical properties in the compounds.

A major drawback for the use of phthalocyanines in e.g. photovoltaic applications is their tendency towards aggregation. The π-electron clouds of two adjacent phthalocyanine molecules tend to interact and the molecules agglomerate together. Hence, the aggregation is often described as $\pi - \pi$ stacking.

Aggregation in organic dyes can be divided in two categories: the H- and J-aggregates. The different aggregation stages can be clearly distinguished in the absorption spectra of the phthalocyanine. Compared to the spectrum of monomeric Pc, the aggregated spectrum shows a decrease in the absorption intensity as well as the growth of a new absorption band on the short-wavelength side of the monomer absorption. The blue-shifted band might even become the dominant feature in the spectrum. Historically, the H-aggregates were named after the blue-shift (the *hypsochromic* shift). For J-aggregates, however, a completely new, intense absorption feature emerges on the long-wavelength side of the monomeric absorption band. The red-shifted J-aggregates (J presumably for Jelley, who discovered the red-shifted aggregates) are much less common than H-aggregates.[25]

On a molecular level, the different aggregates are explained by different positioning of the individual molecules in the aggregates. For phthalocyanine aggregates, the Pc molecules are organized at a certain tilt angle (α) between the long axis of the molecule and the axis of the aggregate (Figure 2.4). In H-aggregates, the tilt angle is 90°(sandwich-type aggregates), whereas in J-aggregates, the tilt angle approaches zero (end-on aggregates).[25,28] The molecular orientations inside the aggregates are schematically presented in Figure 2.4.

As mentioned, aggregation changes the optical properties of the Pcs drastically. The close proximity of two or more adjacent Pc molecules also affects the performance of Pc-based photovoltaic devices. When an aggregated ensemble of Pcs is excited, the closely-packed molecules interact with each other, opening up relaxation channels that compete with the desired reactions (electron and/or energy transfer into an external acceptor). Therefore, it is crucial to avoid and reduce the aggregation as much as possible.

In solar cell applications, phthalocyanines are adsorbed onto a semiconductor surface, resulting in a solid thin film. In a system like this, there are two effective ways to reduce the aggregation: (i) "dilution" of the film by mixing the Pc with a suitable co-adsorbate, and (ii) substituting the phthalocyanine core with bulky substituents.

The use of molecular co-adsorbates has been a popular approach in aggregation-reduction. The aim is to incorporate other molecules with roughly the same size in the Pc matrix. With another molecule in the thin film, the Pc molecules stay further away from each other and therefore retain their monomeric form. The method is simple because no chemical modification of the phthalocyanine itself is needed. Chenodeoxycholic acid (CDCA) has received a lot of attention as a co-adsorbate in photovoltaic applications.[29–34]

Chemical modification of the phthalocyanine structure is a more delicate procedure towards reduced degree of aggregation. Bulky substituents especially in the β positions of the Pc core (Figure 2.3) comprise steric hindrance, and thus increase the distance between two adjacent Pc molecules in any environment (solution and thin films). In addition to aggregation-reduction, substitution of the Pc core may have a major effect on the optical properties of the compound, as well as its solubility in organic solvents. Therefore, careful planning and synthetic effort are needed for creating compounds with reduced aggregation together with other properties suitable for the desired application. It has been shown, however, that the substitution approach is more efficient in reducing the aggregation in photovoltaic devices through increased performance of the devices.[32,35–38]

In this thesis, both methods are tested and their effect on the kinetics of the photoinduced reactions is evaluated. Five different phthalocyanine derivatives with different substitution are used. The degree of aggregation is also excpected to be different in the differently substituted Pc derivatives. Two different co-adsorbates (CDCA and oleic acid, OA) and their effect on the aggregation is studied.

2.2 Organic–semiconductor interfaces

2.2.1 Semiconductor surfaces

Transparent conductive oxides (TCOs) are often used as electrodes in dye-sensitized photovoltaic devices. For optimal performance of the devices, a high photocurrent is needed. The current results from photoinduced charge separation reactions at the organic–semiconductor interface. In other words, the more efficient the interaction between the organic dye and the semiconductor, the higher the efficiency of the solar cell. The most effective interaction between the two moieties is achieved with a dense monolayer of the organic sensitizer on the semiconductor surface. A flat monolayer, however, cannot absorb enough light for the photocurrent generation to be very efficient. The solution is to increase the specific surface area of the semiconductor substrate by "folding" or wrapping the surface. When the folding is done in a very minuscule size domain, one can talk about nanostructured semiconductor electrodes. For nanostructured materials, the specific surface area can be hundreds of times larger than the apparent (macroscale) area of the electrode.

Nanostructured semiconductors come in various shapes and morphologies. Spherical nanoparticles are perhaps the most common, and the TiO_2 nanoparticles and quantum dots used in this thesis are essentially nanospheres with different sizes.[4,39] The third material used in this thesis, zinc oxide, is well-known for its substantial selection of

available nanomorphologies. ZnO can be produced in cylindrical assays (rods, wires and tubes), tetrapods, spheres and shells, helices as well as propeller-like structures.[40–43]

The QDs used in this thesis are used in their colloidal form and no apparent area is to be defined, but TiO_2 is used as an mesoporous network of interconnected nanoparticles, and ZnO as pillar-like nanorods (ZnOr). TiO_2 NP films are known to have a specific surface area of 100 – 200 times the apparent area, whereas ZnO nanorods increase the apparent area by 30 – 50 times. TiO_2 nanoparticle films are commonly used in DSSC applications. The electron mobility in ZnO is, however, at least an order of magnitude greater than in TiO_2.[44] ZnO is also a safe, naturally abundant and cost-efficient material. Therefore, there has been a growing interest in replacing TiO_2 in solar cells with ZnO-based structures.

2.2.2 Self-assembled monolayers

The history of self-assembled monolayer (SAMs) is often thought to have begun in the 1980s, when Nuzzo and Allara reported the adsorption of dense alkanethiolate monolayers on gold surfaces.[45,46] Research on the topic, however, dates back all the way to the 1940s, when Zisman *et al.* reported on dense monolayers of several different organic compounds on clean metal surfaces.[47] The early experiments did not reach large interest, because the potential of this simple method was not yet recognized. Nowadays, self-assembly is a widely used method covering a broad range of substrates, compounds as well as binding groups.

Ulman[46] defines SAMs as "ordered molecular assemblies formed by the adsorption of an active surfactant on a solid surface". In other words, organic compounds with suitable functional groups spontaneously form dense monolayers on a solid surface upon immersing a solid substrate into a solution containing the compound in a low to moderate concentration. The variety of available substrate materials is broad: metals, other elements (such as silicon), oxides, and other covalently bound compounds are the most commonly used.[46,48–53]

Both the substrate and the binding anchor are chosen according to the desired application. Thiols and thiolates are often used on metal surfaces, phosphonic acid and carboxylic acid on metal oxides, and siloxanes on silicon oxide (glass and quartz). The binding strength varies from the near-covalent bonds in thiols on Au surfaces to electrostatic interactions in acid – metal oxide systems. Figure 2.5 presents possible different binding modes for a carboxylic acid anchoring group on a metal oxide surface. The two-dentate binding modes result in stronger binding than the unidentate modes, chelating and bridging modes being the most stable and thus the most common binding modes for carboxylic acids on ZnO and TiO_2 surfaces.

The advantage of the SAM method over several other thin film preparation methods lies in the simplicity of the deposition. No harsh conditions (e.g. vacuum) are needed, nor is specialized equipment. SAMs can be produced on both planar and curved surfaces, and even on porous surfaces (taken that the pore size in the substrate structure is considerably larger than the size of the adsorbate). Reaction conditions (solvent, concentration, temperature, immersion time, etc.) for SAM deposition depend largely on the substrate – adsorbate system. As an example, dye monolayers for dye-sensitized solar cells are typically prepared from a millimolar solution, at room temperature, and with 20 – 24 h immersion time. Optical absorbance of SAM layers is expected to be proportional to the surface area (taken that the monolayer formation is complete). Therefore, SAM

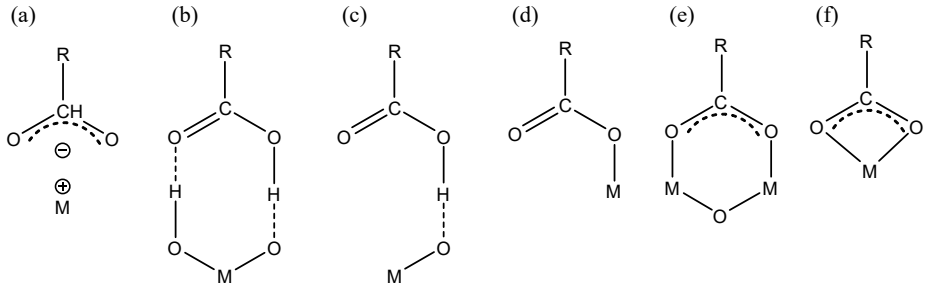

Figure 2.5: Possible binding modes for a carboxylic group on a metal oxide surface: (a) electrostatic interaction, (b) double-handed hydrogen bonding, (c) single-handed hydrogen bonding, (d) ester-like bonding, (e) bridging, and (f) chelating.[54]

absorption can be used as an estimate of the specific surface area compared to a flat surface.[55]

In this work, carboxylic acid is used as the SAM anchoring group. It is known to form good-quality monolayers on metal oxides, and given that the electronic structure of the used QD material (ZnS in the QD shell) is similar to ZnO, COOH group is expected to produce a rather stable bond on the QD surface as well.

2.3 Photoinduced processes at organic–semiconductor interfaces

When an organic molecule is attached onto a semiconductor surface, it is doomed to interact with the semiconductor. There are two possibilities for the processes following photonic excitation: energy transfer (EnT) and charge transfer (CT). An energy transfer process would end up in the energy acceptor in the excited state and the energy donor back in the ground state (eq. 2.1):

$$\mathrm{D}^* + \mathrm{A} \rightarrow \mathrm{D} + \mathrm{A}^*. \tag{2.1}$$

In a photovoltaic device, however, it is crucial to get electrons to flow into an external circuit, and therefore energy transfer reactions are not desired in such applications.

Different photoinduced processes at an organic–semiconductor interface are illustrated in Figure 2.6. Positions of the energy levels of the organic compound with respect to the conduction and valence bands of the semiconductor play a key role in determining the direction of the electron transfer.

In Figure 2.6(a) and 2.6(b), the semiconductor acts as the photoactive moiety. If the CB edge of the semiconductor is located higher in energy than the lowest unoccupied molecular orbital (LUMO) of the organic compound, electron transfer from the semiconductor to the organic compound can occur (Figure 2.6(a)). Respectively, if the highest occupied molecular orbital (HOMO) of the organic compound lies higher in energy than the semiconductor VB edge, an electron may transfer from the organic HOMO to the semiconductor VB, leaving an electron vacancy in the organic HOMO. This process is also termed a photoinduced hole transfer (Figure 2.6(b)).

The situation is opposite in Figure 2.6(c) and 2.6(d): The organic moiety is excited, and depending on the mutual orientation of the energy levels, either photoinduced electron

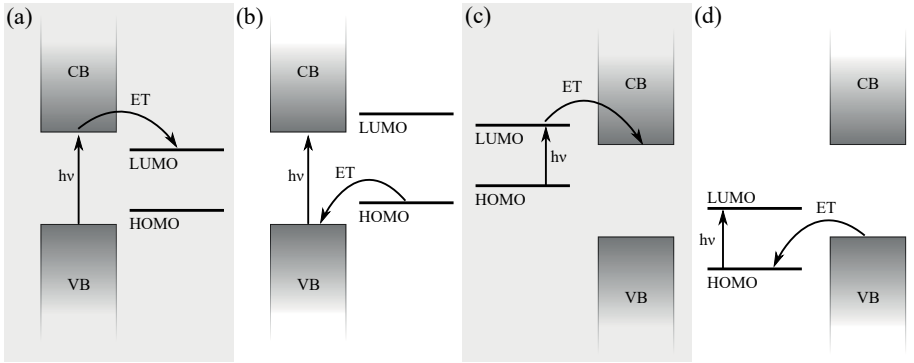

Figure 2.6: Schematic presentation of possible electron transfer reactions at an organic–semiconductor interface: (a) Photoinduced ET from the semiconductor CB to organic LUMO; (b) Photoexcitation followed by ET from organic HOMO to semiconductor VB; (c) Photoinduced ET from organic LUMO to semiconductor CB; (d) Photoexcitation followed by ET from semiconductor VB to organic HOMO.

transfer from the organic LUMO to the semiconductor CB (Figure 2.6(c)) or photoinduced hole transfer from the organic HOMO to the semiconductor VB (Figure 2.6(d)) may take place. For example in dye-sensitized solar cells, the process depicted in Figure 2.6(c) is the primary photoinduced process.

Kinetics of these ET processes are affected by various factors, such as the binding strength of the organic compound, the energy level positions, and the density of states in the semiconductor. Separation of all the different factors is rather difficult, but for an ET process to be as effective as possible, at least the following properties should be optimized:

Energy levels. As visualized in Figure 2.6, positioning of the semiconductor CB edge and organic LUMO level determine whether an electron transfer reaction is thermodynamically possible.

Density of states (DOS). The energy levels are continuously spread in the semiconductor conduction band. The distribution of the energy levels can be expressed with a density function, and the higher the density, the more states there are ready to accept an electron. Therefore, a high DOS at the conduction band renders a fast electron transfer process in an organic-to-SC electron transfer. In SC-to-organic transitions, the density of states does not play such a remarkable role, because the excited electron quickly relaxes to the conduction band edge and is then transferred into a single molecular orbital.

Orientation of the organic molecules. Organic chromophores always have a certain degree of freedom in a SAM. Thus, they can take different conformations on the semiconductor surface. The tilt angle of the molecules may vary, and thus the distance of the photoactive moiety and the semiconductor varies as well. Because the electron transfer reaction in these organic–semiconducor systems occurs in the through-space regime, the distance has a direct impact on the ET rate. The closer the chromophore is to the semiconductor surface, the faster the electron transfer.

Molecular aggregation. For an efficient solar cell, it is convenient to load as much of the photosensitizer in the cell as possible. In very dense monolayers, however, the

organic molecules might interact with each other, opening competitive relaxation channels for the excited state, as already discussed in more detail in Section 2.1.2. In solar cell applications, two aggregation-reducing mechanisms are predominant: bulky substitution of the dye as well as the use of co-adsorbates. For a SC-to-organic electron transfer, the aggregation does not have such a remarkable effect on the ET rate: the organic compound remains in the ground state as long as it receives the electron and anionizes.

Electronic coupling. The ET rate between a donor and an acceptor moiety strongly depends on the electronic coupling between the two moieties. The electronic coupling is in turn proportional to the overlap of the organic molecular orbitals and the semiconductor energy bands, and is therefore also dependent on the dye–semiconductor distance. In the high coupling regime, the ET is adiabatic and believed to occur *via* a concerted motion of nuclei, through a transition state. In the low coupling (or non-adiabatic) regime, on the other hand, the ET reaction mechanism is a quantum-mechanical transition from the donor to the acceptor. A non-adiabatic ET reaction may be as fast as an adiabatic ET, if the DOS of the acceptor is high enough, i.e. for an organic-semiconductor system with the LUMO of the organic dye inside the semiconductor CB.

2.4 Solar cells

Grätzel and O'Regan[4] opened a new era in solar cell research by publising a new type of solar cells in the early 1990s, the dye-sensitized solar cell (DSSC). Compared to the conventional Si solar cells, dye-sensitized cells are a low-cost and environmentally sustainable choice. They are based on a TiO_2 nanoparticle film sensitized with an organic dye. The cells are completed with an electrolyte solution and a counter electrode. The highest efficiencies for DSSCs range to more than 14%.[6] For the family of dyes chosen for this thesis, phthalocyanines, the highest power conversion efficiencies obtained are close to 7%.[56,57]

There are, however, some obstacles to overcome before DSSCs may become a mainstream solution for solar energy harvesting. Especially the liquid electrolyte poses corrosion and leakage problems in long-term use. During the recent years, there has been a growing interest in replacing the liquid electrolyte by a solid hole-transporting material (HTM). These kind of DSSCs are called solid-state DSSCs (ssDSSCs). Several solid HTMs have been investigated, including both polymers (e.g. poly(3-hexylthiophene, P3HT) and small molecules (e.g. 2,2',7,7'-tetrakis(*N*,*N*-di-*p*-methoxyphenylamino)-9,9'-spirobifluorene, spiro-MeOTAD).[58,59]

Figure 2.7 presents the basic structure of a solid-state DSSC. The photogenerated electrons move from the sensitizer dye into the TiO_2 NPs and further towards the bottom electrode (FTO). The dye cations are regenerated by hole transfer into the HTM and the top electrode (Ag).

Performance of a solar cell is measured using a solar simulator. The solar spectrum is mimicked with a standardized (AM1.5) light source, and electric current through the cell is measured over a certain voltage range, yielding a current–voltage curve (IV-curve). A typical IV-curve is presented in Figure 2.8. Current flowing in the solar cell is plotted in Figure 2.8 with red. Some of the quantities characterizing the cell are indicated in the plot: short-circuit current (J_{sc}) is the current at zero bias voltage, and open-circuit voltage (V_{oc}) is the voltage at open circuit conditions (current = 0).

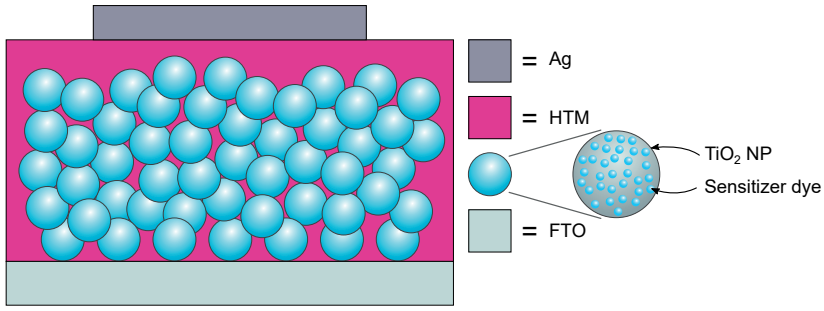

Figure 2.7: Schematic structure of a solid-state dye-sensitized solar cell.

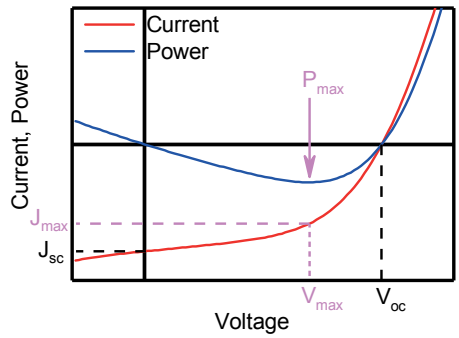

Figure 2.8: Example of an IV curve (red) and the calculated power generated by the solar cell (blue). The short-circuit current (J_{sc}) and open-circuit voltage (V_{oc}) are indicated in the plot. The negative power and current values indicate work generated by the device. Maximum power point (P_{max}) shown in magenta, together with the corresponding current and voltage values.

The blue plot indicates the power generated or consumed by the cell; the negative values indicate net power generated by the cell. The point where the generated power is maximized is indicated in the plot with magenta (P_{max}). The corresponding current and voltage values (J_{max} and V_{max}, respectively) are likewise indicated.

Efficiency of the cell is described with a few different characteristic numbers. The overall efficiency is best described with the power conversion efficiency, η (eq. 2.3). Goodness of the sample in regard to the shape of the IV-curve is portrayed by the fill factor, FF (eq. 2.2). The number of photons converted into electrons in the cell are described by two quantities, the incident photon-to-current efficiency, $IPCE$ (or the external quantum yield, eq. 2.4), and the absorbed photon-to-current efficiency, $APCE$ (internal quantum yield, eq. 2.5).

$$FF = \frac{(JV)_{max}}{J_{sc}V_{oc}} = \frac{P_{max}}{J_{sc}V_{oc}} \tag{2.2}$$

$$\eta = \frac{P_{max}}{P_{in}} \tag{2.3}$$

$$IPCE(\lambda) = \frac{N_{e^-}}{N_{phot}} = \frac{q\lambda J_{sc}(\lambda)}{hcP_{in}(\lambda)} \tag{2.4}$$

$$APCE(\lambda) = \frac{N_{e^-}}{N_{abs.}} = \frac{IPCE(\lambda)}{1 - 10^{-A(\lambda)}} \tag{2.5}$$

The photon-to-current efficiencies here are wavelength-dependent quantities. They are calculated from a so-called photocurrent action spectrum (PCAS). The short-circuit current of the cell is measured as a function of excitation wavelength (monochromatic illumination). By comparing the generated J_{sc} to the input power (P_{in}) at a certain wavelength, the number of electrons generated per each photon arriving at the device can be calculated. The resulting IPCE spectrum should follow the shape of the absorption spectrum of the sample. APCE takes into account the number of absorbed photons in the sample, better describing the ability of the device to convert photons into electrons if the absorbance is low.

3 Materials and Methods

This chapter presents the experimental methods that were used in the thesis. Section 3.1 introduces the photoactive compounds. The thin film preparation methods used to build the solid samples are described in Section 3.2, and the methods used to characterize the samples are briefly discussed in Section 3.3. Because the ultrafast spectroscopy instruments require the most handwork, they are described in deeper detail than the routinely used absorption and emission spectrometers as well as the scanning electron microscope. The data fitting models used to analyze the time-resolved data are also described. More details on the experimental methods can be found in publications **I**–**IV** and the references therein.

3.1 Compounds

3.1.1 CdSe/ZnS quantum dots

The CdSe/ZnS quantum dots used in the thesis (Paper **I**) were purchased from PlasmaChem GmbH. The QDs consist of a spherical cadmium selenide (CdSe) core and an epitaxial zinc sulfide (ZnS) shell of approx. 0.6 nm thickness.[60] The shell passivates the QD surface, giving rise to the high fluorescence quantum yields. Furthermore, the QDs are covered by an organic capping agent (trioctylphosphine oxide, TOPO) to make the QDs readily soluble in hydrophobic organic solvents.

3.1.2 Organic photoactive compounds

Structures of the organic photoactive compounds used in the thesis are presented in Figure 3.1. The fullerene derivative C_{60} was synthesized at the Laboratory of Chemistry and Bioengineering at Tampere University of Technology.[61,62] The zinc phthalocyanines (ZnPc **1**–ZnPc **5**) were synthesized at Universidad Autónoma de Madrid.[29,32,37,63] All of the compounds studied here bear a carboxylic group that serves as the anchor when assembling onto semiconductor surfaces (QDs, TiO_2 NPs, and ZnO nanorods).

Fullerene derivatives are known for their electron-accepting properties.[22,64,65] For the QD–C_{60} hybrids, a fullerene derivative with moderate solubility in organic solvents was chosen. Moreover, the carboxylic anchor group has a higher binding constant on QD surfaces than the original QD capping agent (TOPO), enabling the C_{60} to replace some of the native capping molecules and bind to the QD surface.

The phthalocyanines ZnPc **1** and ZnPc **2** are structurally very alike, the only difference being the length of the spacer between the carboxylic anchor and the phthalocyanine core. They have bulky substituents in the phtalocyanine peripheral area, making them less prone to aggregation than the less substituted ZnPc **3** and ZnPc **4**. The least substituted ZnPc,

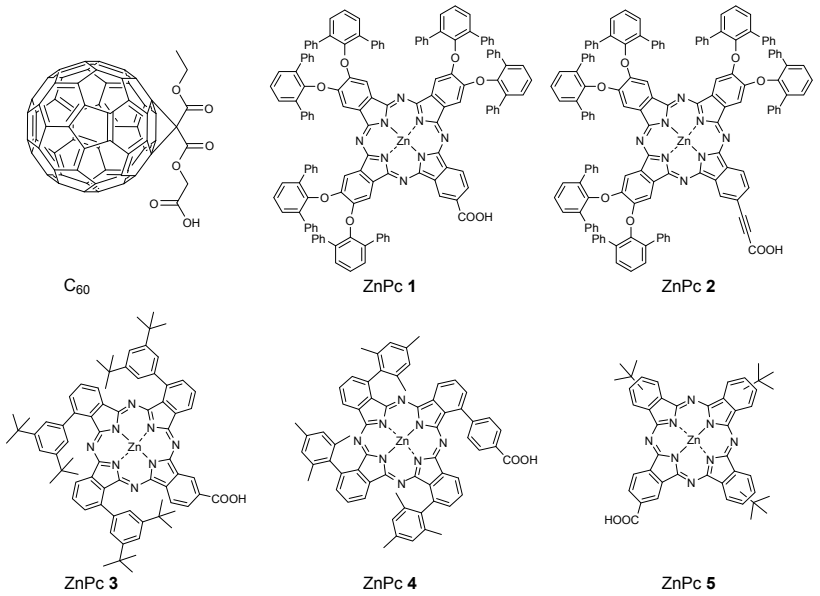

Figure 3.1: Structures of the organic compounds.

ZnPc **5**, is known to aggregate in organic solvents and in solid films.[29,32,37] Therefore, ZnPcs **1**–**4** were selected for studying the effect of substitution on the phthalocyanine aggregation on semiconductor surfaces, whereas ZnPc **5** is a good candidate for the co-adsorbate studies.

3.2 Sample preparation methods

3.2.1 QD–C_{60} hybrids

QD–fullerene hybrids are QDs where the fullerene derivative has replaced some of the capping agent molecules on the QD surface, and is either chemically or electrostatically bound to the semiconductor surface. The binding mechanism is essentially a SAM on a semiconductor substrate (Section 2.2), but only a few organic molecules being linked to each individual QD.

Preparation of the QD–fullerene hybrids was described in Paper **I**. Briefly, the QDs were dispersed in hexane and mixed with C_{60} in increasing concentrations. Absorption and emission spectra as well as the fluorescence lifetimes were recorded before the C_{60} addition and after each addition. For the transient absorption measurements, the QD-to-C_{60} ratio was chosen based on the titration experiments. In the TA samples, the QD emission was quenched by more than 90%, leading to the assumption that most of the QDs in the solution were hybridized with at least one fullerene molecule.

3.2.2 ZnO nanorod growth

ZnO is known for its ability to form nanostructured single-crystalline ensembles in various shapes. In this thesis, ZnO was used thanks to its good electron transport properties

(electron mobility in single-crystalline ZnO should be at least an order of magnitude greater than in TiO_2 NP films).[66,67] ZnO nanorods offer a well-structured nanoscale substrate with an increase in the specific surface area of ca. 10 – 20 times compared to a flat layer. Growth of the ZnO nanorods is relatively easy to control using a hydrothermal method.[68] The method consists of two steps: first, a thin ZnO seed layer is prepared. Then, the single crystal nanorods are grown on top of the seed layer.

The ZnO seed layers were prepared by spin-coating a zinc acetate (ZnAc) precursor solution (ZnAc in 2-methoxyethanol:ethanolamine 96:4 by volume) onto UV-ozone treated ITO substrates. For all spin-coated layers in this thesis, a Laurell WS-400B-6NPP/LITE spin-coater was used. To convert the ZnAc to ZnO, the substrates were annealed in air at 380 °C for 20 min. The resulting seed layer is thin (ca. 25 nm) and porous.[68]

The actual nanorod growth was carried out at 85 °C. The ZnO seed layer substrates were placed upside down in a container filled with the ZnO nanorod precursor solution, zinc nitrate and hexamethylene tetramine (HMTA) in H_2O. The container was then placed in a water bath and the nanorods were grown for 6 h (1 h warming up the precursor solution, 5 h actual nanorod growth). After the reaction, the ZnO nanorod substrates were rinsed with milli-Q H_2O and dried in air. The nanorods were approx. 790 ±25 nm in length and 38 ±1 nm nm in diameter (Paper **III**).

3.2.3 TiO_2 layers

TiO_2 NP layers were used for transient absorption measurements as well as for ssDSSCs. Since many samples were directly used for both purposes, the sample preparation is described for the photovoltaic device fabrication. Some of the samples were used only for TA measurements. Those samples were prepared without layers such as the top electrode; crucial for the solar cell function but not directly involved in the primary photoinduced reactions.

FTO pre-cleaning and patterning

The TiO_2 layers were prepared on fluorine-doped tin oxide (FTO, surface resistivity 7 Ω/□) coated glass substrates. The substrates were purchased as 30×30 cm sheets. The large sheets were cut to approx. 2×2 cm substrates with a glass cutter.

The substrates were patterned with a grinding tool (Dremel) using a grinding stone. Figure 3.2a depicts the pattern that was ground on the substrates, serving 4 parallel solar cell samples on each individual substrate. After the patterning, the substrates were cleaned in an ultrasonic bath in Hellmanex® III washing agent and 2-propanol.

TiO_2 compact layer

A typical hole-blocking layer in TiO_2-containing solar cells is a thin, continuous layer of TiO_2. This blocking layer, or compact layer, can be produced *via* a variety of methods: spray pyrolysis[69–71], sputtering[72,73], sol-gel method[74], cathodic arc plasma[75], liquid-phase deposition[76] and spin-coating.[77] In this thesis, spin-coating was chosen since the process is simple and easy to modify.

The TiO_2 compact layers (CL) were prepared by spin-coating an acidic solution of titanium isopropoxide onto the pre-cleaned FTO substrates. The spin-coating solution was prepared by first mixing 1.5 ml of ethanol with 21 μl of HCl (2 M aq.), and then dissolving 210 μl of titanium isopropoxide in 1.5 ml EtOH. These two solutions were mixed

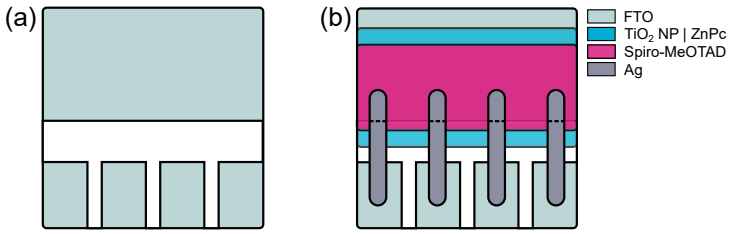

Figure 3.2: (a) FTO patterning, and (b) schematic structure of the ssDSSC samples.The active area is the intersection of the Ag top electrode and the TiO_2 NP | ZnPc, depicted by the dashed lines.

dropwise with vigorous stirring. The resulting Ti isopropoxide solution was spin-coated on top of the FTO substrates, followed by annealing in air at 120 °C for ca. 10 min.

TiO_2 NP mesoporous layers

The TiO_2 NP layers serve as a mesoporous substrate for the organic sensitizing dyes, as well as an electrode in the ssDSSCs. The layers were prepared by either screen-printing or spin-coating. Screen-printing is a very feasible technique when it comes to producing several samples at a time with high reproducibility in thickness. The downside, however, is that whenever the desired film thickness changes, a new printing screen with different mesh properties is needed. With the spin-coating technique it is easier to produce different film thicknesses for testing purposes for small sample batches.

A printing screen with 77–55 mesh (mesh thickness 87 μm) was used to produce 2 μm thick TiO_2 NP electrodes. Solaronix Ti-Nanoxide T/SP nanoparticle paste was screen-printed on top of the FTO | TiO_2 CL substrates. The resulting TiO_2 NP films were dried for ca. 15 min in air to let the solvent evaporate. For thinner TiO_2 NP samples, Dyesol 18 NR-T TiO_2 paste, diluted at a 2:5 weight ratio in EtOH, was spin-coated on top of the FTO | TiO_2 CL substrates, followed by annealing in air at 120 °C for ca. 10 min to evaporate the solvent residues.

$TiCl_4$ treatment

The surface roughness of TiO_2 NP layers can be increased by treating the layers with titanium tetrachloride ($TiCl_4$), leading to higher dye loading in a DSSC and therefore higher efficiencies.[78,79] First, an aqueous stock solution of $TiCl_4$ was prepared: 1.56 ml of H_2O was frozen in a small vial together with a stirring bar. Once frozen, the vial was placed in an ice bath and 440 μl of $TiCl_4$ was added dropwise. The solution was stirred for 10 min, and the resulting 2 M solution was stored in the freezer. Strictly speaking, the result is not an aqueous solution of $TiCl_4$; $TiCl_4$ reacts with the H_2O to form several different titanium oxides and oxychlorides.[80] The details of these reactions are beyond the scope of this work, and this procedure is simply referred to as $TiCl_4$ treatment.

For the $TiCl_4$ treatment, the stock solution was diluted to 0.02 M, and the TiO_2 NP substrates were immersed into the solution at 70 °C for 30 min, and thoroughly washed with milli-Q H_2O.

Sintering

All of the aforementioned TiO_2 layers were sintered in a furnace to burn the solvents and binding agents and to form solid nanoparticle layers. The samples were placed into the furnace at room temperature, and the temperature was increased at a rate of 20 °C/min up to 475 °C. This temperature was maintained for 45 min, followed by slow cooling to avoid cracking of the substrates.

3.2.4 SAMs

The ZnPcs used in this thesis were deposited onto the ZnO nanorods and TiO_2 NP surfaces *via* the self-assembly method. The details for the monolayer formation (choice of solvent, concentration, reaction time) vary according to the compound and the substrate. For the ZnO nanorods, 30 min reaction time was sufficient, whereas with the thicker TiO_2 NP layers, 20-24 h reaction times were used.

The choice of solvent for the ZnPc SAMs on ZnO nanorods is explained in Paper **III**. Briefly, toluene was the first solvent tested. Unfortunately, absorbances for the ZnOr | ZnPc **1** SAMs were consistently lower than for ZnOr | ZnPc **2**. Therefore, two-component solvent mixtures were tested. Toluene:EtOH mixtures did not produce good-quality SAMs, but *t*-BuOH:MeCN 1:1 (vol:vol) seemed to produce good-quality ZnOr | ZnPc SAMs with absorbances close to 0.2 at the maximum. Concentrations of the studied SAM solutions varied from 0.03 to 0.1 mM, 0.03 mM being concentration used for the *t*-BuOH:MeCN solutions.

Based on the experiences with ZnOr SAMs, the SAMs on TiO_2 NPs were consistently prepared from *t*-BuOH:MeCN. However, due to the higher specific surface area of the TiO_2 NPs, higher solution concentrations were needed. The dye concentration in these solutions was typically 0.1 mM. When studying the effect of co-adsorbates (Paper **IV**), the co-adsorbates were added directly to the SAM solutions in molar proportions 1:1 ... 1:100. This means that the co-arsorbate concentrations in the solutions ranged from 0.1 to 10 mM.

The samples were immersed into the SAM solutions in ambient conditions. After the reaction, the unbound ZnPc molecules were removed by immersing the samples for 5 min into the same solvent that was used for the monolayer formation. Absorption spectra for the samples were measured before and after each reaction, with care taken that the samples were positioned in the absorption spectrometer sample compartment similarly in both cases. Therefore, the absorption spectra should be comparable and the substrate spectra could be subtracted from the sample spectra, giving the absorbance of the dye layers only.

3.2.5 Hole-transporting layer: Spiro-MeOTAD

The hole-transporting layer, spiro-MeOTAD, was deposited on top of the ZnPc SAMs on ZnO nanorods and TiO_2 NPs by spin-coating. The purpose of the hole-transporting layer is to transfer the photogenerated holes into the solar cell cathode as well as to serve as an electron reservoir for dye regeneration.

For the ZnO nanorod samples, spiro-MeOTAD was dissolved in anhydrous chlorobenzene. For the TiO_2 NP samples for ssDSSCs, small amounts of LiTFSI and *t*-BP were added for enhanced hole-transporting capability. Also, the spiro-MeOTAD concentration was

higher for the TiO_2 NP samples because of the thicker film and larger specific surface area of the TiO_2 NP films compared to ZnOr.

3.2.6 Solar cell samples

For ssDSSC samples, Ag top electrodes were prepared. The TiO_2 | ZnPc | spiro-MeOTAD samples were masked with a shadow mask to obtain four parallel solar cell samples on each substrate. The resulting active electrode areas were ca. 2 mm^2. The ssDSSC samples are illustrated in Figure 3.2b.

The Ag top electrodes were prepared using an Edwards Auto 306 vacuum evaporator under a high vacuum (ca. 5×10^{-6} mbar). The silver is placed as a granule onto a molybdenum boat, that is then resistively heated. Given the reduced pressure, the silver melts and evaporates at lower temperatures than at atmospheric pressure. Once evaporated from the granule, the gaseous Ag atoms travel through the sample chamber and immobilize on the substrate surface. The electrode thickness was ca. 75 nm, giving a reasonable conductivity for the top electrode without penetrating the silver too much into the spiro-MeOTAD layer.

3.3 Sample characterization

3.3.1 Scanning electron microscopy

Scanning electron microscopy was used to investigate the morphology of TiO_2 NP and ZnO nanorod surfaces (Papers **II**–**IV**). A FE-SEM instrument (Carl Zeiss Ultra 55) was used for the imaging. Two types of images were taken: top images to show the quality of the topmost layer of the substrate, and cross-section images to examine the sample thickness, layer quality as well as spiro-MeOTAD infiltration. Typically, the images were taken with a 30 μm aperture and 0.75 – 1.5 kV acceleration voltage. Low acceleration voltages were used especially for the spiro-MeOTAD-containing samples to avoid the electron beam passing through the organic material.

3.3.2 Steady-state spectroscopy

Steady-state absorption and emission spectra were used for routine analysis of the samples and to plan the time-resolved measurements. Absorption spectra of the samples were measured using Shimadzu UV-1800 and UV-3600 UV-Vis-NIR spectrophotometers, typically in the wavelength range 300 – 850 nm. Emission spectra were recorded using a ISA – Jobin Yvon – SPEX – Horiba Fluorolog-3-111 fluorometer, typically with excitation at 440 nm and monitoring in 480 – 850 nm range. The raw signals were corrected using a correction function supplied by the manufacturer.

3.3.3 Time-resolved spectroscopy

Emission decay kinetics were studied for the QD – C_{60} hybrids (Paper **I**) using the time-correlated single photon counting (TCSPC) method (PicoQuant GmbH.). The samples were excited at 483 nm by a pulsed laser diode. The excitation wavelength was chosen to be as close to the local minimum of C_{60} absorption as possible to excite mainly the QDs. Fluorescence decays of the samples were recorded using a photomultiplier tube in 0 – 200 ns range. The QD emission maxima for each QD sample were used as the monitoring wavelengths.

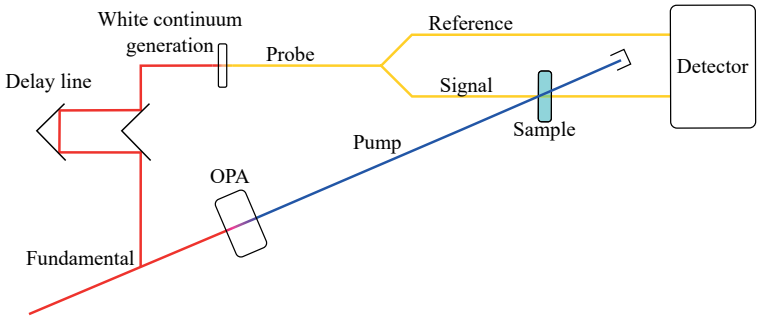

Figure 3.3: Simplified scheme of the pump-probe instrument.

Ultrafast transient absorption spectroscopy was used to investigate the kinetics of the photoinduced processes both in solutions (QD-C_{60} hybrids, Paper **I**) and in solid samples (TiO_2 NPs and ZnO nanorods, Papers **II**–**IV**). Conceptually, all transient absorption measurements consist of collecting time profiles of the sample absorption after a photonic excitation. This can be done at one wavelength or multiple wavelengths at a time, the latter resulting in a transient absorption spectrum. Since most compounds have different absorption spectra in the ground, excited, and ionic states, the time evolution of the absorption at different wavelengths reveals which intermediate states are present in the samples at different times.

The time-resolved transient absorption spectra were measured in the picosecond time scale using the so-called pump-probe method. The heart of a pump-probe system are two ultrashort light pulses, the excitation (pump) pulse and the monitoring (probe) pulse. Both pulses are generated from the same fundamental pulse using e.g. an optical parametric amplifier (OPA) or a white-continuum generator (WCG). One of the pulses is passed through a delay line, providing a tunable time gap between the pump and probe arrival at the sample. Absorption spectra of the sample are measured at different time delays after the excitation, providing the transient absorption data. Figure 3.3 depicts a simplified scheme of the pump-probe instrument.

In the system used in this thesis, the fundamental pulses at 800 nm are generated using a Libra F laser system (Coherent Inc.) at a pulse repetition rate 1 kHz. The fundamental pulse duration is approx. 100 fs, and the pulse energy 1 mJ. The fundamental pulse is then split in two: the majority (ca. 90%) is guided into the OPA (Topas C, Light Conversion Ltd.) to produce an excitation pulse at the desired wavelength (483 nm for the QD–C_{60} hybrids and 695 nm for the ZnPcs on semiconducting supports), and then directed into the sample compartment. The rest (10%) of the fundamental pulse is used for the monitoring. The beam is directed into a white continuum generator (sapphire crystal), split into reference and signal beams and then guided into the sample. Before the white continuum generator, the probe pulse is passed through a delay line to provide a tunable time gap between the pump and probe arrival at the sample. The signals were measured using an ExciPro TA spectrometer (CDP Inc.) with a CCD array for the visible wavelengths or an InGa array for the NIR wavelength range.

The measurements were carried out either in cuvettes made of special optical glass with 2 mm optical path length, or by directly guiding the beam at the solid samples. Typically, the spectra were measured by averaging over 5 s. To avoid photodegradation, the solution

samples were stirred during the measurements to obtain a fresh specimen for each arriving pump pulse. For the solid samples, moving the sample during the measurement was not a feasible option (overlap of the pump and probe beams might be lost), so the degradation was monitored by checking the signal intensity again after the measurements. If a similar signal intensity was obtained again after the measurement, the sample was considered not degraded. Moreover, the ZnO nanorod samples (Papers **II** and **III**) were measured in N_2 atmosphere to avoid degradation.

3.3.4 Fitting of the time-resolved data

A home-made program was used for data analysis. The aquired signals were first fitted globally using a multiexponential global fitting model:

$$\Delta A(\lambda, t) = A_0(\lambda) + \sum A_i(\lambda) e^{-\frac{t}{\tau_i}}, \tag{3.1}$$

where $A_i(\lambda)$ are the pre-exponential factors and τ_i are the time constants for each decay component. The multiexponential fitting model was used for time-resolved emission and absorption data alike. For the QD emission time profiles, weighted averages of the lifetimes (τ_{avg}) were calculated in order to be able to compare the different samples in a quantitative manner:

$$\tau_{avg} = \frac{\sum \tau_i A_i}{\sum A_i}. \tag{3.2}$$

Due to the heterogeneity of the samples, the multiexponential fitting model did not yield adequate fitting quality. For the QD samples, decay models were developed for both the emission decays and the TA data that take into account the distribution in the lifetimes due to the statistical nature of the hybrid formation (Paper **I**).

For the emission decays, as many as four exponential components were needed to achieve an adequate fitting quality. Therefore, the data were fitted using the so-called maximum entropy method (MEM). The MEM fitting model extracts a distribution of the decay lifetimes with the smallest number of components.[81,82] The emission decay is written as

$$I(t) = \int_0^\infty p(\tau) \mathrm{e}^{-\frac{t}{\tau}} d\tau, \tag{3.3}$$

where τ is the time constant, and $p(\tau)$ is the probability density to find a decay with a time constant τ. The probability density is adjusted to minimize the function

$$S = \int_0^\infty \left(p(\tau) - p(\tau) \ln p(\tau)\right) d\tau, \tag{3.4}$$

keeping the weighted mean square deviation, χ^2, close to unity. For all the presented results, the χ^2 value is in the range 0.99–1.05. The MEM fitting model allowed to estimate the number of non-hybridized QDs in the dispersions, and therefore, helped to estimate the average QD-to-C_{60} ratio in the hybrids.

The number of C_{60} molecules per QD in each hybrid follows the Poisson statistics reasonably well.[83–85] Therefore, the relative concentration of C_{60} molecules in each hybrid, c, can be estimated. For the TA data, the decay is then written as

$$A(t,c) = A_0 \exp\left[-\frac{t}{\tau_0} - c(1 - e^{-\frac{t}{\tau_{ET}}})\right], \tag{3.5}$$

where the pre-exponential factor A_0 is determined by the population of the excited state immediately after excitation, τ_0 is the lifetime of a non-hybridized QD, and τ_{ET} is the electron transfer time constant for an ideal 1:1 hybrid, i.e. the *intrinsic* ET time constant. The total electron transfer time constant, τ, is inversely proportional to the number of fullerenes in a hybrid ($\tau = \tau_{ET}/n$).

Similarly, the surface traps in the QDs are considered to follow Poisson statistics, and a relative surface trap concentration can be estimated. Furthermore, the charge recombination needs to be taken into account in the model. The CR is expected to be rather slow, and it is fitted with a single exponential term. Thus, the global fitting model is written as

$$\begin{aligned} A(t,\lambda) = A_0(\lambda) \exp\left[-\frac{t}{\tau_0} - c_t(1 - e^{-\frac{t}{\tau_t}}) - c(1 - e^{-\frac{t}{\tau_0}})\right] \\ + A_1(\lambda) \exp\left(-\frac{t}{\tau_1}\right) + A_2(\lambda) \exp\left(-\frac{t}{\tau_{CR}}\right), \end{aligned} \tag{3.6}$$

where c_t is the relative concentration of surface traps in the QD, τ_t is the quenching time constant for a QD with a single trap, τ_1 is the time constant associated with the vibrational relaxation of the photoexcited QDs, and τ_{CR} is the charge recombination time constant. The fitting yields three decay associated spectra: $A_0(\lambda)$, $A_1(\lambda)$, and $A_2(\lambda)$, associated with fast thermalization, the QD excited state and the QD–C_{60} charge-separated state, respectively. The Poisson fitting model allows to separate the spectral features of the fullerene anion more clearly than the exponential fitting model. Furthermore, it helps to reveal the spectroscopic features of QD cations.

For the phthalocyanine samples, a so-called *small energy distribution model* was used in combination with the multiexponential model.[86] In the small energy distribution model, some of the exponential components were replaced with a term allowing for variation in the Gibbs free energy (or, if needed, in the reorganization energy) of the electron transfer reaction:

$$f(t) = \frac{1}{\sqrt{\pi}\Delta E} \int_{-X}^{X} \exp\left(-\frac{x^2}{\Delta E^2}\right) \exp\left(-\frac{t}{\tau_0} e^{\frac{ax}{k_B T}}\right) dx, \tag{3.7}$$

where ΔE is the width of the distribution in the Gibbs free energies. The integration limit X should be large enough to cover the entire distribution in the energy values ($X \gg \Delta E$). τ_0 is the non-disturbed time constant (according to the classical Marcus theory), $a = -\frac{\Delta G_0 + \lambda_0}{2\lambda_0}$ is a factor that determines how sensitive the decay profile is to energy distribution, ΔG_0 is the non-disturbed Gibbs free energy, and λ_0 is the non-disturbed reorganization energy.[86]

The small energy distribution model accounts for the variations in the electron transfer rates in the Pc–semiconductor samples. The local environments of the individual Pc molecules are different due to e.g. different orientations on the semiconductor surface, causing a distribution in the ET time constants. With the small energy distribution model, the number of components in the fitting is reduced and all the components are based on parameters that are physically meaningful. Furthermore, the different samples can be compared in a quantitative manner.

NB! The longest-lived transient absorption time constants (for all measurements shown in the thesis) are rather inaccurate due to the fact that the time window of the experiments is limited to 6 ns.

3.3.5 Solar cell characterization

Performance of the solar cell samples was studied under white light illumination as well as monochromatic illumination at different wavelengths.

Overall performance of the solar cells was studied by measuring the current-voltage curves (IV curves) in the dark and under white light illumination. The white light was produced with a standardized (AM 1.5) solar simulator (Sciencetech SS150), and the samples were excited at one sun (100 mW/cm^2). The IV curves were measured with a source/monitoring unit (SMU, Agilent Tech. E5272A).

A home-built system was used for the photocurrent spectrum measurements. A xenon lamp (Oriel Apex, Newport Corp.) was coupled with a computer-controlled monochromator (CM110, Spectral Products). The light was directed at the sample at approx. 3 cm^2 spot. The Agilent SMU was used for measuring the photocurrent at zero bias voltage at 10 nm intervals. The incoming light power was measured using a photodiode (S120VC, Thorlabs, Inc.) at the same wavelengths.

4 Results and Discussions

This chapter describes the most important results and observations made in Papers **I**–**IV**. Some of the results, especially in Section 4.2 dealing with the reduction of aggregation in ZnPc monolayers, have been revised. The transient absorption spectra have been refitted using the small energy distribution model (eq. 3.7) to reduce the number of used decay components and to make the results more easily interpretable.

4.1 Photoinduced electron transfer on different semiconductor surfaces

Photoinduced processes were investigated on two different types of organic–semiconductor interfaces: in QD–C_{60} hybrids and in SAMs of phthalocyanine derivatives on TiO_2 NPs and ZnO nanorods. On a phenomenological level, however, the processes are not too different. The electronic states involved are the ground and excited states as well as ionic states of organic compounds, and valence and conduction bands of semiconductors.

Figure 4.1 presents SEM images of the three semiconductor platforms. The QDs were deposited on a Si wafer for imaging purposes. There are large clusters of several QDs as well as individual QDs to be seen. The individual QDs are approx. 6 ± 1 nm in diameter and reasonably well resolved in the SEM image (Figure 4.1a). The ZnO nanorods (Figure 4.1b) and TiO_2 NPs (Figure 4.1c) were imaged using real sample substrates, cleaved for the cross-section imaging. The ZnO nanorods are approx. 800 nm in length and 30 nm in diameter. The TiO_2 NP film is deposited on top of the FTO | TiO_2 CL, and the mesoporous film thickness is approx. 2.5 μm. Individual TiO_2 NPs are approx. 15-20 nm in diameter.[87]

4.1.1 QD–fullerene hybrids (QD–C_{60})

The QD–C_{60} hybrids are a unique system in that the semiconductor support actually serves as the chromophore as well. Also, the direction of the electron transfer is opposite to that observed on other semiconductors in this thesis: from the QDs to the organic compound.

Figure 4.2 shows typical titration data for a QD–C_{60} system. The quantum dots have a rather high emission quantum yield and a relatively narrow (FWHM < 40 nm) emission spectrum. When hybridized with the C_{60}, the QD emission is quenched, indicating either energy or electron transfer (Figure 4.2). The titration experiments, however, provide no evidence on the nature of the QD-C_{60} interaction since the fullerene does not emit.

The C_{60} excited and anion states have absorption features distinguishable from the ground-state absorption. The transient absorption decay component spectra for QDs

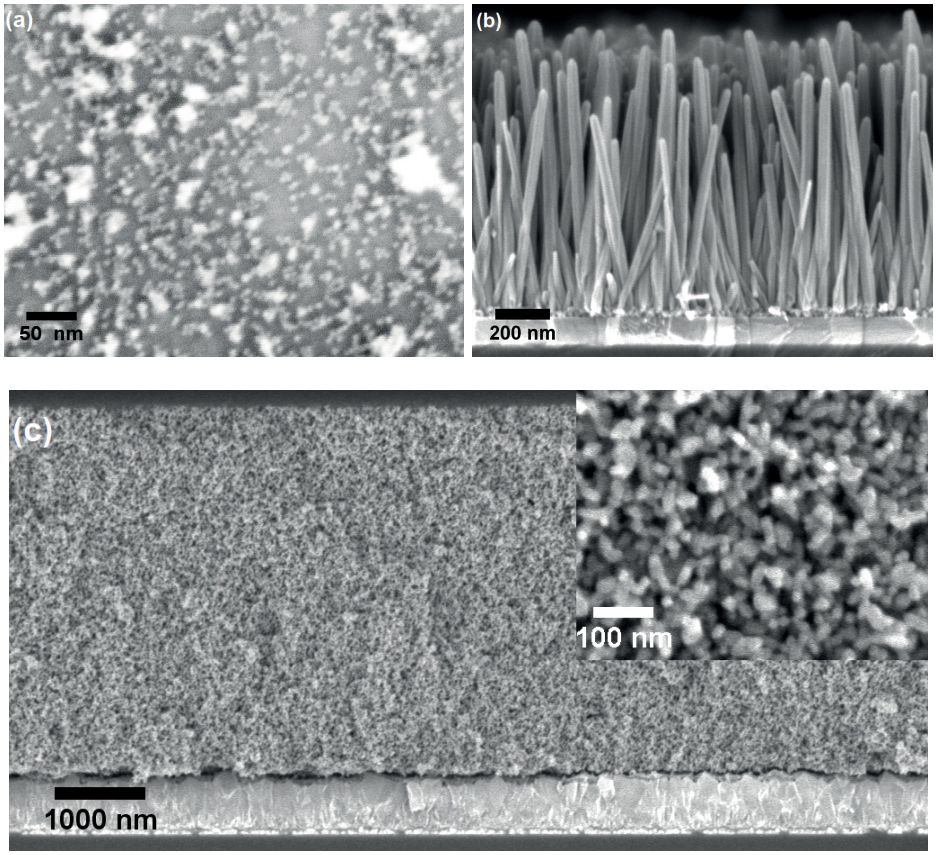

Figure 4.1: SEM images of the three semiconductor surfaces: (a) CdSe/ZnS QDs on Si support, (b) cross-section of ZnO nanorods (Paper **III**), and (c) cross-section of TiO_2 NP film. Inset: high magnification top image of the same sample.

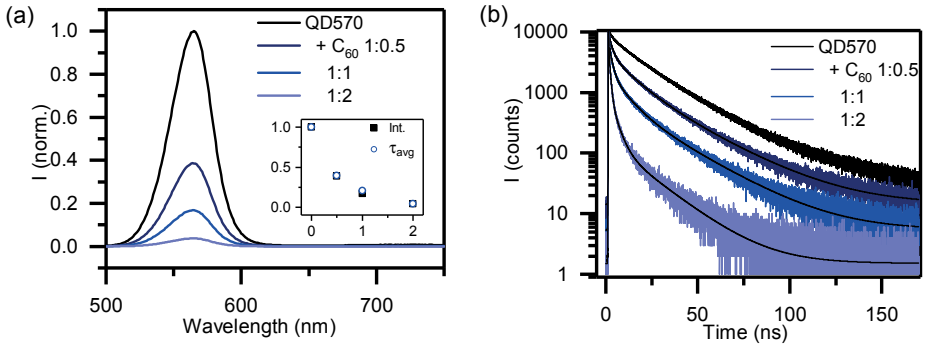

Figure 4.2: (a) Emission spectra and (b) fluorescence decay curves for the QD570 and QD570–C_{60} hybrids. The inset in (a) shows the decrease of the emission intensity as well as the average fluorescence lifetime as a function of the fullerene content. Paper **I**.

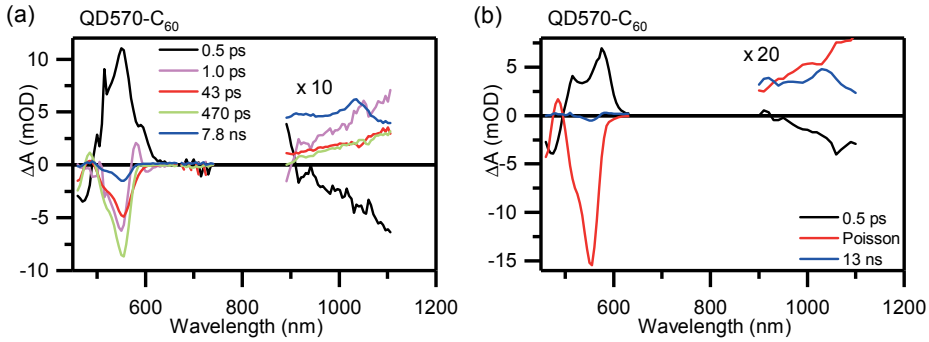

Figure 4.3: Decay component spectra for the QD570−C_{60} hybrid using (a) exponential fit and (b) Poisson fit of the TA data. Excitation wavelength was 440 nm. Paper **I**.

Table 4.1: Estimated QD−C_{60} molar ratios, fullerene anion formation time constants ($\tau_{C_{60}^-}$), intrinsic electron transfer time constants (τ_{ET}), and charge recombination time constants (τ_{CR}) for the studied QD−C_{60} hybrids. Paper **I**.

Sample	QD−C_{60} ratio	Exponential fit			Poisson fit	
		$\tau_{C_{60}^-}$ (ps)	τ_{ET} (ps)	τ_{CR} (ns)	τ_{ET} (ps)	τ_{CR} (ns)
QD540	1:2.4	80	194	2.2	453	14
QD570	1:2.0	43	86	7.8	655	13
QD600	1:1.9	50	96	12	133	14
QD630	1:1.7	77	132	6.7	98	50

with 540 nm emission maximum with C_{60} are presented in Figure 4.3a.

The raw signals were fitted into a sum of five exponentials. Not all of the decay components have a clear physical meaning, but due to the statistical (and therefore heterogeneous) nature of the hybrid formation, they were needed in order to obtain a good-quality fit. The most important decay components are the formation (43 ps, red) and decay (7.8 ns, blue) of the fullerene radical anion (C_{60}^-). The former describes the rate of electron transfer from the QD conduction band to the C_{60}, and the latter the charge recombination from the C_{60} radical anion into the QD valence band. Table 4.1 summarizes the decay components for all QD samples. In the table, time constant for the C_{60}^- formation is denoted with $\tau_{C_{60}^-}$, and the charge recombination with τ_{CR}, respectively. The C_{60}^- formation lifetimes are, however, not directly comparable for different QD sizes due to the changing QD-to-C_{60} ratio from sample to sample. Therefore, the intrinsic electron transfer time constants (τ_{ET}) were estimated by multiplying $\tau_{C_{60}^-}$ by the relative amount of C_{60} present in each QD−C_{60} hybrid.

In Paper **I**, the Poisson fitting model was also used. The decay component spectra with the Poisson model (eq. 3.6) are presented in Figure 4.3b. In the fitting, the shortest-lived component (hot exciton cooling; black) and the longest-lived component (decay of the C_{60}^-; blue) were still fitted to exponential functions, but the middle components were replaced by the term accounting for the surface traps as well as the Poisson distribution of the C_{60} molecules in the hybrids (red).

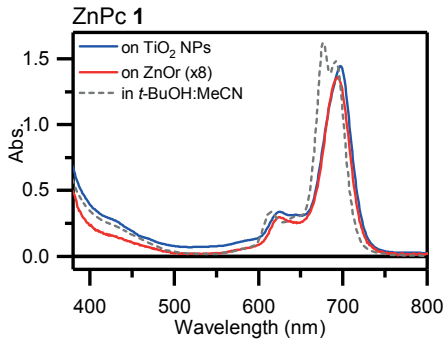

Figure 4.4: Absorption spectra of ZnPc **1** on TiO_2 NPs (blue), ZnO nanorods (red, multiplied by 8), and in *t*-BuOH:MeCN solution (gray, dashed). Paper **II**.

Comparing to the multiexponential fitting model, the Poisson model makes the picture clearer and more informative. Now there are only three components: hot exciton cooling, formation of the C_{60}^- (or electron transfer) and decay of the C_{60}^- (charge recombination). However, when compared to the multiexponential fit, the Poisson model gives remarkably longer lifetimes. The lifetimes are compared in Table 4.1.

For example, for the QD570 sample, the intrinsic electron transfer time constant obtained from the multiexponential fit is 86 ps, whereas it is 655 ps for the Poisson model. A reason for this discrepancy might lay in the simplifications made in the Poisson model. It has to be noted that the Poisson model is a simplification of a heterogeneous system, and thus tends to overestimate the electron transfer time constants. For example, there is most probably a distribution of electron transfer time constants due to the different orientations of individual C_{60} molecules on the QD surface. The linker connecting the binding COOH group to the C_{60} core is somewhat flexible, giving rise to several possible orientations and thus several distances between the active moieties. However, the advantage of the Poisson model is the more clearly resolved C_{60}^- band.

4.1.2 ZnPc on ZnO nanorods and TiO_2

Roles of the organic moiety and the semiconductor are reversed in ZnPc–semiconductor systems compared to the QD–C_{60} hybrids. Upon photoexcitation, electron transfer is expected from the excited organic sensitizer into the semiconductor conduction band. Kinetics of the electron transfer, or *injection*, are investigated for ZnPc **1** on two substrates: ZnO nanorods and TiO_2 NPs.

Thickness of the used TiO_2 NP layers varied from 2 to 3 μm. Given the greater layer thickness and the mesoporous structure of the TiO_2 NPs, the specific surface area is 100-fold compared to a flat surface. For the ZnO nanorods, the increase in the surface area is ca. 20-30-fold. The difference in the surface areas is well seen in absorption spectra of the phthalocyanine SAM prepared on both substrates. Figure 4.4 presents the absorption spectrum of ZnPc **1** on both TiO_2 NPs and ZnO nanorods.

Absorbance of the phthalocyanine is almost 10 times higher on TiO_2 NPs (blue) than on ZnO nanorods (red, raw data multiplied by 8). The difference can be explained by the different specific surface areas of these two substrates. The shape of the phthalocyanine absorption spectrum, however, is very similar on both substrates. Moreover, the spectral

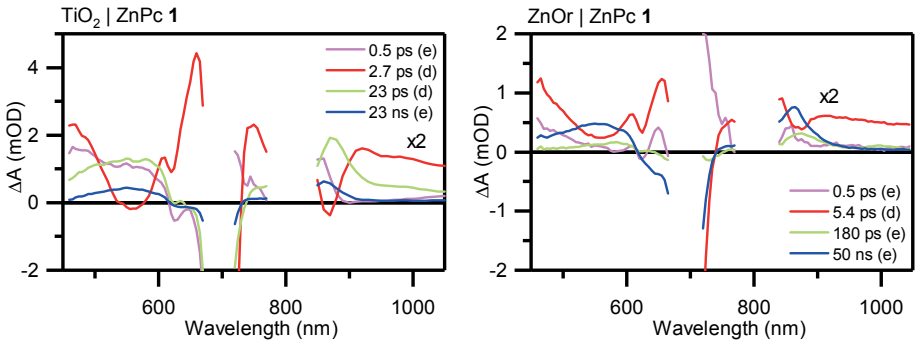

Figure 4.5: Transient absorption component spectra of ZnPc **1** on (a) TiO_2 NPs and (b) ZnO nanorods. Paper **II**.

shape is very similar to the spectrum of ZnPc **1** in solution (gray, dashed), indicating no phthalocyanine aggregation.

Figure 4.5 presents the transient absorption decay component spectra for ZnPc **1** on TiO_2 NP and on ZnO nanorods. The results were fitted to a sum of exponential (eq. 3.1) and small energy distribution (eq. 3.7) functions. The small energy distribution model reduces the number of needed components and therefore simplifies the interpretation of the spectra. On the first look, the spectra seem similar for the TiO_2 and ZnO nanorod samples. However, there are differences especially in the relative intensities of the decay components.

The shortest-lived components (0.5 ps for both samples, denoted with magenta) is associated with the thermal relaxation of the singlet excited state. The decay components denoted with red (2.7 ps for TiO_2 and 5.4 ps for ZnOr) bear features typical of phthalocyanine cation formation: a negative peak centered at 860 nm and a broad negative band between 500 and 600 nm. Opposedly, the longest-living components (23 ns for TiO_2, 50 ns for ZnOr, denoted with blue) have the same features with positive intensity. They are associated with the decay of the same state, Pc^+.

The main difference between the two semiconductor substrates is found in the relative intensities of the longest-lived (blue) components and the middle-lifetime components in the spectra (23 ps for TiO_2, 180 ps for ZnOr, denoted with green). For the TiO_2 | ZnPc **1** sample, the 23 ps component is much stronger in intensity than the long-lived component. For the ZnOr | ZnPc **1** sample, on the contrary, the long-lived component is much more intense than the 180 ps component. Both the middle-lifetime and the long-lived components bear spectral features of Pc^+ decay, but with very different lifetimes. Evidently, there are phthalocyanine cations with very different local environments. It is not clear, though, why the lifetimes differ so much for the samples on different substrates.

In Paper **II**, the green component was associated with the recombination of an intermediate interfacial charge transfer complex (ICTC) for the ZnOr sample. For the TiO_2 NP sample, existence of the ICTC is not a feasible explanation for this component, since several reports have shown much faster electron injection in TiO_2 systems.[44,88] Instead, the 23 ps component was associated with charge recombination inside a single TiO_2 nanoparticle before the photogenerated electron hops from one nanoparticle to the next. As soon as

the electron leaves the nanoparticle where it was generated, it continues its way as a free carrier.

Equation 4.1 schematically presents the fate of the electron on TiO_2 and ZnOr surfaces.

$$\begin{array}{ccccc} \mathrm{Pc}^* & \xrightarrow{\tau_{inj}} & e^- \,|\, \mathrm{Pc}^+ & \xrightarrow{\tau_l} & \mathrm{Pc}^+ \\ & & \downarrow \tau_{int} & & \downarrow \tau_{cr} \\ & & \mathrm{Pc} & & \mathrm{Pc} \end{array} \tag{4.1}$$

τ_{inj} describes the electron injection, corresponding to the short-lived components in Figure 4.5. The state denoted with $e^- \,|\, \mathrm{Pc}^+$ is the ICTC in the case of ZnO nanorods. For TiO_2, it can be thought of the charge separated state at short time intervals (before the electron leaves the first TiO_2 nanoparticle). This state can either recombine (τ_{int}) or dissociate to give free charge carriers in the semiconductor CB (τ_l). The final charge-separated state recombines with τ_{CR}.

Experimentally, one can observe τ_{inj}, τ_{CR}, and $\left(\tau_{int}^{-1} + \tau_l^{-1}\right) = \tau_s$. The time constants do not directly reveal which portion of the photogenerated ZnPc cations is recombined and which portion facilitates a free electron in the semiconductor CB. This information can, however, be retrieved from the relative amplitudes of the TA signal for the different samples. The population of long-lived cations was modelled in Paper **II**, and it seems that at longer delay times, > 20 ps, the portion of cations is higher in the ZnOr | ZnPc **1** sample than in TiO_2 | ZnPc **1**. In other words, in the TiO_2 sample, the cations are generated faster, but due to the interfaces between individual nanoparticles, they also recombine faster, and eventually (at long delay times) the cation yield is higher in ZnO nanorods. It has to be noted, however, that in a functioning solar cell, a few tens of picoseconds should be well enough for the dye regeneration through hole transfer into the HTM. Therefore, both materials should perform as efficiently in solar cells.

4.2 Aggregation reduction in phthalocyanine SAMs

Papers **III** and **IV** were dedicated to reducing the phthalocyanine aggregation in SAMs on different semiconductor surfaces with two different methods. The effect of the reduced aggregation on the photoinduced electron transfer efficiency is also discussed.

4.2.1 Aggregation reduction through bulky substituents

In Paper **III**, phthalocyanines with bulky substituents (ZnPc **1**–ZnPc **4**) were used. The substituents were designed to sterically hinder the stacking of neighboring ZnPc molecules, thus reducing aggregation and undesired intermolecular interactions.

Based on steady-state absorption spectra, none of the compounds shows clear signs of aggregation. Typically, H-type aggregation induces blue-shift in the absorption maximum as well as broadening of the spectrum. For the ZnPcs studied here, probably the most pronounced absorption changes are observed for ZnPc **3**. Figure 4.6 shows the absorption spectra for ZnPc **3** in solution and as a SAM on ZnO nanorods. The absorption maximum is slightly shifted to the red (11 nm in the SAM compared to the solution), and the FWHM changes from 29 nm (solution) to 55 nm (SAM). The shift in the absorption maximum is, however, not typical for H-type aggregates, and could be caused by the different environment in the SAM compared to the solution.

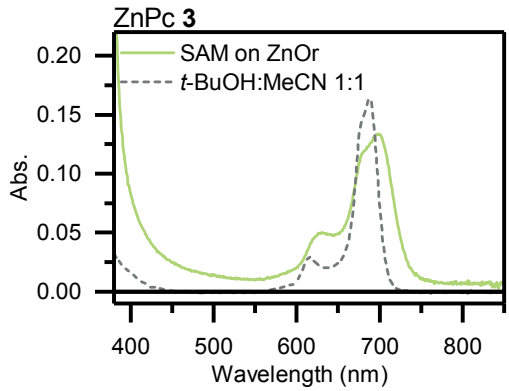

Figure 4.6: Absorption spectra of ZnPc **3** in *t*-BuOH:MeCN solution and as a SAM on ZnO nanorods. The absorbance of ZnO nanorods has been subtracted. Paper **III**.

Even though the steady-state absorption spectra do not reveal clear evidence of aggregation, the situation is different when looking at the transient absorption data. Figure 4.7 shows the decay component spectra for ZnPc **2** and ZnPc **3** SAMs on ZnO nanorods. The data presented in Paper **III** were refitted using a combination of the multiexponential (eq. 3.1) and small energy distribution (eq. 3.7) models. Similar data for ZnPc **1** can be found in Figure 4.5b, and for ZnPc **4** in ref. 89.

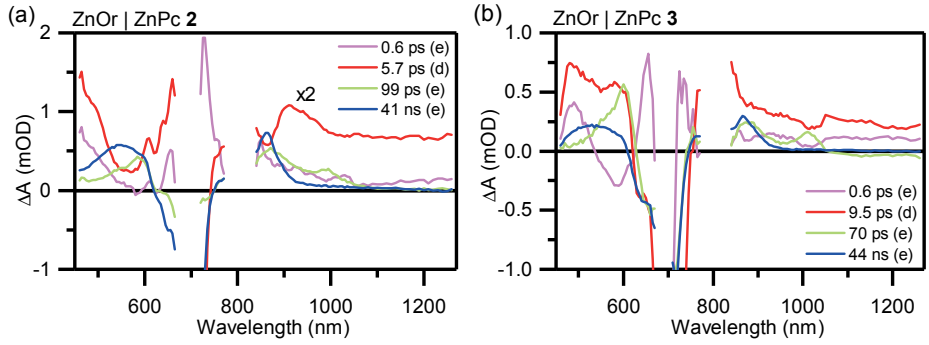

Figure 4.7: Transient absorption decay component spectra for (a) ZnOr | ZnPc **2** and (b) ZnOr | ZnPc **3**. Refitted from Paper **III** using a combination of the exponential (eq. 3.1) and the small energy distribution (eq. 3.7) models.

The spectral interpretation for ZnPc **2** is very similar to ZnPc **1**. The shortest-lived component (0.6 ps, denoted with magenta) is attributed to the thermal relaxation of the singlet excited state. The 5.7 ps component (red) describes the formation of the Pc cation. The longest-lived component (41 ns, blue) is associated with the cation decay, or charge recombination. The middle component for ZnPc **2** (99 ps, green), however, cannot be explained by recombination in the intermediate ICTC like in the case of ZnPc **1**. There are additional bands at ca. 590 and 1000 nm. In Paper **III**, these bands are associated with the phthalocyanine anion (Pc^-). The only feasible pathway leading to the formation of Pc^- is intermolecular charge separation in the phthalocyanine aggregates:

$$Pc^{*}-Pc \rightarrow Pc^{+}-Pc^{-}. \quad (4.2)$$

For ZnPc **3**, the phthalocyanine cation features are surprisingly observed already in the shortest-lived component (0.6 ps, magenta). The same features are further observed in the 9.5 ps component (red), indicating that there are phthalocyanine cations with different environments present in the ZnPc **3** sample. The 70 ps component (green) shows features typical of both Pc cation and Pc anion decay. These two observations point to the presence of phthalocyanine aggregates. The longest-lived component (44 ns, blue) is again assigned to the decay of the Pc^{+}. The electron injection and charge recombination lifetimes for the samples are summarized in Table 4.2.

It is a bit surprising that the electron injection time constants for ZnPc **1** and ZnPc **2** are practically similar. ZnPc **2** has a longer spacer between the binding group and the phthalocyanine core, and thus a longer electron injection time constant is expected. Some explanations are given by molecular modelling carried out in Paper **III**. For ZnPc **1** and ZnPc **2**, the similar electron injection time constants are explained by the molecular orientation on the semiconductor surface. The longer spacer gives ZnPc **2** more degrees of freedom to tilt on the ZnO surface, despite the seemingly rigid structure of the spacer (triple bond). As a result, the distances from the Pc core to the ZnO are rather similar for the two phthalocyanines.

4.2.2 Aggregation reduction by co-adsorbates

The second method to reduce phthalocyanine aggregation that was investigated in the thesis was to use a phthalocyanine with small substituents and a co-adsorbate to suppress the intermolecular interactions between individual phthalocyanine molecules (Paper **IV**). Two co-adsorbates were used: chenodeoxycholic acid (CDCA) and oleic acid (OA). TiO_2 was chosen as the semiconductor substrate due to the faster electron injection as well as the higher specific surface area, leading to higher phthalocyanine absorptions.

The phthalocyanine used in Paper **IV**, ZnPc **5**, is known to aggregate in concentrated solutions and on semiconductor surfaces. However, with the well-known co-adsorbate CDCA, it shows moderate solar cell efficiencies in liquid electrolyte dye-sensitized solar cells.[29] Figure 4.8 shows the absorption spectra for ZnPc **5** in solutions with and without a co-adsorbate, as well as in a SAM on TiO_2 NP.

The spectral broadening is apparent in the solution spectra, Figure 4.8a. Solution with a 200-fold molar excess of CDCA is considered non-aggregated. Compared to that, the other spectra are considerably broader, and the fine structure in the bands is lost. Moreover, the band centered at ca. 630 nm gets much more pronounced in the spectrum of ZnPc **5** alone. The relative intensity of this band compared to the Q band maximum (at ca. 690 nm) can be used as the first measure on the degree of aggregation.

Absorption spectrum of the SAM of ZnPc **5** without a co-adsorbate (Figure 4.8b, denoted with blue) is even further broadened compared to the solution spectrum. The aggregated band at 630 nm is in fact higher than the monomeric absorption band for this sample. Adding a co-adsorbate clearly reduces the aggregation (seen in the normalized absorption spectra in Figure 4.8c). However, also the absolute absorbance of the sample decreases drastically, as shown in Figure 4.8b. The co-adsorbates bind onto the TiO_2 surface together with the ZnPc, taking some space on the semiconductor surface. At the same

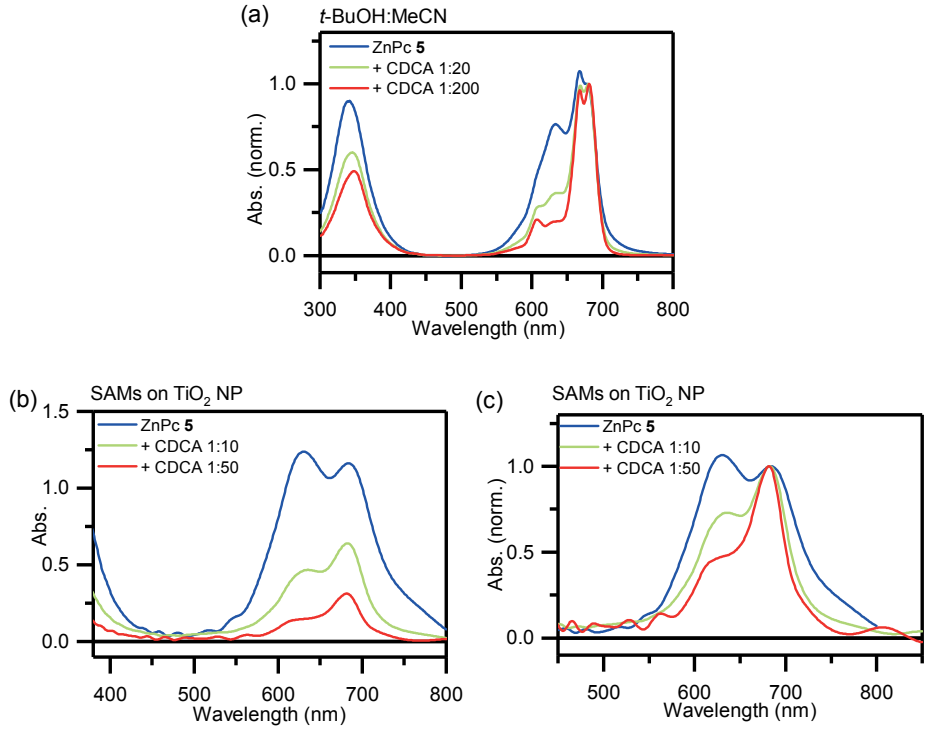

Figure 4.8: Absorption spectra of ZnPc **5** with an increasing concentration of CDCA in (a) *t*-BuOH:MeCN solutions, (b) SAMs on TiO_2 NPs, and (c) SAMs on TiO_2 NPs with a normalized absorbance scale. Paper **IV**.

time, they prevent the ZnPc **5** molecules from stacking together and therefore reduce the unwanted Pc–Pc interactions.

Figure 4.9 shows the decay component spectra for SAMs of ZnPc **5** and ZnPc **5** with a 50-fold molar excess of CDCA. The data originally published in Paper **IV** were refitted using a combination of the exponential (eq. 3.1) and the small energy distribution (eq. 3.7) models. The observations that can be made are rather similar to other systems discussed previously. The non-aggregated sample, ZnPc **5** + CDCA 1:50 (Figure 4.9a), shows electron injection with associated time constant 0.5 ps (magenta) and charge recombination in the 2 ps–42 ns components. Spreading of the decay over such a large range of lifetimes probably arises from the differences in the local environment for individual phthalocyanine molecules. There is always a distribution of orientations in which the co-adsorbates and ZnPc **5** are organized, and therefore, each ZnPc **5** molecule might exhibit different kinetics on the TiO_2 surface. For the heavily aggregated sample (ZnPc **5**, Figure 4.9b), the shortest decay component (77 fs, magenta) is considerably shorter than for the less aggregated samples. Moreover, the short component bears features of both Pc cation and anion formation. The short component is therefore attributed to charge separation inside the phthalocyanine aggregates. The 6.9 ps component (red) is associated with the electron injection into the TiO_2, resulting in a better resolved Pc^+ spectrum. The longer components (79 ps, green, and 20 ns, blue) are associated with charge recombination in both the aggregates (79 ps) and the long-lived cation (20 ns).

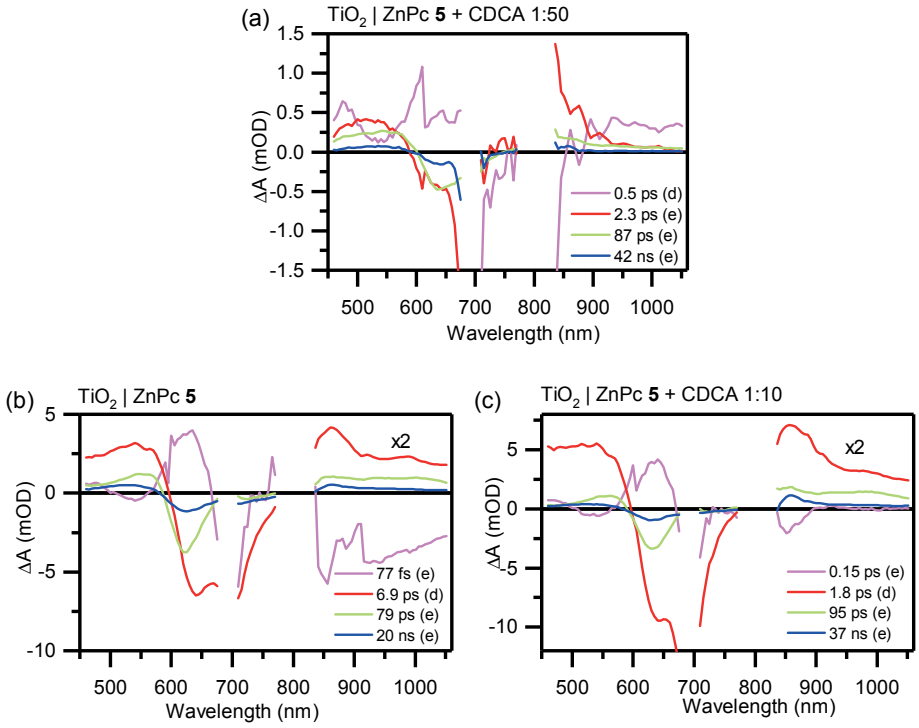

Figure 4.9: Decay component spectra for (a) ZnPc **5** + CDCA 1:50, (b) ZnPc **5**, and (c) ZnPc **5** + CDCA 1:10. Excitation wavelength was 695 nm. Refitted from Paper **IV** using a combination of the exponential (eq. 3.1) and the small energy distribution (eq. 3.7) models.

For the samples with moderate amounts of the co-adsorbate (Figure 4.9c), the results fall rather logically in between the non-aggregated and the heavily aggregated samples. The charges separate with a 0.15 ps time constant (magenta) in the Pc aggregates, the electron injection is completed in 1.8 ps (red), and charge recombination time constants range from 95 ps (green) to 37 ns (blue).

Similar samples were prepared with oleic acid (OA) as the co-adsorbate (1:10 and 1:100 molar excess compared to ZnPc **5**). Unfortunately, the samples degraded during the TA measurements, and the results might not be reliable especially for the ZnPc **5** + OA 1:100 sample. Figure 4.10 presents the decay component spectra for these samples. The data were refitted using the exponential (eq. 3.1) and the small energy distribution (eq. 3.7) models. The decay components are similar to the CDCA-containing samples: charge separation inside the Pc aggregates in ca. 0.2 ps (magenta), electron injection in less than ten picoseconds (red), and charge recombination ranging from ca. 100 ps to several tens of nanoseconds (green and blue).

Table 4.2 summarizes the time constants obtained from ultrafast transient absorption spectroscopy for the studied ZnPc derivatives. The electron injection from the excited phthalocyanine occurs within the first few ps for all of the samples. Interestingly, the electron injection time constants are much closer to each other in the compounds bearing bulky substituents, the major differences arising from the structural differences in the compounds. The compounds bearing the bulkiest substituents (ZnPc **1** and ZnPc **2**)

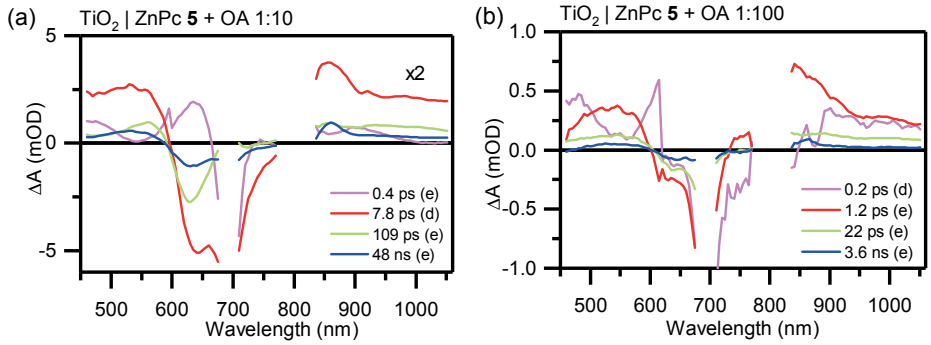

Figure 4.10: Decay component spectra for (a) ZnPc **5** + OA 1:10 and (b) ZnPc **5** + OA 1:100. Excitation wavelength was 695 nm. The samples were degraded during the measurements, which might render the results unreliable. Refitted from Paper **IV** using a combination of the exponential (eq. 3.1) and the small energy distribution (eq. 3.7) models.

Table 4.2: Time constants for the photoinduced processes at different ZnPc–semiconductor interfaces. τ_{inj} is the time constant for electron injection, τ_{ICTC} for the recombination of the ICTC complex, τ_{agg} for the charge separation inside the ZnPc aggregates, and τ_{CR} for the charge recombination of the Pc cations (see text for details). Refitted from Papers **II**–**IV** using a combination of the exponential (eq. 3.1) and the small energy distribution (eq. 3.7) models.

Compound	τ_{inj} (ps)	τ_{ICTC} (ps)	τ_{CR} (ps)	τ_{CR} (ns)
ZnOr | ZnPc **1**	5.4	180	-	50
ZnOr | ZnPc **2**	5.7	-	99	41
ZnOr | ZnPc **3**	0.7	-	70	50
ZnOr | ZnPc **4**	1.4	-	850	

Compound	τ_{agg} (ps)	τ_{inj} (ps)	τ_{CR} (ps)	τ_{CR} (ns)
TiO_2 | ZnPc **1**	-	2.7	23	23
TiO_2 | ZnPc **5**	0.08	6.9	79	20
+ CDCA 1:10	0.15	1.8	95	37
+ CDCA 1:50	-	0.5	87	42
+ OA 1:10	0.4	7.8	109	48
+ OA 1:100	0.2	1.2	22	3.6

have the longest electron injection time constants, apparently due to the steric hindrance caused by the substituents.

In the co-adsorbate containing systems, charge separation inside the aggregates seems to get faster with more severe aggregation, leading to shorter intra-aggregate CS time constants. The electron injection is faster for the co-adsorbate containing systems compared to ZnPc **1**–ZnPc **4**. There are possibly two factors contributing to the faster electron injection: the TiO_2 substrate and the aggregation. As discussed in Section 4.1, the electron injection is generally faster on TiO_2 surfaces than on ZnO nanorods. Moreover, the electron injection gets faster with reducing degree of aggregation. In the less aggregated systems, there are more monomeric phthalocyanine molecules present capable of injecting an electron into the semiconductor when excited, making the injection faster and more efficient.

The charge recombination rates do not seem to follow a clear trend according to the degree of aggregation. This is not surprising, considering the nature of the charge recombination process. It is the back electron transfer from the CB of the semiconductor material into the HOMO of the (monomeric) phthalocyanine cation.

The degree of aggregation in the phthalocyanine samples evidently has an effect on the

Table 4.3: Relative transient absorptions for the Pc cations and Pc anions. The $\Delta A^{rel.}$ were calculated by dividing ΔA at the selected decay time by ΔA at 540 nm at short delay time for characteristic Pc^+ and Pc^- wavelengths. Pc^+ yield was calculated by dividing $\Delta A^{rel.}_{Pc^+}$ by $\Delta A^{rel.}_{Pc*}$. Refitted from Papers **III**–**IV** using a combination of the exponential (eq. 3.1) and the small energy distribution (eq. 3.7) models.

Sample	$\Delta A^{rel.}_{Pc*}$	$\Delta A^{rel.}_{Pc^+}$	Pc^+ yield	$\Delta A^{rel.}_{Pc^-}$
ZnOr | ZnPc **1**	0.91	0.38	0.42	0.09
ZnOr | ZnPc **2**	0.79	0.27	0.34	0.11
ZnOr | ZnPc **3**	1.19	0.29	0.24	0.18
ZnOr | ZnPc **4**	0.37	0.20	0.55	0.08
TiO_2 | ZnPc **5**	0.56	0.06	0.10	0.27
+ CDCA 1:10	0.57	0.06	0.10	0.19
+ CDCA 1:50	1.09	0.08	0.07	0.06
+ OA 1:10	0.75	0.12	0.17	0.23
+ OA 1:100	1.56	0.09	0.06	0.05

electron injection kinetics. The time constants, however, do not provide direct information on the degree of aggregation. Instead, the TA signal intensities at different delay times can be used to estimate the aggregation degree, at least on a qualitative level.

First, the efficiency of the electron injection reaction is affected by the aggregation. By estimating the number of monomeric (or long-living) phthalocyanine cations in the samples, one can estimate the efficiency of electron injection and therefore the degree of aggregation. A high yield of long-lived Pc cations (calculated from the transient absorption signal intensity at 860 nm at 2 ns delay) can be considered as an indication of low degree of aggregation; the Pc^+–Pc^- pairs recombine in the picosecond time scale.

The presence of aggregates results in the formation of phthalocyanine anions in the samples due to the intra-aggregate charge separation. As mentioned, the Pc^- signal at ca. 1000 nm is stronger for the more severely aggregated samples. Therefore, using the Pc^- signal intensity, at least relative estimates on the aggregation degree can be drawn. Quantitative estimation of the degree of aggregation is difficult due to the different absolute absorbances of the samples. The transient absorptions were taken at a moderate delay (30 ps), after the charge separation in the aggregates but before the recombination. Table 4.3 presents the relative Pc^+ and Pc^- yields for the studied ZnPcs. The data presented in Papers **III**–**IV** were refitted using the exponential (eq. 3.1) and the small energy distribution (eq. 3.7) models to obtain a better comparison between the different sample types.

Similar trends on the aggregation degree can be observed in both the Pc cation yield and the Pc anion yield. Considering the sample series with bulky substituents, the least aggregated samples are ZnPc **1** and ZnPc **4**. They have the highest Pc^+ yields (0.42 for ZnPc **1** and 0.55 for ZnPc **4**, respectively) and the lowest Pc^- absorptions (0.09 and 0.08, respectively) in this sample series. ZnPc **3** appears the most aggregated given the lowest Pc^+ yield (0.24) and the highest Pc^- absorbance (0.18).

Looking back at the chemical structures of the compounds, the low aggregation in ZnPc **1** seems reasonable: the Pc peripheral substitutes are large and bulky, rendering the molecules quite large and non-planar. Likely reasonable is the highest aggregation in ZnPc **3**, with smaller substituents and a more exposed Pc core prone to stacking. The aggregation tendency of ZnPc **2**, on the other hand, is somewhat surprising. It is

structurally very similar to ZnPc **1**, the only difference being the length of the spacer between the Pc core and the binding carboxylic group. Perhaps the increased freedom at the semiconductor surface, brought about by the longer linker, enables an enhanced stacking in the layer compared to ZnPc **1**. The signs of low aggregation in ZnPc **4** are also somewhat surprising, given it is structurally somewhat similar to ZnPc **3** The peripheral substituents are even smaller in ZnPc **4** than in ZnPc **3**, and the linker is longer.

For the co-adsorbate containing samples, the Pc^+ yield does not correlate with the expected degree of aggregation. The absolute absorbances of the samples might be too different to reliably compare these samples. The Pc^- signal, however, shows a clear trend: a decrease in the relative Pc^- absorption with an increase in the co-adsorbate content. The least aggregated samples, ZnPc **5** + CDCA 1:50 and ZnPc **5** + OA 1:100, have Pc^- intensities of 0.06 and 0.05, respectively, whereas the anion absorption for ZnPc **5** without co-adsorbates is 0.27.

It can be also noted in Table 4.3 that oleic acid is not as efficient in reducing the sample aggregation as CDCA. The Pc^- signal intensity is consistently higher for a similar co-adsorbate content. Apparently the larger CDCA molecules take up more space at the semiconductor surface, pushing the phthalocyanine molecules away from each other more effectively than OA molecules.

4.3 Long-lived charge separation: Spiro-MeOTAD

In a working solar cell, a hole-transporting material (HTM) is needed. In this work, a solid HTM, spiro-MeOTAD, was used because of the easy deposition using spin-coating and no need of liquid electrolytes in the cells.

Figure 4.11 presents cross-sectional SEM images of ZnO nanorods and TiO_2 NPs covered by spiro-MeOTAD. Complete coverage of the semiconductor by spiro-MeOTAD is essential for optimal solar cell performance. For ZnO nanorods (Firue 4.11a), it can be seen that the spiro-MeOTAD coverage is rather good, the spiro-MeOTAD layer extends to the nanorod bottom, and the voids between individual nanorods are filled by the HTM. For the TiO_2 NP layers (Figure 4.11b), the HTM is visual in the SEM images throughout the whole TiO_2 layer. There is an overlayer of spiro-MeOTAD seen at the top of the image; it is needed for functioning solar cells. High magnification images of the bottom part of the TiO_2 layer before and after adding spiro-MeOTAD are shown in Figures 4.11c and 4.11d, respectively. According to the images, spiro-MeOTAD seems to fill the voids between the nanoparticles all the way to the bottom.

4.3.1 Steady-state absorption

Figure 4.12 presents the effect of spiro-MeOTAD on the absorption spectra of the ZnPc SAMs. The effect is rather different for the non-aggregated samples and the aggregated samples. For the samples with low degree of aggregation (Figures 4.12a, 4.12b and 4.12f), the spiro-MeOTAD layer does not cause major differences in the shapes of the absorption spectra. Spiro-MeOTAD itself has a low, broad absorbance through the visible spectrum and a sharp absorption maximum at 390 nm. The absorption of the non-aggregated samples is essentially a superposition of the SAM and spiro-MeOTAD absorptions.

For the aggregated samples (Figures 4.12c, 4.12d and 4.12e), the situation is different. The spectrum gets sharper and narrower upon spiro-MeOTAD addition, and the absorption intensity increases. This is often considered as a sign of reduced aggregation. Being a small

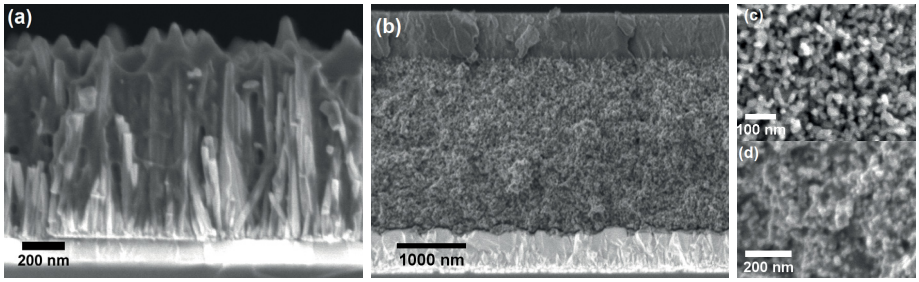

Figure 4.11: Cross-sectional SEM images of (a) ZnOr | ZnPc **1** | spiro (Paper **III**), (b) TiO_2 | ZnPc **5** | spiro, (c) close-up image of TiO_2 | ZnPc **5** and (d) close-up image of TiO_2 | ZnPc **5** | spiro.

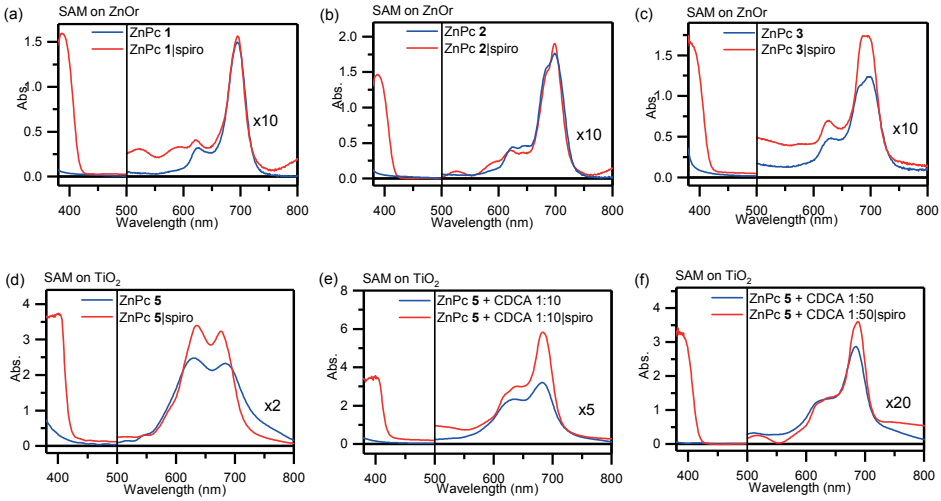

Figure 4.12: Absorption spectra of spiro-MeOTAD-coated SAMs on the different semiconductor substrates. Data from Papers **III-IV**.

molecule compound, spiro-MeOTAD infiltrates in between the ZnPc molecules in the SAMs. Apparently it also induces changes in the morphology of the ZnPc aggregates. The ratio of the 630 and 690 nm bands can be used as a measure of the degree of aggregation, as discussed earlier. This ratio does, however, not change in the ZnPc **5** | spiro-MeOTAD sample (Figure 4.12d). It seems then that the relative portion of aggregated ZnPc molecules does not change upon spiro-MeOTAD addition, but the aggregates are more homogeneous and better organized.

4.3.2 Charge separation efficiency

Spiro-MeOTAD has a major effect on the ZnPc transient absorption data. Let us first examine the simplest cases with low degree of aggregation: ZnPc **1** and ZnPc **5** + CDCA 1:50. Figure 4.13 presents the transient absorption decay component spectra for these two samples. The data were fitted with a combination of the exponential (eq. 3.1) and the small energy distribution (eq. 3.7) models.

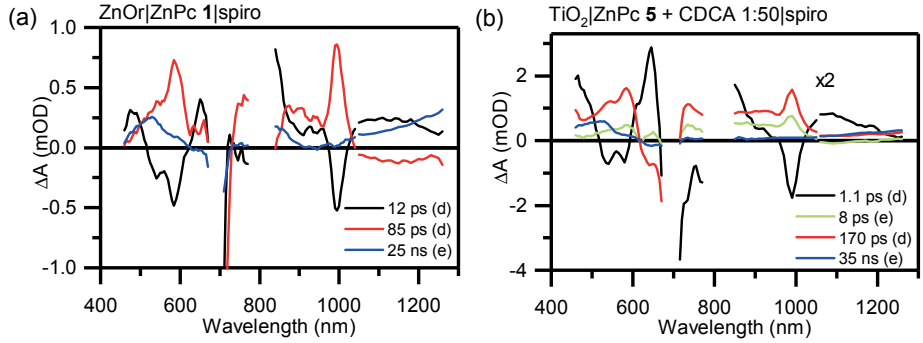

Figure 4.13: Transient absorption decay component spectra for (a) ZnOr | ZnPc **1** | spiro, and (b) TiO_2 | ZnPc **5** + CDCA 1:50 | spiro-MeOTAD. The samples were excited at 695 nm. Papers **III**-**IV**.

Spiro-MeOTAD has an evident effect on the transient absorption of these samples. Let us compare the TA signals presented in Figure 4.13 to the signals from the same samples without spiro-MeOTAD: ZnPc **1** on ZnO nanorods (Figure 4.5b) and ZnPc **5** + CDCA 1:50 (Figure 4.9a). Upon addition of spiro-MeOTAD, new bands emerge at ca. 530, 590 and 1000 nm. Moreover, a smooth rise in the absorption is observed in the NIR range. These bands were attributed to the ZnPc anion and to the spiro-MeOTAD cation in Papers **III** and **IV**. The Pc^- spectral features were discussed in the section dealing with phthalocyanine aggregation, and it was noted that the 590 nm and the 1000 nm bands are attributed to Pc^-. The 530 nm band as well as the absorption rise in the NIR wavelengths are attributed to spiro-MeOTAD cation. Moreover, the long-lived components do not show features of the phthalocyanine cation, indicating that the dye molecules have been regenerated through the electron injection.

The data were fitted using a combination of the exponential (eq. 3.1) and the small energy distribution (eq. 3.7) models. For ZnOr | ZnPc **1** | spiro, a reasonable fit accuracy was obtained using two exponentials and two small energy distribution components. The shortest exponential function ($\tau \approx 70$ fs, not shown) bears features of the ZnPc singlet excited state, and is attributed to thermal relaxation of the excited ZnPc. The 12 ps component (denoted with black) is attributed to the formation of the phthalocyanine anion, having some features of $spiro^+$ formation as well. The 85 ps component (red) is associated with the decay of the Pc^-, and the spectrum is transformed into the long-lived spectrum (25 ns, blue), describing the decay of the spiro-MeOTAD cation.

For TiO_2 | ZnPc **5** + CDCA 1:50 | spiro-MeOTAD, altogether 4 exponential functions and 2 small energy distribution components were needed to obtain a good-quality fit. The singlet excited state relaxation was fitted with two exponents (16 and 70 fs, not shown). Formation of the phthalocyanine anion is described by the 1.1 ps band (black), but the Pc^- decay was fitted with a combination of an exponential (8 ps, green) and a small energy distribution (170 ps, red) function. Again, the long component (35 ns, blue) is attributed to the spiro-MeOTAD cation decay.

There are two possible pathways for the long-lived charge separation in the semiconductor | ZnPc | spiro systems:

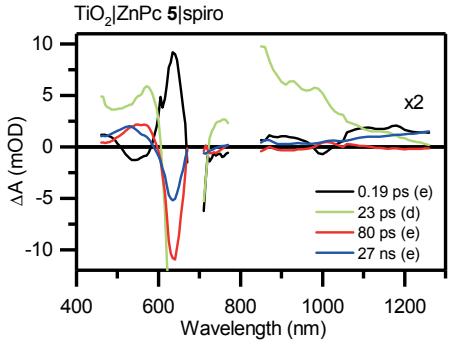

Figure 4.14: Transient absorption decay component spectra for TiO_2 | ZnPc **5** | spiro. Refitted from Paper **IV** using a combination of the exponential (eq. 3.1) and the small energy distribution (eq. 3.7) models.

$$\mathrm{SC} \mid \mathrm{Pc}^{*} \mid \mathrm{spiro} \rightarrow \mathrm{SC}^{-} \mid \mathrm{Pc}^{+} \mid \mathrm{spiro} \rightarrow \mathrm{SC}^{-} \mid \mathrm{Pc} \mid \mathrm{spiro}^{+} \tag{4.3}$$

$$\mathrm{SC} \mid \mathrm{Pc}^{*} \mid \mathrm{spiro} \rightarrow \mathrm{SC} \mid \mathrm{Pc}^{-} \mid \mathrm{spiro}^{+} \rightarrow \mathrm{SC}^{-} \mid \mathrm{Pc} \mid \mathrm{spiro}^{+} \tag{4.4}$$

In the first pathway (eq. 4.3), the excited phthalocyanine first injects an electron into the semiconductor and then recombines *via* a hole transfer to the spiro-MeOTAD layer. In the second pathway (eq. 4.4), the charge transfer occurs in reversive order: the charge separation at the ZnPc | spiro interface occurs first, yielding a phthalocyanine anion and a spiro-MeOTAD cation. The Pc anion then injects the extra electron into the conduction band of the semiconductor. Based on our data, the second pathway dominates the excited-state relaxation, because Pc anion signals would not be expected for the first pathway. Moreover, the formation of the spiro-MeOTAD cation and the Pc^{-} share the same lifetimes, indicating that the reactions indeed follow the pathway in eq. 4.4.

Splitting of the Pc^{-} decay into two components for the TiO_2 | ZnPc **5** + CDCA 1:50 | spiro sample might arise from aggregation. If there are some Pc aggregates in the sample resulting in Pc^{+}–Pc^{-} pairs, it is likely for the Pc anions in these aggregates to recombine much faster than the monomeric phthalocyanine anions. Thus, the 8 ps component could be attributed to the decay of Pc anions inside the aggregates, and the 170 ps component to the electron injection from the phthalocyanine anion into the semiconductor.

Effect of aggregation

With the heavily aggregated samples, the situation gets more complex. There are additional relaxation pathways induced by the aggregation, making fitting and interpretation of the TA data more difficult. Figure 4.14 shows the decay component spectra of an aggregated sample (TiO_2 | ZnPc **5** | spiro). The data originally published in Paper **IV** were refitted using a combination of the exponential (eq. 3.1) and the small energy distribution (eq. 3.7) models. The short-lived component (0.19 ps, black) is attributed to Pc^{-} formation. The components with moderate time constants (23 ps, green; and 80 ps, red) bear features of both Pc^{+} and Pc^{-} decay, and the longest-living component (27 ns, blue) shows the rising absorption of $spiro^{+}$ at the NIR range. The signal at the NIR range is, however, rather weak compared to the visible range.

Table 4.4: Time constants for the spiro-MeOTAD containing samples. $\tau_{agg.}$ is the time constant for intra-aggregate charge separation, τ_{CS} for the charge separation at the ZnPc | spiro interface, τ_{ET} for the electron transfer from the Pc^- into the semiconductor, and τ_{CR} for the charge recombination. Refitted from Papers **III**–**IV** using a combination of the exponential (eq. 3.1) and the small energy distribution (eq. 3.7) models.

Sample	$\tau_{agg.}$ (ps)	τ_{CS} (ps)	τ_{ET} (ps)	τ_{CR} (ns)
ZnOr | ZnPc **1**	-	12	130	22
ZnOr | ZnPc **2**	1.1	11	125	31
ZnOr | ZnPc **3**	0.2	1.5	104	29
ZnOr | ZnPc **4**	-	0.5	120	12
TiO_2 | ZnPc **5**	0.12	1.3	322	35
+ CDCA 1:10	0.09	1.2	182	37
+ CDCA 1:50	-	1.1	170	35
+ CDCA 1:100	-	0.5	151	42
+ OA 1:10	0.08	1.0	102	18
+ OA 1:100	0.14	1.7	152	31

The very fast formation of phthalocyanine anions is not expected for the reaction pathway depicted in eq. 4.4. The charge separation at the ZnPc | spiro interface yields phthalocyanine anions in the 1-10 ps timescale for the non-aggregated samples. Decay of the Pc anion band is split into several exponents, indicating that there are anions with very different local environments present. Moreover, the components associated with the Pc^- decay also bear features of the phthalocyanine cation. These facts indicate that the majority of the excited ZnPcs relax through intermolecular charge transfer and recombination inside the aggregates. Formation of the spiro-MeOTAD cation is not resolved for this sample. The long-lived component, however, shows the $spiro^+$ band, indicating that some phthalocyanine molecules get in contact with the HTM layer and undergo the charge separation at the ZnPc | spiro interface.

Similar analysis for the samples containing moderate amounts of the co-adsorbates (CDCA and OA, 1:10) show that the samples still contain a high number of aggregates and that the number of electrons leaving the ZnPc layer is low. The vast majority of the ZnPc molecules relax through the charge separation and recombination inside the aggregates. Table 4.4 summarizes the time constants for the different photoinduced processes in the spiro-MeOTAD-containing samples.

Time constants for the charge separation at the ZnPc | spiro-MeOTAD interface (τ_{CS}) are considerably longer for the ZnPcs aggregation-protected with bulky substituents (ZnPc **1** and **2**) than for the ZnPcs with smaller substituents (ZnPc **3**–**5**). Probably the bulky substituents in ZnPc **1** and **2** comprise a steric hindrance for efficient contact between the HTM and the phthalocyanine. For the aggregated samples, the Pc^- formation is spread across two components, the shorter one arising from the intra-aggregate charge separation ($\tau_{agg.}$) and the longer one associating with the Pc | spiro charge separation (τ_{CS}).

Time constants for the electron transfer from Pc^- into the semiconductor (τ_{ET}) are surprisingly similar for all samples, ranging from ca. 100 to 300 ps. There are no differences between the differently substituted phthalocyanines, even though the electron injection time constants without the spiro-MeOTAD overlayer showed a clear dependence on the substituent size. This would indicate that the environment for the electron transfer

Table 4.5: Relative transient absorptions for the Pc cations, Pc anions, and spiro-MeOTAD cations. The $\Delta A^{rel.}$ were calculated by dividing ΔA at the selected decay time by ΔA at 540 nm at short delay time for characteristic Pc^- and $spiro^+$ wavelengths. $Spiro^+$ yield was calculated by dividing $\Delta A^{rel.}_{spiro^+}$ by $\Delta A^{rel.}_{Pc*}$. Refitted from Papers **III**–**IV** using a combination of the exponential (eq. 3.1) and the small energy distribution (eq. 3.7) models.

Sample	$\Delta A^{rel.}_{Pc*}$	$\Delta A^{rel.}_{Pc^-}$	$\Delta A^{rel.}_{spiro^+}$	$spiro^+$ yield
ZnOr | ZnPc **1**	1.06	0.52	0.34	0.32
ZnOr | ZnPc **2**	1.21	0.50	0.20	0.17
ZnOr | ZnPc **3**	0.85	0.22	0.20	0.23
ZnOr | ZnPc **4**	1.02	0.44	0.35	0.35
TiO_2 | ZnPc **5**	0.64	0.18	0.09	0.13
+ CDCA 1:10	0.80	0.22	0.15	0.19
+ CDCA 1:50	0.71	0.36	0.13	0.18
+ CDCA 1:100	0.87	0.28	0.19	0.22
+ OA 1:10	0.72	0.14	0.02	0.03
+ OA 1:100	0.84	0.20	0.12	0.14

is different with and without the HTM. It was discussed earlier that upon infiltration into the phthalocyanine SAM, spiro-MeOTAD helps the Pc molecules to organize better on the semiconductor surface. Probably the molecules take such conformations that the distance between the Pc core and the semiconductor surface is rather similar for all samples, leading to minor differences in the electron transfer rate.

The charge separation efficiency was estimated for the spiro-MeOTAD-containing samples with a similar manner than for the samples without spiro-MeOTAD in Section 4.2.2 and presented in Table 4.5. The data presented in Papers **III**–**IV** were refitted for this sample series as well. As discussed earlier, the expected reaction pathway goes through a charge separation at the ZnPc | spiro interface, followed by electron injection from the Pc anion into the semiconductor. Thus, TA signal intensities of the Pc anion and spiro-MeOTAD cation are plausible options for estimating the charge separation efficiency. For Pc^-, 1000 nm was chosen as the representative wavelength and 30 ps as the representative time. For spiro-MeOTAD, the most distinctive spectral feature is the rising absorption at the NIR wavelengths. At 1250 nm, there are no other species absorbing at longer delays (2 ns). Thus, the relative absorption change at this wavelength can be taken as an indicator of the number of formed spiro-MeOTAD cations, and therefore, and indicator of the efficiency of the charge separation at the Pc | spiro interface.

The TA signal intensities are not perfectly comparable for the different substrates. However, similar trends can be observed for both aggregation-reducing methods. The least aggregated samples (ZnPc **1**, ZnPc **4**, and ZnPc **5** with a large excess of co-adsorbates) show the highest Pc^- and $spiro^+$ intensities. Whenever the aggregation increases, efficiency of the charge separation decreases. For the samples with bulky substituents, the Pc anion intensity increases by more than 130% when comparing the least aggregated sample (ZnPc **1**; 0.52) to the most severely aggregated sample (ZnPc **3**; 0.22). Moreover, the spiro-MeOTAD cation yield is also increased by almost 40% (0.32 for ZnPc **1**, 0.23 for ZnPc **3**, respectively). The use of co-adsorbates is almost as efficient in reducing the aggregation. When comparing ZnPc **5** with and without a co-adsorbate, the Pc^- intensity increases by 100% (0.18 for ZnPc **5**, 0.36 for ZnPc **5** + CDCA 1:50, respectively) and spiro-MeOTAD cation intensity by close to 40% (0.13 for ZnPc **5**, 0.18 for

ZnPc **5** + CDCA 1:50, respectively).

It has to be noted that in the oleic acid containing samples, the relative Pc anion and spiro-MeOTAD cation intensities are consistently lower than for CDCA with the same molar excess. Thus, it would seem that oleic acid is less efficient in lowering the degree of aggregation in the samples. The reason for this might lay in the structure of the co-adsorbates. The steroid core of CDCA requires more space on the TiO_2 surface than OA with a long hydrocarbon tail. Thus, more OA is required for a similar aggregation-reducing effect.

4.4 Photocurrent generation

Solar cell performance of ZnPc **5** was investigated by building full ssDSSCs. Performance of the cells was studied by standard IV measurements, and more interestingly, the incident photon-to-current efficiencies were estimated.

Figure 4.15 presents the IV curves for two sample series with CDCA and OA as the co-adsorbates. The solar cell characteristics are summarized in Table 4.6.

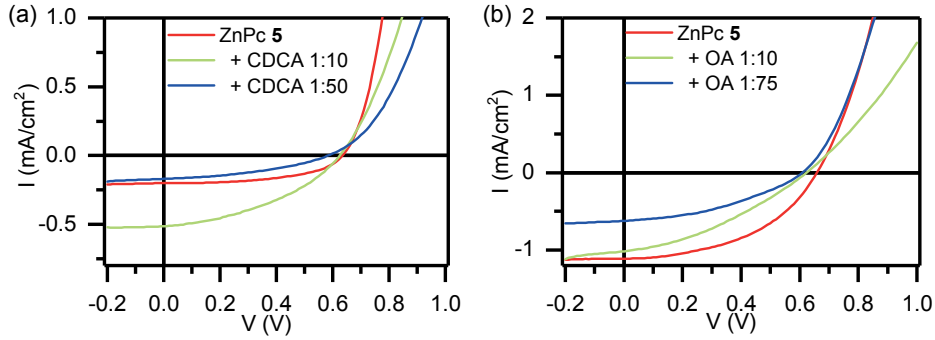

Figure 4.15: IV curves for solar cells using ZnPc **5** as the sensitizer with increasing concentration of co-adsorbates. Data from Paper **IV**.

The two sample series are not directly comparable, because the series with CDCA was prepared with a spin-coated TiO_2 NP layer and not the screen-printed layer. The prepared spin-coated layers were thinner than the screen-printed layers (0.8 μm for the spin-coated layers and 2.5μm for the screen-printed layers, respectively). Samples inside one sample series can, however, be compared.

The aggregation-reducing effect of CDCA and OA is not evident based on the solar cell data. The power conversion efficiency decreases upon co-adsorbate addition (with the exception of CDCA in 1:10 ratio). The loss in efficiency arises mostly from the decreasing short-circuit current. Remembering the absorption spectra, the decrease in the power conversion efficiency can be explained by the smaller amount of dye adsorbed onto the TiO_2 surface. Thus, a more detailed analysis taking into account the number of absorbed photons is needed.

Incident photon to current efficiency (IPCE) spectra were measured to better resolve the effect of the aggregation reduction. The resulting values were converted to absorbed photon to current spectra using eqs. 2.4–2.5. Both the IPCE and APCE spectra are

Table 4.6: IV characteristics for the ssDSSC samples. A total of eight parallel samples were prepared for each structure. The values are presented for the sample with the highest power conversion efficiency for each structure. I_{sc} is the short-circuit current density, U_{oc} open-circuit voltage, FF fill factor, η overall power conversion efficiency, and IPCE$_{max}$ and APCE$_{max}$ the maximum values for the incident photon-to-current efficiency and the absorpbed photon-to-current efficiency, respectively. Data from Paper **IV**.

Sample	I_{sc} (mA/cm^2)	U_{oc} (V)	FF	η (%)	IPCE$_{max}$ (%)	APCE$_{max}$ (%)
TiO_2 | ZnPc **5**	0.20	0.64	0.52	0.07	2.4	3.7
+ CDCA 1:10	0.51	0.63	0.40	0.13	1.5	3.5
+ CDCA 1:50	0.17	0.60	0.42	0.04	1.8	7.2
TiO_2 | ZnPc **5**	0.96	0.72	0.50	0.35	4.0	4.4
+ OA 1:10	1.02	0.63	0.35	0.22	1.4	1.5
+ OA 1:75	0.81	0.60	0.34	0.16	1.0	1.5

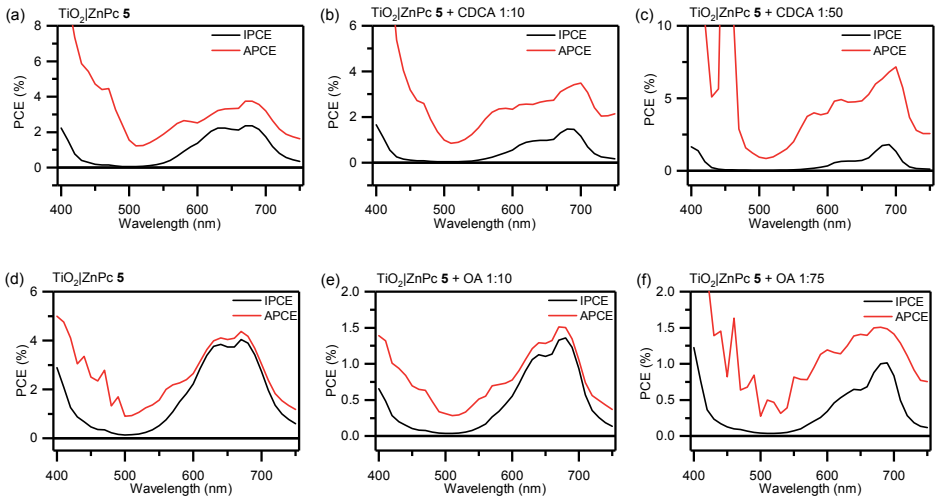

Figure 4.16: Photocurrent action spectra. Data from Paper **IV**.

presented in Figure 4.16, and the maximum values for both efficiencies are listed in Table 4.6. The PCE results presented in Paper **IV** were estimated using the white light IV measurement data; the results presented here utilize monochromatic illumination.

The IPCE values follow the same trend already seen in the overall efficiencies of the devices: the decreasing absorption decreases the produced photocurrent due to the decreased dye content in the layers. The reduced aggregation is visible in the IPCE spectra as the decrease in the photocurrent at ca. 630 nm. Looking at the APCE spectra, differences between the samples are easy to notice. For ZnPc **5** without co-adsorbates, the maximum APCE is approx. 4%. With the CDCA-containing samples, the APCE value increases by 85%. On the contrary, APCE values for the OA-containing samples are even lower than for ZnPc **5** without the co-adsorbates. It seems that adding oleic acid does not increase the number of phthalocyanine molecules capable of injecting electrons into the external circuit and therefore contributing to the photocurrent.

5 Conclusions

This thesis investigated the photoinduced processes at an organic–semiconductor interface. The studied systems included semiconductor QD–C_{60} hybrids as well as ZnPc self-assembled monolayers on ZnO nanorod and TiO_2 NP surfaces. Special attention was paid on different methods for aggregation-reduction in the ZnPc samples. The following conclusions can be drawn based on the presented results:

- Electron transfer reactions were observed in organic–semiconductor hybrids in both directions, from organic to semiconductor and from semiconductor to organic material. The ET rates vary from a few picoseconds to a few tens of picoseconds depending on the system.
- Aggregation of aggregation-prone phthalocyanines can be reduced both by functionalizing the phthalocyanine core with bulky substituents and by adding molecular co-adsorbates. The substitution mechanism was observed to be more effective in reducing phthalocyanine aggregation in terms of lifetime of the charge-separated state. However, the electron injection was slower for the substituted ZnPc samples than for the co-adsorbate containing samples.
- Adding spiro-MeOTAD as a HTM induces a reaction sequence where the charges first separate at the ZnPc | spiro interface, followed by electron injection from the ZnPc anion into the semiconductor. This reaction sequence is rather slow, but apparently long enough for photocurrent generation. The HTM seemed to be in good contact with the ZnPc SAM, and especially for the aggregated samples, spiro-MeOTAD infiltrates between the aggregates and renders the SAM in a better organized state.
- The studied ZnPcs were successfully utilized as sensitizers in solid-state dye-sensitized solar cells. The absorbed photon-to-current efficiency was increased with a decreasing degree of aggregation. Unfortunately, using co-adsorbates lowered the absorbance of the samples, such that the overall power conversion efficiency was left lower than without the co-adsorbate.

It was noted that the electron injection from a zinc phthalocyanine into the semiconductor CB was faster for TiO_2 NP than for ZnO nanorods. Unfortunately, also the charge recombination was faster, apparently due to the interfaces between individual NPs. It was stated, however, that in a complete solar cell sample, the electrons are withdrawn from the TiO_2 NP layer into the anode sufficiently fast, so that the effect of charge recombination on the solar cell performance is minor. Thus, both materials should be suitable for solar cell photoanodes. The potential of ZnO as a photoanode material is being studied quite

intensely; ZnO would be a cost-effective, naturally abundant alternative to TiO_2. The results presented in this thesis support this conception.

When studying the effect of aggregation, the most interesting finding was that the substitution of the ZnPc core had such a large effect on the electron injection time constants. When comparing the series of ZnPcs on ZnO nanorod surface, the electron injection time did not actually depend on the degree of aggregation, but on the size of the substituents attached on the phthalocyanine core. As a downside, the faster electron injection also meant a faster CR. Therefore, the aggregation-protection with bulky substituents not only prevents the phthalocyanines from aggregation, but also provides longer lifetimes for the charge-separated state.

Based on the findings reported in this thesis, it is recommended to use chemical aggregation-reducing methods when designing novel solar cell architectures utilizing phthalocyanines. The highest yield of long-living Pc cations was obtained with the phthalocyanine with the bulkiest substituents, ZnPc **1**. With spiro-MeOTAD as the HTM, over 30% of the excited phthalocyanine molecules generated a charge-separated state.

When utilizing phthalocyanines for solar cell applications, one admittedly needs to take into account the rather narrow spectral coverage of the compound. Phthalocyanines absorb mainly in the red wavelengths, and the shorter wavelength regions of the solar spectrum are left unutilized. A broader spectral coverage could be obtained by mixing the phthalocyanines with other dyes whose absorption falls in the 400 – 600 nm range. Mixing of different dyes might also reduce the tendency of the phthalocyanine molecules to form aggregates, which would further increase the potential of these compounds in photovoltaic devices.

Bibliography

[1] International Energy Agency, "Key world energy statistics 2018," 2018, accessible at: webstore.iea.org/statistics-data.

[2] D. L. Hartmann, A. M. G. Klein Tank, M. Rusticucci, L. V. Alexander, S. Brönnimann, Y. Charabi, F. J. Dentener, E. J., Dlugokencky, D. R. Easterling, A. Kaplan *et al.*, "Observations: Atmosphere and surface," in *Climate Change 2013: The Physical Science Basis*, T. F. Stocker, D. Qin, G.-K. Plattner, M. Tignor, S. K. Allen, A. N. J. Boschung, Y. Xia, V. Bex, and P. M. Midgley, Eds. Cambridge, United Kingdom and New York, NY, USA: Cambridge University Press, 2013, ch. 2, pp. 159 – 254, accessible at: www.climatechange2013.org.

[3] Intergovernmental Panel on Climate Change, "Global warming of 1.5 °C," 2018, accessible at: www.ipcc.ch/report/sr15.

[4] B. O'Regan and M. Grätzel, "A low-cost, high-efficiency solar cell based on dye-sensitized colloidal TiO_2 films," *Nature*, vol. 353, no. 6346, pp. 737 – 740, 1991.

[5] Y. Cao, Y. Saygili, A. Ummadisingu, J. Teuscher, J. Luo, N. Pellet, F. Giordano, S. M. Zakeeruddin, J.-E. Moser, M. Freitag *et al.*, "11% efficiency solid-state dye-sensitized solar cells with copper (II/I) hole transport materials," *Nature Communications*, vol. 8, p. 15390, 2017.

[6] K. Kakiage, Y. Aoyama, T. Yano, K. Oya, J.-i. Fujisawa, and M. Hanaya, "Highly-efficient dye-sensitized solar cells with collaborative sensitization by silyl-anchor and carboxy-anchor dyes," *Chemical Communications*, vol. 51, no. 88, pp. 15 894 – 15 897, 2015.

[7] W. Zhou and J. J. Coleman, "Semiconductor quantum dots," *Current Opinion in Solid State and Materials Science*, vol. 20, no. 6, pp. 352 – 360, 2016.

[8] W. C. W. Chan, D. J. Maxwell, X. Gao, R. E. Bailey, M. Han, and S. Nie, "Luminescent quantum dots for multiplexed biological detection and imaging," *Current Opinion in Biotechnology*, vol. 13, no. 1, pp. 40 – 46, 2002.

[9] X. Michalet, F. F. Pinaud, L. A. Bentolila, J. M. Tsay, S. Doose, J. J. Li, G. Sundaresan, A. M. Wu, S. S. Gambhir, and S. Weiss, "Quantum dots for live cells, in vivo imaging, and diagnostics," *Science*, vol. 307, no. 5709, pp. 538 – 544, 2005.

[10] X. Tong, Y. Zhou, L. Jin, K. Basu, R. Adhikari, G. S. Selopal, H. Zhao, S. Sun, A. Vomiero, Z. M. Wang *et al.*, "Heavy metal-free, near-infrared colloidal quantum dots for efficient photoelectrochemical hydrogen generation," *Nano Energy*, vol. 31, pp. 441 – 449, 2017.

[11] Z. Tan, Y. Zhang, C. Xie, H. Su, J. Liu, C. Zhang, N. Dellas, S. E. Mohney, Y. Wang, J. Wang, and J. Xu, "Near-band-edge electroluminescence from heavy-metal-free colloidal quantum dots," *Advanced Materials*, vol. 23, no. 31, pp. 3553–3558, 2011.

[12] Y. Wang, X. Li, J. Song, L. Xiao, H. Zeng, and H. Sun, "All-inorganic colloidal perovskite quantum dots: A new class of lasing materials with favorable characteristics," *Advanced Materials*, vol. 27, no. 44, pp. 7101–7108, 2015.

[13] Y. Wang, X. Li, J. Song, L. Xiao, H. Zeng, and H. Sun, "All-inorganic colloidal perovskite quantum dots: A new class of lasing materials with favorable characteristics," *Advanced Materials*, vol. 27, no. 44, pp. 7101–7108, 2015.

[14] K. Hoshi, T. Chiba, J. Sato, Y. Hayashi, Y. Takahashi, H. Ebe, S. Ohisa, and J. Kido, "Purification of perovskite quantum dots using low-dielectric-constant washing solvent "diglyme" for highly efficient light-emitting devices," *ACS Applied Materials & Interfaces*, vol. 10, no. 29, pp. 24 607–24 612, 2018, pMID: 29968455.

[15] P. Capper, S. Irvine, and T. Joyce, "Epitaxial crystal growth: Methods and materials," in *Springer Handbook of Electronic and Photonic Materials*. Springer, 2017, pp. 309–341.

[16] K. I. Hunter, J. T. Held, K. A. Mkhoyan, and U. R. Kortshagen, "Nonthermal plasma synthesis of core/shell quantum dots: Strained Ge/Si nanocrystals," *ACS Applied Materials & Interfaces*, vol. 9, no. 9, pp. 8263–8270, 2017.

[17] U. Kortshagen, L. Mangolini, and A. Bapat, "Plasma synthesis of semiconductor nanocrystals for nanoelectronics and luminescence applications," in *Nanotechnology and Occupational Health*. Springer, 2006, pp. 39–52.

[18] Y. Pu, F. Cai, D. Wang, J.-X. Wang, and J.-F. Chen, "Colloidal synthesis of semiconductor quantum dots toward large-scale production: A review," *Industrial & Engineering Chemistry Research*, vol. 57, no. 6, pp. 1790–1802, 2018.

[19] B. Zhang, T. Zhu, M. Ou, N. Rowell, H. Fan, J. Han, L. Tan, M. T. Dove, Y. Ren, X. Zuo *et al.*, "Thermally-induced reversible structural isomerization in colloidal semiconductor CdS magic-size clusters," *Nature Communications*, vol. 9, no. 1, p. 2499, 2018.

[20] Y. Guo, K. Marchuk, S. Sampat, R. Abraham, N. Fang, A. V. Malko, and J. Vela, "Unique challenges accompany thick-shell CdSe/nCdS ($n > 10$) nanocrystal synthesis," *The Journal of Physical Chemistry C*, vol. 116, no. 4, pp. 2791–2800, 2012.

[21] "Carbon," in *Encyclopaedia Britannica*. Encyclopaedia Britannica, inc., 2018, accessible at: www.britannica.com.

[22] S. Kirner, M. Sekita, and D. M. Guldi, "25th anniversary article: 25 years of fullerene research in electron transfer chemistry," *Advanced Materials*, vol. 26, no. 10, pp. 1482–1493, 2014.

[23] H. W. Kroto, J. R. Heath, S. C. O'Brien, R. F. Curl, and R. E. Smalley, "C_{60}: Buckminsterfullerene," *Nature*, vol. 318, no. 6042, p. 162, 1985.

[24] M. A. Dahlen, "The phthalocyanines: A new class of synthetic pigments and dyes," *Industrial & Engineering Chemistry*, vol. 31, no. 7, pp. 839–847, 1939.

[25] A. W. Snow, "Phthalocyanine aggregation," in *The Porphyrin Handbook: Phthalocyanines: Properties and Materials*, K. M. Kadish, K. M. Smith, and R. Guilard, Eds. San Diego, California, USA: Elsevier Science, 2003, vol. 17, ch. 109, pp. 129 – 176.

[26] T. Rawling and A. McDonagh, "Ruthenium phthalocyanine and naphthalocyanine complexes: Synthesis, properties and applications," *Coordination Chemistry Reviews*, vol. 251, no. 9-10, pp. 1128 – 1157, 2007.

[27] F. D'Souza and O. Ito, "Supramolecular donor – acceptor hybrids of porphyrins/phthalocyanines with fullerenes/carbon nanotubes: Electron transfer, sensing, switching, and catalytic applications," *Chemical Communications*, no. 33, pp. 4913 – 4928, 2009.

[28] E. S. Emerson, M. A. Conlin, A. E. Rosenoff, K. S. Norland, H. Rodriguez, D. Chin, and G. R. Bird, "The geometrical structure and absorption spectrum of a cyanine dye aggregate," *The Journal of Physical Chemistry*, vol. 71, no. 8, pp. 2396 – 2403, 1967.

[29] J.-J. Cid, J.-H. Yum, S.-R. Jang, M. K. Nazeeruddin, E. Martínez-Ferrero, E. Palomares, J. Ko, M. Grätzel, and T. Torres, "Molecular cosensitization for efficient panchromatic dye-sensitized solar cells," *Angewandte Chemie International Edition*, vol. 46, no. 44, pp. 8358 – 8362, 2007.

[30] W. Shi, B. Peng, Y. Guo, L. Lin, T. Peng, and R. Li, "Synthesis of asymmetric zinc phthalocyanine with bulky diphenylthiophenol substituents and its photovoltaic performance for dye-sensitized solar cells," *Journal of Photochemistry and Photobiology A: Chemistry*, vol. 321, pp. 248 – 256, 2016.

[31] L. Yu, L. Lin, X. Zhang, R. Li, T. Peng, and X. Li, "Highly asymmetric phthalocyanine-sensitized solar cells: The effect of coadsorbent and adsorption temperature of phthalocyanine," *Electrochimica Acta*, vol. 111, pp. 344 – 350, 2013.

[32] L. Tejerina, M. V. Martínez-Díaz, M. K. Nazeeruddin, and T. Torres, "The influence of substituent orientation on the photovoltaic performance of phthalocyanine-sensitized solar cells," *Chemistry – A European Journal*, vol. 22, no. 13, pp. 4369 – 4373, 2016.

[33] L. Martín-Gomis, F. Fernández-Lázaro, and Á. Sastre-Santos, "Advances in phthalocyanine-sensitized solar cells (PcSSCs)," *Journal of Materials Chemistry A*, vol. 2, no. 38, pp. 15 672 – 15 682, 2014.

[34] N. R. Neale, N. Kopidakis, J. van de Lagemaat, M. Grätzel, and A. J. Frank, "Effect of a coadsorbent on the performance of dye-sensitized TiO_2 solar cells: Shielding versus band-edge movement," *The Journal of Physical Chemistry B*, vol. 109, no. 49, pp. 23 183 – 23 189, 2005.

[35] P. Y. Reddy, L. Giribabu, C. Lyness, H. J. Snaith, C. Vijaykumar, M. Chandrasekharam, M. Lakshmikantam, J.-H. Yum, K. Kalyanasundaram, M. Grätzel *et al.*, "Efficient sensitization of nanocrystalline TiO_2 films by a near-IR-absorbing unsymmetrical zinc phthalocyanine," *Angewandte Chemie International Edition*, vol. 46, no. 3, pp. 373 – 376, 2007.

[36] S. Mori, M. Nagata, Y. Nakahata, K. Yasuta, R. Goto, M. Kimura, and M. Taya, "Enhancement of incident photon-to-current conversion efficiency for phthalocyanine-sensitized solar cells by 3D molecular structuralization," *Journal of the American Chemical Society*, vol. 132, no. 12, pp. 4054 – 4055, 2010.

[37] M.-E. Ragoussi, J.-H. Yum, A. K. Chandiran, M. Ince, G. de la Torre, M. Grätzel, M. K. Nazeeruddin, and T. Torres, "Sterically hindered phthalocyanines for dye-sensitized solar cells: Influence of the distance between the aromatic core and the anchoring group," *ChemPhysChem*, vol. 15, no. 6, pp. 1033 – 1036, 2014.

[38] L. Lin, B. Peng, W. Shi, Y. Guo, and R. Li, "Synthesis of zinc phthalocyanine with large steric hindrance and its photovoltaic performance for dye-sensitized solar cells," *Dalton Transactions*, vol. 44, no. 12, pp. 5867 – 5874, 2015.

[39] W. W. Yu, L. Qu, W. Guo, and X. Peng, "Experimental determination of the extinction coefficient of CdTe, CdSe, and CdS nanocrystals," *Chemistry of Materials*, vol. 15, no. 14, pp. 2854 – 2860, 2003.

[40] A. Djurišić, A. Ng, and X. Chen, "ZnO nanostructures for optoelectronics: Material properties and device applications," *Progress in Quantum Electronics*, vol. 34, no. 4, pp. 191 – 259, 2010.

[41] A. B. Djurišić, X. Chen, Y. H. Leung, and A. M. C. Ng, "ZnO nanostructures: growth, properties and applications," *Journal of Materials Chemistry*, vol. 22, no. 14, pp. 6526 – 6535, 2012.

[42] Z. L. Wang, "Nanostructures of zinc oxide," *Materials Today*, vol. 7, no. 6, pp. 26 – 33, 2004.

[43] J. Y. Lao, J. G. Wen, and Z. F. Ren, "Hierarchical ZnO nanostructures," *Nano Letters*, vol. 2, no. 11, pp. 1287 – 1291, 2002.

[44] P. Tiwana, P. Docampo, M. B. Johnston, H. J. Snaith, and L. M. Herz, "Electron mobility and injection dynamics in mesoporous ZnO, SnO_2, and TiO_2 films used in dye-sensitized solar cells," *ACS Nano*, vol. 5, no. 6, pp. 5158 – 5166, 2011.

[45] R. G. Nuzzo and D. L. Allara, "Adsorption of bifunctional organic disulfides on gold surfaces," *Journal of the American Chemical Society*, vol. 105, no. 13, pp. 4481 – 4483, 1983.

[46] A. Ulman, "Formation and structure of self-assembled monolayers," *Chemical Reviews*, vol. 96, no. 4, pp. 1533 – 1554, 1996.

[47] W. C. Bigelow, D. L. Pickett, and W. A. Zisman, "Oleophobic monolayers: I. Films adsorbed from solution in non-polar liquids," *Journal of Colloid Science*, vol. 1, no. 6, pp. 513 – 538, 1946.

[48] J. C. Love, L. A. Estroff, J. K. Kriebel, R. G. Nuzzo, and G. M. Whitesides, "Self-assembled monolayers of thiolates on metals as a form of nanotechnology," *Chemical Reviews*, vol. 105, no. 4, pp. 1103 – 1170, 2005.

[49] P. E. Laibinis, G. M. Whitesides, D. L. Allara, Y. T. Tao, A. N. Parikh, and R. G. Nuzzo, "Comparison of the structures and wetting properties of self-assembled monolayers of *n*-alkanethiols on the coinage metal surfaces, copper, silver, and gold," *Journal of the American Chemical Society*, vol. 113, no. 19, pp. 7152 – 7167, 1991.

[50] V. Colvin, A. Goldstein, and A. Alivisatos, "Semiconductor nanocrystals covalently bound to metal surfaces with self-assembled monolayers," *Journal of the American Chemical Society*, vol. 114, no. 13, pp. 5221 – 5230, 1992.

[51] D. Aswal, S. Lenfant, D. Guerin, J. Yakhmi, and D. Vuillaume, "Self assembled monolayers on silicon for molecular electronics," *Analytica Chimica Acta*, vol. 568, no. 1-2, pp. 84–108, 2006.

[52] W. Gao, L. Dickinson, C. Grozinger, F. G. Morin, and L. Reven, "Self-assembled monolayers of alkylphosphonic acids on metal oxides," *Langmuir*, vol. 12, no. 26, pp. 6429–6435, 1996.

[53] J. Bang and P. Kamat, "CdSe quantum dot–fullerene hybrid nanocomposite for solar energy conversion: Electron transfer and photoelectrochemistry," *ACS Nano*, vol. 5, no. 12, pp. 9421–9427, 2011.

[54] T. J. Meyer, G. J. Meyer, B. W. Pfennig, J. R. Schoonover, C. J. Timpson, J. F. Wall, C. Kobusch, X. Chen, and B. M. Peek, "Molecular-level electron transfer and excited state assemblies on surfaces of metal oxides and glass," *Inorganic Chemistry*, vol. 33, no. 18, pp. 3952–3964, 1994.

[55] S. Thyagarajan, E. Galoppini, P. Persson, J. M. Giaimuccio, and G. J. Meyer, "Large footprint pyrene chromophores anchored to planar and colloidal metal oxide thin films," *Langmuir*, vol. 25, no. 16, pp. 9219–9226, 2009.

[56] H. E. A. Ali, A. Altındal, S. Altun, and Z. Odabaş, "Highly efficient dye-sensitized solar cells based on metal-free and copper (II) phthalocyanine bearing 2-phenylphenoxy moiety," *Dyes and Pigments*, vol. 124, pp. 180–187, 2016.

[57] M. Ince, J.-H. Yum, Y. Kim, S. Mathew, M. Grätzel, T. Torres, and M. K. Nazeeruddin, "Molecular engineering of phthalocyanine sensitizers for dye-sensitized solar cells," *The Journal of Physical Chemistry C*, vol. 118, no. 30, pp. 17 166–17 170, 2014.

[58] X. Zhao and M. Wang, "Organic hole-transporting materials for efficient perovskite solar cells," *Materials Today Energy*, vol. 7, pp. 208–220, 2018.

[59] X. Yang, H. Wang, B. Cai, Z. Yu, and L. Sun, "Progress in hole-transporting materials for perovskite solar cells," *Journal of Energy Chemistry*, 2018.

[60] PlasmaChem, GmbH, "CdSe/ZnS hydrophobic QDs home page," accessible at: www.plasmachem.com.

[61] K. Stranius, L. George, A. Efimov, T.-P. Ruoko, J. Pohjola, and N. V. Tkachenko, "Photophysical study of a self-assembled donor-acceptor two-layer film on TiO_2," *Langmuir*, vol. 31, no. 3, pp. 944–952, 2015.

[62] J.-F. Nierengarten, A. Herrmann, R. R. Tykwinski, M. Rüttimann, F. Diederich, C. Boudon, J.-P. Gisselbrecht, and M. Gross, "Methanofullerene molecular scaffolding: Towards C_{60}-substituted poly(triacetylenes) and expanded radialenes, preparation of a C_{60}-C_{70} hybrid derivative, and a novel macrocyclization reaction," *Helvetica Chimica Acta*, vol. 80, no. 1, pp. 293–316, 1997.

[63] M.-E. Ragoussi, J.-J. Cid, J.-H. Yum, G. de la Torre, D. Di Censo, M. Grätzel, M. K. Nazeeruddin, and T. Torres, "Carboxyethynyl anchoring ligands: A means to improving the efficiency of phthalocyanine-sensitized solar cells," *Angewandte Chemie International Edition*, vol. 51, no. 18, pp. 4375–4378, 2012.

[64] O. Ito and F. D'Souza, "Recent advances in photoinduced electron transfer processes of fullerene-based molecular assemblies and nanocomposites," *Molecules*, vol. 17, no. 5, pp. 5816–5835, 2012.

[65] H. Imahori and Y. Sakata, "Fullerenes as novel acceptors in photosynthetic electron transfer," *European Journal of Organic Chemistry*, vol. 1999, no. 10, pp. 2445–2457, 1999.

[66] J. A. Anta, E. Guillen, and R. Tena-Zaera, "ZnO-based dye-sensitized solar cells," *The Journal of Physical Chemistry C*, vol. 116, no. 21, pp. 11 413–11 425, 2012.

[67] Q. Zhang, C. S. Dandeneau, X. Zhou, and G. Cao, "ZnO nanostructures for dye-sensitized solar cells," *Advanced Materials*, vol. 21, no. 41, pp. 4087–4108, 2009.

[68] H. Saarenpää, E. Sariola-Leikas, A. P. Perros, J. M. Kontio, A. Efimov, H. Hayashi, H. Lipsanen, H. Imahori, H. Lemmetyinen, and N. V. Tkachenko, "Self-assembled porphyrins on modified zinc oxide nanorods: Development of model systems for inorganic–organic semiconductor interface studies," *J. Phys. Chem. C*, vol. 116, no. 3, pp. 2336–2343, 2012.

[69] P. J. Cameron and L. M. Peter, "Characterization of titanium dioxide blocking layers in dye-sensitized nanocrystalline solar cells," *The Journal of Physical Chemistry B*, vol. 107, no. 51, pp. 14 394–14 400, 2003.

[70] C. Jiang, W. L. Koh, M. Y. Leung, W. Hong, Y. Li, and J. Zhang, "Influences of alcoholic solvents on spray pyrolysis deposition of TiO_2 blocking layer films for solid-state dye-sensitized solar cells," *Journal of Solid State Chemistry*, vol. 198, pp. 197–202, 2013.

[71] X. Li, B. Xu, P. Liu, Y. Hu, L. Kloo, J. Hua, L. Sun, and H. Tian, "Molecular engineering of d–a–π–a sensitizers for highly efficient solid-state dye-sensitized solar cells," *Journal of Materials Chemistry A*, vol. 5, pp. 3157–3166, 2017.

[72] B.-J. Li, L.-J. Huang, N.-F. Ren, and M. Zhou, "Titanium dioxide-coated fluorine-doped tin oxide thin films for improving overall photoelectric property," *Applied Surface Science*, vol. 290, pp. 80–85, 2014.

[73] W. Ke, G. Fang, J. Wang, P. Qin, H. Tao, H. Lei, Q. Liu, X. Dai, and X. Zhao, "Perovskite solar cell with an efficient TiO_2 compact film," *ACS Applied Materials & Interfaces*, vol. 6, no. 18, pp. 15 959–15 965, 2014.

[74] J. N. Hart, D. Menzies, Y.-B. Cheng, G. P. Simon, and L. Spiccia, "TiO_2 sol–gel blocking layers for dye-sensitized solar cells," *Comptes Rendus Chimie*, vol. 9, no. 5-6, pp. 622–626, 2006.

[75] S. Sansongsiri, T. Kaewmanee, D. Boonyawan, L. D. Yu, and S. Thongtem, "Effect of titanium dioxide blocking layer deposited by cathodic arc plasma on the energy conversion efficiency of dye-sensitized solar cells," *Surface and Coatings Technology*, vol. 306, pp. 257–261, 2016.

[76] J.-J. Huang, S.-P. Chiu, M.-J. Wu, and C.-F. Hsu, "Effect of titanium oxide compact layer in dye-sensitized solar cell prepared by liquid-phase deposition," *Applied Physics A*, vol. 122, no. 11, p. 971, 2016.

[77] U. Bach, D. Lupo, P. Comte, J. E. Moser, F. Weissörtel, J. Salbeck, H. Spreitzer, and M. Grätzel, "Solid-state dye-sensitized mesoporous TiO_2 solar cells with high photon-to-electron conversion efficiencies," *Nature*, vol. 395, no. 6702, p. 583, 1998.

[78] S. Ito, P. Liska, P. Comte, R. Charvet, P. Péchy, U. Bach, L. Schmidt-Mende, S. M. Zakeeruddin, A. Kay, M. K. Nazeeruddin *et al.*, "Control of dark current in photoelectrochemical ($TiO_2/I^- - I^{3-}$) and dye-sensitized solar cells," *Chemical Communications*, no. 34, pp. 4351 – 4353, 2005.

[79] B. C. O'Regan, J. R. Durrant, P. M. Sommeling, and N. J. Bakker, "Influence of the $TiCl_4$ treatment on nanocrystalline TiO_2 films in dye-sensitized solar cells. 2. Charge density, band edge shifts, and quantification of recombination losses at short circuit," *The Journal of Physical Chemistry C*, vol. 111, no. 37, pp. 14 001 – 14 010, 2007.

[80] T.-H. Wang, A. M. Navarrete-López, S. Li, D. A. Dixon, and J. L. Gole, "Hydrolysis of $TiCl_4$: Initial steps in the production of TiO_2," *The Journal of Physical Chemistry A*, vol. 114, no. 28, pp. 7561 – 7570, 2010.

[81] R. Esposito, C. Altucci, and R. Velotta, "Analysis of simulated fluorescence intensities decays by a new maximum entropy method algorithm," *J. Fluorescence*, vol. 23, no. 1, pp. 203 – 211, 2013.

[82] A. A. Maskevich, V. I. Stsiapura, and P. T. Balinski, "Analysis of fluorescence decay kinetics of thioflavin t by a maximum entropy method," *J. Appl. Spectroscopy*, vol. 77, no. 2, pp. 194 – 201, 2010.

[83] N. Song, H. Zhu, S. Jin, W. Zhan, and T. Lian, "Poisson-distributed electron-transfer dynamics from single quantum dots to C_{60} molecules," *ACS Nano*, vol. 5, no. 1, pp. 613 – 621, 2011.

[84] A. J. Morris-Cohen, M. T. Frederick, L. C. Cass, and E. A. Weiss, "Simultaneous determination of the adsorption constant and the photoinduced electron transfer rate for a CdS quantum dot – viologen complex," *J. Am. Chem. Soc.*, vol. 133, no. 26, pp. 10 146 – 10 154, 2011.

[85] S. Sadhu, M. Tachiya, and A. Patra, "A stochastic model for energy transfer from CdS quantum dots/rods (donors) to nile red dye (acceptors)," *J. Phys. Chem. C*, vol. 113, no. 45, pp. 19 488 – 19 492, 2009.

[86] H. Lehtivuori, A. Efimov, H. Lemmetyinen, and N. V. Tkachenko, "Distributed decay kinetics of charge separated state in solid film," *Chemical Physics Letters*, vol. 437, no. 4-6, pp. 238 – 242, 2007.

[87] Solaronix SA, "Solaronix materials," accessible at: shop.solaronix.com.

[88] H. Němec, J. Rochford, O. Taratula, E. Galoppini, P. Kužel, T. Polívka, A. Yartsev, and V. Sundström, "Influence of the electron-cation interaction on electron mobility in dye-sensitized ZnO and TiO_2 nanocrystals: A study using ultrafast terahertz spectroscopy," *Physical Review Letters*, vol. 104, p. 197401, May 2010.

[89] H. Hakola, E. Sariola-Leikas, A. Efimov, and N. V. Tkachenko, "Effect of hole transporting material on charge transfer processes in zinc phthalocyanine sensitized ZnO nanorods," *J. Phys. Chem. C*, vol. 120, no. 13, pp. 7044 – 7051, 2016.

Publications

Publication I

Kirsi Virkki, Sinem Demir, Helge Lemmetyinen, and Nikolai V. Tkachenko. Photoinduced Electron Transfer in CdSe/ZnS Quantum Dot–Fullerene Hybrids, *Journal of Physical Chemistry C*, vol. 119, no. 31, pp. 17561–17572, 2015.

THE JOURNAL OF PHYSICAL CHEMISTRY C

Article

pubs.acs.org/JPCC

Photoinduced Electron Transfer in CdSe/ZnS Quantum Dot−Fullerene Hybrids

Kirsi Virkki,* Sinem Demir, Helge Lemmetyinen, and Nikolai V. Tkachenko*

Department of Chemistry and Bioengineering, Tampere University of Technology, P. O. Box 541, FI33101 Tampere, Finland

Supporting Information

ABSTRACT: Photoinduced electron transfer (ET) in CdSe/ZnS core−shell quantum dot (QD) − fullerene (COOH−C_{60}) hybrids was studied by the means of time-resolved emission and absorption spectroscopy techniques. A series of four QDs with emission in the range 540−630 nm was employed to investigate the dependence of the electron transfer rate on the QD size. Emission of the QDs is quenched upon hybrid formation, and the quenching mechanism is identified as photoinduced electron transfer from the QD to the fullerene moiety due to the fullerene anion signature observed in transient absorption. In order to obtain quantitative information on the ET reaction, several kinetic data analysis techniques were used, including a conventional multiexponential fitting and a maximum entropy method for emission decay analysis, as well as a distributed decay model based on the Poisson distribution of fullerenes in the hybrids. The latter gradually simplifies the interpretation of the transient absorption spectra and indicates that the spectra of QD cations are essentially similar to those of neutral QDs, differing only by a minor decrease in the intensity and broadening. Furthermore, only a minor decrease in the ET rate with the increasing QD size was observed, the time constants being in the range 100−200 ps for all studied QDs. The charge recombination is extended to 10 ns or longer for all hybrids.

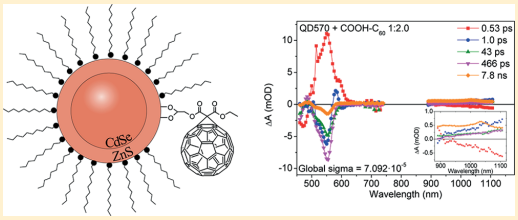

INTRODUCTION

The interest in semiconductor quantum dots (QD) rises rapidly due to their advanced photophysical properties and the possibility to relatively simply tune their key characteristics in order to better suit the requirements of various applications, ranging from solar cells[1] and light emitting devices[2] to molecular[3] and ion sensors.[4] Even greater functionality and flexibility can be achieved by combining QDs with organic dyes to form hybrids with advanced photoinduced energy or electron transfer properties.[5−9] One essential advantage of such hybrid systems is the possibility to tune the energetics of the electron transfer reaction by simply changing the QD size, which means that the same synthetic routes could potentially be used to produce electron donating and electron accepting QDs with respect to an organic counterpart and thus control the direction of the transfer.

One of the most widely used types of quantum dots are CdSe QDs and their core−shell modifications. They are available commercially in a range of sizes corresponding to virtually any emission wavelength in the visible part of the spectrum. They are characterized by emission quantum yields of 50% and higher, and long lifetimes of the excited state, typically greater than 20 ns. The photodynamics of these QDs have been intensively studied by time-resolved spectroscopy methods.[10,11] The studies have shown that a number of important processes take place at early times of the excitation relaxation, including exciton thermalization in the subpicosecond time domain and electron or hole trapping in a few tens of picoseconds. The latter is one of the possible reasons reducing the emission quantum yield, and in many cases, it is attributed to surface defects. The defects are not present in each QD and there can be different defects in different QDs, which makes virtually all QD samples heterogeneous. In fact, for high quality QDs, only a minor part of QDs have such defects, but since there is always a distribution of sizes and shapes, some heterogeneity remains, which also affects the electronic properties of the QDs.

Another important advantage of the QD−organic hybrid approach is the relative simplicity of the hybrid assembly. The organic counterpart has to be provided with a proper binding group, such as thiol or carboxyl in the case of CdSe QDs, and the complex formation takes place spontaneously in solutions.[5−7,9] A downside of this approach is the statistical nature of the hybrid formation, resulting in a distribution of hybrids with different number of organic ligands per QD.

Examples of successful formation of CdSe QD-organic hybrids with photoinduced electron transfer properties include QD−fullerene,[6,9,12] QD−anthraquinone,[13,14] QD−Co(III),[15,16] and QD−rhodamine[5] complexes. In the three former cases, the QD acts as an electron donor, and in the latter as an electron acceptor, though there are competing energy transfer reactions. The electron transfer was studied by time-resolved spectrosco-

Received: May 4, 2015
Revised: July 5, 2015
Published: July 8, 2015

DOI: 10.1021/acs.jpcc.5b04251
J. Phys. Chem. C 2015, 119, 17561−17572

py techniques, and considering the rather strong spectroscopic responses of the QDs, monitoring the changes in QD emission or absorption behavior upon addition of organic molecules is a typical approach to study the photoinduced interactions between the QDs and organic dyes. This, however, leaves questions on the distinguishing between the charge and energy transfer reactions, as well as on the determination of the lifetime of the charge separated state, as spectral properties of the charged QDs are not well studied.

This study is devoted to QD-fullerene hybrids (schematically presented in Figure 1) where the QD acts as an electron donor

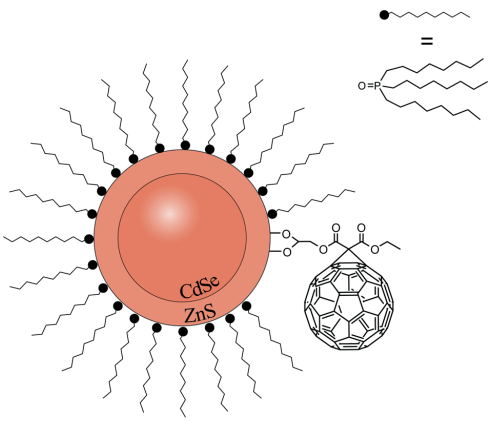

Figure 1. Schematic presentation of a 1:1 QD−COOH−C_{60} hybrid.

and the fullerene moiety as an electron acceptor. Unlike in the previous QD-fullerene hybrid studies,[6,9] core−shell QDs were used as they are more stable, better protected from the capping agent effects, and have a higher emission quantum yield compared to core-only QDs. The core−shell QDs have been used previously in hybrid structures with different dyes, and efficient photoinduced electron transfer was reported for a variety of systems.[12,13,15,16] Also, a decrease in the electron transfer rate with an increase in the shell thickness was studied, and a damping factor of 0.35 $Å^{-1}$ was reported for the charge separation rate.[13] Within this study, QDs with 6 Å shell thickness were used, which may lead to a 5−10 times deceleration of the photoinduced electron transfer compared to core-only QDs, though direct comparison is complicated by the fact that the shell-free QDs have a higher density of defects, which reduces the efficiency of the electron transfer.

The study is aimed at (1) a careful analysis of the fullerene transient absorption response, and (2) attempting to evaluate the spectra of positively charged CdSe/ZnS core−shell QDs. A set of four QDs was used to compare the dependence of the charge separation and recombination time constants on the QD size. The band gap of the QDs decreases as the QD size increases, which leads to a smaller energy difference between the quantum dot conduction band (CB) and the fullerene LUMO level (see Figure 2) for the larger QDs, and therefore, a reduced driving force for the electron transfer. Previous studies with core-only CdSe QD−C_{60} hybrids have shown[6] that the electron transfer rate indeed decreases with the increasing QD size. Electron transfer reactions have been demonstrated in several CdSe/ZnS core−shell QD−C_{60} hybrids,[9,17−19] but to the best of our knowledge, no detailed analysis of the QD size

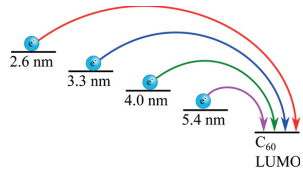

Figure 2. Schematic representation of the conduction band energies for the studied QDs compared to the LUMO level of fullerene. The QD core diameters are taken from ref 20. The driving force for the electron transfer decreases as the QD size increases.

dependence on the ET kinetics in such core−shell QD−fullerene systems has been reported.

The investigation was carried out using two complementary methods allowing to monitor the QD emission decays with a picosecond time resolution and the transient absorption of the whole hybrid with a femtosecond time resolution.

METHODS AND MATERIALS

Materials. Core−shell CdSe/ZnS quantum dots were purchased from PlasmaChem GmbH. According to the manufacturer, the QDs consist of a spherical CdSe core capped with an epitaxial ZnS shell of ca. 0.6 nm thickness.[20] The QDs are capped with trioctylphosphine oxide (TOPO) and they are dispersible in nonpolar organic solvents. Four different QD sizes with different emission wavelengths (emission maxima at approximately 540, 570, 600, and 630 nm) were utilized.

Synthesis of the fullerene derivative (COOH−C_{60}) used in this study was described elsewhere.[21,22] The QD−fullerene hybrids were assembled using a fullerene derivative with a carboxylic acid functionalization for binding. The carboxylic acid binding has been utilized in QD−organic hybrids by e.g. Zhu et al.[13] Thus, the carboxylic acid binding is assumed to be rather stable.

Sample Preparation. The QDs were supplied as a powder. They were dispersed in hexane in 5 to 20 μM concentrations for steady-state and transient absorption measurements, respectively.

QD−COOH−C_{60} complexes were prepared by adding COOH−C_{60} solution (0.55 mM in $CHCl_3$) into the QD dispersion under vigorous stirring in a series of different concentrations. The final COOH−C_{60} concentrations were calculated from the estimated QD molar absorption coefficients in order to yield QD−COOH−C_{60} ratios from 1:0.5 to 1:2.

Steady-State Spectroscopy. The UV−vis absorption spectra of the QD−COOH−C_{60} hybrids were measured with a Shimadzu UV-3600 UV−vis-NIR spectrophotometer. The fluorescence emission spectra were recorded with an ISA−Jobin Yvon−SPEX−Horiba Fluorolog-3-111 fluorometer. The raw signals were corrected using an instrument response function provided by the manufacturer.

Time-Correlated Single Photon Counting. The fluorescence lifetimes were measured using a time-correlated single photon counting (TCSPC) system by PicoQuant GmbH. The TCSPC system consists of a PicoHarp controller and a PDL-800-B driver. The samples were excited by a pulsed laser diode (LDH-P-C-485) at 483 nm. Fluorescence decays were monitored at the emission maxima of the quantum dots. Time resolution of the TCSPC system was approximately 120 ps.

DOI: 10.1021/acs.jpcc.5b04251
J. Phys. Chem. C 2015, 119, 17561−17572

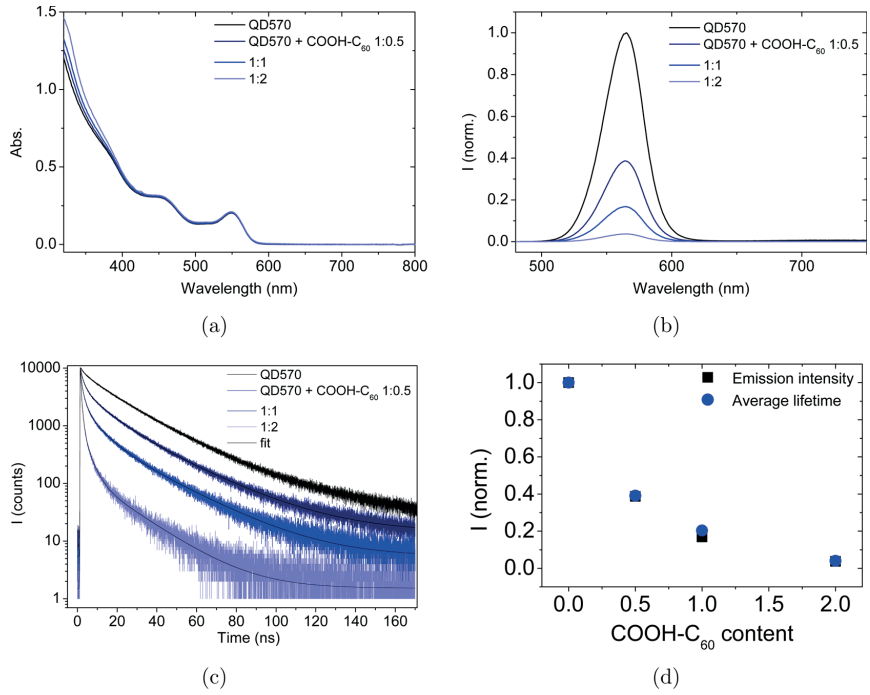

Figure 3. (s) Absorption and (b) emission spectra, (c) fluorescence decay curves and (d) the decrease of the emission intensity as well as the average fluorescence lifetime as a function of the fullerene content for the QD570 and QD570−COOH−C_{60} hybrids.

Transient Absorption Spectroscopy. The transient absorption spectroscopy measurements were carried out using a femtosecond pump−probe system. A Libra F laser system (Coherent Inc.) was used to create fundamental light pulses at 800 nm at a repetition rate of 1 kHz. The pulse energy was 1 mJ, and the pulse duration was approximately 100 fs. The fundamental beam was split in two, and the majority of the beam energy (roughly 90%) was directed to a Topas C optical parametric amplifier (Light Conversion Ltd.) to produce excitation pulses at the desired wavelength. The rest of the fundamental beam was delivered to a white continuum generator (sapphire crystal) for sample probing. The probe beam was split in two to record reference and signal responses. The measurement system (ExciPro, CDP Inc.) was equipped with a silicon CCD array for measurements in the visible part of the spectrum, and an InGa diode array for the near-infrared (NIR) wavelengths. The measurements were carried out by comparing responses with and without excitation using a chopper synchronized with the fundamental laser pulses. The spectra were typically acquired by recording 5000 shots, i.e. averaging over 5 s. Excitation energies were sufficiently low to avoid multiple exciton generation; this was verified by recording a series of measurements with different excitation energies for the same sample. No excitation energy dependence of the response was observed. Two wavelength ranges were recorded: visible (460−740 nm) and NIR (880−1100 nm).

Analysis of Time Resolved Spectroscopy Data. The time-resolved data, transient absorption and emission decays, were first fitted to a sum of exponentials. The exponential functions were convoluted with the instrument response function to improve the accuracy of the fits at short delay times. Typically, the fitting procedure was started with a reasonably small number of exponents and then increasing the number as long as the fit goodness, the σ-value, was improved by at least 10%.

For the emission decays, as many as four exponents were needed in the fits for reasonable fit goodness. Since there was no clear discrimination criteria for the number of exponents to be used for data fitting, and since the studied systems were intrinsically heterogeneous, the emission decays were additionally fitted using the so-called maximum entropy method (MEM).[23,24] This method aims at extracting a decay lifetime distribution with the smallest number of components. The emission decay is presented as

$$I(t) = \int_0^\infty p(\tau) \mathrm{e}^{-t/\tau}\, \mathrm{d}\tau \tag{1}$$

where τ is the lifetime and $p(\tau)$ is the probability density to find a decay with the lifetime τ, which is adjusted to minimize the function

$$S = \int_0^\infty (p(\tau) - p(\tau) \ln p(\tau))\, \mathrm{d}\tau \tag{2}$$

but keeping the value of the weighted mean square deviation, χ^2, close to unity. A homemade program implementing the algorithm proposed by Velotta et al.[23] was used for this data analysis. For all the presented results, the χ^2 was in the range 0.99−1.05.

A global fit was applied to the transient absorption data to obtain the so-called decay component spectra, that were used

DOI: 10.1021/acs.jpcc.5b04251
J. Phys. Chem. C 2015, 119, 17561−17572

Table 1. QD Core Diameters (ϕ_{core}), Molar Masses (M), Measured Band Edge Absorption Maxima (λ_{abs}), Estimated Molar Absorption Coefficients (ε), Measured Emission Wavelengths (λ_{em}), and Fluorescence Quantum Yields (Φ_F) for the Studied Series of QDs

sample	ϕ_{core} [a] [nm]	M [a] [Da]	λ_{abs} [nm]	ε [M^{-1} cm^{-1}]	λ_{em} [nm]	Φ_F [%]
QD540	2.6	59 000	521	12 000	541	23
QD570	3.3	93 000	550	40 400	565	37
QD600	4.0	173 000	592	33 800	605	11
QD630	5.4	375 000	619	120 900	634	28

[a]According to manufacturer specifcations.

to identify the transient states. The method is described elsewhere.[25,26] Briefly, the decays at all wavelengths were fitted to a sum of exponents with the same time constants, but the pre-exponential factors were allowed to vary from wavelength to wavelength. A home-written program was used for this type of data analysis. However, the multiexponential fitting has no physical meaning in this case. To distinguish between contributions from different processes and reactions overlapping in time, a model describing the photophysics of QD−COOH−C_{60} hybrids more realistically has to be used. There are two main goals for using this more realistic model: (1) better separation of the C_{60}^- signal in the NIR part of the spectrum and (2) distinguishing the spectral features of QD cations from those of excited QDs.

The first problem in developing a physically meaningful model is the simultaneous formation of hybrids with different QD−fullerene ratios. The proportion between the different hybrids is described reasonably well by Poisson statistics:[17,27,28]

$$p_n = \frac{c^n}{n!}e^{-c} \tag{3}$$

where n is the number of fullerene molecules in the hybrid, p_n is the probability to find a hybrid with n fullerenes, and c is the relative molar concentration of fullerenes. We will assume that the Poisson statistics hold in this case and no free COOH−C_{60} is left in the dispersion. The second assumption is that the electron transfer time constant is inversely proportional to the number of fullerenes in the hybrid, i.e. τ_{ET}/n, where τ_{ET} is the ET time constant in a 1:1 hybrid (the so-called "intrinsic" ET time constant). Now we need to sum the decays with different rates and account for the different concentrations in different hybrids, which was shown to yield[28]

$$A(t, c) = A_0 \exp[-t/\tau_0 - c(1 - e^{-t/\tau_{ET}})] \tag{4}$$

where τ_0 is the lifetime of a nonhybridized QD and A_0 is a constant determined by the initial population of the excited state. This model has the apparent drawback of predicting a monoexponential decay for QDs without fullerenes ($c = 0$), which is not correct due to the intrinsic heterogeneity of the QD sample caused by the surface defects and the distribution of QD sizes (see Figure 3c for the fluorescence decay curve of the QDs). There are QDs with long lifetime (≥20 ns), but also QDs with a much shorter lifetime, resulting in a more complex emission decay profile. In the first approximation, the surface traps can be considered in a similar manner assuming Poisson distribution for the traps and a constant quenching time constant, τ_t, for a quantum dot with a single trap. Then one can write[28]

$$A(t, c, c_t) = A_0 \exp[-t/\tau_0 - c_t(1 - e^{-t/\tau_t}) - c(1 - e^{-t/\tau_{ET}})] \tag{5}$$

where c_t is the relative concentration of traps. This model does not account for the thermal relaxation in case of excitation at a wavelength shorter than the lowest energy absorption band of the QD. According to our preliminary multiexponential fittings, this process is much faster than all the others, and will be accounted for by an additional exponent with a (short) time constant τ_1. Next, the transient absorption decay of QDs only was fitted to $A_1 \exp(-t/\tau_1) + A_0 \exp[-t/\tau_0 - c_t(1 - e^{-t/\tau_t})]$ at the wavelength corresponding to the lowest energy absorption band. This gives an estimation for τ_0, τ_1, τ_t, and c_t. Finally, we fit the transient absorption decay of QD−COOH−C_{60} to eq 5 plus $\exp(-t/\tau_1)$ and $\exp(-t/\tau_{CR})$ to determine τ_{ET}, c, and the charge recombination time constant, τ_{CR}.

RESULTS AND DISCUSSION

The interactions between QDs and COOH−C_{60} were investigated both by steady-state and time-resolved spectroscopic methods. The absorption and emission spectra for the studied quantum dots can be found in the Supporting Information. Table 1 summarizes their basic spectroscopic properties. It has to be noted that the molar absorption coefficients (ε) presented in Table 1 are rather rough estimations. The ε values were estimated using the average molar weights provided by the QD manufacturer;[20] concentrations of the measured QD dispersions were calculated according to the weighed masses and these molar weights. The molar absorption coefficients were then estimated using the measured absorbance data. Thus, any error in either the estimated molar weight or in weighing the QD powder might result in errors in the ε values. The CdSe core diameters presented in Table 1 were estimated by the QD manufacturer according to the procedure reported by Yu et al.[29] All QDs had ca. 0.6 nm ZnS shell according to the manufacturer specification.

Typical of highly monodisperse colloidal QDs, the emission spectra for all QDs are narrow, with fwhm less than 40 nm. The Stokes shifts for the different quantum dots range from 10 to 20 nm, and the measured emission maxima are very close to those reported by the manufacturer. Fluorescence quantum yields (Φ_F) of the QDs were determined using Rhodamine 6G (Rh6G, 8 μM in EtOH; $\Phi_F = 0.98$) as a standard compound. The QDs were dispersed in hexane in ca. 1 μM concentration, and the samples were excited at the intersection of sample and Rh6G absorptions. The absorption and emission spectra for the Φ_F measurements can be found in the Supporting Information. Despite the fact that the emission spectra are narrow, the fluorescence quantum yields remain under 40% for all QD sizes. In fact, only the QDs with the emission maximum at 570 nm (QD570) showed a Φ_F value greater than 30%. The fluorescence quantum yields are higher than for core-only QDs, where the surface defects suppress the emission, but fairly low in comparison with other core−shell QDs; the most

DOI: 10.1021/acs.jpcc.5b04251
J. Phys. Chem. C 2015, 119, 17561−17572

Table 2. Fluorescence Lifetimes (τ_i) and Relative Pre-Exponential Factors (A_i) as Well as the Average Lifetimes (τ_{av}) for the QD570 and QD570−COOH−C_{60} Hybrids

QD−COOH−C_{60} ratio	τ_1 [ns]	A_1 [%]	τ_2 [ns]	A_2 [%]	τ_3 [ns]	A_3 [%]	τ_4 [ns]	A_4 [%]	τ_{av} [ns]
1:0	0.14	45.1	4.40	13.5	20.0	39.5	67.8	2.0	9.91
1:0.5	0.12	57.6	2.01	22.5	11.0	12.5	26.6	7.4	3.87
1:1	0.18	63.5	1.63	25.1	7.86	7.7	24.4	3.7	2.02
1:2	0.086[a]	79.5	0.80	17.2	3.52	2.7	18.4	0.5	0.39

[a]On the time resolution limit of the measurement.

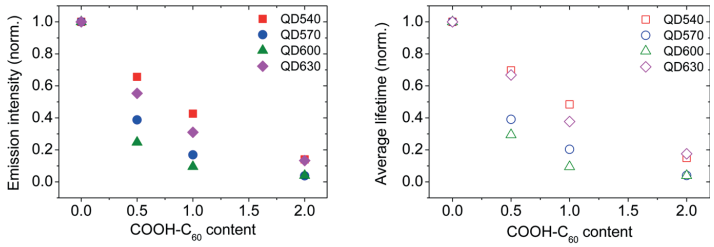

Figure 4. Decrease of (a) emission intensity and (b) average lifetime as a function of the fullerene content for the different QD−COOH−C_{60} hybrids.

sophisticated synthesis methods result in QDs with Φ_F values higher than 50%, and even approaching unity.[13,30−32] Therefore, suspicions about an incomplete surface passivation by the ZnS shell arise. This would lead to surface traps of some kind and therefore to a reduced emission intensity. However, the broad, red-shifted surface trap emission typical of core-only QDs is not observed.[13]

Titration of QDs with COOH−C_{60}. The QD−COOH−C_{60} hybrids were prepared using a carboxylic acid functionalized fullerene derivative (see Figure 1). Upon addition of COOH−C_{60} to a QD dispersion, fullerene molecules bind on the QD surface through the COOH group, partly replacing the weakly bound native trioctylphosphine oxide (TOPO) ligands. Since the carboxyl group is a stronger ligand than TOPO, we expect that there are no free fullerenes left in the dispersion. As reported for several core-only QDs,[33−37] the capping agent itself may have drastic effects on the photophysical properties of QDs. Therefore, in order to investigate the effect of the COOH group on the QD emission intensity, stearic acid was added to a dispersion of QDs, and the emission spectra and lifetimes of the QD−stearic acid complexes were measured. No noticeable changes in either emission spectra, quantum yields or lifetimes were detected up to 1:100 relative concentration of stearic acid.

The effect of COOH−C_{60} on the quantum dot emission intensity was investigated in so-called titration experiments. In a typical titration, COOH−C_{60} solution was added into the QD dispersion in three different relative concentrations (QD−COOH−C_{60} molar ratios ranging from 1:0 to 1:2). For each sample, steady state absorption and emission spectra as well as emission decays were measured. The excitation wavelength (440 nm) for the emission measurements was chosen to be at a local minimum of COOH−C_{60} absorption in order to minimize direct excitation of the C_{60} moiety. The decrease in the integrated emission intensity as well as in average emission lifetimes were recorded.

Figure 3 shows the absorption and emission spectra as well as the fluorescence lifetimes for the titration of QD570. The absorbance of the fullerene moiety is relatively small compared to the QD absorbance over the majority of the measured wavelength range; however, at wavelengths shorter than 400 nm, the fullerene absorbance gets more pronounced. The absorption spectrum of the hybrid is a superposition of the QD and fullerene absorbances, which suggests that there are no ground state interactions between the moieties. The effect of the COOH−C_{60} on the emission intensity and the fluorescence lifetime is, however, drastic. Adding COOH−C_{60} in a 1:0.5 molar ratio already quenches the emission of the QDs down to ca. 40% of the original value. With the 1:2 molar ratio, the emission intensity is reduced down to less than 10% of the initial value. Assuming that the residual emission intensity describes the amount of QDs left without any fullerenes,[27] the quenching is somewhat stronger than expected. This discrepancy can be explained by the fact that the QD concentrations, and therefore, the QD−COOH−C_{60} molar ratios, are only rough estimations.

Similar changes can be observed in the time-resolved measurements. The emission decay curves for QD570 and the corresponding hybrids are shown in Figure 3, and the fitting results are summarized in Table 2. It has to be noted that for the QDs only already, the emission decay is not mono-exponential. Thus, a multiexponential fitting model was used, and up to four exponents were needed to obtain a reasonable fit (χ^2-value close to one). In addition to the individual lifetime components, average lifetimes were calculated for each QD−COOH−C_{60} molar ratio using the fit data. The average lifetimes are also presented in Table 2. To get more insight into QD and hybrid photophysics, the emission decay data were analyzed by another approach as well, the maximum entropy method (MEM). The results of this analysis will be discussed later. The general trend is, however, shortening of the lifetimes as the fullerene content in the hybrid increases.

The emission quenching is essentially similar for the other QD sizes. Figure 4 summarizes the decrease in the integrated emission intensities as well as the average lifetimes as a function of the COOH−C_{60} concentration for all QD sizes. No apparent trend of the quenching efficiency dependence on the QD size

DOI: 10.1021/acs.jpcc.5b04251
J. Phys. Chem. C 2015, 119, 17561−17572

was observed. There are at least two reasons for this. First, the concentrations of QDs were calculated based on the estimated molar masses provided by the QD manufacturer, and thus they are assumed to be rather inaccurate. Second, for any QD size, a 2-fold excess of COOH−C_{60} is enough to bring the emission intensity down by at least 80% from the original value. This indicates that as soon as the hybrid is formed, the emission efficiency and lifetime are dropped down by more than an order of magnitude, and the static quenching rather reflects the concentration ratio than the efficiency of the interaction between the QD and fullerene in the hybrids. Absorption and emission spectra as well as fluorescence decay curves for all the QD−COOH−C_{60} titrations can be found in the Supporting Information.

Evidently, the use of a four-exponential fitting has no clear justification and does not provide much information on the processes taking place during the excitation relaxation. It is widely accepted that a distribution of lifetimes is expected for heterogeneous systems like QD−COOH−C_{60} hybrids. Therefore, the maximum entropy method (MEM) was used to analyze the emission decays.[23,24] A series of 100 lifetimes distributed evenly in the logarithmic scale was used for the MEM analysis, and the results for the titration data for QD570 as well as the QD570−COOH−C_{60} hybrids are presented in Figure 5. First of all, for all samples there is a relatively sharp peak at 21 ns. This peak is attributed to nonquenched QDs without defects or any other imperfections, which could reduce the excited state lifetime. This peak decreases rapidly as the relative COOH−C_{60} concentration increases. The peak can be used as an indicator of the relative amount of nonhybridized QDs in the QD−COOH−C_{60} hybrid samples. Second, even for the QDs only, there is a sensible number of QDs with emission lifetimes much shorter than 21 ns. This can be seen directly from the decay curves of pure QDs that all have a faster decay at the beginning. To quantify this observation, one can divide the spectrum in two parts at 11 ns and calculate the relative intensity for the QDs with a lifetime shorter than this discrimination value. For QD570, the relative amount of the short-lived QDs is 35%. The short lifetime of these QDs is most probably due to different sorts of imperfections and defects, and this estimation suggests that from defect-free QDs the emission quantum yield would be 35% higher than that obtained from steady state emission measurements, i.e., it would be close to 50%. One can also notice that there is a distinct but minor band at 75 ns.

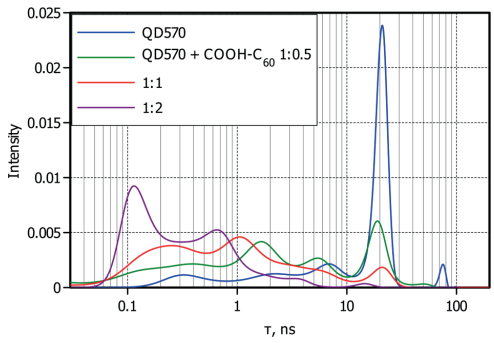

Figure 5. Emission decay distribution obtained from the MEM analysis for the QD570 and QD570−COOH−C_{60} hybrids.

Addition of COOH−C_{60} has a 2-fold effect on the lifetime spectrum. First, the number of free QDs decreases as mentioned above, and second, new bands with increasing intensities are formed at the short lifetime side. At the same time, there are no distinct peaks corresponding to the lifetimes of QD−COOH−C_{60} hybrids with a molar ratio 1:1, 1:2, and so on, which could be expected in the case of ideal hybrid structures. This can be interpreted in favor of a number of arrangements with different distances and orientations of QD−COOH−C_{60} complexes, and consequently a distribution of lifetimes for distinct complexes with the molar ratios 1:1, 1:2, etc. Qualitatively, the results presented in Figure 5 are consistent with the expectation: the increase of the fullerene concentration increases the relative amount of quenched QDs and reduces the lifetime of the dots.

Essentially the same results were obtained for the other QD sizes (see Supporting Information). In all cases, there is a peak at around 20 ns, the intensity of which decreases as the relative concentration of COOH−C_{60} increases, and the relative contribution of the short-lived part increases. Furthermore, the time resolution limit (roughly 100 ps) restricts the lifetime analysis as the strong peaks for the samples with high COOH−C_{60} concentration are found at this limit for all samples. Calculating the relative concentration of the short-lived QDs

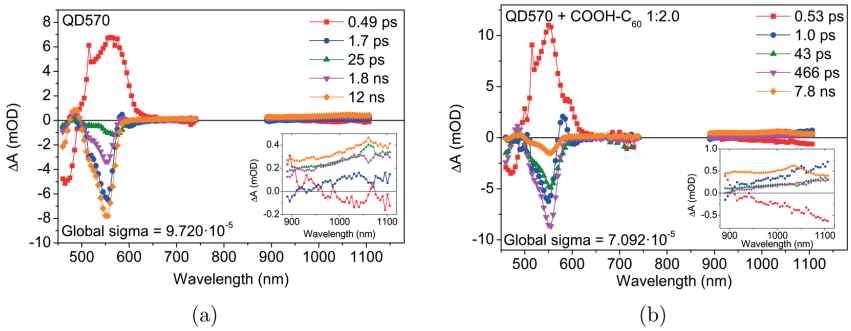

Figure 6. Transient absorption decay component spectra for the QD570 and QD570−COOH−C_{60} hybrid measured by the pump−probe method. Excitation wavelength is 440 nm.

DOI: 10.1021/acs.jpcc.5b04251
J. Phys. Chem. C 2015, 119, 17561−17572

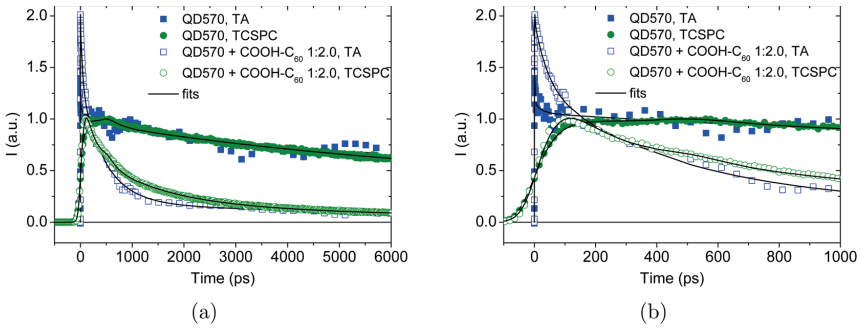

Figure 7. Transient absorption (TA) vs emission (TCSPC) decays for the QD570 and QD570−COOH−C_{60} hybrid. The transient absorption signals at 555 nm were inverted and scaled to match the normalized emission decays at 570 nm.

gives fluorescence quantum yields close to 50% from the defect-free QDs for all QD sizes.

Clearly, addition of the fullerene derivative into a QD dispersion has a drastic effect on the emission intensity and kinetics of the quantum dots. However, the only information we can get from the emission measurements is the relaxation kinetics of the QD excited state; no information on the relaxation mechanism is obtained. There are at least two possible relaxation pathways that result from the QD−COOH−C_{60} interaction: photoinduced electron transfer and energy transfer from the QD to the fullerene moiety. The emission measurements do not reveal any information on which relaxation pathways are active, and thus we need to turn into transient absorption measurements.

Transient Absorption Spectroscopy. Two wavelength ranges of interest for this study are around the ground state absorption of the QDs, which is 500−700 nm, and around 1000 nm, where one can expect to monitor formation and decay of the fullerene anion.[6,38,39] To couple the relaxation of the QD excitation with the anion formation, a global fit of the data in both ranges was done. The decay is nonexponential due to the surface defects in the QDs as well as the distribution of arrangements in the spatial organization of the QD−fullerene linkage. However, as the first step, a multiexponential fit was used, which required as many as five exponentials to achieve a reasonable fit goodness. Because of the nonexponential nature of the decay, the decay model utilizing the Poisson distribution of the hybrid formation was also implemented, and the results of this analysis will be discussed later.

Figure 6 shows the decay component spectra obtained from the transient absorption measurement of the QD570 as well as the QD570−COOH−C_{60} hybrid. For the quantum dots only (Figure 6(a)), the main spectral feature is the ground-state bleach (GSB) signal centered at 550 nm. The fastest decay component (0.49 ps) with an induced absorption at ca. 500−600 nm is attributed to the QD relaxation to the lowest excited state,[10,40,41] i.e. hot exciton cooling. This assumption is supported by the fact that the induced absorption is absent when the sample is excited directly at the first excitonic band (at 550 nm for QD570, see Figure S8 in Supporting Information).

The 1.7 ps component shows a recovery of the QD ground state absorption and some small induced absorption on the red side of the ground-state bleach band, that probably still shows a trace of the hot exciton cooling. The red-shifted absorption could as well result from fast trapping of the exciton. Similar features in the two shortest lifetime components are observed for QDs alone as well as the QD−COOH−C_{60} samples and will not be discussed further.

The rest of the components at the visible range describe the ground state bleach recovery. Noticeably, there is still a reasonable amount of the absorption left after several nanoseconds. The lifetime for the longest-living component (12 ns) exceeds the time window of our measurement system (ca. 6 ns), and thus it is rather inaccurate. In the NIR part of the spectrum, the signals are broad and featureless. There is a small induced absorption that decays with time together with the ground state bleach signal.

There are clear differences in the TA signals for the QD−COOH−C_{60} hybrid sample at delay times longer than a few picoseconds (TA decay component spectra shown in Figure 6b) when compared to the QDs only sample. First, the ground state bleach signal at the visible wavelengths recovers significantly faster in the QD570−COOH−C_{60} sample: the lifetimes describing the GSB recovery are shorter than for the QDs only sample, and the intensity of the longest-living decay component is much smaller for the QD570−COOH−C_{60} hybrid than for QD570. The second major difference is found in the NIR spectral region. There is a band centered at ca. 1040 nm, the formation of which is associated with the 43 ps component and that decays with the 7.8 ns time constant. This band is assigned to the fullerene radical anion (C_{60}^-).[6,21,38,39] The only feasible pathway leading to the C_{60}^- radical anion is through a photoinduced electron transfer from the excited quantum dot. Thus, the 43 ps decay component in Figure 6b describes the electron transfer from the QD to fullerene (photoinduced charge separation), and the 7.8 ns component the back electron transfer (charge recombination).

Given that the QD emission overlaps somewhat with the fullerene absorption, an energy transfer between these two moieties could be possible and would result in QD emission quenching as well. The energy transfer would yield the fullerene singlet excited state. The fullerene singlet state has a minor band around 1050 nm, that is less pronounced in intensity and shifted to the red compared to the anion radical. The signal for the singlet excited state can be difficult to discriminate from the C_{60}^- signal, if they cannot be observed separately.[26] However, the intersystem crossing is an effective pathway for the fullerene singlet excited state relaxation, and the energy transfer from the excited QD to the fullerene moiety would eventually lead to the formation of a fullerene triplet excited state, that should show an absorption in the 700−800 nm region.[42−44] However, no

DOI: 10.1021/acs.jpcc.5b04251
J. Phys. Chem. C 2015, 119, 17561−17572

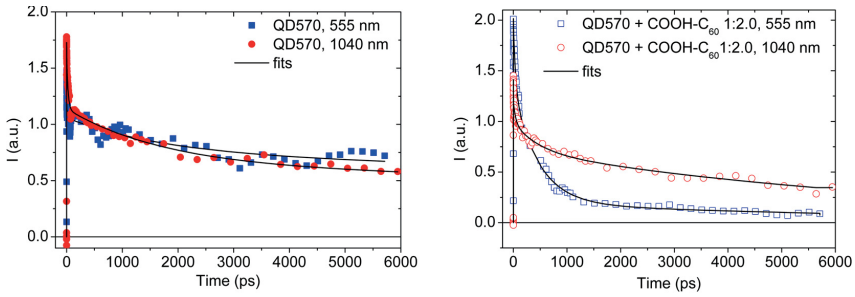

Figure 8. Transient absorption decays at 555 and 1040 nm for the QD570 and QD570−COOH−C_{60} hybrid. The transient decays at 555 nm were scaled and inverted for comparison.

Table 3. Estimated QD−C_{60} Molar Ratios, Fullerene Anion Formation Lifetimes ($\tau_{C_{60}^-}$), Intrinsic Electron Transfer Lifetimes (τ_{ET}), and Charge Recombination Lifetimes (τ_{CR}) for the Studied QD−COOH−C_{60} Hybrids

sample	QD−C_{60} ratio	$\tau_{C_{60}^-}$ [ps]	τ_{ET} [ps]	τ_{CR} [ns]	τ_{ET}(Poisson) [ps]	τ_{CR}(Poisson) [ns]
QD540	1:2.4	80	194	2.2	453	14
QD570	1:2.0	43	86	7.8	655	13
QD600	1:1.9	50	96	12	133	14
QD630	1:1.7	77	132	6.7	98	50

induced absorption bands were observed for any of the QD−COOH−C_{60} hybrid samples in this region, which led us to the conclusion that the QD excited state relaxes primarily through the photoinduced electron transfer to the fullerene, not through the energy transfer.

For the quantum dots alone, the ground state bleach recovery results from the depopulation of the singlet excited state of the QDs and repopulation of the ground state, and thus the GSB recovery rate should correspond to the emission decay rate measured by the TCSPC method. The transient absorption and TCSPC decays for QD570 are compared in Figure 7. Indeed, the TA decays correspond very well to the fluorescence emission decays for these QDs. For the QD570−COOH−C_{60} sample, the situation is more complex. The singlet excited state of the QD−COOH−C_{60} hybrid does not relax back to the ground state.Instead, the exited state relaxes yielding a charge-separated state (QD^+−C_{60}^-). Therefore, one could expect a different decay rate for the transient absorption and TCSPC signals. However, we observe that the GSB signal recovers together with the relaxation of the excited state (Figure 7).

It is well-known that electrons in the conduction band have a much stronger effect on the QD absorption spectrum than holes in the valence band,[27,40,41] which makes monitoring of the QD cations problematic. Instead, one can compare the transient absorption decays at 555 and 1040 nm for QDs only and QD−COOH−C_{60}, presented in Figure 8. For the QDs only, the signal in the NIR part of the spectrum disappears essentially with a similar rate as in the visible part. On the contrary, the NIR response of QD−COOH−C_{60} is virtually the same as in the visible part only for a short period of few tens of ps, but then the NIR signal stays almost constant, whereas the decay at 555 nm shows almost complete recovery of the bleached band within the time scale of the transient absorption measurements, 6 ns. The absorption band at 1040 nm was attributed to C_{60}^-, as it has a relatively long lifetime of ca. 8 ns. Almost complete recovery of the band at 555 nm indicates that the absorption of QD cations (QD^+) is almost indistinguishable from that of neutral QDs.

Comparison of the decay component spectra leads to the same conclusion: the charged QDs are spectroscopically very similar to neutral QDs. The longest-lived component (Figure 6b) has a clear band at 1040 nm, but only a very weak bleaching of the QD ground state band at 555 nm, the latter being most probably due to a small amount QDs without fullerenes. The component assigned to the charge separation, 43 ps, shows some reshaping of the spectrum in the near IR part, and gradual recovery of the 555 nm band in the visible region. There are no new visible spectral features, that could be assigned to QD^+ within the framework of exponential data fitting, and the only evidence for the electron transfer reaction comes from the characteristic anion band of fullerene.

The TA decay component spectra for QD540, QD600, and QD630 as well as the corresponding QD−COOH−C_{60} hybrids are presented in the Supporting Information. It has to be noted that the C_{60}^- radical anion signal gets somewhat weaker for the larger QDs. This might result from a smaller driving force for the electron transfer for the hybrids with larger QDs, and thus a slower and less efficient formation of the charge-separated state.

Table 3 summarizes the transient absorption results for all QD samples. When comparing the electron transfer rates in different-sized quantum dots, one needs to take into account the different QD−COOH−C_{60} ratios in the different QD samples. Because the quenching efficiency of the fullerene derivative varied for the different QD sizes, different QD−COOH−C_{60} ratios were used in the transient absorption measurements; the samples were prepared so that the emission intensity was suppressed by at least 80%. The QD−COOH−C_{60} ratios have been estimated utilizing the method described by Morris-Cohen et al.[27] using the pump−probe signals at long delay times (>2 ns) at the GSB wavelength of each QD sample. The lifetimes associated with COOH−C_{60} radical anion

DOI: 10.1021/acs.jpcc.5b04251
J. Phys. Chem. C 2015, 119, 17561−17572

formation have been scaled according to the QD−C_{60} ratio to yield the intrinsic electron transfer time constant.[27]

The electron transfer rate seems to correlate reasonably well with the QD size. With the exception of QD540, the electron transfer slows down with the increasing QD size. However, the differences between the different QD sizes are rather small. This observation is in good agreement with the estimated conduction band (CB) energies[45] for the QDs (see Figure S11 in Supporting Information). Although the method for estimating the quantum dot energy levels was developed for core-only QDs, the results can qualitatively be applied in the case of core−shell QDs as well. The model suggests that the differences in the CB energies decrease with the increasing size, resulting in a smaller ET driving force for the larger QDs. Similar size dependence for the ET rate was earlier observed for core-only QD−C_{60} hybrids by Bang and Kamat.[6] They concluded that the electron transfer reaction occurs in the Marcus normal regime, i.e. the electron transfer gets slower with increasing QD size. Our results support this conclusion. We implied the classical Marcus theory[46] to estimate the reorganization energies and electronic coupling for the ET and CR reactions. The results indicate that the reorganization energies are fairly similar for all QD sizes being roughly 0.6−0.7 eV, and thus, no major differences in the ET rates can be expected. The electronic coupling is the factor determining the distance dependence of the ET reactions. The electronic coupling was estimated based on the classical Marcus theory as well, and it is also insensitive to the size of QDs, being roughly 0.002 eV. The most straightforward interpretation of this outcome is that the distance of the fullerene moiety from the QD surface, rather than from the QD center, determines the electronic coupling.

The charge recombination rate does not depend strongly on the QD size either. In fact, the differences in the QD valence band (VB) energies are even smaller than for the CB energies (Figure S11), which suggests that the back-electron transfer would occur with a rather similar rate in different-sized QDs. Furthermore, the measured CR lifetimes are rather inaccurate due to the limited time window of the used measurement system (ca. 6 ns), and thus, no further conclusions about the correlation between the QD size and the CR rate can be drawn.

The exceptionally slow electron transfer (and fast charge recombination) in the QD540−COOH−C_{60} hybrid could result from less optimal QD surface due to defects, which trap the electrons and therefore hinder the electron transfer. Another explanation could be the smaller size of the QDs; perhaps the COOH−C_{60} orientation on the QD surface is less optimal for electron transfer on the smaller QDs.

The excitation of the QD occurs in the CdSe core. However, to be available for the ET to the fullerene moiety, the excited electron needs to travel through the ZnS shell, i.e., the CB electron and fullerene LUMO wave functions need to overlap. The inorganic shell is known to act as an additional barrier for the electron transfer. However, the study on the effect of the ZnS shell thickness on the electron transfer rate in CdSe QD−anthraquinone hybrids revealed a damping factor of 0.35 $Å^{-1}$ only.[13] The shell thickness of the QDs used in this study was ca. 6 Å, which can result in eight times slower ET compared to that of core-only QDs. However, the higher probability of defects in the core-only QDs may result in an overall lower ET efficiency compared to the better protected core−shell QDs. Furthermore, it has been demonstrated that an increase in the shell thickness slows down the charge recombination much more than the charge separation.[13] Therefore, using core−shell QDs in the QD−organic hybrids seems feasible, not only because of the higher emission quantum yields that provide a simple method for following the ET reaction by the emission quenching, but also because of the prolonged CS lifetimes.

The results of the Poisson fitting procedure applied to QD570 and the corresponding hybrid are presented in Figure 9. The fits are reasonably good considering that a very

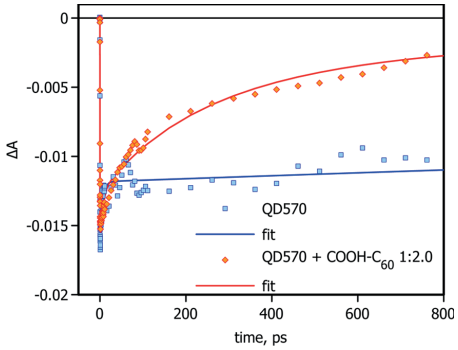

Figure 9. Transient absorption decays for the QD570 and the QD570−COOH−C_{60} hybrid at 550 nm (symbols) fitted to the model assuming a Poisson distribution of fullerenes and surface traps (solid lines). See text for details.

simplified model was used. The best fit parameters are τ_0 = 10 ± 3 ns, c_t = 0.34 ± 0.1, τ_t = 6 ± 4 ps, c = 2.1 ± 0.3, and τ_{ET} = 650 ± 130 ps. In fact, the value of c_t can be estimated without fitting, it is the relative contribution of the fast (≈6 ps) decay at the beginning. The value of τ_t is not accurate, as there are different types of traps. The value of c is reasonable and agrees with the steady-state emission quenching. Finally, the value of τ_{ET} looks to be overestimated. Two possible reasons for this are the fixed value of τ_0 = 10 ns taken from the decay fit for the QDs only, and the ignored distribution of τ_{ET} due to the "flexibility" of the QD−fullerene linkage (the distribution of orientations of the fullerene moiety with respect to the QD surface).

Considering that the decay model provided by eq 5 gives a reasonable approximation at the wavelength of the strongest transient absorption response, we can extend it to fit the data in the whole spectrum range. To do so, we will assume that the charge recombination is slow and can be accounted for by a single exponential term. Thus, our global fit model is

$$A(t,\lambda) = A_0(\lambda)\exp\left[-\frac{t}{\tau_0} - c_t(1-e^{-t/\tau_t}) - c(1-e^{-t/\tau_0})\right] + A_1(\lambda)\exp\left(-\frac{t}{\tau_1}\right) + A_2(\lambda)\exp\left(-\frac{t}{\tau_{CR}}\right), \quad (6)$$

where τ_{CR} is the time constant for the charge recombination and $A_0(\lambda)$, $A_1(\lambda)$, and $A_2(\lambda)$ are the decay component spectra associated with a fast thermalization, excited and charge separated states, respectively. The fit results, the spectra $A_0(\lambda)$, $A_1(\lambda)$, and $A_2(\lambda)$, are presented in Figure 10 with the

DOI: 10.1021/acs.jpcc.5b04251
J. Phys. Chem. C 2015, 119, 17561−17572

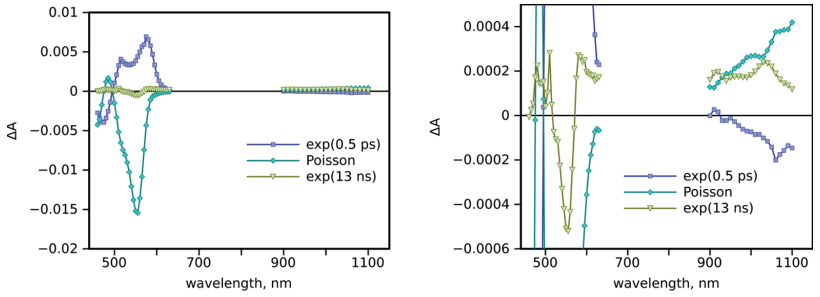

Figure 10. Decay component spectra for the QD570−COOH−C_{60} hybrid obtained from the global transient absorption data fitting to eq 6. The plot on the right presents the same data with extended absorption scale. See text for details.

new fit parameter being τ_{CR} = 13 ± 9 ns. As expected, the spectrum of the charge separated state ($A_2(\lambda)$) has a very weak absorption around 560 nm, as compared to that of the excited state ($A_0(\lambda)$), roughly 30 times lower. Second, the fullerene anion is much clearer in $A_2(\lambda)$ than in the long-lived component obtained from the exponential fit (presented in Figure 6b). This was the aim for developing the model, and can be attributed to a better separation of the remaining excited state transient absorption of QDs (small fraction of QDs without fullerenes) and QD cations. Third, although the absorption of the charge separated state, $A_2(\lambda)$, around 560 nm is weak, its shape is clearly different from that of the excited state, $A_0(\lambda)$. The $A_0(\lambda)$ spectrum suggests the bleaching of the ground state absorption, but the $A_2(\lambda)$ spectrum is consistent with a broadening of the band and a reduction in the intensity at the maximum, though the overall difference in absorption spectra of neutral QDs and positively charged QDs is minor and does not exceed 5%.

Although the model allows to minimize the number of intermediate states in the excitation relaxation and gives reasonable spectra for those states, it is definitely an oversimplification in particular in the assumption that all 1:1 hybrids have the same time constant for the charge separation and that there is only one type of surface traps with the same trapping time constant. QD570 are the best QDs in the series in that they have the lowest concentration of traps and thus the highest emission quantum yield. The same data analysis procedure was applied to the other QD−COOH−C_{60} hybrids, and the transient absorption decays as well as the decay component spectra can be found in Supporting Information. The fitted τ_{ET} and τ_{CS} values are shown in Table 3. However, the high concentration of traps and the broader spreading of the trapping times start to interfere with the electron transfer time constant and makes the separation of τ_t and τ_{ET} even less accurate. Nevertheless, the general trends and observations are the same for all hybrids: (1) the identification of the fullerene anion spectra is more clear with this model; (2) the spectral response of the QD cations is a few tens of times lower than that of the excited QDs; (3) the spectral perturbation of the QD cation is a minor broadening and reduction in the intensity.

Table3 summarizes the results from both the exponential fitting and the Poisson fitting of the transient absorption signals. The two different fitting models do not yield very comparable results. As noted earlier, the Poisson fit tends to overestimate the electron transfer time constants, and in fact, based on the Poisson fit, the electron transfer would seem faster in the larger quantum dots. This result, however, does not seem reliable based on the present discussion on the energy levels and the Marcus theory. Comparing the charge recombination time constants is likewise difficult, because the fitted lifetimes are longer than our measurement window. Therefore, the main advantage of the Poisson fitting procedure seems to be the easier observation of the C_{60}^- band as well as the identification of the QD cation spectral features in a qualitative manner.

CONCLUSIONS

Photoinduced electron transfer in CdSe/ZnS core−shell quantum dot (QD)−fullerene (COOH−C_{60}) hybrids was studied. The results show that after excitation of the quantum dot, the electron transfer to the fullerene moiety takes place in ca. 100−200 ps, and the charge separated state has a lifetime of several nanoseconds. The CS time constant is rather long for the QD−COOH−C_{60} hybrids, despite the fact that the fullerene moiety is bound to the QD surface with a considerably shorter linker than, e.g., in the CdSe QD−C_{60} hybrids built by Bang and Kamat.[6] This can be attributed to the effect of the QD shell which increases the barrier for the electron transfer.

We used a carboxyl-acid functionalized fullerene derivative for the hybrid formation instead of the more widely used thiol binding. The advantages of the carboxylic group over the thiol group are the more simple synthesis and the much weaker effect of binding group on QD photophysiscs. Furthermore, carboxyl-bound chromophores have previously shown to successfully adsorb on CdSe/ZnS QDs.[13] Our results also suggest that the binding is rather reliable, leaving no unbound fullerene in the dispersion.

In addition to the widely used multiexponential fitting procedure, more advanced methods of data analysis were utilized. The emission decay data were analyzed using the so-called maximum entropy method (MEM), that produces a distribution of the fluorescence lifetimes and therefore describes the heterogeneous QD ensemble in a more realistic way than just an exponential fitting. In particular, a peak around 20 ns was observed for virtually all hybrids. It corresponds to the nonhybridized QDs, and can be used to evaluate the relative concentration of fullerenes in the sample more accurately. At the same time, no distinct peaks were observed for complexes with the molar ratios 1:1, 1:2, etc., which suggests a relatively strong heterogeneity of the complexes.

DOI: 10.1021/acs.jpcc.5b04251
J. Phys. Chem. C 2015, 119, 17561−17572

The transient absorption spectroscopy data were analyzed taking into account the statistical manner of the QD−COOH−C_{60} hybrid formation. The results of this analysis revealed the fullerene anion signature at the NIR spectral region more clearly than a simple multiexponential fitting. Furthermore, the spectroscopical features of the QD cations were revealed: the QD cation spectrum is broader and less intense than that of neutral QDs in the ground state. However, the difference in the absorption spectra is minor.

Apparently the inorganic shell protects the hybrid in two ways: (1) by suppressing the effects of surface defects, and therefore enhancing the fluorescence quantum yields of the QDs as well as the yield of charge separation, and (2) by prolonging the lifetime of the charge-separated state while not retarding the electron transfer too much. The effect of the shell still needs to be verified in future studies by comparing the ET rates in core-only and core−shell QDs with the same chromophore.

■ ASSOCIATED CONTENT

Supporting Information

Absorption and emission spectra for all the studied QDs; measurement data for the fluorescence quantum yields, titration results and the MEM analysis results; transient absorption decay component spectra from multiexponential as well as the Poisson fitting; energy levels for the QD conduction and valence bands. The Supporting Information is available free of charge on the ACS Publications website at DOI: 10.1021/acs.jpcc.5b04251.

■ AUTHOR INFORMATION

Corresponding Authors

*(K.V.) E-mail: kirsi.virkki@tut.fi.

*(N.V.T.) E-mail: nikolai.tkachenko@tut.fi.

Notes

The authors declare no competing financial interest.

■ ACKNOWLEDGMENTS

The Academy of Finland (Grant No. 263594) and TUT's graduate school are acknowledged for funding.

■ REFERENCES

(1) Kamat, P. V. Quantum Dot Solar Cells. The Next Big Thing in Photovoltaics. *J. Phys. Chem. Lett.* **2013**, *4*, 908−918.

(2) Guzelturk, B.; Martinez, P. L. H.; Zhang, Q.; Xiong, Q.; Sun, H.; Sun, X. W.; Govorov, A. O.; Demir, H. V. Excitonics of Semiconductor Quantum Dots and Wires for Lighting and Displays. *Laser Phot. Rev.* **2014**, *8*, 73−93.

(3) Yue, Z.; Lisdat, F.; Parak, W. J.; Hickey, S. G.; Tu, L.; Sabir, N.; Dorfs, D.; Bigall, N. C. Quantum-Dot-Based Photoelectrochemical Sensors for Chemical and Biological Detection. *ACS Appl. Mater. Interfaces* **2013**, *5*, 2800−2814.

(4) Lou, Y.; Zhao, Y.; Chen, J.; Zhu, J.-J. Metal Ions Optical Sensing by Semiconductor Quantum Dots. *J. Mater. Chem. C* **2014**, *2*, 595−613.

(5) Boulesbaa, A.; Huang, Z.; Wu, D.; Lian, T. Competition between Energy and Electron Transfer from CdSe QDs to Adsorbed Rhodamine B. *J. Phys. Chem. C* **2010**, *114*, 962−969.

(6) Bang, J. H.; Kamat, P. V. CdSe Quantum DotFullerene Hybrid Nanocomposite for Solar Energy Conversion: Electron Transfer and Photoelectrochemistry. *ACS Nano* **2011**, *5*, 9421−9427.

(7) Ren, S.; Chang, L.-Y.; Lim, S.-K.; Zhao, J.; Smith, M.; Zhao, N.; Bulović, V.; Bawendi, M.; Gradečak, S. Inorganic-Organic Hybrid Solar Cell: Bridging Quantum Dots to Conjugated Polymer Nanowires. *Nano Lett.* **2011**, *11*, 3998−4002.

(8) Iagatti, A.; Flamini, R.; Nocchetti, M.; Latterini, L. Photoinduced Formation of Bithiophene Radical Cation via a Hole-Transfer Process from CdS Nanocrystals. *J. Phys. Chem. C* **2013**, *117*, 23996−24002.

(9) Stewart, M. H.; et al. Competition between Förster Resonance Energy Transfer and Electron Transfer in Stoichiometrically Assembled Semiconductor Quantum Dot-Fullerene Conjugates. *ACS Nano* **2013**, *7*, 9489−9505.

(10) Kambhampati, P. On the Kinetics and Thermodynamics of Excitons at the Surface of Semiconductor Nanocrystals: Are There Surface Excitons? *Chem. Phys.* **2015**, *446*, 92−107.

(11) Ma, H.; Jin, Z.; Zhang, Z.; Li, G.; Ma, G. Exciton Spin Relaxation in Colloidal CdSe Quantum Dots at Room Temperature. *J. Phys. Chem. A* **2012**, *116*, 2018−2023.

(12) Xu, Z.; Cotlet, M. Quantum Dot-Bridge-Fullerene Heterodimers with Controlled Photoinduced Electron Transfer. *Angew. Chem., Int. Ed.* **2011**, *50*, 6079−6083.

(13) Zhu, H.; Song, N.; Lian, T. Controlling Charge Separation and Recombination Rates in CdSe/ZnS Type I Core-Shell Quantum Dots by Shell Thicknesses. *J. Am. Chem. Soc.* **2010**, *132*, 15038−15045.

(14) Zhu, H.; Song, N.; Lian, T. Wave Function Engineering for Ultrafast Charge Separation and Slow Charge Recombination in Type II Core/Shell Quantum Dots. *J. Am. Chem. Soc.* **2011**, *133*, 8762−8771.

(15) Huang, J.; Mulfort, K. L.; Du, P.; Chen, L. X. Photodriven Charge Separation Dynamics in CdSe/ZnS Core/Shell Quantum Dot/Cobaloxime Hybrid for Efficient Hydrogen Production. *J. Am. Chem. Soc.* **2012**, *134*, 16472−16475.

(16) Pal, A.; Srivastava, S.; Gupta, R.; Sapra, S. Electron Transfer from CdSe-ZnS Core-Shell Quantum Dots to Cobalt(III) Complexes. *Phys. Chem. Chem. Phys.* **2013**, *15*, 15888−15895.

(17) Song, N.; Zhu, H.; Jin, S.; Zhan, W.; Lian, T. Poisson-Distributed Electron-Transfer Dynamics from Single Quantum Dots to C_{60} Molecules. *ACS Nano* **2011**, *5*, 613−621.

(18) Zang, H.; Xu, Z.; Cotlet, M. Core-Size Dependent Photoluminescence Blinking of Isolated Quantum Dot-Fullerene Hybrids. *Biophys. Rev. Lett.* **2013**, *8*, 255−264.

(19) Danilov, V. V.; Panfutova, A. S.; Khrebtov, A. I.; Ambrosini, S.; Videnichev, D. A. Optical Limiting as Result a of Photoinduced Electron Transfer in Hybrid Systems with CdSe/ZnS Quantum Dots, C_{60}, and Perylene. *Opt. Lett.* **2012**, *37*, 3948−3950.

(20) PlasmaChem GmbH, *Nanomaterials and Related Products. Catalog and Price List*; PlasmaChem: Berlin, 2014; ISBN:978-3-00-034019-2, available at www.plasmachem.com.

(21) Stranius, K.; George, L.; Efimov, A.; Ruoko, T.-P.; Pohjola, J.; Tkachenko, N. V. Photophysical Study of a Self-Assembled Donor-Acceptor Two-Layer Film on TiO_2. *Langmuir* **2015**, *31*, 944−952.

(22) Nierengarten, J. F.; Herrmann, A.; Tykwinski, R. R.; Rüttimann, M.; Diederich, F.; Boudon, C.; Gisselbrecht, J. P.; Gross, M. Methanofullerene Molecular Scaffolding: Towards C_{60}-Substituted Poly(triacetylenes) and Expanded Radialenes, Preparation of a C_{60}-C_{70} Hybrid Derivative, and a Novel Macrocyclization Reaction. *Helv. Chim. Acta* **1997**, *80*, 293−316.

(23) Esposito, R.; Altucci, C.; Velotta, R. Analysis of Simulated Fluorescence Intensities Decays by a New Maximum Entropy Method Algorithm. *J. Fluoresc.* **2013**, *23*, 203−211.

(24) Maskevich, A. A.; Stsiapura, V. I.; Balinski, P. T. Analysis of Fluorescence Decay Kinetics of Thioflavin by a Maximum Entropy Method. *J. Appl. Spectrosc.* **2010**, *77*, 194−201.

(25) Tkachenko, N. V.; Rantala, L.; Tauber, A. Y.; Helaja, J.; Hynninen, P. H.; Lemmetyinen, H. Photoinduced Electron Transfer in Phytochlorin-[60]Fullerene Dyads. *J. Am. Chem. Soc.* **1999**, *121*, 9378−9387.

(26) Pelado, B.; Abou-Chahine, F.; Calbo, J.; Caballero, R.; de la Cruz, P.; Junquera-Hernández, J. M.; Ortí, E.; Tkachenko, N. V.; Langa, F. Role of the Bridge in Photoinduced Electron Transfer in Porphyrin-Fullerene Dyads. *Chem. - Eur. J.* **2015**, *21*, 5814−5825.

DOI: 10.1021/acs.jpcc.5b04251
J. Phys. Chem. C 2015, 119, 17561−17572

(27) Morris-Cohen, A. J.; Frederick, M. T.; Cass, L. C.; Weiss, E. A. Simultaneous Determination of the Adsorption Constant and the Photoinduced Electron Transfer Rate for a CdS Quantum Dot - Viologen Complex. *J. Am. Chem. Soc.* **2011**, *133*, 10146−10154.
(28) Sadhu, S.; Tachiya, M.; Patra, A. A Stochastic Model for Energy Transfer from CdS Quantum Dots/Rods (Donors) to Nile Red Dye (Acceptors). *J. Phys. Chem. C* **2009**, *113*, 19488−19492.
(29) Yu, W. W.; Qu, L.; Guo, W.; Peng, X. Experimental Determination of the Extinction Coefficient of CdTe, CdSe, and CdS Nanocrystals. *Chem. Mater.* **2003**, *15*, 2854−2860.
(30) Hao, J. J.; Zhou, J.; Zhang, C. Y. A Tri-n-octylphosphine-assisted Successive Ionic Layer Adsorption and Reaction Method to Synthesize Multilayered Core-Shell CdSe-ZnS Quantum Dots with Extremely High Quantum Yield. *Chem. Commun.* **2013**, *49*, 6346−6348.
(31) Jun, S.; Jang, E. Bright and Stable Alloy Core/Multishell Quantum Dots. *Angew. Chem., Int. Ed.* **2013**, *52*, 679−682.
(32) Xie, R.; Kolb, U.; Li, J.; Basché, T.; Mews, A. Synthesis and Characterization of Highly Luminescent CdSe-core $CdS/Zn_{0.5}Cd_{0.5}S$/ZnS Multishell Nanocrystals. *J. Am. Chem. Soc.* **2005**, *127*, 7480−7488.
(33) Baker, D. R.; Kamat, P. V. Tuning the Emission of CdSe Quantum Dots by Controlled Trap Enhancement. *Langmuir* **2010**, *26*, 11272−11276.
(34) Bullen, C.; Mulvaney, P. The Effects of Chemisorption on the Luminescence of CdSe Quantum Dots. *Langmuir* **2006**, *22*, 3007−3013.
(35) Green, M. The Nature of Quantum Dot Capping Ligands. *J. Mater. Chem.* **2010**, *20*, 5797−5809.
(36) Liu, I.-S.; Lo, H.-H.; Chien, C.-T.; Lin, Y.-Y.; Chen, C.-W.; Chen, Y.-F.; Su, W.-F.; Liou, S.-C. Enhancing Photoluminescence Quenching and Photoelectric Properties of CdSe Quantum Dots With Hole Accepting Ligands. *J. Mater. Chem.* **2008**, *18*, 675−682.
(37) Querner, C.; Reiss, P.; Bleuse, J.; Pron, A. Chelating Ligands for Nanocrystals' Surface Functionalization. *J. Am. Chem. Soc.* **2004**, *126*, 11574−11582.
(38) Sension, R. J.; Szarka, A. Z.; Smith, G. R.; Hochstrasser, R. M. Ultrafast Photoinduced Electron Transfer to C_{60}. *Chem. Phys. Lett.* **1991**, *185*, 179−183.
(39) Fukuzumi, S.; Suenobu, T.; Patz, M.; Hirasaka, T.; Itoh, S.; Fujitsuka, M.; Ito, O. Selective One-Electron and Two-Electron Reduction of C_{60} with NADH and NAD Dimer Analogues via Photoinduced Electron Transfer. *J. Am. Chem. Soc.* **1998**, *120*, 8060−8068.
(40) Klimov, V. I. Optical Nonlinearities and Ultrafast Carrier Dynamics in Semiconductor Nanocrystals. *J. Phys. Chem. B* **2000**, *104*, 6112−6123.
(41) Cooney, R. R.; Sewall, S. L.; Dias, E. A.; Sagar, D. M.; Anderson, K. E. H.; Kambhampati, P. Unified Picture of Electron and Hole Relaxation Pathways in Semiconductor Quantum Dots. *Phys. Rev. B: Condens. Matter Mater. Phys.* **2007**, *75*, 245311 (1−13).
(42) Ebbesen, T. W.; Tanigaki, K.; Kuroshima, S. Excited-State Properties of C_{60}. *Chem. Phys. Lett.* **1991**, *181*, 501−504.
(43) Palit, D. K.; Sapre, A. V.; Mittal, J. P.; Rao, C. N. R. Photophysical Properties of the Fullerenes, C_{60} and C_{70}. *Chem. Phys. Lett.* **1992**, *195*, 1−6.
(44) Kadish, K. M., Ruoff, R. S. *Fullerenes: Chemistry, Physics, and Technology*; John Wiley & Sons: New York, 2000.
(45) Jasieniak, J.; Califano, M.; Watkins, S. E. Size-Dependent Valence and Conduction Band-Edge Energies of Semiconductor Nanocrystals. *ACS Nano* **2011**, *5*, 5888−5902.
(46) Isosomppi, M.; Tkachenko, N. V.; Efimov, A.; Vahasalo, H.; Jukola, J.; Vainiotalo, P.; Lemmetyinen, H. Photoinduced Electron Transfer of Double-Bridged Phthalocyanine-Fullerene Dyads. *Chem. Phys. Lett.* **2006**, *430*, 36−40.

DOI: 10.1021/acs.jpcc.5b04251
J. Phys. Chem. C 2015, 119, 17561−17572

Publication II

Kirsi Virkki, Essi Tervola, Mine Ince, Tomás Torres, and Nikolai V. Tkachenko. Comparison of Electron Injection and Recombination on TiO_2 Nanoparticles and ZnO Nanorods Photosensitized by Phthalocyanine, *Royal Society Open Science*, vol. 5, no. 7, p. 180323, 2018.

ROYAL SOCIETY OPEN SCIENCE

rsos.royalsocietypublishing.org

Research

Cite this article: Virkki K, Tervola E, Ince M, Torres T, Tkachenko NV. 2018 Comparison of electron injection and recombination on TiO_2 nanoparticles and ZnO nanorods photosensitized by phthalocyanine. *R. Soc. open sci.* **5**: 180323.
http://dx.doi.org/10.1098/rsos.180323

Received: 28 February 2018
Accepted: 7 June 2018

Subject Category:
Chemistry

Subject Areas:
nanotechnology/spectroscopy/photochemistry

Keywords:
TiO_2 nanoparticles, ZnO nanorods, phthalocyanine, semiconductor–organic interface, photo-induced electron transfer

Author for correspondence:
N. V. Tkachenko
e-mail: nikolai.tkachenko@tut.fi

This article has been edited by the Royal Society of Chemistry, including the commissioning, peer review process and editorial aspects up to the point of acceptance.

THE ROYAL SOCIETY PUBLISHING

Comparison of electron injection and recombination on TiO_2 nanoparticles and ZnO nanorods photosensitized by phthalocyanine

K. Virkki[1], E. Tervola[1], M. Ince[2,3,4], T. Torres[2,5,6] and N. V. Tkachenko[1]

[1]Laboratory of Chemistry and Bioengineering, Tampere University of Technology, PO Box 541, 33101 Tampere, Finland
[2]Departamento de Química Orgánica, Universidad Autónoma de Madrid, Cantoblanco, 28049 Madrid, Spain
[3]Advanced Technology Research and Application Center, Mersin University, Ciftlikkoy Campus, 33343 Mersin, Turkey
[4]Department of Energy Systems Engineering, Faculty of Tarsus Technology, Mersin University, 33480 Mersin, Turkey
[5]Institute for Advanced Research in Chemical Sciences (IAdChem), Universidad Autónoma de Madrid, 28049 Madrid, Spain
[6]IMDEA Nanociencia, C/Faraday, 9, Cantoblanco, 28049 Madrid, Spain

NVT, 0000-0002-8504-2335

Titanium dioxide (TiO_2) and zinc oxide (ZnO) semiconductors have similar band gap positions but TiO_2 performs better as an anode material in dye-sensitized solar cell applications. We compared two electrodes made of TiO_2 nanoparticles and ZnO nanorods sensitized by an aggregation-protected phthalocyanine derivative using ultrafast transient absorption spectroscopy. In agreement with previous studies, the primary electron injection is two times faster on TiO_2, but contrary to the previous results the charge recombination is slower on ZnO. The latter could be due to morphology differences and the ability of the injected electrons to travel much further from the sensitizer cation in ZnO nanorods.

1. Introduction

Titanium dioxide (TiO_2) is the most widely used anode material in dye-sensitized solar cell (DSSC) applications [1], and the highest

power conversion efficiencies achieved for DSSCs so far were achieved for cells built on a layer of TiO_2 nanoparticles [2]. There are a few promising alternative materials under development, probably the most well known being ZnO [3]. ZnO has a band gap position very close to that of TiO_2, but has higher electron mobility. It is naturally abundant and a few inexpensive methods exist to produce nanoparticles, nanorods and nanowires for DSSC applications. However, the power conversion efficiencies of most ZnO-based DSSCs are lower than those of the best TiO_2-based DSSCs [4]. However, for TiO_2 and ZnO cells with identical morphologies, the efficiencies of the two anode materials match each other well, though different factors contribute to their efficiencies [5]. This stimulated our research on the primary electron injection, regeneration, recombination and other reactions at the semiconductor–sensitizing dye interfaces of the two materials [6].

A large number of comparative studies carried out with different sensitizers indicated that electron injection is faster on TiO_2 than on ZnO [7–11]. It has also been demonstrated that photoinduced electron injection itself is not a simple single-step reaction. At first, an electron–cation complex is formed at the interface which later may yield a 'free electron' in the conduction band (CB) of the semiconductor [12,13]. The primary photoinduced electron injection from a sensitizer to an anode can be monitored by ultrafast absorption spectroscopy, which is observation of the sensitizer cation formation in most cases. The separation of the electron–cation complex does not change sample absorption in the visible (Vis)–near-IR (NIR) range, but can be studied by ultrafast terahertz spectroscopy (e.g. [12,14]), and it has been shown that the electron leaves the interface faster in the case of TiO_2 than in ZnO. A characteristic time scale for this process is around a picosecond for the TiO_2 interface and up to a few hundreds of picoseconds for ZnO.

It should be noted, however, that for both semiconductor materials (TiO_2 and ZnO) the electron injection is sufficiently fast for most of the studied sensitizers, and the time constant of the charge separation at the interface alone should not lead to a dramatic difference in the efficiency of photocurrent generation. Another clear difference between TiO_2 and ZnO materials used as photo-anodes is the crystallinity and electronic band structure. Mostly, anatase TiO_2 nanoparticles are used to fabricate photo-anodes. ZnO nanoparticles are also commonly used for photo-anodes. Also ZnO nanorods with a distinct wurtzite crystal structure are an attractive alternative material not fully exploited yet [3]. ZnO belongs to the group of direct band gap semiconductors, whereas TiO_2 has a more complex band structure, which also affects the charge separation at the anode surface [13].

The aim of this study was to compare primary photoinduced reactions on TiO_2 and ZnO anodes. Standard TiO_2 anatase nanoparticles were used to prepare TiO_2 anodes. ZnO nanorods were selected as a model system for the ZnO anodes, as these anodes have well-defined crystallinity (wurtzite) and morphology [15]. Based on our previous experience, a special phthalocyanine derivative was selected as the organic sensitizer [16–18]. This phthalocyanine (Pc) has specifically designed bulky peripheral groups which prevent aggregation and eliminate inter-chromophore interactions. An important advantage of the Pc selected for this study is the strong and sharp absorption features of the ground, excited and cation states, which allow reliable and quantitative characterization based on ultrafast transient absorption measurements. Another important feature is picosecond electron injection, which allows the 'pure' excited state to be observed with an instrument limited to 100 fs in time resolution.

2. Material and methods

2.1. Materials

The chemical structure of the phthalocyanine (Pc) used is shown in figure 1 and its synthesis is described elsewhere [16]. Ethanol (EtOH) (≥99.5% by mass) was purchased from Altia Plc. Acetonitrile (MeCN), *t*-butanol (*t*-BuOH), ethanolamine, hexamethylene tetramine, 2-methoxyethanol, toluene, zinc acetate dihydrate and zinc nitrate hexahydrate were purchased from Sigma-Aldrich. TiO_2 nanoparticle paste was purchased from Solaronix (Ti-Nanoxide T/SP) and from Dyesol (18NR-T). Fluorine–tin oxide (FTO)-coated glass substrates (TEC7) were purchased from Sigma-Aldrich and cleaned as described in [18].

2.2. Samples

Previously developed and tested procedures were used to prepare nanostructures [15,19–21]. In brief, TiO_2 nanoparticle (anatase, average size 20 nm) films were prepared by spin-coating on FTO glasses pre-coated by a thin TiO_2 compact layer [19,20]. The thickness of the TiO_2 nanoparticle layer was determined by scanning electron microscope (SEM) (figure 2*a*) and was typically 2–2.3 µm. ZnO nanorod

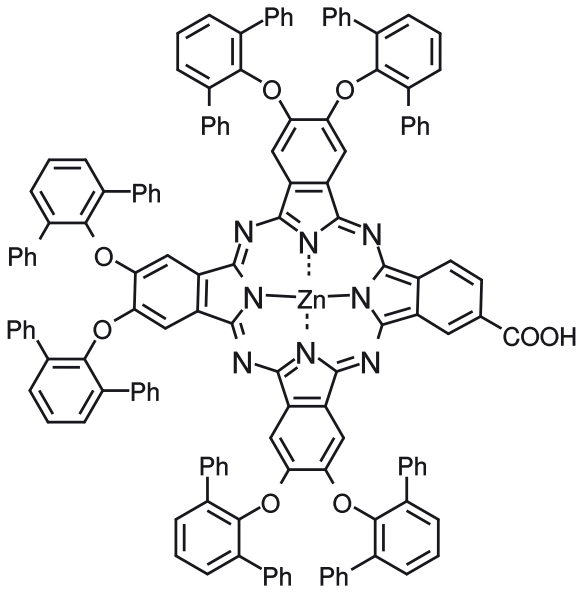

Figure 1. Phthalocyanine (Pc) structure.

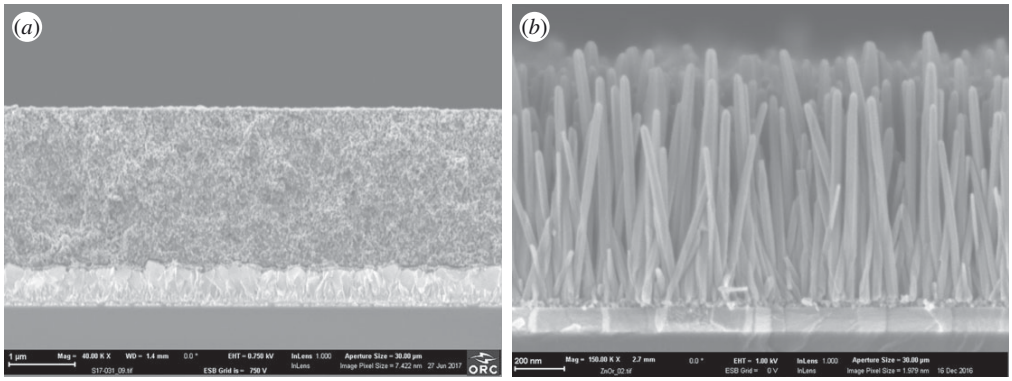

Figure 2. SEM cross-section images of (*a*) a TiO_2|Pc sample (the lighter-coloured layer in the bottom is FTO with a thin compact layer; the scale bar is 1 µm) and (*b*) a ZnO|Pc sample (the lighter-coloured layer in the bottom is ITO with a thin seed ZnO layer on top; the scale bar is 200 nm).

photo-anodes were prepared using a hydro-thermal method on indium–tin oxide (ITO)-coated glasses following the procedure described previously [15,18]. The typical length of the nanorods was 800–1000 nm and diameters were around 50 nm (figure 2*b*). For the studied samples, the specific surface area of the ZnO nanorod samples was estimated to be approximately 10 times smaller than that of the TiO_2 samples.

Self-assembled monolayers (SAMs) of Pc were deposited by dissolving Pc in a mixture of BuOH : MeCN 1 : 1 (by volume) at a concentration of 0.03–0.1 mM, immersing the substrates into solution for 30 min and washing away the phys-adsorbed excessive Pc with pure solvent, as described elsewhere [18].

2.3. Instruments

Absorption spectra of the samples were measured using a Shimadzu UV-3600 UV-VIS-NIR spectrophotometer. The sample morphology was investigated using a field emission SEM (FE-SEM; Carl Zeiss Ultra 55). Ultrafast transient absorption (TA) responses of the samples were measured using a pump–probe system described previously [20,22]. Briefly, samples were excited at 695 nm (pump) by roughly 100 fs pulses at a repetition rate of 1 kHz (Libra F, Coherent Inc., coupled with

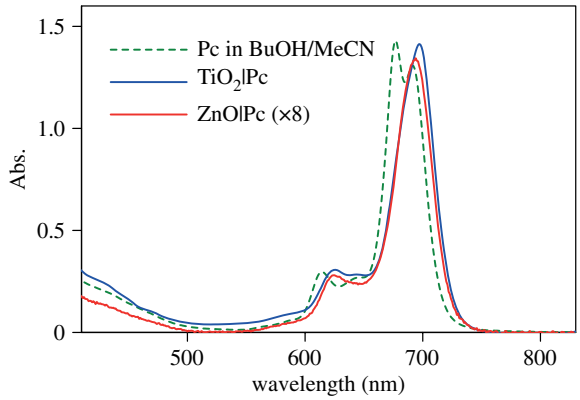

Figure 3. Absorption spectra of TiO_2|Pc and ZnO|Pc samples after subtracting substrate spectra, and Pc in mixture of BuOH : MeCN. The spectrum of ZnO|Pc sample was multiplied by eight to match the scale.

Topas C, Light Conversion Ltd). White continuum probe pulses were generated by a small fraction of fundamental pulses produced by the generator (Libra F) focused on a sapphire crystal. The time-resolved transient absorption spectra were recorded using an ExciPro TA spectrometer (CDP, Inc.) in two wavelength ranges: 460–770 nm and 850–1050 nm. Home-developed software (decfit.py) was used to process and analyse the pump–probe measurements. The program carries out group velocity dispersion compensation, convolution with an instrument response function and a global data fit to a sum of exponential, stretched exponential and distributed decay functions [23].

3. Results

3.1. Samples

Absorption spectra of the Pc-sensitized samples are presented in figure 3 together with the solution spectrum. The absorption spectra of the substrates, TiO_2 nanoparticle film and ZnO nanorod array were subtracted; therefore, the spectra shown represent absorption of Pc SAMs. Owing to the thickness and morphology differences, the TiO_2 samples had an approximately 10 times higher surface specific area than the ZnO samples [15]. Therefore, to compare Pc spectra in TiO_2 and ZnO, the spectrum of the ZnO | Pc sample was multiplied by 8. The resulting absorption spectra of the Pc SAMs on both ZnO and TiO_2 are reasonably close to each other in shape, and show no evidence of Pc aggregation. One may notice a red shift (by roughly 8 nm) and some differences in the shapes of the spectra in the Q-band area (650–710 nm region) of the SAMs compared with the solution. However, the band width is the same 37 nm (full width half-maximum) in both cases, which indicates no aggregation effect on the spectra of the SAMs.

3.2. Transient absorption spectroscopy

The photoinduced reactions in the samples were studied by measuring the transient absorption responses (pump–probe method) in two wavelength ranges, 460–770 nm and 850–1050 nm, with excitation at 695 nm. The time-resolved differential absorption spectra of TiO_2 | Pc and ZnO | Pc samples at selected delay times are presented in figure 4. At a qualitative level, the spectra at a short delay time, e.g. at 0.2 ps, can be attributed to the singlet excited state of Pc formed immediately after the excitation, and at a longer delay time, e.g. at 1 ns, they can be attributed to the Pc cation [24]. The responses of two samples in figure 4 have much in common in terms of spectral shapes, though lifetimes and relationships between different spectral features are clearly different.

The transient absorption response of the ZnO | Pc sample can be fitted reasonably well by a sum of three exponential and one distributed decay functions as discussed in [18]. The resulting decay-associated component spectra are presented in figure 5*b*. These are spectra of the transient absorption responses associated with corresponding fit functions, exponential and distributed decays denoted as 'exp(. . .)' and 'dist(. . .)', respectively. To obtain an equally good fit of the TiO_2 | Pc data, a combination of two exponents and two distributed decays had to be used (figure 5*a*). The spectral shapes are highly

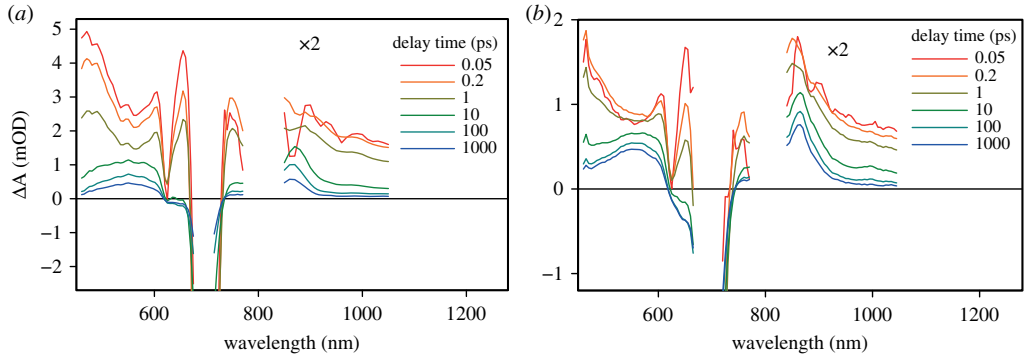

Figure 4. Time-resolved transient absorption spectra of (*a*) TiO_2|Pc and (*b*) ZnO|Pc samples at a few selected delay times. The data were corrected for the group velocity dispersion.

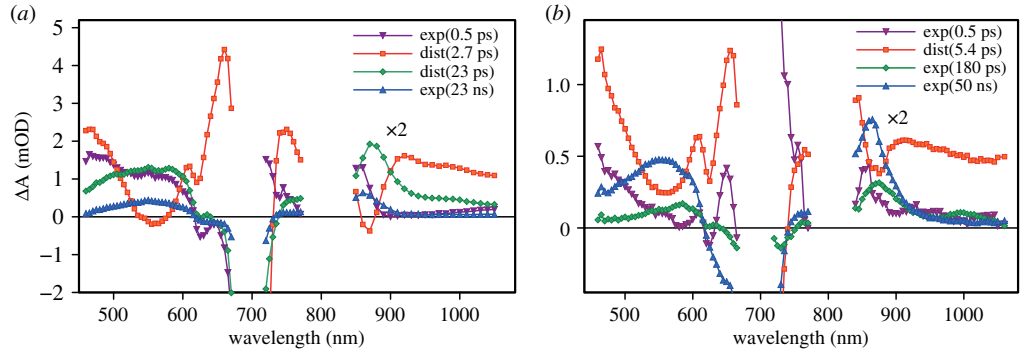

Figure 5. Transient absorption component spectra of Pc on (*a*) TiO_2 nanoparticles and (*b*) ZnO nanorods. The fit model consisted of the sum of the exponential and distributed decays denoted as exp(. . .) and dist(. . .), respectively, with characteristic time constants indicated in brackets. The NIR part of the spectra ($\lambda > 800$ nm) is magnified two times.

similar for the two sets of the component spectra, even though the relative intensities and corresponding time constants are different.

The wavelength of most different decay profiles of the transient absorptions of TiO_2 and ZnO samples is 865 nm. The normalized decays at 865 nm are shown in figure 6. This figure illustrates also the fit quality (solid lines): there were no regular deviations of the fits from the data through the whole spectrum range and typical sigma-values were 0.01–0.02 mOD.

4. Discussion

4.1. Long-lived charge separation

In both cases, the longest-lived components (figure 5) have decay times much longer than the maximum delay time available to the instrument (6 ns); therefore, the calculated decay time values are not accurate. However, the spectra of the components are very much alike and show a relatively narrow absorption band at 865 nm and a broad absorption band around 560 nm in addition to strong bleaching of the Q-band around 700 nm. These features are typical for the Pc cation, Pc^+ [18,24,25]. The relative intensities of the long-lived components are rather different in the two samples, being much stronger in the ZnO | Pc sample.

4.2. Electron injection

Another component with clear and distinct features is the distributed decay component with an average time constant of 2.7 ± 0.2 ps in the case of the TiO_2 | Pc sample and 5.4 ± 0.7 ps for the ZnO | Pc sample. It has a sharp band at 650 nm, a relatively sharp negative peak at 870 nm and a broad negative peak around 560 nm. These features are consistent with transition from the singlet excited state to the Pc cation, which

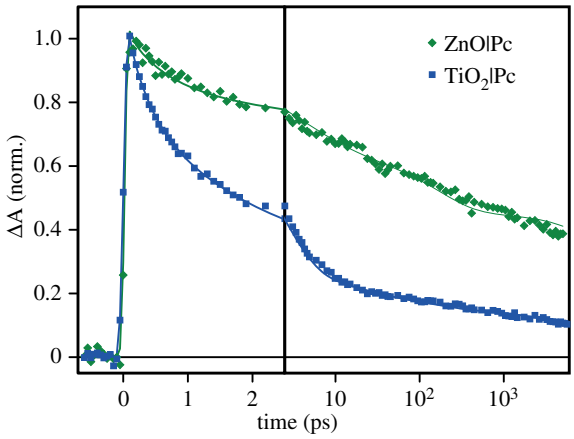

Figure 6. Transient absorption decays at 865 nm of Pc on TiO_2 and ZnO. The symbols are the measured data points and the solid lines are the fits.

is caused by electron injection to TiO_2,

$$TiO_2 \,|\, Pc^* \xrightarrow{\tau_{inj}} TiO_2^- \,|\, Pc^+. \tag{4.1}$$

The distributed decay model operates with three parameters [23]: the average (or non-disturbed) time constant (τ_{inj}) indicated for the corresponding decay components in figure 5, the width of the free and/or reorganization energy distribution ($\triangle E$), and the sensitivity factor (a). The time constant is approximately two times larger for the ZnO | Pc sample, but the other two parameters are nearly identical for the two samples, $\triangle E = 0.022 \pm 0.004$ eV and $a = 1.0 \pm 0.2$ for TiO_2 | Pc and $\triangle E = 0.028 \pm 0.007$ eV and $a = 1.2 \pm 0.3$ for ZnO | Pc. This means that the electron injection is two times faster in the TiO_2 | Pc sample, but otherwise the mechanism of electron transfer is the same.

There is a fast 0.5 ps component in the response of both samples. It has an effect of a minor absorption decay in the visible part of the spectrum and some reshaping around 850 nm, but it does not lead to the formation of an intermediate state with new distinct spectral properties (figure 4). This component is tentatively attributed to the thermal relaxation of the singlet excited state and will not be discussed further.

4.3. Fast charge recombination at the interface

The last component to discuss is that of the 180 ps time constant in the case of the ZnO | Pc sample and the 23 ps average time constant (distributed decay component) for the TiO_2 | Pc sample. The spectral shapes of this component are rather close for the two samples but the relative intensities are different. It is a minor component for the ZnO | Pc sample and one of the strongest for the TiO_2 | Pc sample. Furthermore, the spectra of these components resemble those of the longest-lived component, with differences mainly seen in the shape of the broad band in the 500–600 nm range and an absorption shoulder (TiO_2 | Pc) or a minor band (ZnO | Pc) in the 950–1050 nm range. The latter can be associated with a Pc anion, which has two characteristic bands: one is close to 1000 nm in the NIR and the other is at 590 nm in the visible part of the spectrum, as was observed for ZnO | Pc covered with a hole-transporting material (electron donor) [18]. The appearance of a Pc anion could be explained by the partial aggregation of the Pc molecules and an intra-aggregate charge separation in the process $Pc^* - Pc \rightarrow Pc^+ - Pc^-$. This could be a reasonable explanation in the case of the ZnO | Pc sample, though for the ZnO | Pc sample it is a minor process in any case. However, in the case of the TiO_2 | Pc sample, there is no band at 1000 nm and the component shape in the 500–620 nm range does not match that of the Pc anion, having a broad band in the 500–600 nm range rather than a relatively narrow anion band at 590 nm. It is more reasonable to attribute this component to a Pc cation, which leaves a question on the origin of two Pc cations with drastically different lifetimes, 23 ps and 23 ns (TiO_2 | Pc) and minor differences in the spectral shapes.

A typical interpretation of a very diverse decay time of one and the same state is inhomogeneity of the Pc arrangement on the TiO_2 surface. However, this can also be ruled out for two reasons. Firstly, the bulky peripheral groups and rigid core of Pc makes a diverse conformation distribution unlikely.

Secondly, the same diversity could be expected for both semiconductor substrates, but in the case of ZnO the fast charge recombination (180 ps) is a minor process, whereas in the case of TiO_2 it is almost the dominating process.

4.4. Interfacial charge transfer complex

There are reports on a two-step charge separation at the semiconductor–organic interface [9,11,12,14]. In the first step, a coupled electron–hole pair is formed with the electron in the CB but electrostatically bound to the sensitizer cation, Pc^+. This state is also termed the interfacial charge-transfer complex (ICTC) [13]. It may recombine or the electron may leave the interface and become a 'free' carrier in the CB. In the spectral range studied, the measured transient absorption response is dominated by the response of the Pc sensitizer, a cation in both the coupled and non-coupled Pc^+ states. Therefore, electron migration from the close proximity of the Pc^+ to the bulk of the semiconductor is expected to have only a minor effect on the transient absorption spectrum shape, which is consistent with the minor spectral differences of the two long-lived components in figure 5.

Taking this two-step charge transfer as a working hypothesis, one could conclude that there is a relatively large probability of charge recombination of the ICTC in the case of TiO_2 | Pc, as the molar absorption coefficients of the 'free' cation Pc^+ and cation in the ICTC must be almost the same. The gradual decay of the signal at 865 nm within a few tens of picoseconds (figure 6) points to the complex recombination but not to the electron shift to the bulk of TiO_2. However, this conclusion contradicts previous studies. First of all, terahertz spectroscopy of similar TiO_2 samples suggests that the ICTC dissociates by yielding free electrons in the CB within 1 ps [12,14], much shorter than the 23 ps time constant discussed here. On the contrary, for ZnO samples, this dissociation time is extended to 100 ps and agrees reasonably well with the 180 ps reported here. Secondly, Chegui and co-workers [13] have shown that the fates of the injected electron are very different in TiO_2 and ZnO due to the different electronic band structures, a direct band gap in ZnO and an indirect one in TiO_2, and ICTC is formed at the ZnO | Pc interface but not at the TiO_2 | Pc interface. Therefore, our results are consistent with an intermediate ICTC complex in the ZnO | Pc sample only.

The 23 ps time constant corresponds to an electron diffusion length of a few tens of nanometres in bulk TiO_2, roughly the size of a nanoparticle. This leads us to the assumption that the fast charge recombination is associated with the probability of the electron remaining in the same nanoparticle into which it was injected. The free electron and Pc^+ cannot recombine as soon as the electron jumps to another nanoparticle, and 23 ps is an average time for the free electron to move from one TiO_2 nanoparticle to another. The characteristic size, the length, of ZnO nanorods is much larger and the carrier mobility is much higher in ZnO, therefore the same fast recombination mechanism in not efficient in ZnO | samples since free electrons move quickly away from the recombination centre, Pc^+. This assumption has no direct proof, however.

4.5. Dynamics of the Pc cation on TiO_2 and ZnO surfaces

The band at 865 nm is a characteristic feature of the Pc cation. Unfortunately, the singlet excited state of Pc also has relatively high absorption at this wavelength, which is the reason why the electron injection (reaction (4.1)) does not lead to an absorption rise at this wavelength in the first few picoseconds of electron injection and cation formation. Nevertheless, at relatively long delay times when the singlet state has already relaxed, e.g. >10 ps, the signal at 865 nm can be used as an indicator of the [Pc^+] population. Comparison of the transient absorption decays at this wavelength is shown in figure 6. Obviously, the charge recombination at the TiO_2 | Pc interface is faster than that at the ZnO | Pc interface, and the most drastic drop of the signal at 865 nm (TiO_2 | Pc sample) takes place within the first 10 ps after the excitation.

A very simplified reaction scheme for both samples is

$$\begin{array}{ccccc} Pc^* & \xrightarrow{\tau_{inj}} & e^- \,|\, Pc^+ & \xrightarrow{\tau_l} & Pc^+ \\ & & \downarrow \tau_{int} & & \downarrow \tau_{cr} \\ & & Pc & & Pc \end{array} \qquad (4.2)$$

where $e^- \,|\, Pc^+$ is the ICTC or any other fast disappearing charge separated state, τ_{int} is the time constant of this state charge recombination, τ_l is the time constant to form a 'long-lived' charge transfer state, and τ_{cr} is the final recombination time constant of Pc^+. Experimentally observable time constants are τ_{int},

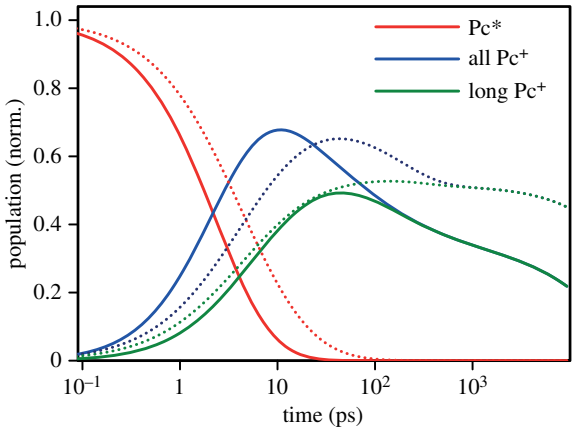

Figure 7. Modelled dynamics of the singlet excited state, Pc* and cation, Pc^+, populations in the TiO_2|Pc (solid lines) and ZnO|Pc (dotted lines) samples. The population of Pc cations was calculated for all Pc^+ and for long-lived Pc^+, see text for the details.

τ_{cr} and $\tau_s = (\tau_{int}^{-1} + \tau_l^{-1})^{-1}$, which are the time constants of the picosecond, 20–200 ps, and nanosecond components in figure 5.

To model the process dynamics, the fit results at 865 nm will be used. Then, we will assume that:

(i) the picosecond component is solely due to the relaxation of the singlet excited state, Pc*; thus the average time constants for the singlet state relaxation are $\tau_{inj} = 2.4 \pm 0.2$ ps and 5.4 ± 0.7 ps for the TiO_2 | Pc and ZnO | Pc samples, respectively;
(ii) only the excited state, Pc*, and cation, Pc^+, contribute to the transient absorption at this wavelength, and absorption of two cations in scheme (4.2) is the same;
(iii) immediately after excitation only Pc* is formed, which means that the time resolution of the instrument is sufficient to resolve the cation formation and it has zero population at zero time.

Within this model, the population decay of the excited state is

$$[Pc^*](t) = \mathrm{dist}(t, \tau_{inj}, \triangle E, a), \tag{4.3}$$

where the function dist() is computed as presented in [23], and it depends on the 'non-disturbed' or average time constant, τ_{inj}, the energy distribution width, $\triangle E$, and the sensitivity factor, a. The population decay of the singlet excited state is shown in figure 7 by the red lines.

The time profile of the total cation population ('all Pc^+' in figure 7, blue lines) can be computed as the difference between the normalized decays at 865 nm ($\triangle A_{\lambda=865\,\mathrm{nm}}(t)$) and [Pc*](t), though this does not give an 'absolute' value of the Pc^+ population since the ratio of molar absorbances of Pc^+ and Pc* is not known. In other words, the sum 'Pc*' and 'all Pc^+' in figure 7 is the normalized measured decay at 865 nm, or the fits shown in figure 6.

Next, the proportion in the branching reactions of the e^- | Pc^+ state can be evaluated from the relative intensities of the decay components with the time constants 23 ps and 23 ns (in the case of the TiO_2 | Pc sample), which gives

$$\tau_{int} = \tau_c \frac{a_{int}}{a_l + a_{int}} \tag{4.4}$$

and

$$\tau_l = \tau_c \frac{a_l}{a_l + a_{int}}, \tag{4.5}$$

where τ_c is the measured time constant of the middle decay component (23 ps for TiO_2). The green lines in figure 7 show cation populations minus the population of the e^- | Pc^+ states; figure 7 also presents the dynamics of the 'long-lived' cations.

The most reliable part here is the separation of the singlet, Pc*, and cation, Pc^+, as it is based on sharp spectral differences between the two states. Division on the 'short'- and 'long'-lived Pc cations (states e^- | Pc^+ and Pc^+ in scheme (4.2)) is rather phenomenological, but it reflects the experimental observation that the cation Pc^+ decay has fast, 23 ps, and slow, 23 ns, components with approximately two-thirds accumulated in the fast decay in the case of the TiO_2 | Pc sample. This is not the case for the

ZnO|Pc sample, for which the fast decay is the minor component. This model suggests that the relative population of Pc^+ is higher in the ZnO|Pc sample at delays longer than 20 ps. Although it has to be noted that in complete solar cells the photon-to-current conversion efficiency depends also on how fast the holes from the sensitizer are transferred to the electrolyte in liquid cells or hole-transporting material in solid-state cells. If this process is sufficiently fast, taking not more than a few tens of picoseconds, both systems, TiO_2|Pc and ZnO|Pc, are expected to be equally efficient. This conclusion is in line with the comparative study of Chandiran *et al.* [5].

5. Conclusion

Figure 7 summarizes the discussion of the differences between the TiO_2 nanoparticles (anatase) and ZnO nanorods (wurtzite) as the electron-collecting materials photosensitized by a Pc. The experimental results suggest that the primary electron injection is faster in the TiO_2 sample, in agreement with numerous previous observations. But the charge recombination is also faster in TiO_2. Furthermore, a relatively large number of the injected electrons recombine with the Pc cation on the semiconductor surface within a few tens of picoseconds in the case of TiO_2, but not in ZnO. Overall, the yield of Pc cations and thus the yield of the electrons injected into the anode is higher in ZnO at delays longer than 20 ps with the difference increasing with the delay time. This advantage of ZnO nanorods may be due to two factors: higher electron mobility in ZnO than in TiO_2, and a longer travelling distance in ZnO nanocrystals and nanorods, which helps to separate electrons and surface cations, Pc^+, more efficiently in the case of ZnO.

Data accessibility. This article has no additional data.

Authors' contributions. N.V.T. and T.T. conceived the project; Pc was designed and synthesized by M.I. and T.T.; solid samples were prepared by K.V. and E.T., and measured by K.V.; the data analysis was carried out by N.V.T. and K.V.; the manuscript was drafted by N.V.T. All authors gave final approval for publication.

Competing interests. The authors declare no competing interests.

Funding. Spanish MINECO (CTQ2017-85393-P) and the Comunidad de Madrid (FOTOCARBON, S2013/MIT-2841) are highly acknowledged.

Acknowledgements. K.V. acknowledges the Doctoral Programme of Tampere University of Technology for the financial support.

References

1. Hardin BE, Snaith HJ, McGehee MD. 2012 The renaissance of dye-sensitized solar cells. *Nat. Photonics* **6**, 162–169. (doi:10.1038/nphoton.2012.22)
2. Ye M, Wen X, Wang M, Iocozzia J, Zhang N, Lin C, Lin Z. 2015 Recent advances in dye-sensitized solar cells: from photoanodes, sensitizers and electrolytes to counter electrodes. *Mater. Today* **18**, 155–162. (doi:10.1016/j.mattod.2014.09.001)
3. Anta JA, Guillén E, Tena-Zaera R. 2012 ZnO-based dye-sensitized solar cells. *J. Phys. Chem. C* **116**, 11 413–11 425. (doi:10.1021/jp3010025)
4. Idígoras J, Sobuś J, Jancelewicz M, Azaceta E, Tena-Zaera R, Anta JA, Ziółek M. 2016 Effect of different photoanode nanostructures on the initial charge separation and electron injection process in dye sensitized solar cells: a photophysical study with indoline dyes. *Mater. Chem. Phys.* **170**, 218–228. (doi:10.1016/j.matchemphys.2015.12.042)
5. Chandiran AK, Abdi-Jalebi M, Nazeeruddin MK, Grätzel M. 2014 Analysis of electron transfer properties of ZnO and TiO_2 photoanodes for dye-sensitized solar cells. *ACS. Nano* **8**, 2261–2268. (doi:10.1021/nn405535j)
6. Listorti A, O'Regan B, Durrant JR. 2011 Electron transfer dynamics in dye-sensitized solar cells. *Chem. Mater.* **23**, 3381–3399. (doi:10.1021/cm200651e)
7. Asbury JB, Hao E, Wang Y, Ghosh HN, Lian T. 2001 Ultrafast electron transfer dynamics from molecular adsorbates to semiconductor nanocrystalline thin films. *J. Phys. Chem. B* **105**, 4545–4557. (doi:10.1021/jp003485m)
8. Szarko JM, Neubauer A, Bartelt A, Socaciu-Siebert L, Birkner F, Schwarzburg K, Hannappel T, Eichberger R. 2008 The ultrafast temporal and spectral characterization of electron injection from perylene derivatives into ZnO and TiO_2 colloidal films. *J. Phys. Chem. C* **112**, 10 542–10 552. (doi:10.1021/jp800980t)
9. Furube A, Katoh R, Hara K. 2014 Electron injection dynamics in dye-sensitized semiconductor nanocrystalline films. *Surf. Sci. Rep.* **69**, 389–441. (doi:10.1016/j.surfrep.2014.09.003)
10. Hakola H, Pyymaki PA, Myllyperkiö P, Kurotobi K, Lipsanen H, Imahori H, Lemmetyinen H, Tkachenko NV. 2014 Photo-induced electron transfer at nanostructured semiconductor–zinc porphyrin interface. *Chem. Phys. Lett.* **592**, 47–51. (doi:10.1016/j.cplett.2013.11.028)
11. Borgwardt M, Wilke M, Kampen T, Mähl S, Xiao M, Spiccia L, Lange KM, Kiyan IY, Aziz EF. 2016 Charge transfer dynamics at dye-sensitized ZnO and TiO_2 interfaces studied by ultrafast XUV photoelectron spectroscopy. *Sci. Rep.* **6**, 24422. (doi:10.1038/srep24422)
12. Němec H, Rochford J, Taratula O, Galoppini E, Kužel P, Polívka T, Yartsev A, Sundström V. 2010 Influence of the electron-cation interaction on electron mobility in dye-sensitized ZnO and TiO_2 nanocrystals: a study using ultrafast terahertz spectroscopy. *Phys. Rev. Lett.* **104**, 197401. (doi:10.1103/PhysRevLett.104.197401)
13. Baldini E, Palmieri T, Rossi T, Oppermann M, Pomarico E, Auböck G, Chergui M. 2017 Interfacial electron injection probed by a substrate-specific excitonic signature. *J. Am. Chem. Soc. C* **139**, 11 584–11 589. (doi:10.1021/jacs.7b06322)
14. Tiwana P, Docampo P, Johnston MB, Snaith HJ, Herz LM. 2011 Electron mobility and injection dynamics in mesoporous ZnO, SnO_2 films used in dye-sensitized solar cells. *ACS. Nano* **5**, 5158–5166. (doi:10.1021/nn201243y)
15. Saarenpää H *et al.* 2012 Self-assembled porphyrins on modified zinc oxide nanorods: development of model systems for inorganic-organic semiconductor interface studies. *J. Phys. Chem. C* **116**, 2336–2343. (doi:10.1021/jp2104769)
16. Ragoussi ME, Yum JH, Chandiran AK, Ince M, de la Torre G, Grätzel M, Nazeeruddin MK, Torres T. 2014 Sterically hindered phthalocyanines for dye-sensitized solar cells: influence of the distance between the aromatic core and the anchoring group. *ChemPhysChem* **15**, 1033–1036. (doi:10.1002/cphc.201301118)
17. Hakola H, Sariola-Leikas E, Efimov A, Tkachenko NV. 2016 Effect of hole transporting material on charge transfer processes in zinc phthalocyanine sensitized ZnO nanorods. *J. Phys. Chem. C* **120**, 7044–7051. (doi:10.1021/acs.jpcc.6b01583)

18. Virkki K *et al.* 2017 Photoinduced electron injection from zinc phthalocyanines into zinc oxide nanorods—aggregation effects. *J. Phys. Chem. C* **121**, 9594–9605. (doi:10.1021/acs.jpcc.7b01562)
19. Ye S *et al.* 2013 Role of adsorption structures of Zn-porphyrin on TiO_2 in dye-sensitized solar cells studied by sum frequency generation vibrational spectroscopy and ultrafast spectroscopy. *J. Phys. Chem. C* **117**, 6066–6080. (doi:10.1021/jp400336r)
20. Stranius K, George L, Efimov A, Ruoko TP, Pohjola J, Tkachenko NV. 2015 Photophysical study of a self-assembled donor-acceptor two-layer film on TiO_2. *Langmuir* **31**, 944–952. (doi:10.1021/la5025873)
21. Hayashi H *et al.* 2009 Effects of electrode structure on photoelectrochemical properties of ZnO electrodes modified with porphyrin-fullerene composite layers with an intervening fullerene monolayer. *J. Phys. Chem. C* **113**, 10 819–10 828. (doi:10.1021/jp902623g)
22. Virkki K, Demir S, Lemmetyinen H, Tkachenko NV. 2015 Photoinduced electron transfer in CdSe/ZnS quantum dot–fullerene hybrids. *J. Phys. Chem. C* **119**, 17 561–17 572. (doi:10.1021/acs.jpcc.5b04251)
23. Lehtivuori H, Efimov A, Lemmetyinen H, Tkachenko NV. 2007 Distributed decay kinetics of charge separated state in solid films. *Chem. Phys. Lett.* **437**, 238–242. (doi:10.1016/j.cplett.2007.02.029)
24. Guldi DM, Zilbermann I, Gouloumis A, Vazquez P, Torres T. 2004 Metallophthalocyanines: versatile electron-donating building blocks for fullerene dyads. *J. Phys. Chem. B* **108**, 18 485–18 494. (doi:10.1021/jp047105z)
25. Fukuzumi S, Ohkubo K, Ortiz J, Gutiérrez AM, Fernández-Lázaro F, Sastre-Santos A. 2005 Formation of a long-lived charge-separated state of a zinc phthalocyanine-perylenediimide dyad by complexation with magnesium ion. *Chem. Commun.* **30**, 3814–3816. (doi:10.1039/b506412k)

Publication III

Kirsi Virkki, Hanna Hakola, Maxence Urbani, Lara Tejerina, Mine Ince, M. Victoria Martínez-Díaz, Tomás Torres, Viktoria Golovanova, Viacheslav Golovanov, and Nikolai V. Tkachenko. Photoinduced Electron Injection from Zinc Phthalocyanines into Zinc Oxide Nanorods: Aggregation Effects, *Journal of Physical Chemistry C*, vol. 121, no. 17, pp. 9594 – 9605, 2017.

THE JOURNAL OF PHYSICAL CHEMISTRY C

Article

pubs.acs.org/JPCC

Photoinduced Electron Injection from Zinc Phthalocyanines into Zinc Oxide Nanorods: Aggregation Effects

Kirsi Virkki,[*,†] Hanna Hakola,[†] Maxence Urbani,[‡,¶] Lara Tejerina,[‡] Mine Ince,[‡,#] M. Victoria Martínez-Díaz,[‡,§] Tomás Torres,[‡,¶,§] Viktoria Golovanova,[∥] Viacheslav Golovanov,[∥] and Nikolai V. Tkachenko[*,†]

[†]Laboratory of Chemistry and Bioengineering, Tampere University of Technology, P.O. Box 541, FI-33101 Tampere, Finland

[‡]Departamento de Química Orgánica, Universidad Autónoma de Madrid, Cantoblanco, 28049 Madrid, Spain

[¶]Instituto Madrileño de Estudios Avanzados (IMDEA)-Nanociencia, C/Faraday, 9, Cantoblanco, 28049 Madrid, Spain

[§]Institute for Advanced Research in Chemical Sciences (IAdChem), Universidad Autónoma de Madrid, 28049 Madrid, Spain

[∥]South−Ukrainian National Pedagogical University, Staroportofrankovskaya str. 26, 65020, Odessa, Ukraine

[#]Department of Energy Systems Engineering Faculty of Tarsus Technology, Mersin University, 33480 Mersin, Turkey

Supporting Information

ABSTRACT: Phthalocyanines (Pc) are well-known light-harvesting compounds. However, despite the tremendous efforts on phthalocyanine synthesis, the achieved energy conversion efficiencies for Pc-based dye-sensitized solar cells are moderate. To cast light on the factors reducing the conversion efficiency, we have undertaken a time-resolved spectroscopy study of the primary photoinduced reactions at a semiconductor-Pc interface. ZnO nanorods were chosen as a model semiconductor substrate with enhanced specific surface area. The use of a nanostructured oxide surface allows to extend the semiconductor-dye interface with a hole transporting layer (spiro-MeOTAD) in a controlled way, making the studied system closer to a solid-state dye-sensitized solar cell. Four zinc phthalocyanines are compared in this study. The compounds are equipped with bulky peripheral groups designed to reduce the self-aggregation of the Pcs. Almost no signs of aggregation can be observed from the absorption spectra of the Pcs assembled on a ZnO surface. Nevertheless, the time-resolved spectroscopy indicates that there are inter-Pc charge separation−recombination processes in the time frame of 1−100 ps. This may reduce the electron injection efficiency into the ZnO by more than 50%, pointing out to a remaining aggregation effect. Surprisingly, the electron injection time does not correlate with the length of the linker connecting the Pc to ZnO. A correlation between the electron injection time and the "bulkiness" of the peripheral groups was observed. This correlation is further discussed with the use of computational modeling of the Pc arrangements on the ZnO surface.

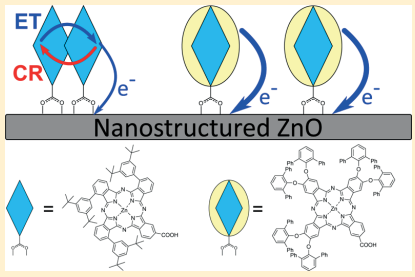

INTRODUCTION

Dye-sensitized solar cells (DSSCs) have received a great attention in the research community ever since the first report by O'Regan and Grätzel.[1−3] When compared to conventional silicon-based solar cells, DSSCs are low-cost, lightweight, and easily scalable. When comparing to all-organic bulk heterojunction solar cells (BHJs), on the other hand, DSSCs provide a way to circumvent the need for a stable low−band gap polymer, which is often the bottleneck in BHJ design.[4,5]

Careful design of the dye is the key to enhance the power conversion efficiency in DSSCs. The dye should be photostable, it should have appropriate energy levels when compared to the semiconductor conduction band (i.e., it should be a good electron donor), and it should absorb throughout the solar spectrum. Especially, high molecular extinction is needed at around 700 nm, where the solar photon flux is maximized. Phthalocyanines (Pc) meet all of these requirements fairly well, and thus, they have been extensively studied in DSSC applications.[4,6−13] The power conversion efficiency for Pc-based DSSCs, however, is lower than that of the best DSSCs based on porphyrin derivatives or ruthenium dyes.[8−11]

The power conversion efficiency of a solar cell is probably the most important parameter characterizing the cell, providing information on the cell performance at a glance. However, when taken alone it does not allow to shed light on the numerous factors contributing to the cell performance. This information would be gravely needed especially if the cell performance is not optimal. The photoinduced electron injection in phthalocyanine- or porphyrin-based DSSCs take place in the femto- to picosecond time scale,[5,14−17] and

Received: February 17, 2017
Revised: April 13, 2017
Published: April 13, 2017

DOI: 10.1021/acs.jpcc.7b01562
J. Phys. Chem. C 2017, 121, 9594−9605

therefore, ultrafast spectroscopic methods are needed to analyze the reaction kinetics and to explain the reasons leading to differences in the performance in different solar cell designs.

Although the photoinduced electron injection is fast, there are a number of alternative deactivation reaction pathways that can compete with it. Probably the most common and well-known deactivation pathway is aggregation of dyes, which may increase the nonradiative relaxation rate through intermolecular interactions or other processes sensitive to aggregation (internal conversion and intersystem crossing).

Reducing aggregation is crucial for improving the solar cell performance. It has been previously reported that the aggregation can be reduced either by adding cosensitizers such as CDCA, or by adding bulky substituents into the phthalocyanine core.[5,12,13] Matsuzaki et al.[5] noted that the substituent approach enhances the performance even more than the use of cosensitizers. This rises the importance of a quantitative evaluation of the degree of aggregation in the Pcs. For phthalocyanine sensitizers particularly, the aggregation has a remarkable effect on the solar cell performance.[13,18−20]

A faster electron injection is a natural way to increase the competitiveness of the desired electron transfer process. The electron transfer reaction is controlled to a great extent by the distance between the semiconductor substrate and the sensitizing dye. Therefore, a detailed understanding of the sensitizing dye orientation and molecular packing on the semiconductor surface is critical for improving the charge transfer parameters. An important tool for analysis of such interfaces is computational modeling. It can address many aspects of practical importance including conformations and arrangements of organic molecules on semiconductor oxide surfaces.[20−23]

In real solar cell devices, the photoinduced electron injection from the sensitizing dye into the semiconductor is just the first step in a series of charge transfer reactions leading to photocurrent generation. In this respect, solid-state hole transporting materials (HTMs) have aroused a growing interest in the recent studies.[24,25] When compared to liquid electrolytes, solid HTMs provide a less complex solar cell design and a better thermodynamic stability.[26] The most widely used solid-state HTM is spiro-MeOTAD, with which over 7% overall power conversion efficiency has been reported.[24,27] Furthermore, direct spectroscopic evidence on the hole transfer into the spiro-MeOTAD layer from the sensitizing dye and on the dye regeneration kinetics can be obtained.[28,29]

Herein we report on a time-resolved spectroscopy study of a series of zinc phthalocyanines on zinc oxide (ZnO) surface. Some of the phthalocyanines were already tested in TiO_2 DSSC applications, demonstrating a reasonable efficiency up to 6%. Unlike in the previous experiments, ZnO nanorods were used here to prepare model samples. ZnO is the second most widely used electrode material after TiO_2.[30−32] One of its advantages is higher electron mobility, but more importantly for this study, vertically aligned ZnO nanorods have simpler morphology. Thus, filling the voids between the nanorods by the HTM can be reliably monitored by electron microscopy. The experimental results, supported by computational modeling, suggest that the peripheral substituents play an important role both in reducing aggregation effects and in achieving a fast electron injection into the semiconductor.

METHODS AND MATERIALS

Materials. Ethanol (EtOH) (≥99.5% by mass) was purchased from Altia Plc. Acetonitrile (MeCN), *tert*-butanol (*t*-BuOH), ethanolamine, hexamethylene tetramine, 2-methoxyethanol, toluene, zinc acetate dihydrate, and zinc nitrate hexahydrate were purchased from Sigma-Aldrich. 2,2′,7,7′-Tetrakis(*N*,*N*-di-*p*-methoxyphenylamino)-9,9′-spirobifluorene (hereafter denoted as spiro-MeOTAD or spiro) was purchased from Lumtec (Luminescence Technology Corp.). All solvents and chemicals were used without further purification. ITO-coated glass substrates (12 × 35 mm, ca. 30 Ω square resistance) were purchased from Solems and cleaned before use as described elsewhere.[29]

Chemical structures of the zinc phthalocyanines used are shown in Figure 1. Synthesis of the Pcs and their operation in

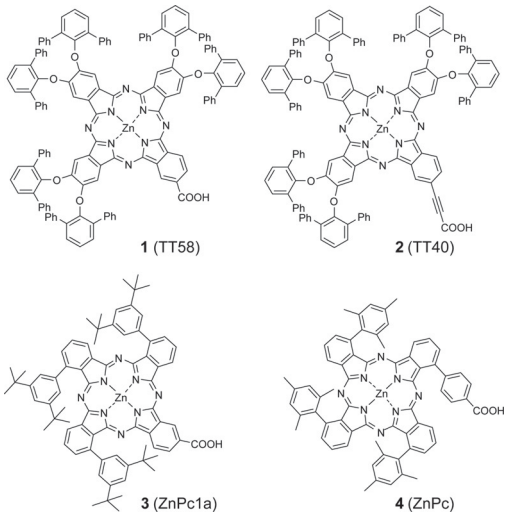

Figure 1. Chemical structures of the zinc phthalocyanines used in this study. The designations in the parentheses indicate the names of the compounds used in previous publications, see the main text for details.

DSSCs were reported previously. Compound **1** was published by Ragoussi et al. (as TT58),[12] compound **2** by Ragoussi et al. (as TT40),[11] and compound **3** by Tejerina et al. (as ZnPc1a).[13] The synthetic procedure, sample preparation details as well as the photophysical behavior of compound **4** on ZnO nanorods were reported elsewhere (as ZnPc).[29]

Sample Preparation. The ZnO nanorods (ZnOr) were grown by a hydrothermal method. The growth method has been extensively described earlier.[29,33] Briefly, a ZnO seed layer was prepared by spin-coating a 0.23 M zinc acetate sol (in 2-methoxyethanol:ethanolamine 96:4 by volume) onto UV-ozone treated (15 min) ITO substrates (1500 rpm, 60 s), and calcined at 380 °C for 20 min to produce ZnO. Then, the substrates were immersed upside down into the nanorod precursor solution (0.03 M zinc nitrate and 0.03 M hexamethylene tetramine in deionized Milli-Q H_2O) at 85 °C for 6 h. After the reaction, the substrates were removed from the precursor solution, rinsed thoroughly with Milli-Q H_2O, and dried in air. Typically, the hydrothermal growth produced ZnO nanorods approximately 790 ± 25 nm in length and 38 ±

DOI: 10.1021/acs.jpcc.7b01562
J. Phys. Chem. C 2017, 121, 9594−9605

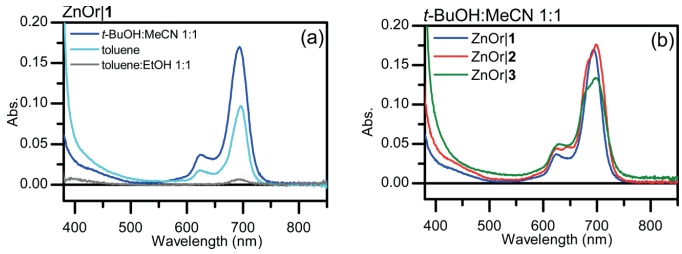

Figure 2. (a) Absorption spectra of ZnOr|**1** SAMs prepared from different solvents: *t*-BuOH:MeCN (blue), toluene (pale blue) and toluene:EtOH 1:1 (gray); (b) absorption spectra of ZnOr|**1** (blue), ZnOr|**2** (red), and ZnOr|**3** (green) SAMs prepared from *t*-BuOH:MeCN. The absorbance of ZnO nanorods has been subtracted from all spectra.

1 nm in diameter, as presented in Figure S1 in the Supporting Information.

The ZnO nanorod substrates were annealed at 300 °C for 30 min immediately prior to the monolayer formation. To deposit self-assembled monolayers (SAMs) of the Pcs, the ZnO nanorod substrates were immersed into solutions of the Pc's, typically for 30 min. The solutions were prepared in either EtOH, toluene, toluene:EtOH 1:1 (by volume), or *t*-BuOH:MeCN 1:1 (by volume) at 0.03−0.1 mM concentrations. After the reaction, the substrates were removed from the Pc solutions and washed by immersing them for 5 min into the pure solvent.

The sensitized ZnO nanorod samples were coated with a hole transporting layer, spiro-MeOTAD, following a reported procedure.[29] The spiro-MeOTAD layer was prepared by spin-coating (2000 rpm, 30 s) a 82 mM solution in anhydrous chlorobenzene onto the sensitized ZnO nanorod substrates.

Sample Characterization. Absorption spectra of the samples were measured using a Shimadzu UV-3600 UV−vis-NIR spectrophotometer in the range 350−850 nm. Absorption spectra of the compounds in *t*-BuOH:MeCN solutions can be found in Figure S2 in the Supporting Information.

Energies of the excited states of the phthalocyanines were estimated by using differential pulse voltammetry (DPV) (see the Supporting Information for details). The measurements show relatively small difference between the compounds (±0.1 eV), but for all Pcs the energy of the excited state is almost 1 eV above the lower edge of ZnO conduction band, which is in agreement with the general notion that Pcs are good photosensitizers in DSSC applications.[7,8]

The sensitized ZnO nanorod samples with and without the spiro-MeOTAD layer were imaged using a field emission scanning electron microscope (FE-SEM, Carl Zeiss Ultra 55).

Ultrafast transient absorption (TA) responses of the samples were measured using a pump−probe system described previously.[17,34] Briefly, the samples were excited by laser pulses at two wavelengths, 400 and 695 nm (Libra F, Coherent Inc., coupled with Topas C, Light Conversion Ltd.). A white continuum generator (sapphire crystal) was used to produce a probe beam. The TA responses were measured using an ExciPro TA spectrometer (CDP Inc.) equipped with a CCD array for the visible spectral range (460−770 nm), and an InGa diode array for the near-infrared wavelengths (840−1045 and 1050−1260 nm). The pulse repetition rate of the laser system was 1 kHz and the spectra were typically acquired by averaging over 5 s. All measurements were carried out with the samples placed in a chamber filled with nitrogen.

Modeling. In order to assess the morphology and conformations of the large Pc molecules on the ZnO surface in a more real condition, we have carried out a canonical ensemble−molecular dynamics simulations at room temperature (298 K) in a constant volume (NVT-MD) using Nose−Hoover thermostat, as implemented in the Forcite module of Materials Studio package.[35] The Dreiding force field[36] was used to evaluate the atomic forces, and the 100 ps trajectories for the studied Pc|ZnO systems were calculated with a 1 ps time step. The nonbonded electrostatic and van der Waals forces were controlled by Ewald and atom-based summation methods with the cutoff distance of 9.5 Å.

The hexagonal wurtzite structure of ZnO is the most common phase under ambient conditions. The structure consists of tetrahedrally coordinated zinc cations and oxygen anions. To model the most energetically favorable nonpolar $(10\bar{1}0)$ ZnO surface, we chose a 6-layer slab with the vacuum thickness in nonperiodic direction of 40 Å. Different supercells consisting of 6 × 3 × 6, 6 × 3 × 9, and 6 × 3 × 12 ZnO unit cells were used to test the interaction between the neighboring Pc molecules. For further calculations, we adapted the 6 × 3 × 9 supercell, since no appreciable correlations in the relaxed surface geometry were found in simulations with a larger supercell. The single phthalocyanine molecule was thus anchored onto a surface area of 29 × 31 Å, which corresponds to a surface coverage of 1/4 of a monolayer. This coverage was chosen to allow the dye to freely change its orientation and tilt angle on the surface. The phthalocyanine molecules were attached onto two zinc atoms via the carboxylic acid groups in a bidentate bridging mode, which ensures a strong chemical bonding and is predominant according to previous reports.[37] The models were optimized by allowing both surfaces of the slab, dye, and linker, to relax.

RESULTS

Sensitization of ZnO Nanorods. Compounds **1** and **2** were previously studied in DSSCs.[12] Then, SAMs of the compounds were deposited onto mesoporous titanium dioxide nanoparticle films from a toluene solution with 4−8 h reaction time. We discovered, however, that in the case of ZnO nanorods, 30 min reaction produces approximately the same absorbance as the longer reaction (see Figure S3 in the Supporting Information for the absorbances of **2**). Therefore, 30 min reaction time was used in all reactions hereafter.

Unfortunately, the absorbances for ZnOr|**1** samples prepared from toluene solutions were consistently lower than those for ZnOr|**2** samples. This was unexpected, since the two compounds are very alike in structure, the only difference

DOI: 10.1021/acs.jpcc.7b01562
J. Phys. Chem. C 2017, 121, 9594−9605

being the length of the spacer connecting the carboxylic group to the phthalocyanine core. Thus, we concluded that toluene might not be an appropriate solvent for the SAM formation for compound **1**. Two-component solvent mixtures were tested: toluene:EtOH (1:1 by volume) and *t*-BuOH:MeCN (1:1 by volume). Absorption spectra for the ZnOr|**1** samples prepared from different solvents are presented in Figure 2a. For the toluene:EtOH mixture, absorbance of the ZnOr|**1** sample was essentially zero. The *t*-BuOH:MeCN mixture, on the other hand, produced a film with a maxmimum absorbance of 0.17. In fact, we observed that *t*-BuOH:MeCN produced films with maximum absorbances of 0.15−0.2 for all of the compounds (see Figure 2(b)), higher than the absorbances achieved using other solvents. This absorbance indicates nearly complete layer formation on ZnO surface with area per molecule being roughly 2 nm^2 (see the Supporting Information for details). Therefore, *t*-BuOH:MeCN was chosen as the solvent mixture to prepare the samples for further studies. Absorption spectra for ZnOr|**2** and ZnOr|**3** prepared from different solvents are presented in Figure S4 in the Supporting Information.

The absorption maximum positions as well as the bandwidths of the absorption spectra (as fwhm) for the studied compounds can be found in Table 1. When comparing the absorption spectra of the phthalocyanine SAMs to those measured from the corresponding *t*-BuOH:MeCN solutions, minor changes were observed. For compounds **1** and **2**, the split feature in the Q-band observed for solutions disappears upon SAM formation. The deformation of the absorption spectrum shape induces a minor red-shift in the position of the absorption maximum. The bandwidth, however, remains practically unchanged for these two compounds. This suggests that there is little or no molecular aggregation in the ZnOr|**1** and ZnOr|**2** samples.

Table 1. Absorption Maximum Positions (λ_{Amax}, ± 1 nm) and Bandwidths (FWHM, ± 3 nm) of the Absorption Spectra for the Phthtalocyanines in Solution and SAMs on ZnO Nanorods[a]

sample	λ_{Amax}/nm	fwhm/nm
1 in *t*-BuOH:MeCN	676 and 691	37
ZnOr|**1**	694	36
ZnOr|**1**|spiro	695	33
2 in *t*-BuOH:MeCN	679 and 693	40
ZnOr|**2**	698	47
ZnOr|**2**|spiro	699	40
3 in *t*-BuOH:MeCN	687	29
ZnOr|**3**	698	55
ZnOr|**3**|spiro	687	45
4 in butanol	679	19
ZnOr|**4**	681	34
ZnOr|**4**|spiro	688	32

[a]The values for **4** have been published earlier.[29]

For compound **3**, the changes are more pronounced. The absorption maximum of the SAM sample is 11 nm red-shifted when compared to the *t*-BuOH:MeCN solution, and the absorption spectrum is clearly broadened (fwhm 29 nm for the solution and 55 nm for the ZnOr|**3** sample, respectively). It seems that there are some molecular aggregates in the ZnOr|**3** sample due to the smaller substituents attached to the Pc core.

The absorption spectrum of **4** was published earlier.[29] Briefly, a minor shift in the absorption maximum as well as a small spectral broadening upon monolayer formation suggest that the degree of aggregation is low in the ZnOr|**4** samples.

Spiro-MeOTAD Coating. The interactions between the Pcs and a hole transporting material were investigated using samples coated with spiro-MeOTAD. The hole transporting layer may affect the system behavior in two ways. First, it may capture the hole left in the Pc SAM after an electron is injected from the photoexcited Pc into the ZnO. This is the role of the HTM in dye sensitized solar cells.[38] Second, the primary charge separation reaction may take place at the Pc|spiro-MeOTAD interface, thus changing the sequence of the photoinduced charge transfer reactions.[29,39]

Absorption spectra of the sensitized ZnO nanorods coated with spiro-MeOTAD are shown in Figure 3, and the absorption maximum positions as well as the bandwidths are summarized in Table 1.

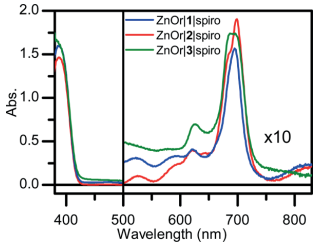

Figure 3. Absorption spectra of ZnOr|**1**|spiro (blue), ZnOr|**2**|spiro (red), and ZnOr|**3**|spiro (green). At 500−830 nm, the values have been multiplied by 10 for clarity. The absorbance of ZnO nanorods has been subtracted from all spectra.

Spiro-MeOTAD has a broad, yet small absorption across the whole visible range and a sharp band centered at ca. 390 nm. Absorption spectra of the ZnOr|dye|spiro samples are close to superpositions of the dye and spiro-MeOTAD absorptions, though for all three dyes the Q-band width is smaller in the presence of spiro-MeOTAD. The most pronounced change was observed for **3**, for which the bandwidth decreases from 55 to 45 nm upon addition of the HTM (See Figure S5 in the Supporting Information for the absorption spectra before and after the spiro-MeOTAD coating). For this compound, also the Q-band maximum shifts to the blue by 11 nm and actually coincides with the absorption maximum in solution. This is in contrast to the change reported by Hakola et al. for **4**,[29] for which the addition of the spiro-MeOTAD layer shifted the absorption maximum to the red and decreased the bandwidth slightly.

Sample Morphology. Morphology of the spiro-MeOTAD layer was investigated by scanning electron microscopy. SEM images of Pc-sensitized and spiro-MeOTAD-covered ZnO nanorods as well as pristine nanorods are presented in Figure 4. The spatial resolution of the utilized SEM instrument is ca. 5 nm, and therefore, the zinc phthalocyanine SAM cannot be resolved from the SEM images. The spiro-MeOTAD layer, however, is clearly visible in all three samples as a gray layer around the nanorods. Practically all the voids between the rods seem to be filled with spiro-MeOTAD. Compared to the ZnO nanorods alone (Figure 4d), the individual nanorods are not seen as clear and there are some darker areas on the nanorod surfaces, indicating a close to complete infiltration of spiro-MeOTAD into the ZnO nanorod layer. The images suggest

DOI: 10.1021/acs.jpcc.7b01562
J. Phys. Chem. C 2017, 121, 9594−9605

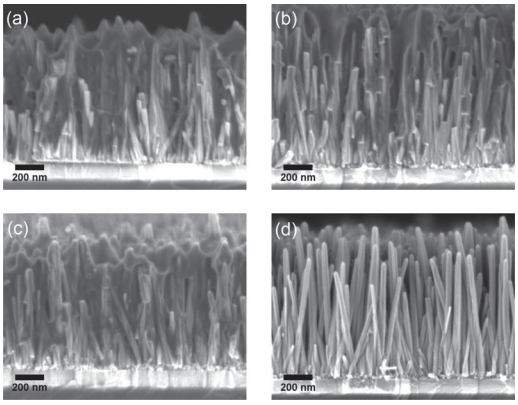

Figure 4. Cross-sectional SEM images of (a) ZnOr|**1**|spiro, (b) ZnOr|**2**|spiro, (c) ZnOr|**3**|spiro, and (d) ZnOr.

that the spiro-MeOTAD coverage is fairly homogeneous, and most of the Pc molecules are covered by the HTM layer.

Transient Absorption. Transient absorption measurements were carried out for SAMs prepared from *t*-BuOH:MeCN. Absorbances of all three samples studied here, ZnOr|**1**, ZnOr|**2** and ZnOr|**3**, were roughly the same and very close to that reported previously for ZnOr|**4**,[29] which suggests that the dye content in the monolayer was similar for these four phthalocyanines.

For the samples without spiro-MeOTAD, there was practically no difference in the transient absorption responses regardless of the excitation wavelength (400 or 695 nm). Spiro-MeOTAD, however, already has absorption at 400 nm. Thus, for spiro-MeOTAD-containing samples, it would be difficult to distinguish between the transient absorption signals arising from the Pc and the spiro-MeOTAD layers. At 695 nm, however, spiro-MeOTAD does not absorb, and selective excitation of the Pcs is achieved. Therefore, only the measurements carried out with excitation at 695 nm will be presented and discussed below.

The transient absorption raw data of ZnOr|**1** and ZnOr|**1**|spiro with corrected dispersion are presented in Figure 5. The response of ZnOr|**1** is relatively simple (Figure 5a). There is a decay with a few picosecond time constant and after that the transient spectrum stays relatively constant with two characteristic features: (i) a relatively narrow absorption band at 860 nm and (ii) a broad absorption in the 540−600 nm range. A similar behavior was observed for ZnOr|**4** in a previous study.[29] These spectral features are typical for phthalocyanine cations.[6,40] Therefore, this reaction was attributed to an electron injection from the singlet excited state of the phthalocyanine into the ZnO nanorod conduction band.

Addition of spiro-MeOTAD changes the response drastically at delay times of a few picoseconds and longer (Figure 5b). There is a new narrow absorption band close to 540 nm at long delay times (>0.5 ps). Furthermore, two distinct bands at 590 and 990 nm at a few picoseconds delay time (5−100 ps) are observed. One can also notice an increasing absorption toward longer wavelengths (>1100 nm) at long delay times (>0.5 ps). The band at 540 nm and the broad absorption in the IR range are typical of a spiro-MeOTAD cation,[38,41] and the bands at 590 and 990 nm are indicative of a Pc anion.[29,42] Therefore, at a

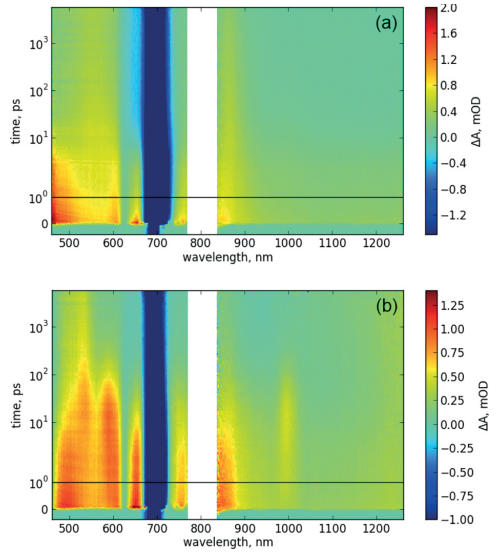

Figure 5. Two-dimensional transient absorption maps of (a) ZnOr|**1** and (b) ZnOr|**1**|spiro. Time scale is linear until 1 ps, and logarithmic at longer delays. The vertical blue strip around 695 nm arises from scattered excitation light.

qualitative level, the observed transient absorption response suggests a primary charge separation at the Pc|spiro interface, which yields a Pc anion and a spiro-MeOTAD cation in a few picoseconds delay time. Then, the Pc anion injects an electron into the ZnO nanorod in a few tens of picoseconds, leaving a long-lived state with the electron in the ZnO and the hole in the spiro-MeOTAD layer.

The heterogeneity of the system makes the quantitative analysis of the transient absorption data complicated. In particular, different molecular conformations and orientations of the Pc molecules on the ZnO surface can result in a distribution of distances and energies associated with the electron injection from the excited Pc into the ZnO. This heterogeneity results in a nonexponential time dependence of the reaction. If the distribution, however, is relatively narrow, a so-called distributed decay model can be used to overcome the problem.[43] This approach was used previously in order to analyze the transient absorption responses of **4** on ZnO nanorods,[29] and will be followed here.

Compound ***1***. The simplest fit model to get a reasonably good approximation for the ZnOr|**1** sample consists of three components: an exponential component with a time constant close to 0.3 ps, and two distributed decay components with average time constants of 5 ± 0.6 ps and 11 ± 5 ns, respectively. The resulting decay component spectra are presented in Figure 6a, together with time-resolved spectra at two characteristic delay times. The fit goodness can be improved by roughly 15% by adding one more exponential component, which results in splitting the fast component (0.3 ps) in two components with time constants 0.06 and 0.6 ps, but the main contribution of both of these components lies around the excitation wavelength (695 nm) and is due to the response perturbation by the scattered excitation light. Therefore, the fast response (<0.4 ps) will be ignored for now.

DOI: 10.1021/acs.jpcc.7b01562
J. Phys. Chem. C 2017, 121, 9594−9605

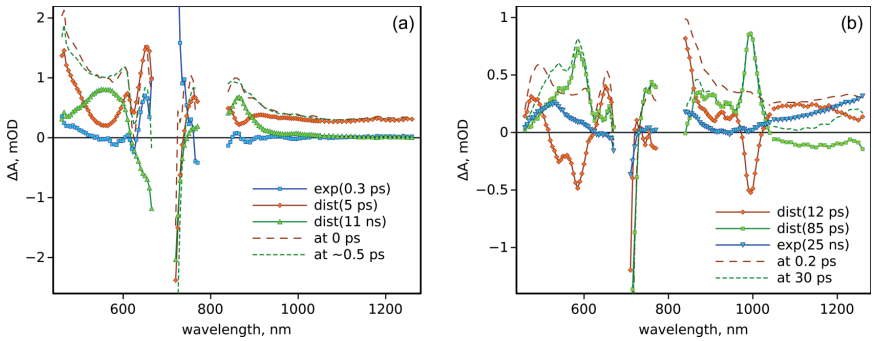

Figure 6. Transient absorption decay component spectra (lines with symbols) and time-resolved spectra (dashed lines) of (a) ZnOr|**1** and (b) ZnOr|**1**|spiro.

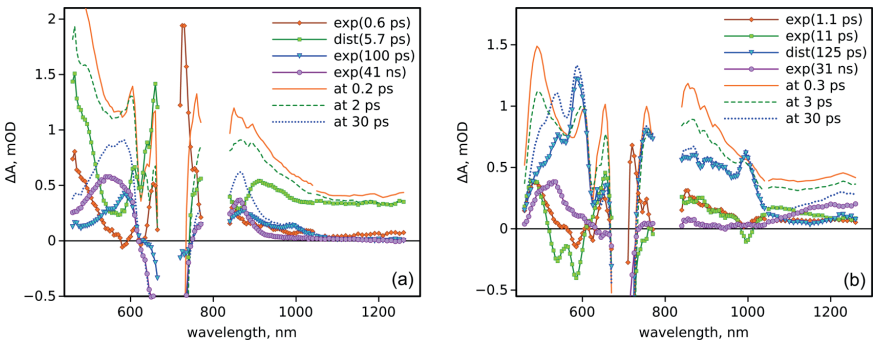

Figure 7. Transient absorption decay component spectra (lines with symbols) and time-resolved spectra (dashed lines) of (a) ZnOr|**2** and (b) ZnOr|**2**|spiro.

The main part of the transient absorption response at delay times of >0.4 ps can be decomposed in two components, as was presumed in the qualitative analysis above. The long-lasting response (11 ns) has a band at 865 nm, almost zero absorption at >960 nm, a broad absorption band around 560 nm and a bleached Q absorption band (around the excitation wavelength, 695 nm). This state can be identified as the Pc cation, Pc^+. The shorter-lived component (5 ps) is associated with the electron injection from the excited state of the Pc to the ZnO, ZnOr|Pc* → $ZnOr^-$|Pc^+.

The transient absorption data of ZnOr|**1**|spiro can be fitted very well with a four-component model. The fastest component has a time constant of only 60 fs, and it is solely due to the disturbance by the excitation light. The three other decay components are presented in Figure 6b, together with two time-resolved spectra at different delay times. The most distinct feature of the fit is the narrow band at 995 nm, which is formed with an average time constant of 12 ± 5 ps and decays with an average time constant of 85 ± 27 ps. There is another relatively sharp band at 585 nm with the same time constants for formation and decay as the 995 nm band. The decay of both of these bands leaves a transient absorption spectrum with a band around 530 nm and a smoothly rising absorption toward the longer wavelengths starting from 1000 nm. The latter can be identified as the spectrum of spiro-MeOTAD cation, and the bands at 585 and 995 nm can be attributed to the Pc anion,[29] which suggests that the main reaction course in this case is

$$\text{ZnOr|Pc*|spiro} \xrightarrow{12\ \text{ps}} \text{ZnOr|Pc}^-\text{|spiro}^+ \xrightarrow{85\ \text{ps}} \text{ZnOr}^-\text{|Pc|spiro}^+ \quad (1)$$

Compound 2. The transient absorption responses of the ZnOr|**2** and ZnOr|**2**|spiro samples were more complex compared to compound **1** (see Figure S6 in the Supporting Information for the 2D transient absorption maps). The minimum number of components to achieve a reasonable approximation is five for both sets of data. The fastest components with time constants of <0.1 ps are due to the excitation pulse disturbance and a side effect of the dispersion compensation, and will be ignored. The four other components (>0.1 ps) for each sample are presented in Figure 7 together with three time-resolved spectra at characteristic delay times. Although the main spectral features of the ZnOr|**2** and ZnOr|**2**|spiro samples are similar to those of the samples with **1**, the behavior of **2** is apparently more complex.

The difference in transient absorption responses of ZnOr|**1** and ZnOr|**2** samples, Figures 6a and 7a, respectively, lies in the fast 0.6 ps and middle 100 ps components observed for the ZnOr|**2** but not for ZnOr|**1**. These components are not strong, but they do have a feature at 990 nm, at the absorption wavelength of the Pc anion. The 100 ps component also shows decays at 585 and 865 nm, which are characteristic wavelengths of the Pc anion and cation, respectively. Presumably, there is a minor relaxation channel when the excited state of Pc generates

DOI: 10.1021/acs.jpcc.7b01562
J. Phys. Chem. C 2017, 121, 9594−9605

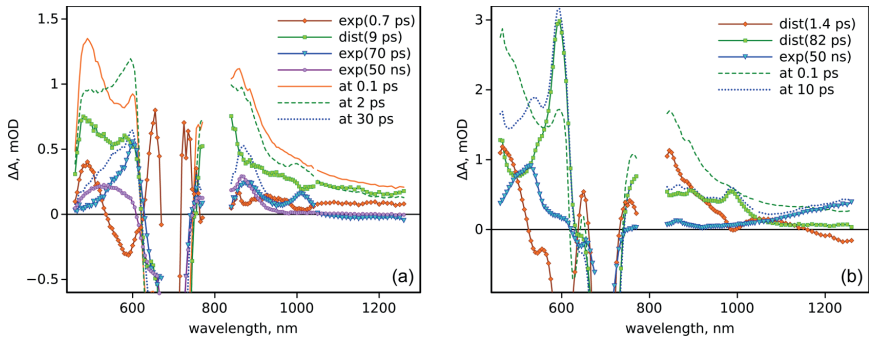

Figure 8. Transient absorption decay component spectra (lines with symbols) and time-resolved spectra (dashed lines) of (a) ZnOr|**3** and (b) ZnOr|**3**|spiro.

a charge-separated state (CS) between two Pc molecules that then recombines without injecting an electron into the ZnO. One can expect this type of a process to take place in Pc aggregates. These aggregates should be located relatively far from the ZnO surface, which will provide a competing quenching channel for the Pc excited state. This option will be discussed later in more detail.

The transient absorption response of ZnOr|**2**|spiro (Figure 7b) is reasonably similar to that of ZnOr|**1**|spiro (Figure 6(b)). Components with time constants 11 ps, 125 ps and 31 ns of ZnOr|**2**|spiro are well comparable to those of ZnOr|**1**|spiro (12 ps, 85 ps and 25 ns), with the main difference being the relative intensities of the Pc anion bands. An additional component in the response of ZnOr|**2**|spiro has a time constant of 1.1 ± 0.4 ps, which is close to 0.6 ± 0.2 ps of the sample without the spiro-MeOTAD layer, and it has also very similar spectrum shape. This is reasonable and indicates that the fast reactions in the ZnOr|**2** structure are not affected by the spiro-MeOTAD layer, that has an effect on the TA response only at a few picosecond delay and longer.

Compound **3**. The results of the transient absorption measurements of the ZnOr|**3** samples with and without spiro-MeOTAD are rather similar to those of the samples with **2**, and are presented in Figures 8 and S7 in the Supporting Information. However, for the ZnOr|**3** sample, the two fast components, 0.7 and 9 ps, have possibly to be assigned in a reverse manner, as will be discussed later. Another difference between the samples is the relatively simple behavior of the ZnOr|**3**|spiro sample. Only three components were sufficient to fit the data at delays >0.1 ps.

With the tentative assignment discussed above, the time constants of the different reactions for all three samples are summarized in Table 2. The electron injection time constant, τ_{inj}, is taken from the samples without the spiro-MeOTAD layer, the charge separation (CS) time constant, τ_{CS}, refers to the CS at the Pc|spiro interface, and the electron transfer, τ_{ET}, refers to the electron injection from the Pc anion into the ZnO that is observed in samples with spiro-MeOTAD as the consequence of the CS at the Pc|spiro interface. The transient absorption responses for **4** were analyzed and published previously.[29]

Table 2. Time Constants for the Electron Injection (τ_{inj}), Charge Separation (τ_{CS}), and Electron Transfer (τ_{ET})[a]

compound	τ_{inj}/ps	τ_{CS}/ps	τ_{ET}/ps
1	5.0 ± 0.6	12 ± 6	85 ± 27
2	5.7 ± 0.7	11 ± 2	125 ± 20
3	0.7 ± 0.2	1.4 ± 0.3	82 ± 5
4	1.4 ± 0.4	0.5 ± 0.3	120 ± 35

[a]The time constants for **4** were published previously.[29].

Modeling. The electron transfer reactions are largely controlled by the distance between the dye and the semiconductor surface plane. To study the distances, molecular dynamics (MD) modeling was employed. The MD modeling provided valuable information on the morphology and the mutual conformations in the organic−semiconductor interface that occur at real temperatures.

Figure 9 represents typical arrangements of the studied Pc molecules on the ZnO surface that were taken as an average from the molecular dynamics modeling at room temperatures. Since the electron density of the excited molecular orbital is distributed over the conjugated π-system, or the Pc macrocycle, the distance from the macrocycle edge to the semiconductor surface is the key parameter to compare the rates of electron transfer for different Pcs. The corresponding distances between the ZnO $(10\bar{1}0)$ surface plane and the nearest edge of the Pc macrocycle are listed in Table 3.

An important outcome of the modeling is that a longer linker ensures more degree of freedom for the single anchored molecule, resulting in a strong tilting and eventually in a shorter distance between the dye and the surface. In particular, compound **2** has a long linker and it therefore exhibits a high flexibility and strongly tilts toward the surface. This results in a substantial decrease in the distance between the Pc macrocycle and the ZnO surface by ca. 2.7 Å comparing to an upright position of the molecule. By contrast, tilting of the bulky **1** molecule with a shorter linker results in lowering of the Pc−ZnO distance only by 0.9 Å due to the steric restrictions.

Modeling of compounds **3** and **4** indicates that they do not tilt significantly, but the specific structure of **4** allows its macrocycle plane to appear much closer to the surface compared to **1** and **2**.

DISCUSSION

Pc Distance from the Surface. There are a few unexpected results in Table 2. First of all, the electron injection time constants for **1** and **2** are practically the same, even though **2** has a longer linker and one would expect a longer distance

DOI: 10.1021/acs.jpcc.7b01562
J. Phys. Chem. C 2017, 121, 9594−9605

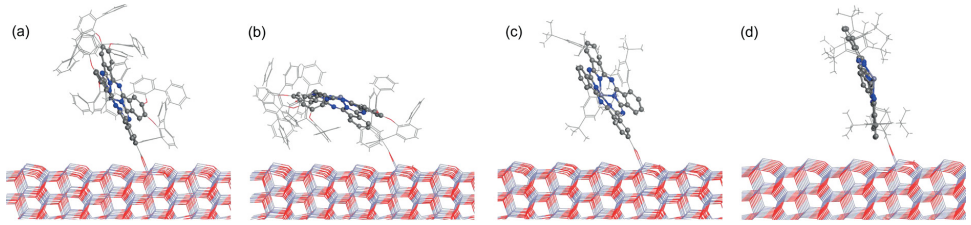

Figure 9. Relaxed geometries of (a) ZnOrl**1**, (b) ZnOrl**2**, (c) ZnOrl**3**, and (d) ZnOrl**4** after MD simulations. The macrocycle planes are rendered in a ball-and-stick model whereas other atoms are not shown by balls.

Table 3. Distance between the ZnO $(10\bar{1}0)$ Surface Plane and the Nearest Pc Macrocycle Edge in an Upright Alignment of the Adsorbed Dye (d_{up}) and after MD Relaxation (d_{tilt})

compound	d_{up}/Å	d_{tilt}/Å
1	4.02	3.10
2	6.63	3.89
3	4.02	3.03
4	2.95	2.62

between the Pc core and the ZnO surface, leading to a slower injection (Figure 1). If the linker between the ZnO surface and the Pc core is perpendicular to the surface, the difference in the distances must be roughly 2.8 Å. Assuming a through-space electron injection with a typical damping factor of 0.4 $Å^{-1}$,[44,45] the electron injection is expected to be three times faster from **1** into the ZnO than from **2**, which is apparently not the case. A similar electron injection time constant can be interpreted as a similar distance between the Pc core and the ZnO surface for these two compounds. The linker can be tilted, but obviously, the tilt angles must be different for **1** and **2**. This is in line with the modeling results showing a much larger tilt for **2** (Figure 9) and a vanishing difference in the macrocycle edge to ZnO surface distance for these two Pcs (Table 3). Therefore, we can conclude that **1** and **2** have different tilt angles, providing roughly the same distances between the Pc core and the ZnO surface for these two phthalocyanines, and thus roughly the same electron injection time constants.

Out of the four phthalocyanices presented in Table 2, the slowest electron injection is observed for **1** and **2** that have the most bulky peripheral groups. These two phthalocyanines are the most restricted when approaching the ZnO surface. The two other phthalocyanines, **3** and **4**, are more relaxed in conformations that allow them to stay closer to the ZnO surface.

Modeling suggests the shortest edge-to-surface distance for **4**, in line with the faster electron injection observed experimentally.[29] Despite the only slightly smaller edge-to-surface distance for compound **3**, the electron injection is faster than for compounds **1** and **2**. There are at least three reasons for this, also showing the complexity of the problem. First, the distance estimations were done for the snapshot conformations that were deduced from the molecular dynamics simulations and shown in Figure 9. These geometries represent the most probable arrangements of the molecule that were averaged from the simulations at real temperatures. Out of the four compounds modeled, **3** is the least restricted and has the most diverse set of conformers. The same conclusion can be drawn indirectly from the TA measurements. The fast response measured for **3** at delays <10 ps was fitted with two components with mixed features. The fit goodness can be improved by adding one more component but the resulting fit components are spectrally indistinguishable, indicating the coexistence of a few conformers. Second, the models were constructed to find orientations of single dyes on ZnO surface, which is achieved at a low surface density of Pcs. Compound **3** is the least protected from intermolecular interactions as will be discussed below, and apparently such interactions have a stronger effect on the surface organization of **3** compared to the other studied compounds. Third, measuring the distance from the Pc macrocycle edge to the ZnO surface plane in the framework of the chosen model essentially underestimates the bond lengths and neglects the actual wave function shapes on both the Pc and the ZnO, which may have an impact on the electron transfer rates, especially at distances as short as a few ångström.

It is worth noticing that the time constant for the electron transfer from the Pc anion into the ZnO nanorod is roughly 100 ps for all the four Pcs (τ_{ET} in Table 2). First, it is much slower than the electron injection from the Pc excited state, τ_{inj}, though in both cases the electron from the Pc LUMO is injected into ZnO. Most probably this difference is due to electrostatic interactions, particularly due to the presence of the spiro-MeOTAD cation nearby, which increases the potential barrier for the electron injection starting from the Pc anion as compared to the excited state. Second, according to our modeling, a characteristic time of motion of a Pc attached to the ZnO surface is in the range 50−100 ps, close to the electron transfer time constant τ_{ET}. Certain reorganization might be required to achieve a conformation favorable for the electron transfer from the phthalocyanine anion. However, this motion does not affect the electron injection of the excited Pc, τ_{inj}, and charge separation, τ_{CS}, which are much faster (<15 ps).

Effect of Aggregation. One of the goals in sensitizing semiconductors with organic dye molecules is to make the dye monolayer as dense as possible. Unfortunately, the higher the monolayer density, the higher the aggregation of dyes, which introduces alternative channels for the excited state relaxation and reduces the efficiency of the electron injection. A common practice to minimize the undesirable effects caused by aggregation is to equip the molecule with bulky peripheral groups that do not allow two dye molecules to stack together but that have no effect on the photophysical properties of the chromophores. All the four phthalocyanines discussed here have such aggregation-reducing groups. Although the quantitative evaluation of the degree of aggregation is rather complex, the first indication of aggregation is the change in the phthalocyanine absorption spectrum shape upon monolayer formation. As discussed earlier, there are some differences

DOI: 10.1021/acs.jpcc.7b01562
J. Phys. Chem. C 2017, 121, 9594−9605

between the solution and monolayer spectra for all the studied phthalocyanines (Figures 2b and S2 in the Supporting Information). The differences are relatively small and little to no aggregation effects can be expected based on the spectra. The transient absorption measurements, however, reveal one indication of the aggregation: a sharp absorption band at 995 nm is observed for ZnOr|**2** and ZnOr|**3** samples, but not for ZnOr|**1** and ZnOr|**4**. The band corresponds to the Pc anion, and the most reasonable cause for anion formation is the charge separation in the Pc aggregates: $Pc^*Pc \rightarrow Pc^+Pc^-$. This process can compete with the electron injection into ZnO: $ZnOr|Pc^* \rightarrow ZnOr^-|Pc^+$, and may reduce the efficiency of the injection. The Pc anion may inject an electron into ZnO and thus result in the $ZnOr^-|Pc^+$ state. However, this process competes with the intermolecular charge recombination, making the electron transfer from the excited state obviously less efficient than in the absence of competing reactions.

Although the absolute value of the electron injection efficiency cannot be easily evaluated from the transient absorption measurements, a relative comparison can be done based on the transient absorbance intensities at a few characteristic wavelengths and delay times. Taking compound **1** as the reference, one can assume that at a short delay after the excitation (roughly at 0.3 ps after excitation), the transient absorption spectrum is that of the singlet exited state. It has two maxima, one at 605 nm and another at 855 nm (Figure 6a, time-resolved spectrum at 0 ps delay). Relative to 605 nm, absorption of the band at 855 nm is 0.85 (Table 4). Relative absorption of the Pc cation band with maximum at 865 nm is 0.58 (Figure 6a, spectrum of the 11 ns component). For compound **2** (Figure 7a), however, the ratios are 0.86 and 0.26. The relative intensities at 855 nm/605 nm, 0.85 for **1** and 0.86 for **2**, are essentially the same, as can be expected since two singlet excited states are compared for rather similar phthalocyanines. The second pair of ratios, 855 nm at 4 ns relative to 605 nm at 0.3 ps, 0.58 for **1** and 0.26 for **2**, shows more than 2-fold difference, suggesting that the relative yield of the Pc cation is roughly two times lower for the sample with **2**.

Similar calculations for compound **3** give the relative intensities 1.21 and 0.29 for the band at 860 nm right after excitation and at 4 ns delay, respectively (Table 4). Substituents in **3** differ from those in **1** and **2**, and this is reflected in a difference in the absorption spectrum of the singlet excited state, 0.85 vs 1.21, for 860 nm band relative to that at 605 nm. Still the relative intensity of the cation band (around 860 nm at long delay time) is at least two times smaller for **3** comparing to **1**, suggesting a lower electron injection yield in the ZnOr|**3** sample relative to the ZnOr|**1** sample, meaning that there is a competing process reducing the injection efficiency. Actually, **3** is structurally more similar to **4**, for which the similar relative band intensities are also presented in Table 4. However, the difference in the intensities of 605 and 860 nm bands at the singlet excited state for these two phthalocyanines is fairly large, 1.21 vs 0.36, making further comparison rather unreliable.

To get some quantitative evaluation on the aggregation process, leading to an inter-Pc charge separation and subsequently to the appearance of a Pc anion as discussed previously, relative intensities at the 995 nm band at a 30 ps delay time are listed in Table 4. At this delay time, the absorption is maximal but the singlet excited state has mostly disappeared. The ZnOr|**3** sample has the strongest relative absorption at this wavelength (0.31, at least two times larger than for any other compound). Thus, ZnOr|**3** is the most aggregated sample out of the four studied here.

Table 4. Transient Absorptions at Selected Wavelengths and Delay Time Relative to That at 605 nm Shortly after Excitation (ca. 0.3 ps)[a]

sample	860 nm at 0.3 ps	860 nm at 4 ns	995 nm at 30 ps	530 nm at 4 ns	1250 nm at 4 ns
ZnOr|**1**	0.85	0.58	0.06	–	0.01
ZnOr|**1**| spiro	2.55	0.46	2.30	0.65	0.76
ZnOr|**2**	0.81	0.26	0.12	–	0.00
ZnOr|**2**| spiro	1.19	0.07	0.65	0.38	0.30
ZnOr|**3**	1.21	0.29	0.31	–	0.00
ZnOr|**3**| spiro	0.91	0.07	0.33	0.49	0.19
ZnOr|**4**	0.36	0.29	0.06	–	0.01
ZnOr|**4**| spiro	1.30	0.53	0.68	0.99	0.64

[a]The wavelengths and delay times are indicative since the values were taken from the maxima which varies within 10 nm from sample to sample. Results shown for **4** were taken from data published previously.[29].

Efficiency of Hole Injection to HTM. As discussed previously, addition of spiro-MeOTAD changes the spectrum of the long-lived state quite drastically. Table 4 presents the relative intensity at 1250 nm as an indicator of the spiro-MeOTAD cation band. The near-infrared wavelength was chosen to represent this moiety for selectivity reasons: no absorption at 1250 nm is expected to arise from the Pcs, as is clearly seen from the samples without spiro-MeOTAD. In addition to the spiro-MeOTAD cation, the remaining Pc cations (or anions) also contribute to the absorption at 530 nm. Thus, by choosing the near-infrared band we can selectively compare the yield of holes in the spiro-MeOTAD layer in the different samples. Comparison of the relative intensities at 1250 nm suggests that **1** and **4** have the highest yield of holes in the spiro-MeOTAD layer (band ratios are 0.76 and 0.64, respectively). For the ZnOr|**2**|spiro sample (ratio is 0.30), the yield of holes is roughly two times lower than the ZnOr|**1**|spiro sample. This comparison should be reasonably accurate, since the two phthalocyanines are structurally very similar, though the proportion of the 860 and 605 nm bands is unexpectedly high for the ZnOr|**1**|spiro sample. The lower yield of holes in the ZnOr|**2**|spiro sample can be explained by the higher degree of aggregation, and eventually a different type of packing of the **2** molecules on the ZnO surface compared to **1**. According to the data presented in Table 4, the lowest yield of holes was observed in the ZnOr|**3**|spiro sample (ratio is 0.19), that also has the strongest Pc anion feature without the spiro-MeOTAD layer. Most probably, **3** forms the most aggregated layer on the ZnO surface, and has the lowest efficiency of the long distance charge separation. Both **1** and **4** are expected to have a long distance charge separation yield close to unity.

Effect of HTM on Pc Layer Organization. Another interesting result is the change in the rate of the primary charge separation reaction of the samples upon addition of the spiro-MeOTAD layer, summarized in Table 2. There are two competing charge transfer reactions after the excitation of the Pc, (i) the electron injection into ZnO before the spiro-MeOTAD deposition, τ_{inj}, and (ii) the charge separation at the Pc|spiro interface, τ_{CS}. With the exception of **4**, an obvious problem is that τ_{CS} is longer than τ_{inj}. The charge separation is

DOI: 10.1021/acs.jpcc.7b01562
J. Phys. Chem. C 2017, 121, 9594−9605

nevertheless a dominating reaction pathway for the Pc excited state relaxation with the spiro-MeOTAD layer. This means that the addition of the spiro-MeOTAD layer gradually slows down the electron injection from the Pc into the ZnO. This observation suggests that the alignment of the phthalocyanine molecules on the ZnO nanorod surface is different with and without the spiro-MeOTAD layer.

Some narrowing of the absorption Q-band upon addition of spiro-MeOTAD layer was noticed (see Table 1) for all four samples, also suggesting a change in arrangement. Actually, narrower bands can be interpreted as lower degree of aggregation. This can be rationalized by assuming that the spiro-MeOTAD molecules partially penetrate between the Pc molecules, which can be visualized by a more upright alignment of the Pcs in the SAMs covered by spiro-MeOTAD, resulting in an increase in the distance from the ZnO surface and a slower electron injection into the ZnO, respectively.

Out of the three studied phthalocyanines studied here, **1** is the least aggregated. No efficiency losses in converting the excitation photons to electrons in the conduction band of ZnO and to holes in the HTM, respectively, were detected in time-resolved spectroscopy study of the system. Therefore, **1** can be considered as a good candidate for solar cell applications. However, it is important to pay attention to the time constant of the electron injection into ZnO, which is close to 5 ps and roughly one order in magnitude slower than that for a porphyrin on ZnO surface.[16] Typical electron injection times for good sensitizers on TiO_2 are also much faster (0.1−2 ps).[14,20,46] Nevertheless, the **1** cation lifetime is rather long (>10 ns) and should be sufficient for the hole utilization by a suitable hole transporting material, e.g., spiro-MeOTAD. Unfortunately, even small, barely detectable aggregation may reduce the charge injection efficiency gradually through an intra-aggregate charge separation−recombination sequence. According to the presented results, the efficiency of the electron injection into ZnO for **2** is 50% lower than that for **1**. This difference can only be identified by an ultafast transient absorption spectroscopy study, whereas simple steady state absorption spectra are unable to reveal any differences between the samples.

Performance of Phthalocyanines in DSSCs. Three of the studied Pcs were tested in traditional DSSC on TiO_2 electrodes, combined with a triiodide/iodide electrolyte.[12,13] Although the operational environments are different with that used in this study, the spectroscopic results presented here agree well with the solar cell studies reported. The internal photon-to-current efficiency (IPCE) was the highest for DSSC sensitized with compound **1**, reaching 95% at maximum. One can conclude that the primary electron injection efficiency at TiO_2|**1** interface is at least 95%. For compound **3**, the IPCE at the maximum was close to 70%, which can be explained by the aggregation and loss in efficiency due to the intermolecular charge separation according to the results presented here.

The reason to use ZnO nanorods in this study instead of TiO_2 is that we have to ensure a complete coverage of the Pc monolayer by the spiro-MeOTAD HTM. This task is rather complicated in the case of a fine mesoporous TiO_2 nanoparticle film, but reasonably easily achievable for ZnO nanorods by taking cross-sectional SEM images of the samples. The same ZnO nanorod structures and spiro-MeOTAD can be used for preparing solid state DSSCs.[47] This may have an advantage of higher electron mobility in bulk ZnO compared to TiO_2. However, a practical complication is to find such deposition conditions for the HTM that it covers all nanorods which have a distribution of lengths, but the HTM layer is not too thick and does not add additional resistivity. This work is under way at present.

CONCLUSIONS

Phthalocyanines are well-known and efficient light-harvesting and electron-donating dyes, which makes them attractive for use in applications such as solar cells. On the other hand, the known drawback of phthalocyanines is their strong tendency toward aggregation. Four zinc phthalocyanine derivatives discussed above were designed to gradually reduce the aggregation by the addition of bulky peripheral groups, and our results indicate that this goal was largely achieved. Electron injection initiated by the excitation of the dyes was observed for all four compounds. However, the electron injection efficiency may vary by more than 50% from sample to sample, being reduced by competing intermolecular charge separation−recombination reactions for two of the phthalocyanines. The rate of the electron injection is very different for the different compounds, and can hardly be predicted considering only the linker connecting the Pc to ZnO surface. It seems that whenever possible, phthalocyanines tend to adopt a conformation with as close as possible positioning of the macrocycle to the ZnO surface. Molecular dynamics modeling of the zinc phthalocyanines has proved the assumption that the macrocycles of all the four molecules examined tend to tilt at different angles relative to the ZnO surface, showing reasonable correlation with the measured reaction time constants. The distance between the macrocycle and the semiconductor surface is determined by factors such as conformations and spatial arrangement of the aggregation-reducing groups, but not solely by the linker length. This makes the design of optimal phthalocyanine dyes a challenging task.

ASSOCIATED CONTENT

Supporting Information

The Supporting Information is available free of charge on the ACS Publications website at DOI: 10.1021/acs.jpcc.7b01562.

Cross-sectional SEM images of the hydrothermally grown ZnO nanorods, molar absorption coefficients of compounds **1**, **2**, and **3** in *t*-BuOH:MeCN, absorption spectra for SAMs of the compounds prepared from different solvents, absorption spectra of ZnO nanorods sensitized with **3** before and after the spiro-MeOTAD layer addition, HOMO and LUMO energies estimated from differential pulse voltammetry, estimations of area per Pc molecule on ZnO surface, and 2D transient absorption maps for the ZnO|**2** and ZnO|**3** samples with and without spiro-MeOTAD (PDF)

AUTHOR INFORMATION

Corresponding Authors

*(K.V.) E-mail: kirsi.virkki@tut.fi.

*(N.V.T.) E-mail: nikolai.tkachenko@tut.fi.

ORCID

Kirsi Virkki: 0000-0003-4976-3917

Nikolai V. Tkachenko: 0000-0002-8504-2335

Notes

The authors declare no competing financial interest.

DOI: 10.1021/acs.jpcc.7b01562
J. Phys. Chem. C 2017, 121, 9594−9605

■ ACKNOWLEDGMENTS

N.V.T. and H.H. are grateful to the Academy of Finland for financial support (No 263486). H.H. also acknowledges "Competitive Funding to Strengthen University Research Profile" by the Academy of Finland (No 310359). K.V. is grateful to the TUT doctoral program. V.G., V.G. and N.V.T. acknowledge NATO SPS Project No. 985043. T.T. acknowledges financial support from MINECO (CTQ2014-52869-P), Spain, and the Comunidad de Madrid (S2013/MIT-2841 FOTOCARBON).

■ REFERENCES

(1) O'Regan, B.; Grätzel, M. A Low-Cost, High-Efficiency Solar Cell Based on Dye-Sensitized Colloidal TiO_2 Films. *Nature* **1991**, *353*, 737−740.
(2) Ye, M.; Wen, X.; Wang, M.; Iocozzia, J.; Zhang, N.; Lin, C.; Lin, Z. Recent Advances in Dye-Sensitized Solar Cells: from Photoanodes, Sensitizers and Electrolytes to Counter Electrodes. *Mater. Today* **2015**, *18*, 155−162.
(3) Armaroli, N.; Balzani, V. Solar Electricity and Solar Fuels: Status and Perspectives in the Context of the Energy Transition. *Chem. - Eur. J.* **2016**, *22*, 32−57.
(4) Cid, J.-J.; Yum, J.-H.; Jang, S.-R.; Nazeeruddin, M.; Martínez-Ferrero, E.; Palomares, E.; Ko, J.; Grätzel, M.; Torres, T. Molecular Cosensitization for Efficient Panchromatic Dye-Sensitized Solar Cells. *Angew. Chem., Int. Ed.* **2007**, *46*, 8358−8362.
(5) Matsuzaki, H.; Murakami, T. N.; Masaki, N.; Furube, A.; Kimura, M.; Mori, S. Dye Aggregation Effect on Interfacial Electron-Transfer Dynamics in Zinc Phthalocyanine-Sensitized Solar Cells. *J. Phys. Chem. C* **2014**, *118*, 17205−17212.
(6) Guldi, D. M.; Zilbermann, I.; Gouloumis, A.; Vazquez, P.; Torres, T. Metallophthalocyanines: Versatile Electron-Donating Building Blocks for Fullerene Dyads. *J. Phys. Chem. B* **2004**, *108*, 18485−18494.
(7) Imahori, H.; Umeyama, T.; Ito, S. Large π-Aromatic Molecules as Potential Sensitizers for Highly Efficient Dye-Sensitized Solar Cells. *Acc. Chem. Res.* **2009**, *42*, 1809−1818.
(8) Ragoussi, M.-E.; Ince, M.; Torres, T. Recent Advances in Phthalocyanine-Based Sensitizers for Dye-Sensitized Solar Cells. *Eur. J. Org. Chem.* **2013**, *2013* (29), 6475−6489.
(9) Martín-Gomis, L.; Fernández-Lázaro, F.; Sastre-Santos, A. Advances in Phthalocyanine-Sensitized Solar Cells (PcSSCs). *J. Mater. Chem. A* **2014**, *2*, 15672−15682.
(10) Kimura, M.; Nomoto, H.; Suzuki, H.; Ikeuchi, T.; Matsuzaki, H.; Murakami, T. N.; Furube, A.; Masaki, N.; Griffith, M. J.; Mori, S. Molecular Design Rule of Phthalocyanine Dyes for Highly Efficient Near-IR Performance in Dye−Sensitized Solar Cells. *Chem. - Eur. J.* **2013**, *19*, 7496−7502.
(11) Ragoussi, M.-E.; Cid, J.-J.; Yum, J.-H.; de la Torre, G.; Di Censo, D.; Grätzel, M.; Nazeeruddin, M. K.; Torres, T. Carboxyethynyl Anchoring Ligands: A Means to Improving the Efficiency of Phthalocyanine-Sensitized Solar Cells. *Angew. Chem., Int. Ed.* **2012**, *51*, 4375−4378.
(12) Ragoussi, M.-E.; Yum, J.-H.; Chandiran, A. K.; Ince, M.; de la Torre, G.; Grätzel, M.; Nazeeruddin, M. K.; Torres, T. Sterically Hindered Phthalocyanines for Dye-Sensitized Solar Cells: Influence of the Distance Between the Aromatic Core and the Anchoring Group. *ChemPhysChem* **2014**, *15*, 1033−1036.
(13) Tejerina, L.; Martínez-Díaz, M. V.; Nazeeruddin, M. K.; Torres, T. The Influence of Substituent Orientation on the Photovoltaic Performance of Phthalocyanine-Sensitized Solar Cells. *Chem. - Eur. J.* **2016**, *22*, 4369−4373.
(14) Imahori, H.; Kang, S.; Hayashi, H.; Haruta, M.; Kurata, H.; Isoda, S.; Canton, S. E.; Infahsaeng, Y.; Kathiravan, A.; Pascher, T.; et al. Photoinduced Charge Carrier Dynamics of Zn−Porphyrin−TiO_2 Electrodes: The Key Role of Charge Recombination for Solar Cell Performance. *J. Phys. Chem. A* **2011**, *115*, 3679−3690.
(15) Martín, C.; Ziółek, M.; Douhal, A. Ultrafast and Fast Charge Separation Processes in Real Dye-Sensitized Solar Cells. *J. Photochem. Photobiol., C* **2016**, *26*, 1−30.
(16) Hakola, H.; Pyymaki Perros, A.; Myllyperkiö, P.; Kurotobi, K.; Lipsanen, H.; Imahori, H.; Lemmetyinen, H.; Tkachenko, N. V. Photo-Induced Electron Transfer at Nanostructured Semiconductor−Zinc Porphyrin Interface. *Chem. Phys. Lett.* **2014**, *592*, 47−51.
(17) Stranius, K.; George, L.; Efimov, A.; Ruoko, T.-P.; Pohjola, J.; Tkachenko, N. V. Photophysical Study of a Self-Assembled Donor-Acceptor Two-Layer Film on TiO_2. *Langmuir* **2015**, *31*, 944−952.
(18) Eu, S.; Katoh, T.; Umeyama, T.; Matano, Y.; Imahori, H. Synthesis of Sterically Hindered Phthalocyanines and Their Applications to Dye-Sensitized Solar Cells. *Dalton Trans.* **2008**, 5476−5483.
(19) Lim, B.; Margulis, G. Y.; Yum, J.-H.; Unger, E. L.; Hardin, B. E.; Grätzel, M.; McGehee, M. D.; Sellinger, A. Silicon-Naphthalo/Phthalocyanine-Hybrid Sensitizer for Efficient Red Response in Dye-Sensitized Solar Cells. *Org. Lett.* **2013**, *15*, 784−787.
(20) Li, Y.; Lu, P.; Yan, X.; Jin, L.; Peng, Z. Non-Aggregated Hyperbranched Phthalocyanines: Single Molecular Nanostructures for Efficient Semi-Opaque Photovoltaics. *RSC Adv.* **2013**, *3*, 545−558.
(21) Niskanen, M.; Kuisma, M.; Cramariuc, O.; Golovanov, V.; Hukka, T.; Tkachenko, N.; Rantala, T. Porphyrin Adsorbed on the $(10\bar{1}0)$ Surface of the Wurtzite Structure of ZnO − Conformation Induced Effects on the Electron Transfer Characteristics. *Phys. Chem. Chem. Phys.* **2013**, *15*, 17408.
(22) Golovanov, V.; Kortelainen, T.; Rantala, T. T.; et al. Stability of Siloxane Couplers on Pure and Fluorine Doped SnO_2 (110) Surface: A First Principles study. *Surf. Sci.* **2010**, *604*, 1784−1790.
(23) Viitala, M.; Cramariuc, O.; Rantala, T. T.; Golovanov, V. Small Hydrocarbon Adsorbates on SnO_2(110) Surfaces: Density Functional Theory Study. *Surf. Sci.* **2008**, *602*, 3038−3042.
(24) Hsu, C.-Y.; Chen, Y.-C.; Lin, R. Y.-Y.; Ho, K.-C.; Lin, J. T. Solid-State Dye-Sensitized Solar Cells Based on Spirofluorene (Spiro-OMeTAD) and Arylamines as Hole Transporting Materials. *Phys. Chem. Chem. Phys.* **2012**, *14*, 14099−14109.
(25) Hardin, B. E.; Snaith, H. J.; McGehee, M. D. The Renaissance of Dye-Sensitized Solar Cells. *Nat. Photonics* **2012**, *6*, 162−169.
(26) Wu, J.; Lan, Z.; Lin, J.; Huang, M.; Huang, Y.; Fan, L.; Luo, G. Electrolytes in Dye-Sensitized Solar Cells. *Chem. Rev.* **2015**, *115*, 2136−2173.
(27) Burschka, J.; Dualeh, A.; Kessler, F.; Baranoff, E.; Cevey-Ha, N.-L.; Yi, C.; Nazeeruddin, M. K.; Grätzel, M. Tris(2-(1H-pyrazol-1-yl)pyridine)cobalt(III) as p-Type Dopant for Organic Semiconductors and Its Application in Highly Efficient Solid-State Dye-Sensitized Solar Cells. *J. Am. Chem. Soc.* **2011**, *133*, 18042−18045.
(28) Cappel, U. B.; Smeigh, A. L.; Plogmaker, S.; Johansson, E. M. J.; Rensmo, H.; Hammarström, L.; Hagfeldt, A.; Boschloo, G. Characterization of the Interface Properties and Processes in Solid State Dye-Sensitized Solar Cells Employing a Perylene Sensitizer. *J. Phys. Chem. C* **2011**, *115*, 4345−4358.
(29) Hakola, H.; Sariola-Leikas, E.; Efimov, A.; Tkachenko, N. V. Effect of Hole Transporting Material on Charge Transfer Processes in Zinc Phthalocyanine Sensitized ZnO Nanorods. *J. Phys. Chem. C* **2016**, *120*, 7044−7051.
(30) Anta, J. A.; Guillén, E.; Tena-Zaera, R. ZnO-Based Dye-Sensitized Solar Cells. *J. Phys. Chem. C* **2012**, *116*, 11413−11425.
(31) Bouclé, J.; Ackermann, J. Solid-State Dye-Sensitized and Bulk Heterojunction Solar Cells Using TiO_2 and ZnO Nanostructures: Recent Progress and New Concepts at the Borderline. *Polym. Int.* **2012**, *61*, 355−373.
(32) Muguerra, H.; Berthoux, G.; Yahya, W.; Kervella, Y.; Ivanova, V.; Bouclé, J.; Demadrille, R. Electrodeposited ZnO Nanowires as Photoelectrodes in Solid-State Organic Dye-Sensitized Solar Cells. *Phys. Chem. Chem. Phys.* **2014**, *16*, 7472−7480.
(33) Saarenpää, H.; Sariola-Leikas, E.; Pyymaki Perros, A.; Kontio, J. M.; Efimov, A.; Hayashi, H.; Lipsanen, H.; Imahori, H.; Lemmetyinen, H.; Tkachenko, N. V. Self-Assembled Porphyrins on Modified Zinc Oxide Nanorods: Development of Model Systems for Inorganic−

DOI: 10.1021/acs.jpcc.7b01562
J. Phys. Chem. C 2017, 121, 9594−9605

Organic Semiconductor Interface Studies. *J. Phys. Chem. C* **2012**, *116*, 2336−2343.
(34) Virkki, K.; Demir, S.; Lemmetyinen, H.; Tkachenko, N. V. Photoinduced Electron Transfer in CdSe/ZnS Quantum Dot−Fullerene Hybrids. *J. Phys. Chem. C* **2015**, *119*, 17561−17572.
(35) Ermer, O. *Bonding forces*; Springer: Berlin and Heidelberg, Germany, 1976; Vol. *27*.
(36) Mayo, S. L.; Olafson, B. D.; Goddard, W. A. I. DREIDING: A Generic Forcefield for Molecular Simulations. *J. Phys. Chem.* **1990**, *94*, 8897−8909.
(37) Moreira, N.; da Rosa, A.; Frauenheim, T. Covalent Functionalization of ZnO Surfaces: A Density Functional Tight Binding Study. *Appl. Phys. Lett.* **2009**, *94*, 193109.
(38) Bach, U.; Lupo, D.; Comte, P.; Moser, J.; Weissörtel, F.; Salbeck, J.; Spreitzer, H.; Grätzel, M. Solid-State Dye-Sensitized Mesoporous TiO_2 Solar Cells with High Photon-to-Electron Conversion Efficiencies. *Nature* **1998**, *395*, 583−585.
(39) Snaith, H. J.; Petrozza, A.; Ito, S.; Miura, H.; Grätzel, M. Charge Generation and Photovoltaic Operation of Solid-State Dye-Sensitized Solar Cells Incorporating a High Extinction Coefficient Indolene-Based Sensitizer. *Adv. Funct. Mater.* **2009**, *19*, 1810−1818.
(40) Fukuzumi, S.; Ohkubo, K.; Ortiz, J.; Gutiérrez, A. M.; Fernández-Lázaro, F.; Sastre-Santos, A. Formation of a Long-Lived Charge-Separated State of a Zinc Phthalocyanine-Perylenediimide Dyad by Complexation with Magnesium Ion. *Chem. Commun.* **2005**, *30*, 3814−3816.
(41) Cappel, U. B.; Gibson, E. A.; Hagfeldt, A.; Boschloo, G. Dye Regeneration by Spiro-MeOTAD in Solid State Dye-Sensitized Solar Cells Studied by Photoinduced Absorption Spectroscopy and Spectroelectrochemistry. *J. Phys. Chem. C* **2009**, *113*, 6275−6281.
(42) Mack, J.; Stillman, M. J. Photochemical Formation of the Anion Radical of Zinc Phthalocyanine and Analysis of the Absorption and Magnetic Circular Dichroism Spectral Data. Assignment of the Optical Spectrum of $[ZnPc(-3)]^-$. *J. Am. Chem. Soc.* **1994**, *116*, 1292−1304.
(43) Lehtivuori, H.; Efimov, A.; Lemmetyinen, H.; Tkachenko, N. V. Distributed Decay Kinetics of Charge Separated State in Solid Films. *Chem. Phys. Lett.* **2007**, *437*, 238−242.
(44) Kang, Y. K.; Rubtsov, I. V.; Iovine, P. M.; Chen, J.; Therien, M. J. Distance Dependence of Electron Transfer in Rigid, Cofacially Compressed, π−Stacked Porphyrin-Bridge−Quinone Systems. *J. Am. Chem. Soc.* **2002**, *124*, 8275−8279.
(45) Ricks, A. B.; Brown, K. E.; Wenninger, M.; Karlen, S. D.; Berlin, Y. A.; Co, D. T.; Wasielewski, M. R. Exponential Distance Dependence of Photoinitiated Stepwise Electron Transfer in Donor−Bridge−Acceptor Molecules: Implications for Wirelike Behavior. *J. Am. Chem. Soc.* **2012**, *134*, 4581−4588.
(46) Antila, L. J.; Myllyperkiö, P.; Mustalahti, S.; Lehtivuori, H.; Korppi-Tommola, J. Injection and Ultrafast Regeneration in Dye-Sensitized Solar Cells. *J. Phys. Chem. C* **2014**, *118*, 7772−7780.
(47) Wright, M.; Uddin, A. Organic−Inorganic Hybrid Solar Cells: A Comparative Review. *Sol. Energy Mater. Sol. Cells* **2012**, *107*, 87−111.

DOI: 10.1021/acs.jpcc.7b01562
J. Phys. Chem. C 2017, 121, 9594−9605

Publication IV

Kirsi Virkki, Essi Tervola, Maria Medel, Tomás Torres, and Nikolai V. Tkachenko. Effect of Co-Adsorbate and Hole Transporting Layer on the Photoinduced Charge Separation at the TiO_2 – Phthalocyanine Interface, *ACS Omega*, vol. 3, no. 5, pp. 4947 – 4958, 2018.

ACS OMEGA

Article

Cite This: ACS Omega 2018, 3, 4947−4958

Effect of Co-Adsorbate and Hole Transporting Layer on the Photoinduced Charge Separation at the TiO_2−Phthalocyanine Interface

Kirsi Virkki,[†] Essi Tervola,[†] Maria Medel,[‡] Tomás Torres,*[,‡,§,∥] and Nikolai V. Tkachenko*[,‡]

[†]Laboratory of Chemistry and Bioengineering, Tampere University of Technology, P.O. Box 541, FI-33101 Tampere, Finland
[‡]Departamento de Química Orgánica, Universidad Autónoma de Madrid, Cantoblanco, E-28049 Madrid, Spain
[§]Institute for Advanced Research in Chemical Sciences (IAdChem), Universidad Autónoma de Madrid, 28049 Madrid, Spain
[∥]IMDEA Nanociencia, C/Faraday, 9, Cantoblanco, 28049 Madrid, Spain

Supporting Information

ABSTRACT: Understanding the primary processes of charge separation (CS) in solid-state dye-sensitized solar cells (DSSCs) and, in particular, analysis of the efficiency losses during these primary photoreactions is essential for designing new and efficient photosensitizers. Phthalocyanines (Pcs) are potentially interesting sensitizers having absorption in the red side of the optical spectrum and known to be efficient electron donors. However, the efficiencies of Pc-sensitized DSSCs are lower than that of the best DSSCs, which is commonly attributed to the aggregation tendency of Pcs. In this study, we employ ultrafast spectroscopy to discover why and how much does the aggregation affect the efficiency. The samples were prepared on a standard fluorine-doped tin oxide (FTO) substrates covered by a porous layer of TiO_2 nanoparticles, functionalized by a Pc sensitizer and filled by a hole transporting material (Spiro-MeOTAD). The study demonstrates that the aggregation can be suppressed gradually by using co-adsorbates, such as chenodeoxycholic acid (CDCA) and oleic acid, but rather high concentrations of co-adsorbate is required. Gradually, a few times improvement of quantum efficiency was observed at sensitizer/co-adsorbate ratio Pc/CDCA = 1:10 and higher. The time-resolved spectroscopy studies were complemented by standard photocurrent measurements of the same sample structures, which also confirmed gradual increase in photon-to-current conversion efficiency on mixing Pc with CDCA.

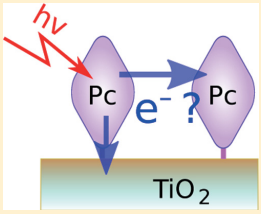

1. INTRODUCTION

The performance and competitiveness of dye-sensitized solar cells (DSSCs) are improving constantly with the power conversion efficiency (PCE) exceeding 12% in laboratory conditions.[1,2] However, the achieved efficiency is still behind the theoretical limit by a factor of 2, and research efforts are refocused to examine and eliminate all pitfalls resulting in the efficiency loss. The final characterization of solar cells is done by measuring I−V characteristics and calculating the maximum PCE or the external quantum efficiency. The PCE is the principal characteristic of the solar cells, but it depends on many internal processes and presents a cumulative effect of losses at different stages starting from the light caption and primary photoinduced charge separation (CS) to power losses due to resistivity of electrodes.[3] Eventually, optimization of the DSSC should be done for all the processes involved and has to be based on the knowledge of all the individual steps of photon-to-current conversion. The very first events of the photon conversion are extremely fast taking place in the femto- to picosecond time domain and were under active investigation for the past few decades using ultrafast optical and terahertz spectroscopy methods.[4−8] The reactions of interest include light harvesting by sensitizers and electron injection to semiconductors in the picosecond time domain and following dye regeneration by electrolytes in the sub-nanosecond time domain in the case of liquid DSSCs.[9,10]

Solid-state DSSCs (ssDSSCs) are relatively new development in which the liquid electrolyte is replaced by a solid hole transporting material (HTM).[11−13] This makes such devices more robust and attractive for large scale applications, though the best efficiencies achieved are roughly 2 times lower than that of traditional liquid DSSCs.[14] Few specific challenges of ssDSSCs are selection of suitable small molecules for the HTM and pore filling by the material,[15] which affect the conversion efficiency drastically and put restrictions on the thickness and porosity of the TiO_2 layer. A common requirement for both liquid and ssDSSCs is design and syntheses of cost efficient sensitizers which have high absorption in the green-red part of the spectrum and close to unity quantum yield of CS at semiconductor−organic interfaces.[12,16,17]

Among a wide range of sensitizers tested in DSSC applications, porphyrin derivatives gained considerable attention recently,[16,18−20] and porphyrin-based sensitizers were used to achieve the highest efficiencies in both types of DSSCs.[1,14] The most efficient sensitizers are complex molecules with

Received: March 29, 2018
Accepted: April 26, 2018
Published: May 7, 2018

specifically designed peripheral groups reducing interchromophore aggregation and implementing the so-called push−pull strategy when the sensitizer is complemented by electron donating and/or withdrawing groups accelerating electron injection to TiO_2 from the photoexcited sensitizer.[1,14,21,22] These are complex state-of-the-art compounds produced using multistep synthetic routes in very small amounts.

Although porphyrin derivatives are very versatile compounds for solar cell applications, they have a disadvantage of exhibiting relatively low absorption intensity in the green-red part of the spectrum. Therefore, another dye from the same group of tetrapyrrole macrocyclic compounds, phthalocyanine (Pc), has attracted attention because it is an equally good electron donor and has a strong absorption band in the red part of the spectrum.[17] A number of Pc derivatives have been tested in DSSCs and demonstrated reasonably good efficiencies,[23,24] though the final PCE was roughly 2 times lower than that of the best porphyrin and Ru-dye derivatives. Aggregation tendency of Pcs was considered to be the main reason for the efficiency loss. This stimulated the synthesis of Pcs with specifically designed bulky peripheral groups to reduce the aggregation,[25,26] though this approach requires again multistep synthesis and thus gradually increases the cost of the compounds. Another possibility to solve the aggregation problem is to use co-adsorbate compounds mixed with the photoactive Pcs during the sensitization process.[27] An advantage of this approach is that it does not require synthesis of new and expensive compounds. This method was tested in a number of studies and has proven to increase the conversion efficiency but the efficiency gain was not as large as one could hope for.

The aims of the study reported herein are to use a reasonably inexpensive sensitizer, Pc derivative known as TT1,[23] to examine the primary photoreactions in ssDSSC model systems, to study the aggregation effect on the carrier generation, and to find out to which extent co-adsorbate may reduce the efficiency loss due to aggregation. To reduce the aggregation, the Pc was mixed with the widely used co-adsorbate, chenodeoxycholic acid (CDCA).[28,29] In addition, oleic acid (OA), a well-known lipid molecule, was tested as a replacement for CDCA. The ssDSSC model samples were completed by infiltrating the layer of photosensitized TiO_2 nanoparticles by the HTM, Spiro-MeOTAD (Spiro).[30,31] The primary photoreactions in the samples were studied by the ultrafast transient absorption (TA) spectroscopy technique also know as the pump−probe method. Both Pc and Spiro have distinct spectroscopy features of their transient states, cations and anions,[32−34] which allow to establish reaction mechanisms and do quantitative evaluation of reaction rates and efficiencies. To compare the results of spectroscopy studies with "real life" use case of ssDSSCs, silver electrodes were deposited on top of the HTM and standard solar cell characterization was carried out for the same sample structures. For the comparison purpose, the quantum yields of photon-to-electron conversion were estimated. The comparison shows that CDCA can effectively reduce aggregation and even as simple Pc as TT1 can reach close to unity quantum yield of photocurrent generation.

2. RESULTS AND DISCUSSION

The chemical structure of zinc carboxyphthalocyanine (Pc) derivative used in this study is presented in Figure 1 together with those of two co-adsorbates, CDCA and OA. 2,2′,7,7′-Tetrakis(*N*,*N*-di-*p*-methoxyphenylamino)-9,9′-spirobifluorene (Spiro-MeOTAD or Spiro) was used as the HTM.

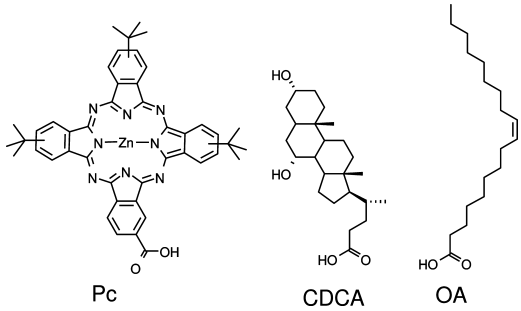

Figure 1. Compounds used to functionalize TiO_2 nanoparticle films.

Samples were prepared on fluorine-doped tin oxide (FTO)-coated glass substrates coated by a thin TiO_2 compact layer, on top of which TiO_2 mesoporous layers were prepared by screen-printing or spin-coated as described in Methods and Materials section below. The typical thickness of screen-printed layer was 2.5 μm and of spin-coated 0.8 μm. Cross-section electron microscopy images of a few samples are shown in Supporting Information Figure S1.

2.1. Absorption Spectra. *2.1.1. Pc Aggregation on the TiO_2 Surface.* Absorption spectra of Pcs change significantly upon aggregation. This change can be used for monitoring the degree of aggregation. The absorption spectrum of the Pc in a good solvent, ethanol (EtOH), at a low concentration (roughly 0.8 μM) is shown in Supporting Information Figure S2. The spectrum has relatively narrow band at 677 nm, the Q-band, and a shoulder in the 600−650 nm range. However, to deposit the Pc onto TiO_2, the concentration of Pc must be much higher. Furthermore, it was noted previously that for similar Pcs, a 1:1 (vol/vol) mixture of *tert*-butanol and MeCN is a better solvent for self-assembled monolayer (SAM) deposition on ZnO.[35] It turned out that the same mixture allows deposition of stable SAMs on TiO_2. Absorption spectra of the Pc in this solvent at a concentration close to what was used for the SAM depositions (roughly 50 μM) are shown in Figure S3 in the Supporting Information. There is noticeable aggregation of Pc in this solution, which also can be reduced by adding a co-adsorbate such as CDCA. The absorption spectra for the Pc/CDCA mixtures with different Pc/CDCA ratios can also be found in Figure S3.

Absorption spectra of a series of Pc SAMs on TiO_2 with varying relative concentrations of the co-adsorbates are presented in Figure 2. As a rough approximation, the absorption spectra in the Q-band area (580−720 nm) can be presented as superposition of two bands, a "blue" band with maximum close to 630 nm and a "red" band with maximum in the 680−690 nm range. A clear sign of aggregation is high relative intensity of the blue band and broadening of the red band. These are typical features of Pc aggregates, and sharp rise of the blue band can be tentatively attributed to H-type aggregation or formation of face-to-face aggregates.[36] The spectrum of the sample without the co-adsorbate is the broadest and it has the highest relative intensity at the blue band, which can be considered as the highest degree of aggregation in this series.

As a measure of aggregation, the relative intensities of the blue band with respect to the red band were calculated by decomposing the spectrum on two Gaussian bands and

DOI: 10.1021/acsomega.8b00600
ACS Omega 2018, 3, 4947−4958

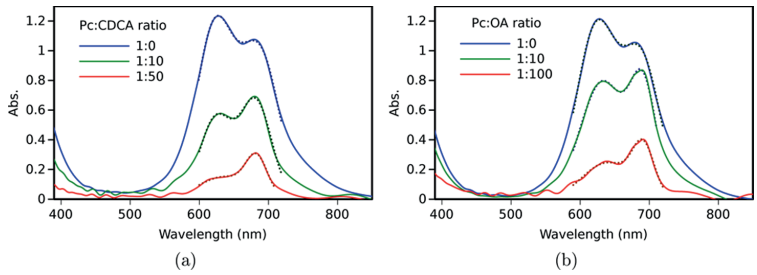

Figure 2. Absorption spectra of Pc SAMs on TiO_2 with different relative concentrations of (a) CDCA and (b) OA. Solid lines are measured spectra after subtracting spectra of TiO_2-covered substrates and dotted lines are two band approximations of the Q-band area.

calculating the ratio of the band intensities (see Table S1 in the Supporting Information). According to this aggregation degree estimation, CDCA reduces the aggregation more efficiently than OA. The ratio decreases from 1.18 for the pure Pc SAM to 0.83 and 0.5 for relative CDCA concentrations of 10 and 50, respectively. However, for OA it decreases to only 1.0 and 0.65 for relative OA concentrations of 10 and 100, respectively. It has to be noted that the lipid structure of the OA molecule might take less space in the SAM than the steroid base CDCA, thus resulting in higher surface density of Pc in OA environment than in CDCA.

Furthermore, the surface binding rate of Pc, CDCA, and OA may differ and the ratio of molecules Pc/CDCA or Pc/OA on the TiO_2 surface may differ from the corresponding ratios in the sensitization solution used to deposit SAM. Estimation of the surface density is a complicated task in this case, but one can compare decrease of absorption intensities at increased co-adsorbate concentrations and make some qualitative conclusions. This analysis is presented in Supporting Information (Table S1, Figure S6, and corresponding comments), and it suggests that (1) co-adsorbate to Pc molecular ratio on the TiO_2 surface is few times lower than that in the layer deposition solution (relative proportion Pc is few times higher in solid samples), which is probably due to higher binding rate of Pc compared to CDCA and OA, and (2) at the same Pc to co-adsorbate molar ratio, the average surface density of the Pc is higher in the OA samples than in the CDCA samples, resulting in a higher absorption for the Pc/OA samples compared to the Pc/CDCA samples. Because accurate estimation of the Pc/co-adsorbate ratio on the TiO_2 surface was not possible at this stage, the samples will be distinguished by the molar ratio in the sensitization solution in this study, meaning that, for example, the ratio 1:10 refers to the ratio in the solution used to prepare the sample. This is justified by reasonably proportional decrease of Pc density with increase of the co-adsorbate concentration in the solution as presented in Supporting Information Figure S6.

Even at the highest relative co-adsorbate concentrations shown in Figure 2, the Pc spectra are still not a perfect match with the Pc spectrum in a good solvent at a low concentration (Figure S2). This can be interpreted as some remaining aggregation. Another reason for the difference is the completely different environment in the SAMs compared to a solution. Higher concentrations of the co-adsorbates were tested but the absorption of such samples was lower with the spectrum shape remaining essentially the same.

Samples with OA co-adsorbate were observed to degrade faster than the CDCA-containing samples. In particular at Pc/OA = 1:100, the sample became colorless after 2 days when kept in the dark. On the contrary, practically no detectable degradation was noticed for the Pc/CDCA = 1:50 sample after a week of storage. Degradation was lower for lower OA concentration, for example at Pc/OA = 1:10 the degradation was less than 20% (of absorption intensity) after a few days.

2.1.2. Effect of Spiro on Pc Absorption. Addition of the HTM had also a strong effect on the steady-state absorption spectra of the samples, as illustrated in Figure 3. In all samples,

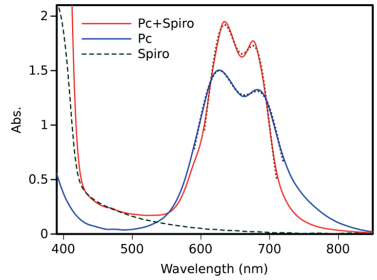

Figure 3. Absorption spectra of Pc SAMs before (blue) and after (red) deposition of Spiro hole transporting layer and absorption spectrum of a reference Spiro sample (green dashed line). Solid lines are measured spectra (after subtracting spectra of TiO_2-covered substrates) and dotted lines are two band approximations of the Q-band area.

the absorption intensity increased slightly in the Q-band region and the spectra became slightly narrower after the deposition of Spiro. It can be noticed that Spiro has negligible absorption in the green-red part of the spectrum. Its absorption dominates in the ultraviolet (UV)-blue region, and it is seen as a sharp rise at wavelengths shorter than 420 nm in Figure 3. Therefore, the absorption in the 550−750 nm region is solely due to the Pc. For the sample shown in Figure 3, the width of the band at 620−630 nm decreases from 30 to 23 nm and for the band at 680−690 nm from 27 to 19 nm on addition of the Spiro layer, which is typically interpreted as lower aggregation degree. However, the band ratio remains virtually the same, 1.23 and 1.25, respectively, which leads to a conclusion that relative proportion of H-type aggregates is the same. If the ratio is taken as a measure of aggregation degree, one may conclude that the type of aggregation does not change, but the aggregates are more homogeneous after Spiro deposition, which results in the band narrowing. Similar changes were observed for other samples, see Figures S4, S5 and Table S1 in the Supporting Information. Importantly, no detectable degradation was observed for any of the samples covered with the Spiro hole

DOI: 10.1021/acsomega.8b00600
ACS Omega 2018, 3, 4947−4958

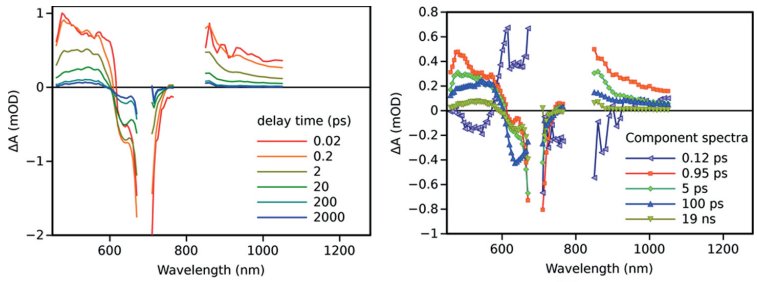

Figure 4. (a) TA spectra and (b) decay component spectra for the Pc/CDCA = 1:50 sample. Excitation wavelength was 695 nm.

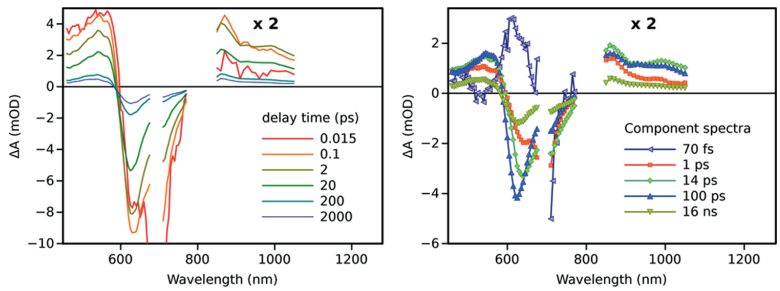

Figure 5. (a) Time-resolved TA spectra and (b) decay component spectra for the Pc sample without a co-adsorbate. Excitation wavelength was 695 nm. The response in the NIR (840−1060 nm) is multiplied by 2 for clarity.

transporting layer within a few weeks, regardless of which co-adsorbate was used.

These changes in the absorption spectra upon addition of the Spiro layer can be rationalized assuming that Spiro has a tendency to fill the space between the Pc molecules, resulting in weaker inter-Pc interactions and thus a lower degree of aggregation. This phenomenon is desired as it may also improve the efficiency of the hole collection from the Pc monolayer after electron injection into TiO_2. It also may result in an efficient electron or hole transfer at the Pc|Spiro interface, as was reported previously,[35] and will be discussed below.

As a summary of the examination of the steady-state absorption spectra, the Pc/CDCA = 1:50 sample is taken as the model example of a virtually nonaggregated sample, although the absorption spectrum of the sample is not a perfect match with the absorption spectrum of this Pc in a good solvent (Figure S2 in the Supporting Information).

2.2. TA Responses of TiO_2−Pc Samples. First, the samples without the Spiro layer were studied. The time-resolved TA spectra of the least aggregated sample, Pc/CDCA = 1:50, are shown in Figure 4a at a few selected delay times. The spectra were corrected for the group velocity dispersion and the instrument response function (roughly 0.1 ps), which is essential for a short delay times and fast decay components. Therefore, the spectrum at 0.02 ps delay time can be considered as an "ideal" spectrum formed instantly after the excitation and can be taken as the spectrum of the singlet excited state, Pc*. It has a relatively flat absorption in the 470−610 nm range and a broad absorption at >850 nm that slowly decreases toward the longer wavelengths. At later delay times, the spectrum is transformed to show a broad absorption band around 540 nm and a relatively sharp band near 860 nm. Both of these features are typical of the Pc cation,[32,35,37,38] which is in agreement with the expected electron injection from the excited Pc* into TiO_2.

In this case, the expected sequence of reactions following photoexcitation of Pc is

$$TiO_2|Pc^* \xrightarrow{\tau_{inj}} TiO_2^-|Pc^+ \xrightarrow{\tau_{cr}} TiO_2|Pc \quad (1)$$

where τ_{inj} is the electron injection time constant and τ_{cr} is the time constant of the charge recombination (CR) at the TiO_2|Pc interface. Despite this rather simple reaction chain, at least five-exponential fit had to be used to obtain a reasonably good approximation of the TA decays in the 460−1050 nm wavelength range (Figure 4b). However, one can notice that there is no significant difference in the component spectra shapes in a wide time domain covering several time constants of the fit (5 ps, 100 ps, and 19 ns). This indicates inhomogeneity in the sample which leads to essentially "nonexponential" decay kinetics of the CR at the TiO_2|Pc interface. Similar nonexponential decays were reported for virtually all similar systems.[4−6,9] On a qualitative level, the fast component, 0.12 ps, has features indicating formation of the bands at 540 and 860 nm and can be attributed to the electron injection from Pc* to TiO_2 with τ_{inj} = 0.12 ps. The following component, 0.95 ps, results in the formation of a better pronounced cation spectrum (Figure 4a, spectrum at 2 ps delay time). It is a mixture of competing electron injection and nonradiative excited state relaxation reactions most probably. After that the spectrum shape virtually does not change and this decay can be attributed

DOI: 10.1021/acsomega.8b00600
ACS Omega 2018, 3, 4947−4958

to the CR at the semiconductor−sensitizer interface which is known to be essentially nonexponential[7,9] and in this case is spread in the time interval from few picoseconds to tens of nanoseconds.

The corresponding time-resolved and decay component spectra for the sample without any co-adsorbate are shown in Figure 5. Although the TA response of the sample seems to be similar to that with CDCA, there are a few essential differences. First of all, it is even more difficult to find a delay time at which the singlet excited state of the Pc would be well-resolved in the sample without a co-adsorbate. The shortest time constant obtained from the fit, 70 fs, is shorter than the time resolution of the instrument (roughly 100 fs), and although it can be assigned to the excited state relaxation, the corrected spectrum generated for a very short delay time (0.015 ps, in Figure 5a) has features deviating gradually from that of the singlet excited state in the visible part of the spectrum, and it has low and "noisy" intensity in the near-infrared (NIR) part of the spectrum. This mismatch between the visible and NIR parts is most probably due to the limited accuracy of the group velocity compensation but not to any real phenomenon. Second, one can notice a relatively high absorption in the 950−1000 nm range for the aggregated sample and even a broad band at these wavelengths in the decay components with time constants 1 and 14 ps. The Pc anion is known to have an absorption band in this wavelength range,[33,39−41] though the band is broader than typically observed for Pc anions, which can be attributed to rather random aggregation of Pcs on the TiO_2 surface. Appearance of this band can be interpreted in favor of a CS reaction in the excited aggregates, or intra-aggregate CS, with a time constant τ_{agg}

$$Pc^* - Pc \xrightarrow{\tau_{agg}} Pc^+ - Pc^- \quad (2)$$

Although the mechanism of CS may be more complex and may involve formation of an intermolecular exciplex prior the complete CS, as was reported for Pc−fullerene dyads with strong electronic coupling.[42] In any case, this is the process competing with the electron injection into TiO_2 from the initially generated excited state, Pc*, and it reduces the lifetime of the singlet excited state compared to that of the nonaggregated sample (Pc/CDCA = 1:50). Within this simplified model, the observed singlet state relaxation time constant is $\tau_s = (\tau_{inj}^{-1} + \tau_{agg}^{-1})^{-1} \approx 70$ fs, and $\tau_{agg} \approx 0.13$ ps, or roughly equal to τ_{inj}.

The TA response of the Pc/CDCA = 1:10 sample takes an intermediate position between responses of the two samples discussed above (see Figure S7 in the Supporting Information).

The time-resolved spectra of the Pc/OA = 1:10 sample are presented in Figure 6. The response is very similar to that of the sample with CDCA as the co-adsorbate, though the spectra at longer delay time are slightly stronger, for example, at 2000 ps, indicating that relative yield of the long-lived Pc^+ is marginally higher in the sample with OA. However, the yield of the long-lived Pc^+ is small in both cases being not more than 20% relative to that of the Pc/CDCA = 1:50 sample.

Because of the rapid degradation of the Pc/OA samples, especially at high OA concentrations, reliable spectroscopic data were not obtained.

The primary CS in both series of samples with CDCA and OA was at the limit of the time resolution of the instrument used, 100 fs. Within this time resolution limit, the two co-adsorbates have the same effect on the relaxation of the singlet excited state, Pc*. The two main processes contributing to the

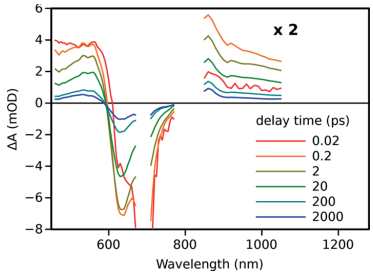

Figure 6. Time-resolved TA spectra of Pc/OA = 1:10 sample. The response in the NIR (840−1060 nm) is multiplied by 2 for clarity.

Pc* relaxation are the electron injection into TiO_2 and intra-aggregate CS. This leads to the disappearance of the Pc singlet excited state within the time interval close to 100 fs. The samples are quite heterogeneous, however, and the Pc* relaxation is not exponential. A "tail" of the singlet relaxation is extended to the picosecond time domain. We cannot exclude nonradiative intra-aggregate relaxation, but its contribution does not seem to be high and it is difficult to quantify.

The wavelength range of the most different decay profiles for the studied samples is 900−1050 nm. Figure 7a presents decays at 990 nm as an example. Two intermediate states have the main contribution to the TA at this wavelength: the singlet excited state, Pc*, and the Pc anion, Pc^-. Being the least aggregated sample, the Pc/CDCA = 1:50 sample shows the fastest decay at this wavelength because there is no intra-aggregate CS and thus no Pc^- formed. Respectively, the sample with no co-adsorbate shows the strongest response at the middle delay times, roughly 1−20 ps, being the most aggregated and thus the most efficient in generating Pc^-. However, the final relaxations of the Pc/CDCA = 1:10 and co-adsorbate-free samples are roughly the same, indicating that the relaxation of Pc^- is not sensitive to the concentration of CDCA.

The OA co-adsorbate is less efficient in reducing aggregation effect, according to the relative intensity of the TA at 990 nm in the 1−20 ps delay time interval. The decay of the sample with OA co-adsorbate is slightly slower than that with CDCA; however, the difference is rather minor.

Another important wavelength is 860 nm, because this is the wavelength of maximum absorption of the Pc cation, Pc^+. The decays at 860 nm are presented in Figure 7b for the same set of samples. Unfortunately, the singlet state has also relatively high absorption at this wavelength. Therefore, the transition Pc* → Pc^+ has virtually no effect on the absorption. Another intermediate state which has a significant contribution to the absorption at this wavelength is the Pc anion, Pc^-. The anion absorption band is at 990 nm, but at shorter wavelengths it has a flat absorption with intensity at 860 nm close to half of that at 990 nm (see below).

Assuming that the Pc/CDCA = 1:50 sample is virtually nonaggregated, the decay at 860 nm can be used to monitor the CR process at the semiconductor−sensitizer interface, eq 1. Then, the first conclusion is that the CR is essentially a nonexponential process, as can be expected. The TA intensity drops by roughly 50% during the first 3 ps, indicating that 50% of the Pc^+ have recombined. Roughly half of the left cations relax in the following 10 ps. For the remaining part, recombination is shifted to hundreds of picoseconds, and roughly 10% of the Pc cations have a lifetime extended to the

DOI: 10.1021/acsomega.8b00600
ACS Omega 2018, 3, 4947−4958

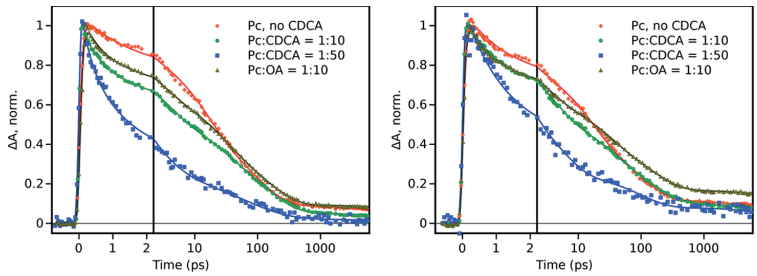

Figure 7. Normalized TA decays at (a) 990 and (b) 860 nm for four samples: Pc SAM without a co-adsorbate, two different relative concentrations of CDCA, 1:10 and 1:50, and OA at 1:10.

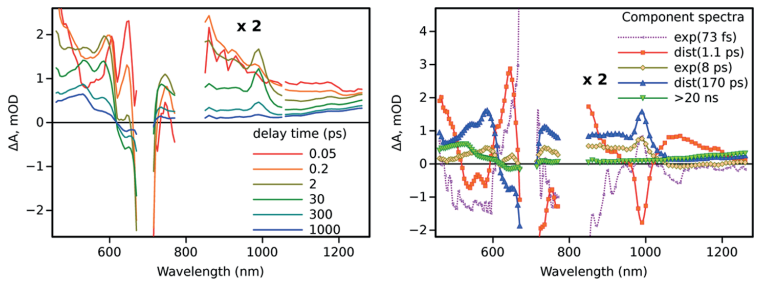

Figure 8. (a) Time-resolved TA spectra and (b) decay component spectra of the sample with Pc/CDCA = 1:50 covered by Spiro. The fit model combined exponential distributed decay functions[35] denoted as exp(τ) and dist(τ_{aver}), respectively. Excitation wavelength was 695 nm. The NIR response (840−1260 nm) is multiplied by 2.

nanosecond time domain. This is rather fast CR. For example, the longest reported half times are >1 ns for porphyrin sensitizer[9,43] and much more than 1 ns for Ru-dyes.[10] Rather fast CR at the TiO_2|Pc interface is surprising and undesired result. It was noticed that the electron injection from sensitizer into TiO_2 takes place in two steps.[7] The first step is an electrostatically coupled electron−cation complex is formed, and then, the electron leaves the surface and becomes a "free" carrier in the conduction band of TiO_2. A possible explanation of a faster recombination is that the electron−cation complex is more stable for Pc than for porphyrin and Ru-dye sensitizers studied previously. This would result in a competition between the CR of the complex and the electron promotion into the TiO_2 bulk, which leaves a long-lived cation on the surface. In the case of the TiO_2|Pc interface, the competition is shifted in favor of the first process, surface complex recombination, which is definitely an undesired process.

For the samples without co-adsorbates or relatively low concentration of co-adsorbates (e.g. 1:10), the cation band at 860 nm cannot be used as an indicator of the CS efficiency at the TiO_2|Pc interface, because the electron injection is competing with CS (eq 2) in the Pc aggregates. The reason for the slower decay of these samples is the slower relaxation of the intra-aggregate charge separated state compared to the CR at the TiO_2|Pc interface.

One can presume that the Pc^- formed as the result of intra-aggregate CS may later inject an electron into TiO_2 and thus contribute to the CS at the organic−semiconductor interface through a two-step process

$$TiO_2|(Pc^* - Pc) \xrightarrow{\tau_{agg}} TiO_2|(Pc^+ - Pc^-) \xrightarrow{\tau_{el}} TiO_2^-|(Pc^+ - Pc) \quad (3)$$

An indication of this process is a slower decay of TA at 860 nm (Pc^+ indicator) compared to that at 990 nm (indicator of Pc^-) for the co-adsorbate-free sample. However, we did not come up with a method of quantitative separation of these two processes. In a qualitative level, the remaining absorption at 860 nm (indicator of Pc^+) is not higher than that of the least aggregated sample with still measurable absorption at 990 nm (indicator of Pc^-). Therefore, the efficiency of reactions in eq 3 is low for all samples.

2.3. Samples with Spiro Overlayer: Effect of the Hole Transporting Layer. The effect of the HTM, Spiro, on the photoinduced CS at the organic−semiconductor interface of the least aggregated sample is very similar to that reported for aggregation protected Pcs on ZnO nanorods.[35] The time-resolved TA spectra of the Pc/CDCA = 1:50 sample covered by the Spiro layer are shown in Figure 8a, and the global fit results using the model combining exponential and distributed decay (see ref 35 for details) are presented in Figure 8b, respectively. Comparing to the sample without the HTM layer, the most obvious difference in the TA response is a rather sharp band at 990 nm which forms with a time constant close to 1 ps and decays with a time constant close to 170 ps (see Figure S7 in the Supporting Information). This band can be attributed to the anion Pc^-.[35,39,40] Another characteristic feature of the anion

DOI: 10.1021/acsomega.8b00600
ACS Omega 2018, 3, 4947−4958

is the band close to 590 nm, which is most clearly seen in the 170 ps component.

The first qualitative conclusion which can be made comparing TA measurements of the Pc/CDCA = 1:50 sample with and without Spiro, presented in Figures 8 and 4, respectively, is that Spiro not only penetrates through the whole 2 μm thick TiO_2 layer, but it is in contact with most Pc sensitizers. This conclusion becomes evident after comparing time-resolved spectra at long delay time. The spectra of the sample with Spiro holds mainly the features of the Spiro cation, the band 590 nm and very weak and featureless absorption in the 850−1100 nm range, and only a minor bleaching at 650 nm which may arise from minor population of Pc not interacting with Spiro. Whereas features of the Spiro-free sample is a band at 860 nm and relatively strong bleaching at 650 nm compared to the broad and featureless induced absorption band at 500−600 nm.

Assuming that Pcs are nonaggregated in the sample with Spiro and the intra-aggregate CS can be excluded, the only feasible reaction to generate Pc^- is the CS at interface between Pc and Spiro

$$Pc^*|Spiro \xrightarrow{\tau_{sp}} Pc^-|Spiro^+ \quad (4)$$

where τ_{sp} is the time constant for the hole transfer from the excited Pc to Spiro. The spectra at long delay times (e.g. at 1000 ps, Figure 8a) and the spectrum of the long-lived component (>20 ns, Figure 8b), respectively, can be attributed to the Spiro cation.[11,34,35,40] It has a band at 530 nm and a broad absorption in the IR region which is observed as a slowly rising absorption toward the longer wavelengths starting from 1000 nm. Therefore, relaxation of the Pc^- can be attributed to the electron injection into TiO_2

$$TiO_2|Pc^-|Spiro^+ \xrightarrow{\tau_{et}} TiO_2{}^-|Pc|Spiro^+ \quad (5)$$

where τ_{et} is the time constant of the electron transfer from Pc^- into TiO_2.

In addition to the reaction sequence depicted by eqs 4 and 5, the long-distance CS state can be obtained by a competing process. Here, the electron is first injected from the Pc* into TiO_2, followed by the hole transfer from the Pc^+ to the Spiro

$$TiO_2|Pc^*|Spiro \xrightarrow{\tau_{inj}} TiO_2{}^-|Pc^+|Spiro \xrightarrow{\tau_{ht}} TiO_2{}^-|Pc|Spiroo^+ \quad (6)$$

where τ_{ht} is the time constant of the hole transfer from Pc^+ to Spiro.

The electron injection time constant, τ_{inj}, in the sample without Spiro is roughly 0.12 ps, and it competes with the CS at Pc*|Spiro having time constant of ≈1 ps. In a homogeneous system, a process with a few times longer time constant would be very inefficient. The Pc monolayer on TiO_2 is, however, not homogeneous. Even more importantly, noticing a gradual change in the absorption spectra of the samples with and without Spiro, one can expect that Spiro changes the packing of the Pc molecules on the semiconductor surface. More specifically, it is likely that Spiro molecules tend to penetrate between the Pcs, thus reducing inter-Pc interactions and enforcing an upright orientation of the Pc molecules on the TiO_2 surface. The latter has an effect of increased distance from the Pc core to the surface and will result in a slower electron injection into TiO_2.

The reaction sequence in eq 6 would result in a relatively sharp transient band at 860 nm and a broad band around 540 nm corresponding to Pc^+, which would later transform into a broad band around 530 nm and a broad absorption in the NIR region. The observed TA response of the TiO_2|Pc/CDCA|Spiro sample has no such features. Furthermore, the singlet excited state features for the Pc can be noticed in the time-resolved spectra at delay times as long as 0.2 ps as sub-band structures in the 590−650 nm region. Therefore, the main relaxation pathway of the excited state is the sequence of reactions 4 and 5, with average reaction time constants $\tau_{sp} \approx 1$ ps and $\tau_{et} \approx 170$ ps.

The TA responses of the most aggregated sample, Pc layer without the co-adsorbate, are shown in Figure 9. The essential

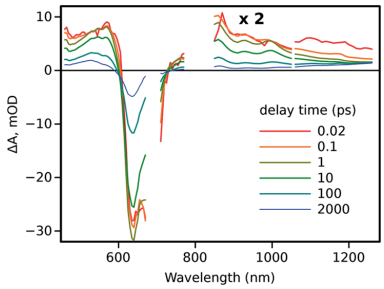

Figure 9. Time-resolved TA spectra of the TiO_2|Pc|Spiro sample. The NIR response (840−1260 nm) is multiplied by 2.

difference with the nonaggregated sample at short delay times is the virtually nonresolved singlet excited state of the Pc. Overall, the spectra of pure Pc samples with (Figure 9) and without (Figure 5a) Spiro are very similar at least within the first 100 ps relaxation time, though the Pc^- band is more pronounced in the sample with Spiro top layer. This suggests that intra-aggregate CS is the dominating reaction pathway. At longer delay times, a broad NIR band attributed to $Spiro^+$ becomes visible, though the intensity of the band is much lower for the sample without a co-adsorbate. The global exponential fitting of the TA data is presented in Figure S9 in the Supporting Information. The fitting results suggest that the intra-aggregate CS takes place with a time constant $\tau_{agg} \approx 0.16$ ps, and the following relaxation of the Pc^- takes place in the time interval 1−300 ps. These time constants are slightly longer than in the case of the sample without Spiro, but the difference is rather marginal.

Comparison of the TA spectra in Figures 8 and 9 indicates that at long delay times the yield of the long-distance CS state, $TiO_2{}^-|Pc|Spiro^+$, is higher in the Pc/CDCA = 1:50 sample, which is seen as higher relative intensities at 530 and 1250 nm. However, there are probably still some losses in the long-distance CS yield at few hundred picosecond delay time even in the 1:50 sample, because the component with the 170 ps time constant (Figure 8b) has an IR tail with intensity rising toward longer wavelengths, though this IR tail is smaller in intensity than that of the longest lived component (>20 ns in Figure 8b). This means that some of the Pc anions may relax as the result of CR at the $Pc^-|Spiro^+$ interface, instead of donating an electron to TiO_2. The effect of this relaxation on the solar cell performance depends on time needed for the hole to reach the cathode, if holes leave the HTM faster than the relaxation constant, the relaxation will have no considerable effect on the cell performance.

DOI: 10.1021/acsomega.8b00600
ACS Omega 2018, 3, 4947−4958

The TA responses for the samples with Pc/CDCA = 1:10 and Pc/OA = 1:10 are shown in the Supporting Information (Figures S10–S13). The responses take intermediate positions between the sample with high concentration of CDCA (Pc/CDCA = 1:50) and the sample without a co-adsorbent, though the response of Pc/CDCA = 1:10 is very close to that of Pc/CDCA = 1:50 sample, whereas the response of the Pc/OA = 1:10 sample is closer to that of the pure Pc sample.

2.4. Solar Cells. To study the effect of aggregation of photocurrent generation in solar cells, silver electrodes were deposited on top of the samples with Spiro hole transporting layer, and standard current–voltage (I–V) characteristics where measured in the dark and under "one sun" (AM 1.5) illumination. Typical I–V curves are presented in Figure 10 for

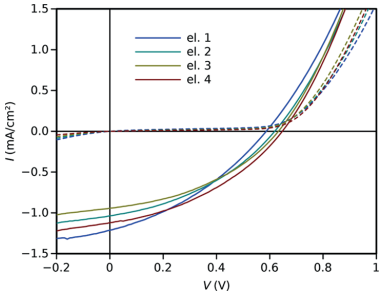

Figure 10. Current–voltage characteristics of Pc/CDCA = 1:20 sample in the dark (dashed lines) and under illumination (solid lines). One sample had four electrode pairs with an overlap area of roughly 2 mm^2.

Pc/CDCA = 1:20 sample. Each sample had four electrode pairs with an overlap area of roughly 2 mm^2. The variation in I–V curves of different electrode pairs on the sample was reasonably small, as can be seen in Figure 10.

The obtained PCEs were in the range 0.1–0.4% for the samples discussed here. This is roughly 1 order in magnitude lower than the efficiencies reported for the best ssDSSCs with the same Pc.[31] However, the primary goal of this part is to compare the results of ultrafast spectroscopy study of the primary photoreactions with the properties of the complete ssDSSCs. Therefore, the samples were optimized to get most out of the spectroscopy measurements but not to achieve the highest PCE. The aim is also to get a fair comparison of different sensitizer/co-adsorbate combinations. This means in particular that all samples have to be prepared with the same TiO_2 base structure to ensure that the samples infiltrated by Spiro similarly. The thickness of the TiO_2 film was selected such that the absorption of Pc at maximum (Q-band) is close to 1 (OD), which is the maximum reasonable value for accurate pump-probe measurement. As the result, the absorption of the sample with a high relative concentration of co-adsorbate (e.g. Pc/CDCA = 1:100 in sensitization solution) was rather low, around 0.15 (OD), which is still sufficient for TA measurements but far from optimum for efficient power conversion.

The parameter of interest for this study is the internal conversion efficiency (ICE), or the ratio of the generated electrons to absorbed photons, ϕ_{ICE}. The electron flux can be obtained directly from the measured short circuit current, I_{sc} (I at V = 0 in Figure 10). However, the number of absorbed photons cannot be measured directly and has to be evaluated from the available data. This number can be evaluated from the excitation photon flux and sample absorption.

The Pc samples have main absorption bands in the range 580–720 nm, which is commonly referred to as the Q-band area. Another absorption band commonly referred to as the Soret band is at wavelengths shorter than 400 nm and its intensity is few times lower than that of the Q-band. Also, the sun intensity is maximal in the Q-band area and decreases sharply at <400 nm. Therefore, the spectral area of significance for the studied samples is the Q-band area, and for all samples, it is within the range 550–750 nm. The sunlight intensity does not change much within this range having the average value P_{650} = 1.24 W m^{-2} nm^{-1} with standard deviation 0.12 W m^{-2} nm^{-1}.[44] Therefore, to compare light harvesting efficiencies of the samples, average absorptances, a_{av}, were calculated in the range 550–750 nm. As an example, the values of a_{av} are 0.37, 0.29, and 0.045 for Pc/CDCA samples with ratios 1:0, 1:10, and 1:100, respectively, which means that the pure Pc sample (1:0) absorbs 37% of photons in the range 550–750 nm, and the 1:100 sample absorbs only 4.5% of photons in this range (see Figure S14 in Supporting Information).

2.4.1. Photocurrent Generation Efficiency. To compare the quantum efficiency of the photocurrent generation, the short circuit I_{sc} was divided by a_{av}, to account for absorbed photons only. Reference samples without the co-adsorbate were prepared a few times (five series) during the tests, and the ratios $I_{norm} = I_{sc}/a_{av}$ for these samples were averaged and used to normalized the ratios obtained for all other samples, thus calculating "relative" current values $I_{rel}(x) = I_{norm}(x)/I_{norm}(0)$, where x is the co-adsorbate concentration and $I_{norm}(0)$ is the average or all samples without the co-adsorbate. The results of calculations are presented in Figure 11 as a function of the

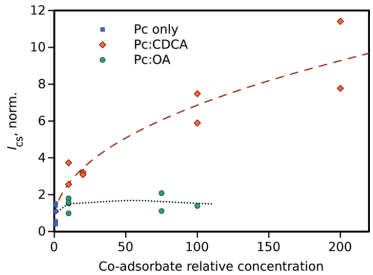

Figure 11. Relative photocurrent generation efficiencies, I_{rel}, plotted as a function of relative co-adsorbate concentration. Values are normalized to the average of the samples without the co-adsorbate. The lines are indicating trends for visual guidance.

relative co-adsorbate concentration and show increase or decrease of ICE of the sample relative to the average value of samples without the co-adsorbate. Although there is relatively large deviation of the result for the samples with the same composition, addition of CDCA has a clear effect of gradual increase of the quantum efficiency of the photocurrent generation. According to this estimation, the quantum efficiency is roughly 3 times higher for 1:10 and 1:20 samples, and it increases furthermore for 1:100 and 1:200 samples.

The same results are summarized in Table 1 by averaging relative efficiencies (I_{rel}) for the samples of the same composition. Also, it has to be noted that the standard deviation of the relative efficiencies were rather high, 20–50%.

DOI: 10.1021/acsomega.8b00600
ACS Omega 2018, 3, 4947–4958

Table 1. Relative Efficiency of the CS at the Semiconductor–Organic Interface of Spiro-Containing Samples Estimated from TA and Photocurrent Measurements[a]

sample	ΔA_{rel} (2 ps)	ΔA_{rel} (2 ns)	I_{rel}
Pc only	0.15	0.12	1.0
Pc/CDCA = 1:10	0.25	0.16	3.1
Pc/CDCA = 1:20			3.2
Pc/CDCA = 1:50	0.29	0.14	
Pc/CDCA = 1:100	0.27	0.20	6.7
Pc/CDCA = 1:200			9.6
Pc/OA = 1:10	0.13	0.06	1.5
Pc/OA = 1:75			1.6
Pc/OA = 1:100	0.16	0.13	1.4

[a]The relative TA values (ΔA_{rel}()) were calculated by taking absorbance change at 1250 nm at 2 ps and 2 ns delay time and dividing by the change at 860 nm right after the excitation, and relative photocurrents (I_{rel}) are the short-circuit currents of the samples with to that without the co-adsorbate and normalized to average sample absorptance (a_{av}) in the 550–750 nm range (see the text for details).

The efficiency estimation of the long-distance CS based on spectroscopy is more complex as it requires quantitative knowledge of the absorption spectra of the intermediate states of interest, namely, primary excited sensitizers and states involved in photocurrent generation. The conduction band electrons in TiO_2 have no distinct spectroscopic features which can be seen on top of TA responses of Pc and Spiro. However, the Spiro cation has two features, the band at 530 nm and the broadband absorption at >1000 nm. The NIR absorption of $Spiro^+$ seems to be a better choice because the Pc cation and anion have negligible absorption at the red side of the measured range. Therefore, the TA response at 1250 nm can be used as an indicator of the $Spiro^+$ yield at least at delay time >1 ps, that is, after relaxation of the singlet excited state of Pc which also has some absorption at this wavelength, as can be seen in response of all samples at short delay time (<0.1 ps). The primary excited sensitizer in our case is the singlet excited state of Pc. The absorption at a short delay time (e.g. at 0.02 ps in Figure 9) is the strongest at 860 nm, and it can be taken as the measure of the number of excited Pcs. Therefore, the ratio of the absorbances at 1250 nm at a long delay time to that at 860 nm right after the excitation, $\Delta A_{rel} = \Delta A_{1260}/\Delta A_{860}$, must be proportional to quantum yield of (absorbed) photons to hole conversion. These relative absorption changes were calculated for two delay times, 2 ps and 2 ns, and presented in Table 1 (denoted as ΔA_{rel}(2 ps) and ΔA_{rel}(2 ns), respectively).

A common trend for both ΔA_{rel} and I_{rel} seen in Table 1 is the increase in the efficiency of $Spiro^+$ and current generation with the increase of CDCA concentration, though the increase of I_{rel} is larger than of ΔA_{rel}. According to the TA responses discussed above, this increase can be attributed to the lower Pc aggregation upon addition of CDCA, suppressing the undesired intra-aggregate CS. Interestingly, at a longer delay time, 2 ns, the yield is virtually the same for three first samples in the table. This may be interpreted in favor of a relatively fast hole diffusion to the electrode, so that slow (nanosecond) CRs does not affect photocurrent generation. Though TA measurements are rather difficult after top electrode deposition and were not carried out.

Both TA and photocurrent measurements do not show significant increase in photon-to-current efficiency on addition of OA co-adsorbate, although the absorption spectra (Figure 2b) suggest a gradual decrease in the aggregation degree. One possible explanation for this difference between CDCA and OA is the length difference between the molecules. A rough estimation of the CDCA molecule length is 1.2 nm, which is close to or a little shorter than the length of Pc molecules standing upright on the TiO_2 surface. The length of OA is roughly 1.6 nm, or longer than the Pc molecule, which may prevent a sufficient contact between the Pc and Spiro needed for efficient electronic interactions at the PcISpiro interface and may thus explain the lower hole transfer efficiency to Spiro in the OA-containing samples. However, this explanation is in contradiction with the observed change in the Pc absorption spectrum after the deposition of Spiro. Still it seems to be reasonable to suggest that some structural difference between the Pc/CDCA and Pc/OA SAMs is responsible for the difference in the photophysics of the samples. Another obvious reason for the relatively poor results with OA co-adsorbate is rather fast sample degradation especially at higher OA concentrations, as was mentioned above.

The absolute value of the quantum efficiency can be estimated using excitation power density, P_{650}, short circuit current, I_{sc}, and average absorptances, a_{av} (see Supporting Information for the details of calculations). This estimation suggests that the quantum yield of photon-to-electron conversion is roughly 13% for the samples without the co-adsorbate, close to 40% for 1:10 and 1:20 Pc/CDCA samples, and approaches 100% for 1:100 and 1:200 samples. The latter is least accurate as the estimation accuracy depends critically on average absorption calculation, which in turn depends on accuracies of subtracting "background absorption" of TiO_2 and spectra correction procedure after the deposition of Spiro.

The absolute values of external PCEs for this series was higher for Pc/CDCA = 1:10 and 1:20 samples than for the samples without CDCA by a factor of 2 (0.4 vs 0.15%). For 1:100 samples the efficiency dropped down to that of the samples without CDCA, but average absorptance, a_{av}, of the 1:100 sample is only 0.045 (in the 550–750 nm range), whereas for the sample without CDCA $a_{av} \approx 0.5$, or the 1:100 sample uses absorbed photons 10 times more efficiently than the sample without CDCA. The 1:100 sample is not efficient in absorbing light because its optical density is only 0.12 at the maximum of the Q-band (695 nm) and the spectrum band width is roughly 30 nm only. One obvious approach to increase cell efficiency could be to increase the thickness of TiO_2 nanoparticle film, though in this case the thickness must be increased by 10 times at least (to be $\geq$20 μm), which will create another problem of pore filling with the HTM.[15]

Another approach to increase the PCE of Pc-based solar cells is to use co-adsorbates with chromophores, which would work as a light harvesting subsystem in a way similar to that reported by M'Sabah et al.,[43] absorbing the solar light and delivering the excited state energy to Pc by the nonradiating energy transfer mechanism. This approach may also help to solve another problem of Pc sensitizers, weak absorption in the green part of the spectrum, if the light harvesting co-adsorbate is designed to cover the green-yellow part of the spectrum. Also, mixing Pc with sensitizers utilizing the green-yellow part of the spectrum, such as porphyrins,[17] may also help to solve the problem.

3. CONCLUSIONS

Aggregation of Pcs is usually considered as the most detrimental factor to the efficiency of Pc-sensitized DSSCs. The results reported here are in full agreement with this notion

DOI: 10.1021/acsomega.8b00600
ACS Omega 2018, 3, 4947–4958

and indicate that intra-aggregate CS is the main mechanism of the excited state deactivation. A traditional method to reduce aggregation is to use co-adsorbate molecules. One of the most widely used compounds for this purpose is CDCA. For comparison, we have used OA as well. Addition of the co-adsorbate reduces the aggregation gradually, as can be seen from the steady-state absorption spectra change and transient responses of the samples.

Addition of a hole-transporting layer of Spiro-MeOTAD changes the primary CS events quite drastically, switching the main reaction route to the CS at the organic−organic interface, Pc|Spiro, instead of the electron injection at TiO_2|Pc. In the case of aggregated Pc layer deposited without the co-adsorbate, the intramolecule interactions compete with the CS and reduce the efficiency of CS at the Pc|Spiro interface. However, mixing Pc with CDCA at ratios larger than 1:20 (in sensitizing solution) reduces the aggregation effect to a negligible level, thus generating the $Pc^-|Spiro^+$ state with almost unity yield.

The increase in quantum yield of photocurrent generation was also confirmed by depositing top electrodes on the TiO_2|Pc|Spiro structures and comparing short circuit currents of the cells. An estimation suggests that the quantum yield of photon-to-current conversion is less than 15% for samples without the co-adsorbate but can be increased to almost unity by mixing Pc with CDCA at ratio 1:100. However, at this ratio, the PCE is few times lower than for the best sample in the series because of very low absorption of the sample (OD < 0.15 at the Q-band maximum).

4. METHODS AND MATERIALS

4.1. Materials. EtOH (≥99.5% by mass) was purchased from Altia Plc. 2,2′,7,7′-Tetrakis(*N*,*N*-di-*p*-methoxyphenylamino)-9,9′-spirobifluorene (Spiro-MeOTAD or Spiro) was purchased from Lumtec (Luminescence Technology Corp.). TiO_2 nanoparticle paste was purchased from Solaronix (Ti-Nanoxide T/SP) and from Dyesol (18NR-T). CDCA and OA were used as co-adsorbates to reduce aggregation in the Pc monolayers. They were purchased from Sigma-Aldrich along with all other solvents and chemicals and used without further purification. FTO-coated glass substrates (TEC7) were purchased from Sigma-Aldrich and cleaned as described below. Zinc carboxyphthalocyanine (Pc, Figure 1) derivative used in this study and also known as TT1 was synthesized according to a protocol described elsewhere.[23]

4.2. Samples. The FTO-coated glass substrates were cut to approx. 20 × 20 mm substrates and patterned by mechanical etching with a grinding tool. After the patterning, the substrates were washed by 15 min sonication in 2% aqueous Hellmanex III solution, followed by 15 min sonication in 2-propanol, and dried under vacuum.

A thin TiO_2 compact layer was used as a hole-blocking layer. The layer was prepared by spin-coating (3000 rpm, 30 s) a 0.22 M solution of titanium isopropoxide in acidic EtOH (13 mM of HCl) onto the cleaned and patterned FTO substrates, followed by sintering at 475 °C for 45 min in air. For better film quality, the spin-coating and sintering procedure was repeated.

TiO_2 mesoporous layers were prepared by screen-printing and by spin-coating. For the screen-printed layers, the Ti-Nanoxide T/SP paste was screen-printed on top of the substrates through a 77−55 mesh (mesh thickness, 87 μm). For the spin-coated layers, the Dyesol 18 NR-T paste was diluted in EtOH at a 2:5 weight ratio and spin-coated (1000 rpm, 45 s) onto the substrates. After depositing the TiO_2 mesoporous layer, the substrates were sintered again at 475 °C. The TiO_2 nanoparticle film thickness was approx. 2.5 μm for the screen-printed layers and approx. 800 nm for the spin-coated layers, respectively. Typical cross-section electron microscopy images are shown in Supporting Information Figure S1.

To increase the surface roughness in the TiO_2 layer and therefore to adsorb more dye, the TiO_2 substrates were treated with aqueous $TiCl_4$. A 2 M aqueous stock solution of $TiCl_4$ was prepared: 1.56 mL of Milli-Q H_2O was frozen with a stir bar, 440 μL of $TiCl_4$ was added dropwise in an ice bath, and the solution was stirred for 10 min. The 2 M stock solution was then diluted into 0.02 M, and the substrates were immersed into this solution at 70 °C for 30 min and washed thoroughly with Milli-Q H_2O. The substrates were sintered after the $TiCl_4$ treatment, and after sintering they were ready for staining.

To deposit SAMs of the Pc with and without the co-adsorbates, the substrates were immersed into solutions of the Pc, typically for 20 h. The solutions were prepared in *t*-BuOH/MeCN 1:1 (vol/vol) at 0.1 mmol/L concentration. The co-adsorbates were added into the solutions at different Pc to co-adsorbate molar ratios ranging from 1:10 to 1:100 or using concentration of co-adsorbates up to 10 mM. After the reaction, the substrates were removed from the Pc solutions and washed by immersing them for 5 min into the *t*-BuOH/MeCN mixture.

The sensitized TiO_2 samples were coated with a hole transporting layer, Spiro, following a reported procedure. Spiro was doped with bis(trifluoromethane)sulfonimide lithium salt (LiTFSI) and 4-*tert*-butylpyridine (*t*-BP) for a better hole conductivity. The hole transporting layer was prepared by spin-coating typically a 214 g/L solution of Spiro with 23 mM of LiTFSI and 233 mM of *t*-BP in anhydrous chlorobenzene onto the sensitized TiO_2 substrates. The solution was allowed to diffuse into the TiO_2 mesoporous layer for 30 s after the spreading. Then, the samples were rotated for 60 s at 1000 rpm. To ensure that sufficient amount of Spiro was deposited, cross-section scanning electron microscopy (SEM) images of the samples were taken, in which a thin Spiro layer on top of the TiO_2 film can be seen (see Supporting Information Figure S1).

For the solar cell measurements, the sample structure was finalized by thermally evaporating a 75 nm Ag electrode on top of the sample structure at a high vacuum (approx. 10^{-6} mbar). The electrode areas were typically 2−3 mm^2.

4.3. Instruments. Absorption spectra of the samples were measured using a Shimadzu UV-1800 UV−Vis−NIR spectrophotometer in the range 350−850 nm.

The sample morphology was investigated using a field-emission SEM (Carl Zeiss Ultra 55).

Standard solar cell characterization was carried out by measuring *I*−*V* curves (Agilent Tech. E5272A source/monitoring unit) in the dark and under one sun (AM 1.5) illumination (Sciencetech SS150 solar simulator).

Ultrafast TA responses of the samples were measured using a pump-probe system described previously.[46,47] Briefly, the samples were excited by laser pulses at 695 nm (Libra F, Coherent Inc., coupled with Topas C, Light Conversion Ltd.). A white continuum generator (sapphire crystal) was used to produce the probe beam. The TA responses were measured using an ExciPro TA spectrometer (CDP, Inc.) equipped with a CCD array for the visible spectral range (460−770 nm) and an InGa diode array for the NIR wavelengths (840−1045 and 1050−1260 nm). The pulse repetition rate of the laser system was 1 kHz and the spectra were typically acquired by averaging

DOI: 10.1021/acsomega.8b00600
ACS Omega 2018, 3, 4947−4958

over 5 s. Typical time resolution of the instrument was 100 fs. Data collected in the three wavelength ranges were fitted globally to a sum of exponential functions or a combination of exponential, stretched-exponential, and distributed decay models.[48] The fit program accounted for the instrument response (through a deconvolution process) and did the group velocity dispersion compensation. Therefore, the generated time-resolved spectra were free of dispersion and had an "improved" time resolution.

■ ASSOCIATED CONTENT

Supporting Information

The Supporting Information is available free of charge on the ACS Publications website at DOI: 10.1021/acsomega.8b00600.

Cross-section SEM images of the studied samples, absorption spectra of Pc in solutions, details of spectra fitting in the Q-band region, spectra fits, absorption spectra of Pc/CDCA = 1:10 and Pc/OA = 1:10 samples, normalized TA decays of Pc/CDCA = 1:50 with Spiro, time-resolved and component TA spectra of Pc/CDCA = 1:10, pure PcISpiro, Pc/CDCA, and PcOA 1:10 with Spiro, absorptance spectra of 1:0, 1:10, and 1:100 Pc/CDCA samples used photocurrent measurements, and dependence of efficiency on the relative concentration of CDCA (PDF)

■ AUTHOR INFORMATION

Corresponding Authors

*E-mail: tomas.torres@uam.es (T.T.).
*E-mail: nikolai.tkachenko@tut.fi (N.V.T.).

ORCID

Kirsi Virkki: 0000-0003-4976-3917
Tomás Torres: 0000-0001-9335-6935
Nikolai V. Tkachenko: 0000-0002-8504-2335

Notes

The authors declare no competing financial interest.

■ ACKNOWLEDGMENTS

K.V. acknowledges the Doctoral Programme of Tampere University of Technology for the financial support. N.V.T. acknowledges NATO SPS project no. 985043. Financial support from Comunidad de Madrid, Spain (S2013/MIT-2841, FOTOCARBON) and MINECO, Spain (CTQ2014-52869-P and CTQ2017-85393-P) is acknowledged. IMDEA Nanociencia acknowledges support from the "Severo Ochoa" Programme for Centres of Excellence in R&D (MINECO, grant SEV-2016-0686).

■ REFERENCES

(1) Yella, A.; Lee, H.-W.; Tsao, H. N.; Yi, C.; Chandiran, A. K.; Nazeeruddin, M. K.; Diau, E. W.-G.; Yeh, C.-Y.; Zakeeruddin, S. M.; Grätzel, M. Porphyrin-Sensitized Solar Cells with Cobalt (II/III)−Based Redox Electrolyte Exceed 12 Percent Efficiency. *Science* **2011**, *334*, 629−634.

(2) Ye, M.; Wen, X.; Wang, M.; Iocozzia, J.; Zhang, N.; Lin, C.; Lin, Z. Recent Advances in Dye-Sensitized Solar Cells: from Photoanodes, Sensitizers and Electrolytes to Counter Electrodes. *Mater. Today* **2015**, *18*, 155−162.

(3) Hagfeldt, A.; Boschloo, G.; Sun, L.; Kloo, L.; Pettersson, H. Dye-Sensitized Solar Cells. *Chem. Rev.* **2010**, *110*, 6595−6663.

(4) Asbury, J. B.; Hao, E.; Wang, Y.; Ghosh, H. N.; Lian, T. Ultrafast Electron Transfer Dynamics from Molecular Adsorbates to Semiconductor Nanocrystalline Thin Films. *J. Phys. Chem. B* **2001**, *105*, 4545−4557.

(5) Furube, A.; Katoh, R.; Hara, K. Electron injection dynamics in dye-sensitized semiconductor nanocrystalline films. *Surf. Sci. Rep.* **2014**, *69*, 389−441.

(6) Martín, C.; Ziółek, M.; Douhal, A. Ultrafast and fast charge separation processes in real dye-sensitized solar cells. *J. Photochem. Photobiol., C* **2016**, *26*, 1−30.

(7) Němec, H.; Rochford, J.; Taratula, O.; Galoppini, E.; Kužel, P.; Polívka, T.; Yartsev, A.; Sundström, V. Influence of the Electron-Cation Interaction on Electron Mobility in Dye-Sensitized ZnO and TiO_2 Nanocrystals: A Study Using Ultrafast Terahertz Spectroscopy. *Phys. Rev. Lett.* **2010**, *104*, 197401.

(8) Milot, R. L.; Moore, G. F.; Crabtree, R. H.; Brudvig, G. W.; Schmuttenmaer, C. A. Electron Injection Dynamics from Photoexcited Porphyrin Dyes into SnO_2 and TiO_2 Nanoparticles. *J. Phys. Chem. C* **2013**, *117*, 21662−21670.

(9) Imahori, H.; Kang, S.; Hayashi, H.; Haruta, M.; Kurata, H.; Isoda, S.; Canton, S. E.; Infahsaeng, Y.; Kathiravan, A.; Pascher, T.; Chábera, P.; Yartsev, A. P.; Sundström, V. Photoinduced Charge Carrier Dynamics of Zn−Porphyrin−TiO_2 Electrodes: The Key Role of Charge Recombination for Solar Cell Performance. *J. Phys. Chem. A* **2011**, *115*, 3679−3690.

(10) Antila, L. J.; Myllyperkiö, P.; Mustalahti, S.; Lehtivuori, H.; Korppi-Tommola, J. Injection and Ultrafast Regeneration in Dye-Sensitized Solar Cells. *J. Phys. Chem. C* **2014**, *118*, 7772−7780.

(11) Cappel, U. B.; Smeigh, A. L.; Plogmaker, S.; Johansson, E. M. J.; Rensmo, H.; Hammarström, L.; Hagfeldt, A.; Boschloo, G. Characterization of the Interface Properties and Processes in Solid State Dye-Sensitized Solar Cells Employing a Perylene Sensitizer. *J. Phys. Chem. C* **2011**, *115*, 4345−4358.

(12) Howard, I. A.; Meister, M.; Baumeier, B.; Wonneberger, H.; Pschirer, N.; Sens, R.; Bruder, I.; Li, C.; Müllen, K.; Andrienko, D.; Laquai, F. Two Channels of Charge Generation in Perylene Monoimide Solid-State Dye-Sensitized Solar Cells. *Adv. Energy Mater.* **2014**, *4*, 1300640.

(13) Humphry-Baker, N.; Driscoll, K.; Rao, A.; Torres, T.; Snaith, H. J.; Friend, R. H. Time-Evolution of Poly(3-Hexylthiophene) as an Energy Relay Dye in Dye-Sensitized Solar Cells. *Nano Lett.* **2012**, *12*, 634−639.

(14) Qin, P.; Sanghyun, P.; Dar, M. I.; Rakstys, K.; ElBatal, H.; Al-Muhtaseb, S. A.; Ludwig, C.; Nazeeruddin, M. K. Weakly Conjugated Hybrid Zinc Porphyrin Sensitizers for Solid-State Dye-Sensitized Solar Cells. *Adv. Funct. Mater.* **2016**, *26*, 5550−5559.

(15) Melas-Kyriazi, J.; Ding, I.-K.; Marchioro, A.; Punzi, A.; Hardin, B. E.; Burkhard, G. F.; Tétreault, N.; Grätzel, M.; Moser, J.-E.; McGehee, M. D. The Effect of Hole Transport Material Pore Filling on Photovoltaic Performance in Solid-State Dye-Sensitized Solar Cells. *Adv. Energy Mater.* **2011**, *1*, 407−414.

(16) Urbani, M.; Grätzel, M.; Nazeeruddin, M. K.; Torres, T. Meso-Substituted Porphyrins for Dye-Sensitized Solar Cells. *Chem. Rev.* **2014**, *114*, 12330−12396.

(17) Ragoussi, M.-E.; Ince, M.; Torres, T. Recent Advances in Phthalocyanine-Based Sensitizers for Dye-Sensitized Solar Cells. *Eur. J. Org. Chem.* **2013**, 6475−6489.

(18) Imahori, H.; Umeyama, T.; Ito, S. Large π-Aromatic Molecules as Potential Sensitizers for Highly Efficient Dye-Sensitized Solar Cells. *Acc. Chem. Res.* **2009**, *42*, 1809−1818.

(19) Higashino, T.; Imahori, H. Porphyrins as excellent dyes for dye-sensitized solar cells: recent developments and insights. *Dalton Trans.* **2015**, *44*, 448−463.

(20) Brogdon, P.; Cheema, H.; Delcamp, J. H. Near-Infrared-Absorbing Metal-Free Organic, Porphyrin, and Phthalocyanine Sensitizers for Panchromatic Dye-Sensitized Solar Cells. *ChemSusChem* **2018**, *11*, 86−103.

(21) Krishna, N. V.; Krishna, J. V. S.; Singh, S. P.; Giribabu, L.; Han, L.; Bedja, I.; Gupta, R. K.; Islam, A. Donor-π-Acceptor Based Stable Porphyrin Sensitizers for Dye-Sensitized Solar Cells: Effect of π-Conjugated Spacers. *J. Phys. Chem. C* **2017**, *121*, 6464−6477.

DOI: 10.1021/acsomega.8b00600
ACS Omega 2018, 3, 4947−4958

(22) Li, X.; Xu, B.; Liu, P.; Hu, Y.; Kloo, L.; Hua, J.; Sun, L.; Tian, H. Molecular engineering of D−A−π−A sensitizers for highly efficient solid-state dye-sensitized solar cells. *J. Mater. Chem. A* **2017**, *5*, 3157−3166.
(23) Cid, J.-J.; Yum, J.-H.; Jang, S.-R.; Nazeeruddin, M. K.; Martínez-Ferrero, E.; Palomares, E.; Ko, J.; Grätzel, M.; Torres, T. Molecular Cosensitization for Efficient Panchromatic Dye-Sensitized Solar Cells. *Angew. Chem., Int. Ed.* **2007**, *46*, 8358−8362.
(24) Ragoussi, M.-E.; Cid, J.-J.; Yum, J.-H.; de la Torre, G.; Di Censo, D.; Grätzel, M.; Nazeeruddin, M. K.; Torres, T. Carboxyethynyl Anchoring Ligands: A Means to Improving the Efficiency of Phthalocyanine-Sensitized Solar Cells. *Angew. Chem., Int. Ed.* **2012**, *51*, 4375−4378.
(25) Li, Y.; Lu, P.; Yan, X.; Jin, L.; Peng, Z. Non-aggregated hyperbranched phthalocyanines: single molecular nanostructures for efficient semi-opaque photovoltaics. *RSC Adv.* **2013**, *3*, 545−558.
(26) Tejerina, L.; Martínez-Díaz, M. V.; Nazeeruddin, M. K.; Torres, T. The Influence of Substituent Orientation on the Photovoltaic Performance of Phthalocyanine-Sensitized Solar Cells. *Chem.—Eur. J.* **2016**, *22*, 4369−4373.
(27) Wang, M.; Plogmaker, S.; Humphry-Baker, R.; Pechy, P.; Rensmo, H.; Zakeeruddin, S. M.; Grätzel, M. Molecular-Scale Interface Engineering of Nanocrystalline Titania by Co-adsorbents for Solar Energy Conversion. *ChemSusChem* **2012**, *5*, 181−187.
(28) Günsel, A.; Güzel, E.; Bilgiçli, A. T.; Şişman, I.; Yarasir, M. N. Synthesis of non-peripheral thioanisole-substituted phthalocyanines: Photophysical, electrochemical, photovoltaic, and sensing properties. *J. Photochem. Photobiol., A* **2017**, *348*, 57−67.
(29) Jungsuttiwong, S.; Sirithip, K.; Prachumrak, N.; Tarsang, R.; Sudyoadsuk, T.; Namuangruk, S.; Kungwan, N.; Promarak, V.; Keawin, T. Significant enhancement in the performance of porphyrin for dye-sensitized solar cells: aggregation control using chenodeoxycholic acid. *New J. Chem.* **2017**, *41*, 7081−7091.
(30) Hsu, C.-Y.; Chen, Y.-C.; Lin, R. Y.-Y.; Ho, K.-C.; Lin, J. T. Solid-state dye-sensitized solar cells based on spirofluorene (spiro-OMeTAD) and arylamines as hole transporting materials. *Phys. Chem. Chem. Phys.* **2012**, *14*, 14099−14109.
(31) Li, X.; Xu, B.; Liu, P.; Hu, Y.; Kloo, L.; Hua, J.; Sun, L.; Tian, H. Molecular engineering of D−A−π−A sensitizers for highly efficient solid-state dye-sensitized solar cells. *J. Mater. Chem. A* **2017**, *5*, 3157−3166.
(32) Nojiri, T.; Alam, M. M.; Konami, H.; Watanabe, A.; Ito, O. Photoinduced Electron Transfer from Phthalocyanines to Fullerenes (C_{60} and C_{70}). *J. Phys. Chem. A* **1997**, *101*, 7943−7947.
(33) Ou, Z.; Jiang, Z.; Chen, N.; Huang, J.; Shen, J.; Kadish, K. M. Electrochemistry and spectroelectrochemistry of tetra-α-substituted metallophthalocyanines. *J. Porphyrins Phthalocyanines* **2008**, *12*, 1123−1133.
(34) Grätzel, M.; Bach, U.; Lupo, D.; Comte, P.; Moser, J. E.; Weissörtel, F.; Salbeck, J.; Spreitzer, H. Solid-State Dye-Sensitized Mesoporous TiO_2 Solar Cells with High Photon-to-Electron Conversion Efficiencies. *Nature* **1998**, *395*, 583−585.
(35) Virkki, K.; Hakola, H.; Urbani, M.; Tejerina, L.; Ince, M.; Martínez-Díaz, M.; Torres, T.; Golovanova, V.; Golovanov, V.; Tkachenko, N. V. Photoinduced Electron Injection from Zinc Phthalocyanines into Zinc Oxide Nanorods: Aggregation Effects. *J. Phys. Chem. C* **2017**, *121*, 9594−9605.
(36) Kakade, S.; Ghosh, R.; Palit, D. K. Excited State Dynamics of Zinc-Phthalocyanine Nanoaggregates in Strong Hydrogen Bonding Solvents. *J. Phys. Chem. C* **2012**, *116*, 15155−15166.
(37) Guldi, D. M.; Zilbermann, I.; Gouloumis, A.; Vázquez, P.; Torres, T. Metallophthalocyanines: Versatile Electron-Donating Building Blocks for Fullerene Dyads. *J. Phys. Chem. B* **2004**, *108*, 18485−18494.
(38) Fukuzumi, S.; Ohkubo, K.; Ortiz, J.; Gutiérrez, A. M.; Fernández-Lázaro, F.; Sastre-Santos, Á. Formation of a Long-Lived Charge-Separated State of a Zinc Phthalocyanine-Perylenediimide Dyad by Complexation with Magnesium Ion. *Chem. Commun.* **2005**, *30*, 3814−3816.
(39) Mack, J.; Stillman, M. J. Photochemical Formation of the Anion Radical of Zinc Phthalocyanine and Analysis of the Absorption and Magnetic Circular Dichroism Spectral Data. Assignment of the Optical Spectrum of $[ZnPc(-3)]^-$. *J. Am. Chem. Soc.* **1994**, *116*, 1292−1304.
(40) Hakola, H.; Sariola-Leikas, E.; Efimov, A.; Tkachenko, N. V. Effect of Hole Transporting Material on Charge Transfer Processes in Zinc Phthalocyanine Sensitized ZnO Nanorods. *J. Phys. Chem. C* **2016**, *120*, 7044−7051.
(41) Konarev, D. V.; Khasanov, S. S.; Lyubovskaya, R. N. Effect of Deprotonation and Reduction on the Molecular Structure and Optical and Magnetic Properties of Metal-Free Phthalocyanine (Pc): Comparison of H2Pc− and HPc− Anions. *Asian J. Org. Chem.* **2017**, *6*, 1028−1033.
(42) Lemmetyinen, H.; Tkachenko, N.; Efimov, A.; Niemi, M. Transient states in photoinduced electron transfer reactions of porphyrin- and phthalocyanine-fullerene dyads. *J. Porphyrins Phthalocyanines* **2009**, *13*, 1090−1097.
(43) Hakola, H.; Perros, A. P.; Myllyperkiö, P.; Kurotobi, K.; Lipsanen, H.; Imahori, H.; Lemmetyinen, H.; Tkachenko, N. V. Photo-Induced Electron Transfer at Nanostructured Semiconductor−Zinc Porphyrin Interface. *Chem. Phys. Lett.* **2014**, *592*, 47−51.
(44) U.S. Department of Energy (DOE)/NREL/ALLIANCE. Reference Solar Spectral Irradiance: Air Mass 1.5. http://rredc.nrel.gov/solar/spectra/am1.5/ (accessed 2018-02-03).
(45) M'Sabah, B. L.; Boucharef, M.; Warnan, J.; Pellegrin, Y.; Blart, E.; Lucas, B.; Odobel, F.; Bouclé, J. Amplification of light collection in solid-state dye-sensitized solar cells via the antenna effect through supramolecular assembly. *Phys. Chem. Chem. Phys.* **2015**, *17*, 9910−9918.
(46) Virkki, K.; Demir, S.; Lemmetyinen, H.; Tkachenko, N. V. Photoinduced Electron Transfer in CdSe/ZnS Quantum Dot−Fullerene Hybrids. *J. Phys. Chem. C* **2015**, *119*, 17561−17572.
(47) Stranius, K.; George, L.; Efimov, A.; Ruoko, T.-P.; Pohjola, J.; Tkachenko, N. V. Photophysical Study of a Self-Assembled Donor-Acceptor Two-Layer Film on TiO_2. *Langmuir* **2015**, *31*, 944−952.
(48) Lehtivuori, H.; Efimov, A.; Lemmetyinen, H.; Tkachenko, N. V. Distributed Decay Kinetics of Charge Separated State in Solid Films. *Chem. Phys. Lett.* **2007**, *437*, 238−242.

DOI: 10.1021/acsomega.8b00600
ACS Omega 2018, 3, 4947−4958